Measurements of W boson properties at $\sqrt{s}$=5 and 13 TeV with the ATLAS detector at the LHC

Tairan Xu

université PARIS-SACLAY

NNT : 2019SACLS282

Thèse de doctorat

UNIVERSITÉ PARIS SUD

Comprendre le monde, construire l'avenir

Measurements of W boson properties at $\sqrt{s} = 5$ and 13 TeV with the ATLAS detector at the LHC

Thèse de doctorat de University of Science and Technology of China
et de l'Université Paris-Saclay
préparée à l'Université Paris-Sud
au sein du CEA/Irfu

Ecole doctorale n°576 Particules, Hadrons, Énergie, Noyau, Instrumentation, Imagerie, Cosmos et Simulation (PHENIICS)
Spécialité de doctorat : Physique des particules

Thèse présentée et soutenue à Gif-sur-yvette, le 25-09-2019, par

TAIRAN XU

Composition du Jury :

M. Réza ANSARI Professeur, Université Paris-Sud (LAL-CNRS/IN2P3)	Président
M. Matthias SCHOTT Professeur, University of Mainz	Rapporteur
M. Yanwen LIU Professeur, University of Science and Technology of China	Rapporteur
M. Aram APYAN Research Associate, Fermi National Accelerator Laboratory	Examinateur
M. Yusheng WU Professeur, University of Science and Technology of China	Examinateur
M. Maarten BOONEKAMP Directeur de Recherche, Université Paris-Saclay (CEA/Irfu)	Co-directeur de thèse
M. Zhengguo ZHAO Professeur, University of Science and Technology of China	Co-directeur de thèse

Abstract

This thesis presents measurements of W boson properties at center-of-mass energies of $\sqrt{s} = 5$ and 13 TeV with special low-pile-up data-set recorded by the ATLAS detector at the LHC. Thanks to an optimal reconstruction of missing transverse momentum, such data have particular importance for precision measurements of W-boson production. Dedicated detector calibration corrections are introduced first in this document, including the reconstruction and energy calibration of the hadronic recoil, the momentum calibration and selection efficiency of leptons. Besides, a new shower-shape reweighting algorithm optimizes the identification electrons with the electromagnetic calorimeter. The thesis describes the selection the W boson signal and devotes specific attention to the evaluation of backgrounds, presenting in particular a new method for the data-driven estimation of backgrounds from multi-jet production. Based on these studies and theoretical predictions, the W-boson transverse momentum distribution and production cross-sections are measured with high precision at two center-of-mass energies. Preliminary studies of the application of these data to the measurement of the W-boson mass are also presented.

Synthèse en français

La motivation

Le modèle standard est l'une des théories les plus réussies en physique des particules, décrivant parfaitement trois types d'interactions et donnant des explications ou des prédictions à toutes les particules qui ont été observées. Dans la validation du modèle standard et la recherche d'une nouvelle physique au-delà du modèle standard, les mesures précises des processus électrofaibles jouent un rôle important. En particulier, le processus de Drell-Yan, défini comme "un boson vectoriel généré à partir de deux quarks se désintègre en deux leptons", est prédit avec précision par la théorie et pragmatique pour une mesure expérimentale d'une extrême précision.

Une opportunité précieuse du processus de Drell-Yan est fournie par la masse de boson-W (M_W). Dans le secteur électrofaible du modèle standard, la masse du boson-W dépend fortement de la masse du quark supérieur (M_t) et du boson de Higgs (M_H). Étant donné les valeurs connues de M_t et M_H, le modèle standard prédit que M_W est de 80360 Mev, avec une incertitude de 8-MeV. Cependant, les effets de diverses théories de BSM, comme la supersymétrie et la théorie efficace sur le terrain, pourrait déplacer la

valeur centrale de M_W de 10-100 MeV. Par conséquent, une mesure directe à M_W avec une incertitude inférieure à de 10 Mev donnera une sonde rigoureuse à la physique BSM. La dernière expérience a été réalisée à l'aide de données recueillies par le détecteur ATLAS au cours du Run-I du LHC, avec une incertitude totale de 19 MeV, y compris des incertitudes théoriques de 14-MeV dues à des effets électrofaibles, à de forts effets d'interaction et à la fonction de distribution des particules (PDF) effets, et conduit par l'incertitude PDF et l'incertitude de W-boson-transverse- impulsion (p_T^W) de la mauvaise modélisation des effets forts. L'incertitude expérimentale est sous-dominante, et peut encore bénéficier des nouvelles connaissances du détecteur ATLAS si réactive la mesure, mais les prévisions théoriques, en particulier les p_T^W et la correction PDF exige des mises à niveau afin d'obtenir la précision cible (10 Mev).

Les PDFs décrivent la fraction de quarks et de gluons en collision, et les réactions partoniques de courte distance utilisent des PDF pour calculer la section transversale. On ne peut pas le prédire directement à partir de la théorie. Au lieu de cela, les intrants expérimentaux à faible échelle énergétique aident PDF à évoluer à toutes les échelles, mais avec une incertitude systématique inévitable. Pour le contraindre, la propriété que PDF est proportionnelle à la section transversale générée du processus de Drell-Yan le long de la rapidité est exploitée. La mesure de la section transversale différentielle du boson W et Z est capable de minimiser l'écart entre la prévision et la réalité, d'où l'incertitude.

L'impulsion transversale du boson W (p_T^W) est caractérisée par des effets forts d'ordre supérieur. L'expérience de la mesure Run-I met en évidence la difficulté que la reprise analytique et la simulation de parton gerbe ne parviennent pas à décrire les données au-dessus du second ordre. Une mesure à p_T^W avec moins de 1% d'incertitude dans les bins de l'étape 5-GeV démêlera cette modélisation erronée afin que toutes les études W-boson puissent en bénéficier, en particulier la mesure de la masse-W où la précision correspondante sera doublée. Cependant, en raison de l'implication profonde des hadrons dans la reconstruction p_T^W, la précision n'est pas réalisable à moins que la collision se produise sous une activité sous-jacente extrêmement faible (interactions autres que le signal), sinon la contamination de fond élevée dégradera la résolution de l'énergie.

L'expérience et les données

La proposition de disposer de ces données spéciales sur les activités sous-jacentes à faible intensité, ou sur les données à faible accumulation est discutée et approuvée. Cette course dédiée est exécutée pendant la Run-II du LHC à$\sqrt{s}$ = 13 TeV et 5 TeV, avec les données recueillies par le détecteur ATLAS, et environ 4 millions et 1,5 millions de W-boson candidats sont recueillis respectivement. Les structures

et mécanismes de l'accélérateur LHC et du détecteur ATLAS sont présentés dans cette thèse. Pour les études sur les bosons-W, les électrons sont reconstruits à partir des traces dans le détecteur interne et des apports d'énergie dans le calorimètre EM; les muons sont reconstruits à partir de pistes enregistrées par le détecteur interne et le spectromètre muon dans champ magnétique supraconducteur; la reconstruction du hadron exploite les informations et les énergies de la voie déposées dans le calorimètre hadronique; les neutrinos sont construits à partir des énergies transversales manquantes des événements entiers. Tous les objets doivent être étalonnés au niveau du détecteur avant d'entrer dans la mesure.

Reconstruction du boson W et étalonnage des objets

Dans un événement de boson-W, la signature principale est un seul électron ou muon et un tas de recul hadronique enregistré dans la direction opposée de boson vecteur. L'énergie, dénotant un mouvement transversal p_T, et la direction, dénotant une pseudo rapidité η. sont deux cinématiques importantes dans la reconstruction. Les bosons-W sont sélectionnés à l'aide de critères de détection, de recul lepton et hadronique bien optimisés pour rejeter les fonds et améliorer la pureté du signal. Le calibrage de l'impulsion des leptons et des recul hadroniques est conçu pour s'adapter à l'environnement à faible accumulation. Et pour rétablir la différence résiduelle entre les leptons dans les données et la simulation, plusieurs corrections sont appliquées. Le facteur d'échelle d'efficacité de la sélection d'électrons nouvellement mesuré introduit la méthode d'extrapolation dans la méthode traditionnelle Tag-and-Probe pour surmonter l'incertitude statistique élevée en adoptant les résultats de l'empilement élevé dans l'étude de faible empilement avec une correction supplémentaire, et réussit à éliminer 70% de l'incertitude dans la mesure de la masse-W. Les précisions des facteurs d'échelle des électrons et des muons sont suffisantes pour toutes les mesures. En outre, en raison du problème d'alignement incorrect dans le suivi muon, l'impulsion muon est biaisé dépendant de la charge. Cependant, la correction officielle d'ATLAS n'a pas permis de rétablir la polarisation sagittale. À l'aide de données à faible accumulation, une correction in situ dérivée des événements de boson-Z explique ce biais avec une incertitude raisonnable. En comparaison avec la version officielle, un changement global est observé, démontrant un terme manquant dans la correction officielle, qui a été rapporté au groupe de performance muon.

Au cours de l'étude de l'identification des électrons, les gerbes électromagnétiques dans le calorimètre ont frappé le point. Suivant la définition, l'identification des électrons repose sur les formes des gerbes, qui montrent un écart observable entre les électrons dans les données et les échantillons simulés en raison de la source inconnue, donc une correction supplémentaire est nécessaire pour couvrir, d'où une incertitude

supplémentaire. Un algorithme de redimensionnement en forme de gerbe est développé pour résoudre ce problème. Les énergies électroniques sont reconstruites à partir d'une structure d'amas cellulaire en calorimètre, et le dépôt d'énergie dans les cellules forment la forme de la gerbe. Par conséquent, cet outil réécrit l'énergie électronique cellule par cellule en fonction de la différence de forme moyenne, puis reconstruit les paramètres de forme de gerbes connexes. Tous les électrons au-dessus d'un seuil d'énergie dans la simulation sont corrigés afin que l'écart soit compris et supprimé. Dans les échantillons corrigés, les gerbes de données sont reproduites, et le rapport d'efficacité d'identification des électrons réels et simulés est nettement plus proche de "1". Cet algorithme est déjà mis en œuvre dans le système logiciel officiel ATALS pour d'autres études, y compris l'identification et l'étalonnage e/gamma, et les analyses de précision du modèle standard.

Mesures des propriétés du boson W

La question suivante pour la mesure du boson-W est l'estimation du contexte, en particulier le multi-jet (MJ), ou le contexte de QCD. Les contextes de MJ impliquent diverses sources et ne peuvent pas être évalués avec précision. L'évaluation axée sur les données est la méthode clé dans l'estimation des nombres et des distributions des contextes de MJ. En commutant la sélection "isolation" de lepton, l'espace de phase inclusif est séparé en ensembles de régions enrichies en jets, où le profil et la quantité du contexte multi-jets sont dérivés et extrapolés à la région de signal. Compte tenu de la luminosité limitée des données à faible accumulation, la stratégie et l'isolement du lepton sont redessinés avec divers tests pour obtenir la précision optimale. L'amélioration la plus significative est une nouvelle correction sur le recul hadronique pour résoudre le problème à long terme resté dans la modélisation de fond et l'extrapolation linéaire. Il corrige l'énergie dans les régions de chevauchement entre les hadrons et les leptons lors du calcul du recul hadronique et après correction, l'accord de données et de prévision est considérablement amélioré. Cette nouvelle stratégie établit une norme avancée ensemble pour l'estimation du contexte multi-jets des études mono-boson-W à faible et élevé empilement.

Trois types de mesures sont prises avec les données à faible accumulation, en commençant par la mesure de la section transversale de production du boson-W. La section transversale est calculée en utilisant la luminosité de collision, le nombre d'événements de signal, le facteur d'acceptation A_W et le facteur de correction C_W correspondant à la fraction d'espace de phase compatible avec le détecteur par rapport à l'espace de phase inclus et la fraction des événements finalement détectés et reconstruits par rapport aux événements qui entrent dans la région compatible avec le détecteur. Les valeurs A_W et C_W sont

évaluées à l'aide de prévisions, multipliées par toutes les données pour les corrections de prévisions. Cette mesure est d'abord effectuée avec une petite quantité de données de 5,02-TeV (un dixième des données à faible accumulation) recueillies en 2015 pour appuyer les études sur les ions lourds et explorer le potentiel des données à faible accumulation. La plupart des méthodes et des corrections présentées ici ont été essayées dans cette mesure. Les sujets non résolus, y compris la modélisation erronée du contexte MJ, le mauvais alignement du muon, l'étalonnage imparfait du recul et les critères de signal trop serrés sont spécifiquement investis plus tard dans les mesures des données à faible accumulation. Malgré le nombre limité d'événements W, l'analyse 5.02-TeV a atteint une précision idéale. Si l'on prend l'ensemble des données à faible accumulation et la méthodologie optimisée, les incertitudes concluantes seront réduites de moitié, et l'accord de canal électron-muon sera considérablement amélioré à $\sqrt{s}$=5 TeV ainsi qu'à 13 TeV, en référence aux résultats avec des données d'empilement élevé à $\sqrt{s}$=13 TeV. Les valeurs de section transversale différentielle de la rapidité sont également mesurées pour limiter les incertitudes PDF, les recherches connexes sont effectuées à$\sqrt{s}$=5.02 TeV, et seront répétées à l'aide des données complètes à faible accumulation. En outre, l'asymétrie de charge et l'asymétrie avant et arrière sont mesurées comme référence des prévisions théoriques.

La distribution transversale de l'impulsion du boson-W est mesurée avec la méthode de dépliage qui une matrice de migration est définie à partir de la simulation pour refléter la connexion entre p_T^W détectée et p_T^W. La stratégie générale est proche de la mesure transversale et la plupart des sources d'incertitude sont les mêmes. Cette mesure n'a pas été menée à terme, mais les résultats actuels satisfont suffisamment l'attente expérimentale, avec moins de 1% d'incertitude dans les différents canaux, qui serait encore supprimée après la combinaison. L'évaluation du contexte multi-jets est validée à l'aide de spectres p_T^W, les formes et les chiffres montrent une excellente qualité avec des incertitudes subdominantes.

La mesure à M_W devrait être effectuée après la finalisation des deux autres, cependant, les données expérimentales de M_W sont suffisantes pour les résultats préliminaires. La mesure M_W est basée sur une liste d'échantillons MC de second ordre avec une masse générée différente de boson-W. Après χ^2-ajuster les spectres de données à ces modèles, la valeur centrale de la masse W est situé au point avec un écart minime. De même, les incertitudes sont estimées en adaptant les pseudo-données aux modèles. Les incertitudes systématiques dues aux corrections du lepton ne sont pas pires que les résultats de 7-TeV malgré moins d'événements. La condition des données à faible accumulationde améliore considérablement les performances de recul hadronique, ainsi que l'estimation du contexte multi-jet. Le dernier, également en ce qui concerne le développement de la méthodologie, contribue à l'amélioration de prime à l'incertitude systématique expérimentale. L'incertitude statistique, qui souffre de la luminosité intégrée finie, est la

principale incertitude dans les résultats individuels et combinés. Compte tenu d'une incertitude statistique idéale est censé être au plus la moitié de l'incertitude systématique, et que les incertitudes systématiques de lepton et la correction de recul sont également touchés par le nombre d'événements Z-boson, 2~3 fois plus de données recueillies à faible de l'accumulation devrait essentiellement être résolu le problème. La perspective d'avoir des données à faible accumulation pendant des semaines à des mois pendant le Run-III ou le LHC à haute luminosité est à l'étude, ce qui devrait être approuvé, va complètement changer le jeu dans les mesures de précision électrofaibles.

Conclusion

En conclusion, pour augmenter encore la précision de la mesure de la masse-W globalement, les mesures transversales de l'impulsion et de la section de production du boson-W sont motivées, et ont procédé avec des données spéciales à faible accumulation prises dans l'accélérateur LHC et le détecteur ATLAS. Cette thèse documente la construction et l'étalonnage d'objets pour la reconstruction du boson-W et l'évaluation des contextes dans l'espace de phase de signal. Il décrit ensuite la méthodologie et les résultats des mesures transversales de la production, de l'impulsion transversale et de la masse-W. Grâce aux faibles activités sous-jacentes et aux stratégies optimisées, la plupart des résultats obtiennent la précision de visée. En particulier, les mesures de la section transversale et de l'impulsion transversale gagnent beaucoup plus de précision que les résultats précédents. Les résultats finaux de ces deux mesures corrigeront les incertitudes théoriques de la masse-W. Dans les résultats préliminaires de la masse-W, les incertitudes expérimentales diminuent et satisfont à l'exigence, mais les incertitudes statistiques sont globalement dominantes. La combinaison des résultats ATLAS entre Run-I et Run-II, avec la correction de p_T^W, les PDF et d'autres mises à jour devrait réduire considérablement l'incertitude totale, fournissant le M_W le plus précis au monde.

Contents

1 Introduction

The origin of various inherent properties of life remains mystery, and one tends to see them as the endued nature that preserves existance from ages and selections. In human nature, curiosity, whether from fear of the unknown, or thirst for knowledge, could be of the most charms and magic. It encourages the thinking reeds to confront with the infinite universe, from which to abstract the most general essence, or truth. Experiences from the pursuing of truth in generations are concluded as science. One essential principle of science is that practice is the sole criterion of truth. Hypotheses, summarized and derived from the observation of reality, provide new predictions, and validated experimentally. Such hypothesis gains credibility in the experimental validation of its prediction, eventually becomes a theory. In this thesis, one particular theory will be invested, the Standard Model (SM) of practical physics. Unlike many other frontiers, for instance, mechanism of the intelligence and cognition (as the "nature"), despite to untangle the fundamental rules of universe is as "ultimate", the SM, has accounted for unbelievable amount of phenomenon, giving explanation or prediction to all particles that have been observed. The last puzzle, Higgs boson has been discovered in 2012 by the ATLAS and CMS detectors on LHC, giving SM with seemingly unbreakable authority.

The achievement of SM is more than a wonder, but will the curiosity be satisfied? We can't compare the string theory with wisdom of ancient Hindu prophet who assumed everything generated from the vibration of "Om", as the pragmatic science has the view of nature that is fitting for a technical age [1]. Equally, the standard model is not guaranteed when technics lead to the new aura. The phenomenal described by the SM could beome the representation of a world at larger energy scale and finer resolution. Extended theories that carry the willing to go beyond the standard model keep emerging, and the sparkling ones, string theory, super symmetry, effective field theory, etc., do carry the thoughts to the limbo of known and unknown. However, as particle physics is about the research of finest objects, and honestly the validation of SM almost exhausts all techniques: the experiments might go beyond the capability before going beyond the standard model. For example, though the superstring provides unified description of gravity and other interactions as an potential extension of the SM, the hierarchy problem that the weak force is 10^{24} times stronger than gravity creates an incredibly large parameter space. Targeting this question is like a Sisyphean vain in the view of nowadays, but reminded that Higgs boson took half century to discover after prediction: to the time to science, and the routine will be enlightened by experimental phenomenons.

On the edge of techniques, more precise results are highly wanted in searching for new phenomenon. New evidences will be either from the direct detections of new particles and properties fail to be predicted by the SM, or obtained indirectly, like from the measurement under extreme precision (comparable to theoretical prediction) whose result disapproves of the standard model. The indirect method is somehow less conclusive, but it holds the strong power to set stringent constraint to all extended theories associated with the measurement, which is particularly helpful at current status. New physics is written to be verified before the exhaustion of parameter space. Therefore here, maybe

during the very childhood, the topic is moved from the general aspect to the tiniest area, to discuss how a small step is made in precision measurement by exploiting the most advanced accelerator LHC and detector ATLAS.

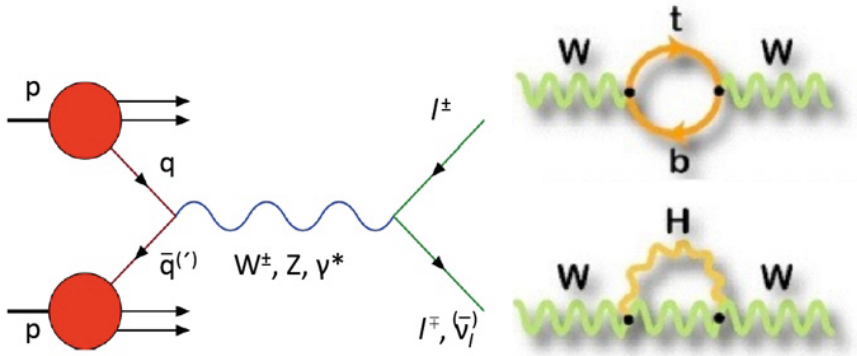

(a) (b)

Figure 1.1: (a) : the vector boson production from proton-proton collision; (b) : weak interaction between W boson and high-mass particles.

Massive vector boson, W and Z, are two kinds of fundamental particle predicted by standard model, and firstly observed in Super Proton Synchrotron experiment in 1983 at CERN [2, 3]. As the carriers of weak force, one of the four fundamental forces, and the production of Higgs mechanism, from which the two kind of gauge bosons gain "mass", their properties and related studies are widely interested since prediction and discovery. The association between W boson and other massive particles reflects on the tiny shift of W-boson mass. Within the standard model frame, this effect is dominated by the top-quark and Higgs boson, giving a prediction with 8-MeV uncertainty [4]. However, should there be additional particles of high mass, the real W mass will be distinct to the prediction, which endues W mass with capability as an excellent probe to potential new physics. By measuring the W mass at a precision comparable to 8 MeV, half of the uncertainty of world-averaging measured W-mass [5], the chance to issue a new challenge to standard model is seemingly touchable.

No doubt doubling the precision in W-mass measurement is an impossible mission right now, yet the shortcut has been found. The previously experiment at LHC using ATLAS detector [5] highlights the key limitation in W-mass measurement is the degradation of neutrino energy resolution due to large additional inelastic pp collisions in the same bunch crossing, or pile-up. Under special low-pile-up conditions, the detecting sensitivity to neutrino will be significantly enhanced, hence the accuracy in W-boson reconstruction. In addition, this low-pile-up data is sufficient in supporting the transverse-momentum and cross-section measurements of W boson at best precision, which will effectively reduce the theoretical uncertainties assigned to W-mass measurement. Although the task won't be accomplished at one stroke, the result with this data will play an important role in the global averaging and illuminate the next step. And this thesis will present how the extreme precision in the detection and reconstruction of W bosons is achieved.

1.1 Structure of the thesis

This thesis describes the W-boson measurements with low-pile-up data in eleven chapters. After the brief introduction of this chapter, chapter 2 presents the motivations of measurements to W-boson with low-pile-up data. Theoretically an overview of standard model and the description of three fundamental interactions, the W-boson production process and its importance in SM are contained. The history of W-mass measurements and current limitation are also reported in Chap. 2, in particular the potential of having the special low-pile-up data.

The complexes of accelerator LHC, and detector ATLAS are described in Chap. 3, in addition to the design and mechanism of sub-detecting system. Followed by the Chapter 4 and 5, composed of the reconstruction and energy calibration of leptonic objects, the calculation of lepton selection efficiencies and an individual section discussing the proposal to reweight the shape of shower energy deposited in electromagnetic calorimeter to optimize the electron and photon reconstruction and identification. Chap.6 reports how the other high-end object, hadronic recoil, used to evaluate the neutrino kinematics, is built in ATLAS.

The MC simulation, used to predict the data properties and evaluate the electroweak and top backgrounds, is one basic tool in W-boson experiments. Another major background, multi-jet, is estimated with data-driven method. The multi-jet background dominates the uncertainties in background estimation of previous W-boson measurements, thus the procedure is dedicatedly studied with low-pile-up data and developed. Sections about the MC simulation, event selection and background estimation are included in Chap. 7.

The methodologies, uncertainties and results of W-boson measurements to the transverse momentum spectrum, production cross-section and invariant mass are given in Chap. 8, 9 and 10 respectively. Due to that it has not been one year since the last data taken in writing, and that validations and calibrations are essential for such "raw" data, complete measurement results are not yet accessible, espeically for W-mass measurement that only preliminary uncertainty studies are included, but both cross-section and transverse-momentum measures are close to accomplishment. Moreover the uncertainties in these two measurements as well as W-mass measurement are sufficiently powerful to demonstrate the pretty precision obtained with studies introduced in previous chapters.

1.2 Personal contribution

The studies in Chap. 4, 5, 7, 9 and 10, besides the partly development and maintenance of analysis framework for group usage, are majorly contributed by me, under the supervision of local analyses group and relevant ATLAS official working groups.

In Chap. 4, the contributions include the calculation of electron efficiencies, scale factors and uncertainties, different prospects in the reduction of uncertainty, and a shower-shape reweighting procedure to calibrate the electromagnetic calorimeter. In Chap. 5, I focus on the mis-alignment study and sagitta-bias correction for muon. The other contents of these two chapters, denoting the energy and momentum calibration of leptons, and the muon efficiency scale factors are performed by colleagues and the muon combination performance group, thus less detailed. Chap. 6 introduces the

reconstruction and calibration of hadronic recoil, referred from Ref. [6] by other co-workers. This chapter is kept individually considering the importance of hadronic recoil in W-boson measurements and the backgrounds estimation as well.

In Chap. 7, I help to define the signal criteria including test of lepton quality requirements and optimization of W-event selections. Furthermore, in the backgrounds estimation part, I propose and complete an upgraded multi-jet background evaluation procedure which significantly enhance the modelling and accuracy of QCD background. Other manuscripts of this chapter, MC generations and theoretical corrections are provided by collaborators and the ATLAS production group.

The measurement of W-boson transvers momentum is mostly performed by the cooperators, but based on the lepton corrections, W-event selection, experimental corrections and well-controlled backgrounds provided by me, and the associated uncertainties are specifically discussed in Chap. 8. Meanwhile I participate the other two measurements, cross-section measurement and mass measurement of W boson, addressing to most of the values and figures presented in Chap 9 and 10. Following the schedule and status of experiment, the uncertainties on W mass are calculated with in-situ low-pile-up date with all corrections described in this thesis, but as preliminary results to illustrate the performance of different corrections and highlight the current difficulties because the results of cross section and transverse momentum are necessary input for W-mass study.

2 Theoretical and experimental background

2.1 The Standard Model

The standard model (SM) is one of the most successful theories in physics to describe three of the four forces or interactions that have been discovered in nature: electromagnetic, weak and strong interactions. The other one, gravity, is mostly explained by the general relativity. Some beyond standard model (BSM) theories provide unified description of gravity and particle physics, but none is validated. Bases on a SU(3) ⊗ SU(2) ⊗ U(1) gauge symmetry, SM make it to perfectly account for all known particles and almost all phenomenon related within its applicability.

Two categories of fundamental particles are exploited in the standard model, overview of which is illustrated in Fig. 2.1: the fermions of spin $\frac{1}{2}$, contain six quarks (up, down, charm, strange, top, bottom) and six leptons (electron, muon, tau and electron neutrino, muon neutrino, tau neutrino); vector bosons with spin 1, consisting of photon, $W^{\pm}$ and Z boson, and eight gluons, as the generators of bosonic fields, mediators of electromagnetic, weak and strong interactions respectively; a special boson of spin 0 is introduced to explain the source of vector boson's non-zero mass, as the production of the spontaneous symmetry breaking, or Higgs mechanism, thus named Higgs boson. Dedicated explanations to interactions will be presented separately in following sections.

2.1.1 Electromagnetic interaction and weak interaction

The quantum field theory (QFT), as the theoretical framework of SM, is initially established from the Quantum Electrodynamics (QED), an U(1) Abelian gauge theory to describe electromagnetic interactions. Lately to include weak processes to the theory, thanks to the efforts of Yang, Mills, Glashow, Weinberg and Salam [7–10], a new proposal to unify both electromagnetic and weak interactions, as electroweak (EW) theory was built. The EW theory is base on $SU(2) \otimes U(1)$ gauge coupling, with four bosons, photon, Z, W^+ and W^-, as the mediators. The U(1) group has one generator Y, called weak hypercharge and SU(2) ground has three generators, τ^a (a= 1,2,3), constructed with Pauli matrices. Y is related to the electric charge: $Y = 2(Q - \tau_3)$. With these generators, the Lagrangian of EW theory is written as:

$$\mathcal{L}_{EW} = -\frac{1}{4}W^a_{\mu\nu}W^{\mu\nu}_a - \frac{1}{4}B_{\mu\nu}B^{\mu\nu} + \sum_{\psi}\bar{\psi}_i\gamma^\mu(i\partial_\mu - \frac{1}{2}g'YB_\mu - \frac{1}{2}g\tau^a_L W^a_\mu)\psi \tag{2.1}$$

where g and g' are weak and electromagnetic couplings, B_μ and W^a_μ are the U(1) and SU(2) gauge fields, $B_{\mu\nu}$ and $W^a_{\mu\nu}$ are the corresponding field strength tensors:

$$B_{\mu\nu} = \partial_\mu B_\nu - \partial_\nu B_\mu \tag{2.2}$$

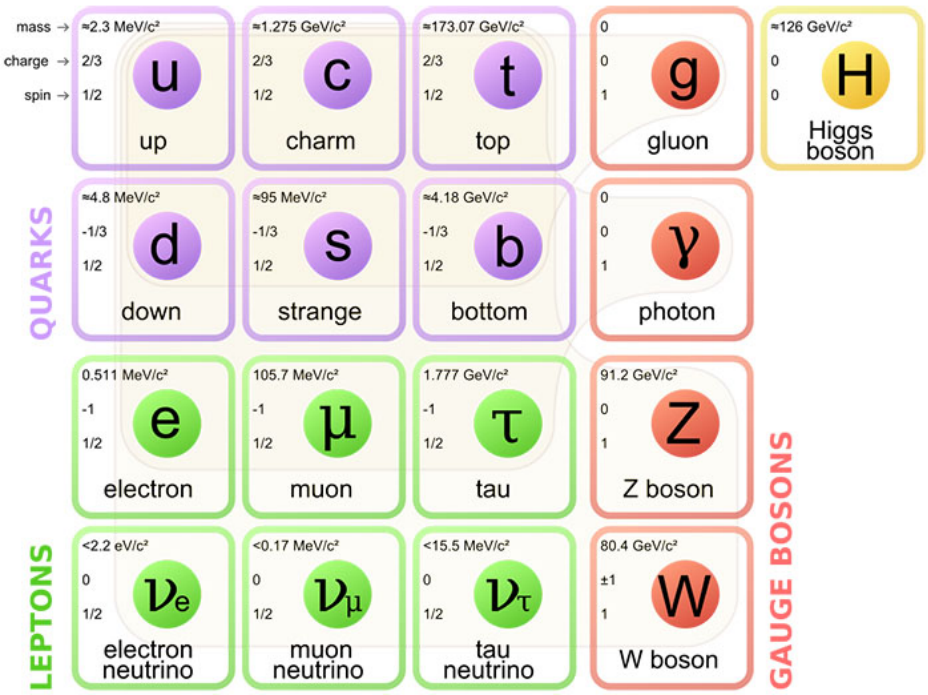

Figure 2.1: Fundamental particles in the standard model

$$W^a_{\mu\nu} = \partial_\mu W^a_\nu - \partial_\nu W^a_\mu + g\epsilon^{abc} W_{b\mu} W_{c\nu} \tag{2.3}$$

B_μ and W^a_μ as gauge fields, give rise to one and three gauge bosons in electromagnetic (photon) and weak interactions (Z, W^+ and W^-). They form as the linear combination of these filed:

$$A_\mu = B_\mu cos\theta_W + W^3_\mu sin\theta_W \tag{2.4}$$

$$Z_\mu = -B_\mu sin\theta_W + W^3_\mu cos\theta_W \tag{2.5}$$

$$W^\pm_\mu = \frac{1}{\sqrt{2}}(W^1_\mu \mp W^2_\mu) \tag{2.6}$$

θ_W is a constant named weak mixing angel, such that $m_W/m_Z = cos\theta_W$. U(1) symmetry requires A_μ, i.e photon, to be massless, therefore it gives $e = gsin\theta_W = g'cos\theta_W$, e being the unit charge.

2.1.2 Strong interaction

Strong interactions is described by Quantum ChromoDynamics (QCD) theory, respecting the SU(3) gauge symmetry with eight generators, corresponding to eight gluons, massless gauge bosons carrying a quantum number named color charge. Colors of three flavors, red (r), green (g) and blue (b), also

exist in each flavor of quarks, and the strong interaction is performed as the exchange of gluon between quarks. Lagrangian expression of QCD is written as:

$$\mathcal{L}_{QCD} = -\frac{1}{4}F^a_{\mu\nu}F^{\mu\nu}_a + \sum_{flavors} \bar{\psi}_i(i\gamma^\mu(\partial_\mu\delta_{ij} - ig_s F^a_\mu T^a_{ij}) - m_\psi\delta_{ij})\psi_j \tag{2.7}$$

where ψ_i are the Dirac spinors of a quark with a color-index a = r,g,b and mass m, G^a_μ (a= 1,2..8) are eight gluon fields, T^a_{ij} are SU(3) generators, i.e. the Gell-Mann matrices, $F^a_{\mu\nu} = \partial_\mu F^a_\nu - \partial_\nu F^a_\mu + g_s f^{abc} F^b_\mu F^c_{nu}$ are the gluon field strength tensors in which f^{abc} are the structure constants of the SU(3) and g_s is the strong coupling constant, universal for all gluons. The first term describes the gluon self interaction and the second term describes the quark-gluon interaction. The coupling constant can be written through the running coupling constant $\alpha_s = g_s^2/4\pi$:

$$\alpha_s(Q^2) = \frac{12\pi}{(11n_c - 2n_f)log(Q^2/\Lambda^2_{QCD})} \tag{2.8}$$

where Q is the energy transferred, $n_c = 3$ and $n_f = 6$, corresponding to the number of colors and quarks, $\Lambda_{QCD} \approx 200$ MeV, is the QCD energy scale. Two important properties of QCD are derived from this equation:

- Confinement: $\alpha_s(Q^2) \to \infty$ as $Q^2 \to 0$, means the interaction between quarks grows as they're separated, and there is a bound state to limit quarks from being free. Therefore quark never appears along, can only be found in hadrons (and quark-gluon plasma under extreme conditions).
- Asymptotic freedom: $\alpha_s(Q^2) \to 0$ as $Q^2 \to \infty$, which means at very high energies or short distance, the strong force between quarks almost disappears, and quarks are close to free states, thus perturbation expansions of QCD (pQCD) is available as an approach in computations [11, 12].

2.1.3 Higgs mechanism

In the EW Lagrangian, to preserve the SU(2)×U(1) gauge symmetry, all particles, whether fermions or bosons, should be massless. To explain how the particles involved in EW processes gain mass, the spontaneous symmetry breaking hypothesis is introduced. This hypothesis, so called Higgs mechanism, by combining the EW theory with an additional Higgs filed which interact with all particles, contributing to spontaneous symmetry breaking, giving extra degree of freedom to gauge bosons, i.e. a finite mass [13–16]. The Higgs filed, ϕ_H, is a four-component scalar field that forms a complex doublet of the weak isospin SU(2) symmetry. The Higgs part of the Lagrangian is

$$\mathcal{L}_H = |(\partial_\mu - igW^a_\mu\tau^a - \frac{1}{2}ig'B_\mu)\phi|^2 + \mu^2\phi^\dagger\phi - \lambda(\phi^\dagger\phi)^2 \tag{2.9}$$

With $\lambda > 0$ and $\mu^2 > 0$ the ground state of potential is non-zero, equal to the vacuum expectation value $|\phi| = \sqrt{\mu^2/2\lambda} = v/\sqrt{2}$. Quadratic terms in W_μ and B_μ arise, which give masses to the W and Z bosons:

$$M_H = \sqrt{2\lambda}v \tag{2.10}$$

$$M_W = \frac{1}{2}vg \tag{2.11}$$

$$M_Z = \frac{1}{2}\sqrt{g^2 + g'^2}v = \frac{M_W}{cos\theta_W} \tag{2.12}$$

Thus W and Z bosons gain masses, related to the Higgs field parameters and weak mixing angel. Fermions' mass are gained from the Yukawa couplings between fermion fields and Higgs fields, in term of:

$$\mathcal{L}_Y = -g\bar{\psi}\psi\phi \rightarrow -g\bar{\psi}\psi\frac{v}{\sqrt{2}} \tag{2.13}$$

v is calculated to be approximately 246 GeV, therefore the masses of W and Z bosons are predicted in SM, but for the mass of Higgs boson, with free parameter λ, can only be measured experimentally.

2.2 Weak boson production

2.2.1 Prediction of Drell-Yan process

W boson in this study are produced from the high-energy proton-proton collisions. Each Proton is made up of two up quarks (u) and one down quark (d), with strong interactions between them through the gluons interchanges. uud are called valence quarks which determine the quantum number of proton. Each gluon can also split into virtual quark-antiquark pairs, called sea-quarks, or produce more gluons through self-interact. During the inelastic scattering of collision, protons are involved as particle systems with complicated and dynamic structure. The scattering , mainly according to the amount of transverse momentum transferred, are divided into soft processes and hard processes, both obey the QCD. Soft process, with low Q^2, includes diffraction, multiple-partonic interactions, soft initial-state and final-state radiation (ISR/FSR), beam-beam remnants at LHC. Vector boson production, usually from the annihilation of an quark and anti-quark into leptons, is a typical hard process, with high Q^2 in interaction and can be Following QCD, hard processes can be calculated perturbatively while soft processes are non-perturbative. In collision event, the collection of all soft processes is named "underlying event", as the side product of hard processes of interest.

The cross section of W/Z-boson production in proton-proton collision can be calculated with the QCD factorization theorem, constructed by Drell and Yan (W and Z production process is called Drell-Yan process) [17], which factorizes the process into the partons interaction (hard scattering) and the partons momentum distribution within protons, or Parton Distribution Functions (PDFs), $f_i(x, Q^2)$. PDFs part contains the non-perturbative soft QCD, but considering at large enough energy scale, $Q^2 = \mu^2$, the non-perturbative processes are sub-dominant, and the cross-section of $q\bar{q} \rightarrow V$ is:

$$\sigma_{pp\rightarrow V} = \sum_{a,b}\int dx_a dx_b f_{a/A}(x_a, \mu_F^2) f_{b/B}(x_b, \mu_F^2) \times \sigma_{ab\rightarrow V}(x_a p_1, x_b p_2, \mu_F^2) \tag{2.14}$$

where a and b denote quarks and anti-quarks, A and B denote corresponding protons. At high energy scale, the hard QCD process $s\sigma_{ab\rightarrow V}$ expansion is:

$$s\sigma_{ab\rightarrow V} = \sigma_0 + \alpha_S(\mu_R^2)\sigma 1 + \alpha_S^2(\mu_R^2)\sigma 2 + O(\alpha_S^3) \tag{2.15}$$

where μ_R is the renormalization scale of the QCD running coupling. The first term σ_0 represents the cross section calculated at Leading Order (LO). The second ($\alpha_S(\mu_R^2)\sigma 1$) and third ($\alpha_S^2(\mu_R^2)\sigma 2$) term are corresponding to Next-to-Leading Order (NLO) and Next-to-Next-to-Leading Order (NNLO). In perturbation theory, the calculation of cross section to all orders are not dependent on the scale parameters μ_F^2 and μ_R^2. However, up to now the calculation of the orders higher than NNLO is absent, which make the specific choice of these two scales necessary for cross section predictions. For Drell-Yan process, the standard choice is $\mu_F = \mu_R = M_Z, M_W$,the mass of vector boson.

In the center-of-mass frame, the four-momenta of the incoming partons can be written as:

$$p_1 = \frac{\sqrt{s}}{2}(x_1, 0, 0, x_1) p_2 = \frac{\sqrt{s}}{2}(x_2, 0, 0, x_2) \tag{2.16}$$

x_1 and x_2 are related to $\hat{s}$ by: $\hat{s} = (p_1 + p_2)^2 = x_1 x_2 s$. And the rapidity of the production is $y = 1/2 log(x_1/x_2)$, and hence

$$x_1 = \frac{M}{\sqrt{s}} e^y, x_2 = \frac{M}{\sqrt{s}} e^{-y}. \tag{2.17}$$

The form of cross section at leading order is:

$$\frac{d\sigma}{dy} = \frac{1}{s} \sum \sigma_0(M) f_1(x_1, M^2) f_2(x_2, M^2) \tag{2.18}$$

At leading order, the rapidity and transverse momentum of the produced lepton pair is zero. The partonic cross sections for W and Z can be derived as:

$$\sigma^{q\bar{q}' \to W} = \frac{\sqrt{2}\pi G_F M_W^2}{3} |V_{q\bar{q}'}|^2 \delta(\hat{s} - M_W^2) \sigma^{q\bar{q} \to Z} = \frac{\sqrt{2}\pi G_F M_Z^2}{3} (v_q^2 + a_q^2) \delta(\hat{s} - M_Z^2) \tag{2.19}$$

where $\hat{s}$ is the square of the parton center-of-mass energy, $V_{q\bar{q}'}$ is the appropriate Cabibbo-Kobayashi-Maskawa matrix element, denoting the strength of the flavour-changing weak interaction, and $v_q(a_q)$ is the vector (axial vector) coupling of the Z to the quarks.

With respect to higher order corrections, there are additional quarks and gluons involved in the collisions, including non-perturbative soft processes between partons which result in gluons radiations, named "parton showers", and one or more emissions of gluons and quarks in the hard process. The recoil of these additional quarks and gluons can generate large transverse momentum of the production. The soft effect on LHC has been studied in fixed-target proton-neutron collisions. And for the effect in hard process, pQCD provides the prediction of higher order calculations. Equation 2.20 gives the next-to-leading-order approximation at high p_T^W:

$$(\frac{d\sigma}{d^2 p_T^W})_{O(\alpha_S)} = \frac{4\alpha_S \sigma 0}{3\pi^2} \frac{1}{(p_T^W)^2} log(\frac{M_W^2}{(p_T^W)^2}) \tag{2.20}$$

However this equation does not work at low p_T^W: when $p_T^W < M_W$, the logarithm becomes large and compensates for the small α_S, diverging the high-order terms. In particular, for higher orders "N", there is a series of terms proportional to $\alpha_S^N log^m(m_W^2/p_T^2)$, $m \leq 2N - 1$. For $p_T \ll M_W$, the "2N-1" term dominates the perturbative prediction and make the high orders non-negligible. This problem is

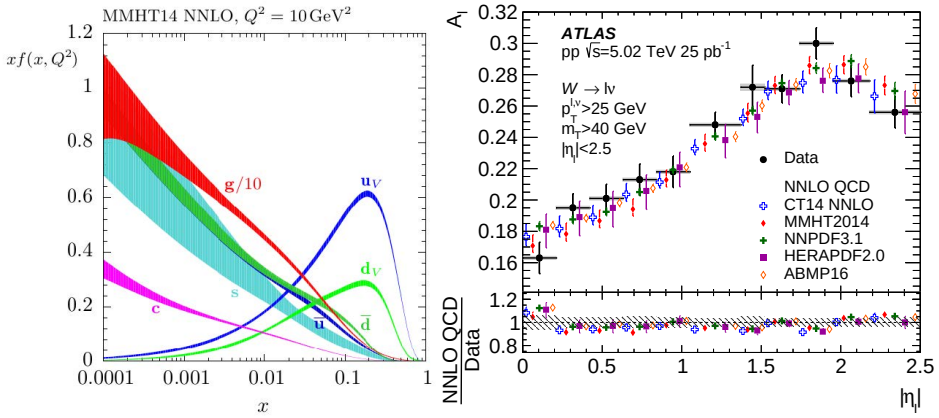

(a) (b)

Figure 2.2: (a) Example of "MMHT14 NNLO" PDF at $Q^2 = 10GeV^2$. (b) Comparison of the W-boson differential cross-section measurement results and PDF predictions using 5.02-TeV data.

solved with a resummation technique which resums all the logarithms to the leading logarithm with the form:

$$(\frac{d\sigma}{d^2p_T^W})_{O(\alpha_S)} = \frac{d}{(dp_T^W)^2} exp(-\frac{2\alpha_S}{3\pi} log^2(\frac{M_W^2}{(p_T^W)^2})) \tag{2.21}$$

Now the overall the differential cross section can be written as

$$\frac{d\sigma}{dp_T} = (\frac{d\sigma}{dp_T})_{pQCD} + (\frac{d\sigma}{dp_T})_{resumm} \tag{2.22}$$

At low p_T the effect is dominated by parton showers, predicted with resummation technique while at high p_T, it's lead by hard emissions, and perturbative QCD is valid to give fixed order descriptions. Currently the accurate theoretical prediction is available up to NNLO and NNLL (next-to-next-to leading logarithms).

2.2.2 Parton distribution function

Parton Distribution Function, or PDF, mentioned in Eq.:

$$\frac{d\sigma_{pp\to W}}{dy} = \frac{1}{s}\sum \sigma_0(M) f_1(x_1, M_W^2) f_2(x_2, M_W^2), \tag{2.23}$$

is used to describe the quarks and gluons distributions in initial state of protons during collision. It works with two parameters, the momentum fraction of giving parton "x", and the energy scale of interaction "Q" ($Q = M_W$ in W production process), written as $f(x, Q^2)$. Fig. 2.2(a) gives an illustration of PDF "MMHT14 NNLO" variation at $Q^2 = 10GeV^2$. As the short-distance partonic reactions with PDF directly enter the calculation of cross section, the accuracy of PDF significantly influences the simulation to all processes.

Experimental results are necessary inputs to PDF. Using the boundary conditions measured in experiments at low Q^2 and multiple parameters, PDF can evolve itself to all energy scales. Based on calculation, various sets of PDFs are provided by many groups, up to NNLO precision, and make different predictions. Eq. 2.23 thereby offers an effective opportunity to test these parton dynamics models. By measuring the Drell-Yan production cross sections in bins of rapidity, on one hand, PDFs that fail to agree with measurement result require modification and correction; on another hand, the PDF parameters can be further constrained to minimize the discrepancy between prediction and measurement (Fig. 2.2(b)). Following the previous experience, introducing the cross-section results to Drell-Yan prediction is able to reduce the PDF uncertainty by approximately 30%.

2.3 W-boson measurements and its history

As discussed above, the invariant mass of W-boson mass is one of the fundamental parameters of standard model, especially the spontaneous symmetry breaking. When neglecting higher order corrections, and exploiting the precisely measured parameters including the fine-structure constant α, the Fermi constant G_μ and the mass of Z boson, M_Z, the mass of W boson, M_W, can be predicted as:

$$M_W^2(1 - \frac{M_W^2}{M_Z^2}) = \frac{\pi\alpha}{\sqrt{2}G_\mu} \tag{2.24}$$

Higher order corrections introduce dependence of the W-boson mass on the gauge couplings and the masses of the heavy particles of the SM. Then the equation becomes:

$$M_W^2(1 - \frac{M_W^2}{M_Z^2}) = \frac{\pi\alpha}{\sqrt{2}G_\mu}(1 + \Delta r) \tag{2.25}$$

where Δr incorporates all higher-order corrections. In SM, Δr is particularly sensitive to top-quark and Higgs-boson masses, while in extended theories, it receives contributions from additional particles and interactions, which makes M_W a stringent probe in the SM consistency demonstration through comparing the M_W from experimental measurement and theoretical prediction. Fig. 2.3 illustrates the current scan of M_W versus M_t and M_H. Given the known value of M_t and M_H, the M_W is predicated to be 80360 ± 8 MeV.

Due to the importance of such parameter in the validation and prediction of SM as well as the search of new physics, the experimental precise measurement to W-boson mass never lose its attraction and countless efforts have been devoted. The measurement was firstly performed at the CERN SPS proton-antiproton ($p\bar{p}$) collider with UA1 and UA2 experiments in 1983, the same time as its discovery. Only six and four W candidates are found by two collaborations, at center-of-mass energies $\sqrt{s}$ = 546 GeV and $\sqrt{s}$ = 630 GeV respectively. The value of M_W were given as 81 ± 5 GeV and $80\pm^{10}_{6}$ GeV [2]. Afterwards various measurements to M_W followed: at Tevatron $p\bar{p}$ collider with the CDF and D0 detectors at $\sqrt{s}$ = 1.8 TeV in Run-I (1987-1996) [19–22] and $\sqrt{s}$ = 1.96 TeV in Run-II (2002-2011), the measurements give combined M_W value of 80.387 ± 0.016 GeV from two experiments; at the LEP electron-positron collider by the ALEPH, DELPHI, L3, and OPAL collaborations at $\sqrt{s}$ = 161 ∼ 209 GeV using $e^+e^- \to W^+W^-$ process, the combined M_W value is 80.376 ± 0.033 GeV [23–26] (Fig. 2.4 (a)).

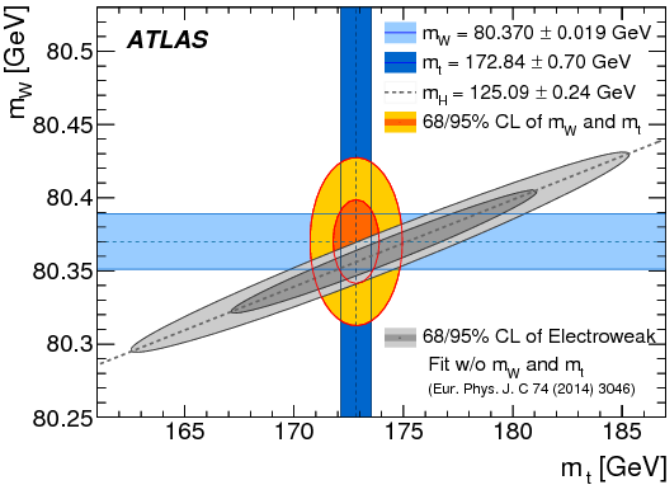

Figure 2.3: The 68% and 95% confidence-level contours of the W-boson mass and top-quark mass indirect determination from the global electroweak fit [4] are compared to the 68% and 95% confidence-level contours of the ATLAS measurements of the top-quark and W-boson masses. The determination from the electroweak fit uses as input the LHC measurement of the Higgs-boson mass [18] and W-boson mass [5].

Displayed in Fig. 2.4 (b), the average of global results is 80385 ± 15 MeV, a superb value neighboring the frontline of experimental technique, but when compared to the SM prediction, 80360 ± 8 MeV, the willing to validate new physics is not yet feasible, limited by the experimental precision. A real breakthrough demands a new measurement with significant improvement in the systematic uncertainty of measured M_W.

2.4 Prospect of a low-pile-up run at the LHC

2.4.1 Limitation in 7-TeV M_W measurement

The latest measurement was performed at LHC proton-proton collider with Run-I data collected by the ATLAS detector at $\sqrt{s}$ = 7 TeV. Benefiting from the largest amount of W-boson events by its high production rate at high energy, the combined M_W result of Run-I data is 80370 ± 19 MeV [5]. In addition, new theoretical corrections from the analytical calculation are introduced in this measurement, which make the result relatively more competitive. This number almost exhausts the potential of ATLAS detector during Run-I, indicating the limitation of precision in W-boson measurements under standard working status of ATLAS and LHC.

The statistical and systematic uncertainties associated to measured M_W at $\sqrt{s}$ = 7 TeV are listed in the first column of Tab. 2.1. Measurement to M_W depends on the observable "p_T^{lep}", transverse momentum of decayed lepton, therefore the lepton-relevant uncertainties (lepton efficiencies and calibrations, explained in Chap. 4) contribute the major of experimental uncertainty. Uncertainty due to the theoretical prediction corrections (Chap. 7) consists of QED correction, vector-boson-polarization

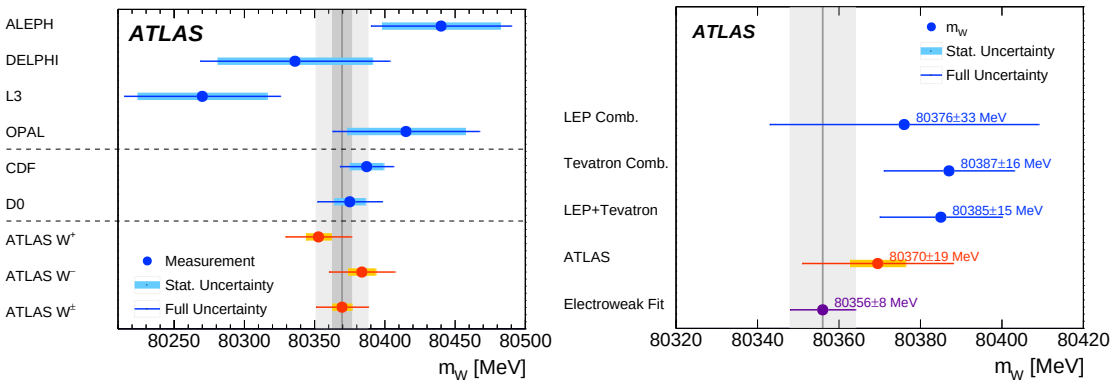

Figure 2.4: Figures from [5] : (a) the published results of M_W, including measurements from the LEP experiments ALEPH, DELPHI, L3 and OPAL [23–26], and from the Tevatron collider experiments CDF and D0 [27, 28]; (b) the present measured m_W is compared to the SM prediction from the global electroweak fit [4] updated using recent measurements of the top-quark and Higgs-boson masses, $m_t = 172.84 \pm 0.70$GeV [29] and $m_H = 125.09 \pm 0.24$GeV [18], and to the combined values of m_W measured at LEP [30] and at the Tevatron collider [31].

correction (QCD(A_i)), the correction to mis-modelled transverse momentum of W boson due to NNL and NNLO effects in pQCD (p_T^W), and PDFs. Comprehensively, the uncertainties from the detection is at the same level to theoretical ones, thus in the perspective of a measurement of W mass with uncertainty below 10 MeV, upgrades in both detection-related and theoretical-correction-related uncertainties are highlighted.

Some optimizations can already be foreseen in the next round of W-boson measurement at ATLAS: the measurement to Z-boson polarization and angular coefficients A_i has been published at $\sqrt{s} = 7$ TeV [32], and the uncertainty is assumed to be reduced by factor 2 if using the full ATLAS Run-II data at $\sqrt{s} = 13$ TeV; precision of EM correction [33] is currently updated from LO to NLO prediction; following the precise W and Z production cross section measurements, the impact on latest PDF sets can be exploited to reduce the PDF uncertainty by approximately 30% (Chap. 2.2.2). Then the exclusive issue is to overcome is the p_T^W mis-modelling, that the pQCD is less capable in the low p_T^W region where M_W has the best sensitivity.

Sufficiently precise p_T^W hasn't been successfully measured and two typical solutions are used in modelling p_T^W: the analytical resummations and the parton-shower simulation. The former is based on calculated prediction up to NNLL, while the later relies on Monta Calor simulation of higher-order processes, for instance randomly generating tiny jets (showers) in every state of the process, adjusted with parameters so that the simulation agrees with observation. This adjustment is usually proceeded with azimuthal variables of Z-boson event, named "AZ tune" [34]. Due to the lack of experimental inputs, both methods fail to precisely describe the p_T^W spectrum, suffering large systematic uncertainty. Predictions based on analytical resummations also show discrepancy with Pythia 8 parton shower prediction when p_T smaller than 5 GeV (Fig. 2.5(b)). Moreover, measured distributions using data W bosons strongly disagree with such predictions.

To minimize the uncertainty, 7-TeV measurement corrects the p_T^W with the measured p_T^Z and predicted

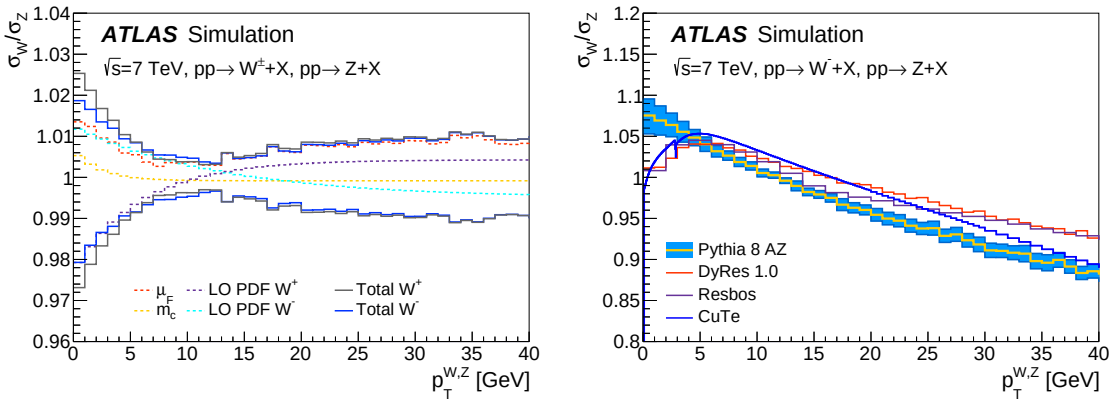

(a) (b)

Figure 2.5: (a) Uncertainties in the extrapolation of the measured p_T^Z distribution to the p_T^W distribution, as derived using Pythia8 for the m_W measurement of Ref. [5]. (b) Comparison of the W/Z p_T distribution ratio for Pythia8 and a set of resummed calculations [5].

ratio of p_T^W to p_T^Z, i.e.:

$$p_T^W(corr) = p_T^Z(measure) \cdot \frac{p_T^W}{p_T^Z}(prediction). \tag{2.26}$$

Illustrated in Fig 2.5(a), the modelling of p_T^W distribution has a uncertainty of approximately 2.5% in the low p_T^W region, contributed by two parts, the measurement of p_T^Z distribution (typically 0.5%) and the theoretical prediction uncertainty of the ratio of W-boson p_T to Z-boson p_T ratio (2.5% estimated with simulation tool).

2.4.2 Prospect of p_T^W measurement and low-pile-up run

The theoretical uncertainties in the extrapolation from Z-boson to W-boson pT distributions are difficult to assess in a rigorous way, and are currently limited by the inability of higher-order predictions to describe the data. An optimal solution is to use directly measured p_T^W, which will provide a comparison with QCD predictions, and help to untangle the mechanisms responsible for the differences between Z-boson and W-boson transverse-momentum distributions. Measuring this distribution over the range p_T^W < 30 GeV with an uncertainty of about 1% in bins of size at most 5 GeV will reduce by half of the QCD modelling related uncertainty in W-mass measurement. In addition, this precision should be achieved separately for W^+ and W^- production, as the p_T^W distributions differ for the two processes (Fig. 2.5(a)), in order to cancel most experimental systematic uncertainties.

Unlike $Z \to e^+e^-$ and $Z \to \mu^+\mu^-$ processes that all final state particles are mostly captured by ATLAS, $W^\pm \to \ell^\pm\nu$ process contains one neutrino in the final state, and neutrino doesn't interact with the detector, estimated as an energy loss in event. In W-boson measurements, the hadronic recoil strategy is introduced for W-boson reconstruction. By collecting all transverse energies captured by

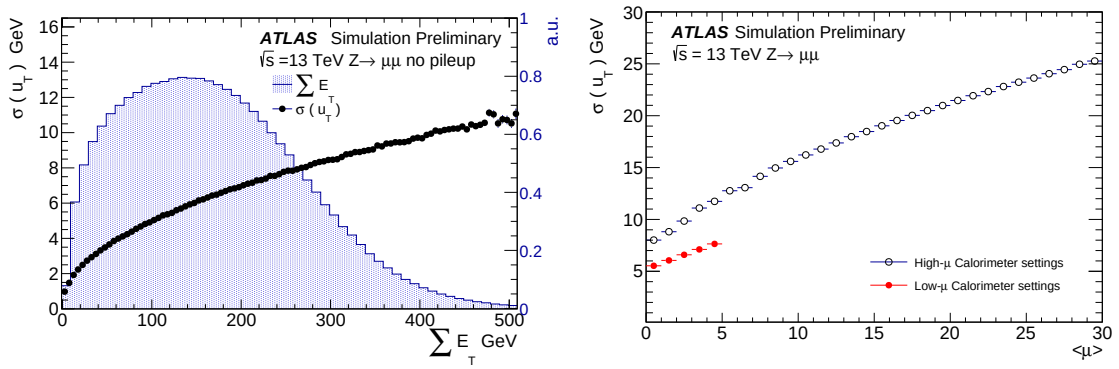

(a) (b)

Figure 2.6: (a) The $\sum \vec{E}_T$ distribution and the corresponding recoil resolution as a function of $\sum \vec{E}_T$ for simulated $Z \rightarrow \mu\mu$ events at $\sqrt{s} = 13$ TeV without pileup. (b) Recoil resolution as a function of $\langle\mu\rangle$ for simulated $Z \rightarrow \mu\mu$ events with two different calorimeter settings.

ATLAS other than the lepton, the recoil of W event is measured, approximately equal to the transverse momentum of W-boson but in opposite direction, written as:

$$\vec{u}_T = \sum_i \vec{E}_{T,i}^{Clusters-lep} \tag{2.27}$$

$$\vec{p}_T^{\,W} = -\vec{u}_T = \vec{p}_T^{\,miss} + \vec{p}_T^{\,l} \tag{2.28}$$

The measurement to p_T^W is then identical to measuring the hadronic recoil transverse momentum, $\vec{u}_T$, in bins of 5 GeV with 1% accuracy, which can only be achieved with a recoil resolution no worse than 5 GeV, otherwise the statistical sensitivity of the measurement would be degraded due to the large bin-to-bin migrations.

This recoil energy resolution, $\sigma(u_T)$ is estimated from the width of $u_\perp$ distribution, the projection of u_T on the plane perpendicular to the boson p_T. Since energy of all jets are exploited, $\sigma(u_T)$ is highly dependent on the jets activity in each event, evaluated by the scalar sum of the transverse energy of all reconstructed final state particles excluding the boson decay product, $\sum \vec{E}_T$. On the other hand, during the running of LHC and ATLAS, the jet activity, or $\sum \vec{E}_T$, relies on the additional inelastic pp collisions in the same bunch crossing, average number of which is referred to "pile-up", or $\langle\mu\rangle$. Fig. 2.6(a) displays the relation between $\sum \vec{E}_T$ and $\sigma(u_T)$ at $\langle\mu\rangle = 0$, and the $\sigma(u_T)$ is proportional to pile-up [35].

It's natural to generate more collisions happen when essential goals of LHC are searching for Higgs boson and new physics, but the value of $\langle\mu\rangle$ also increases. $\langle\mu\rangle$ is around 9 in the dataset collected in 2011, used for M_W measurement at $\sqrt{s} = 7$ TeV, and gets larger in data taken later, approximately 21 in 8-TeV data of 2012, 13, 25, and 38 in the Run-II data of year 2015, 2016 and 2017 respectively [36]. As illustrated in Fig. 2.6(b), the increasing of pile-up violates the experimental resolution of hadronic recoil, which is the crucial limitation of Run-II W-boson measurements of p_T^W as well as M_W.

However, it also indicates that using the data collected in low-pile-up conditions would unambiguously optimize the recoil performance and allow precise measurements of the p_T^W. The missing energy reconstruction can benefit from the optimization of hadronic recoil: in cross-section measurement, it will provide more accurate kinematics modelling; in M_W measurement, the better resolution of missing energy denotes new qualified observable in mass fit. Furthermore, in such data, jets are less activated thus the uncertainty associated to jet background estimation, main contribution of background uncertainty, will highly decrease. These advantages conclude the prospect to have the best W-boson properties measured at high energies, including p_T^W, Drell-Yan cross-sections and W-boson mass, as the experimental inputs to theoretical studies and probe to new physics, at "low pile-up".

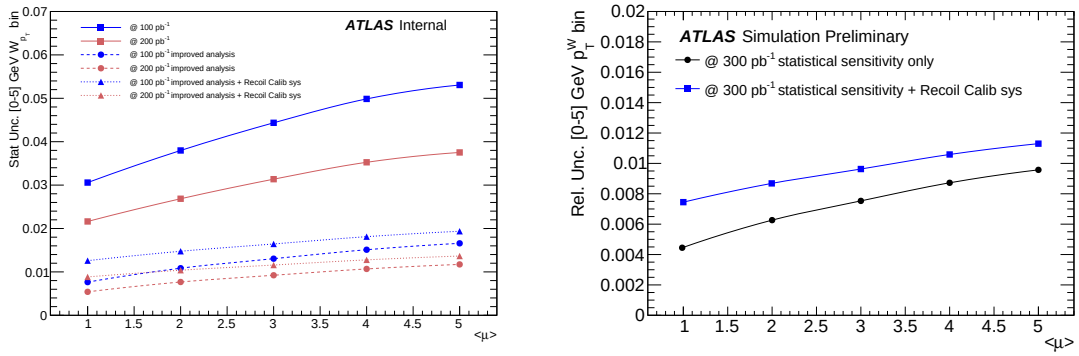

(a) (b)

Figure 2.7: Expected relative statistical uncertainty on the first bin of the p_T^W spectra as a function of μ for different integrated luminosities at a center of mass energy of $\sqrt{s}$ = 13 and 5 TeV [35].

Besides, the low-pile-up data demands sufficient statistics to support these measurements. A first analysis yields an expected statistical uncertainty in the first p_T^W bin of $\sim$ 3% with 100 pb^{-1} of integrated luminosity (refers to number of collisions, introduced in Chap. 3) and $\sim$ 2% with 200 pb^{-1} at $\sqrt{s}$ = 13 TeV, as shown in Figure 2.7.

The request was submitted to LHC committee and arrest wide interest. Finally two special low-pile-up runs were committed: in Nov. 2017, ATLAS collected 258.4 pb^{-1} of low-pile-up data at $\sqrt{s}$ = 5 TeV and 146.6 pb^{-1} at $\sqrt{s}$ = 13 TeV; in July 2018, additional 193.185 pb^{-1} data at $\sqrt{s}$ = 13 TeV was taken. Very few pp collision studies are performed at $\sqrt{s}$ = 5 TeV, the energy of heavy ion $PbPb$ collision, therefore the precise pp results are valuable to both experiments. Fig. 2.8 (b) illustrates their $< \mu >$ distributions. Datasets of $\sqrt{s}$ = 13 TeV and 5 TeV both have $< \mu > \sim 2$. Ahead of all, a pretty tiny amount of data (25 pb^{-1}) at $\sqrt{s}$ = 5.02 TeV with $< \mu > \sim 1$ was collected during 2015, as an early access to low-pile-up data. The usage of this data is presented in Chap. 9.

Despite the low integrated luminosity (the left tale of Fig. 2.8) comparing to full ATLAS Run-II data, the predicted p_T^W precision with 300 pb^{-1} data is expected to be smaller than 1% in the first 5 GeV bin for 13 TeV data and further better for 5 TeV data as shown in Fig. 2.7 (b). All corrections and procedures in p_T^W are directly applicable to the cross-section measurements, therefore the improvements to p_T^W is equally important to W-boson production cross sections, and the results of both measurements will be ultimately taken into the newly measured W mass. The later two columns of table 2.1 display the

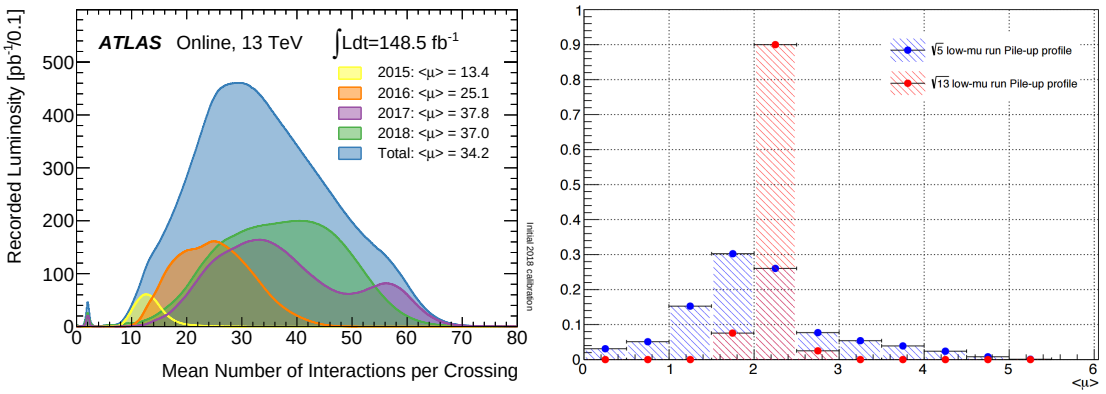

(a) (b)

Figure 2.8: (a) The luminosity of 13-TeV data at different pile-up collected by ATLAS [36]; (b) The pile-up distribution of low-pile-up data at $\sqrt{s}$ = 5 and 13 TeV.

preliminary estimate of the expected uncertainties in m_W, including the optimizations in the statistical and systematic uncertainties already discussed. It confirms that the a precision of 15 MeV is about to achieve at the 13 TeV with different dominant sources of uncertainties hence low correlation with the previous measurements, which is particularly competitive in global averaging. To achieve this extreme precision, all corrections and uncertainties in Tab. 2.1 will be calculated in-situ with low-pile-up data and simulations, starting with the introduction to the acceleration and detection system and corresponding experimental uncertainties.

Data sample	7 TeV, $\mu \sim 9$	13 TeV, μ ~25–30	13 TeV, $\mu \sim 1$	5 TeV, $\mu \sim 2$
Luminosity	4.5 fb^{-1}	~120 fb^{-1}	~ 200 pb^{-1}	~ 200 pb^{-1}
Nb. of candidates	$\sim 15 \times 10^6$	$\sim 750 \times 10^6$	$\sim 2 \times 10^6$	$\sim 0.7 \times 10^6$
Most sensitive dist.	p_{T}^{ℓ}	p_{T}^{ℓ}	m_{T}^{W}	m_{T}^{W}
Stat.	7	5	9	15
Lepton calibration	7	3	3	3
Lepton efficiencies	7	7	7	7
Recoil calibration	3	6	6	10
Backgrounds	5	8	2	2
EW	5	2	2	2
QCD (p_T^W)	6	6	< 3	< 3
QCD (A_i)	6	6	< 3	< 3
PDFs	9	6	6	6
Total	19	18	15	23

Table 2.1: Preliminary estimates of the uncertainty of future m_W measurements. Compared to the first column which summarizes the 7 TeV result, the following assumptions have been made for the extrapolations:

- lepton calibration : the calibration is mostly universal in high-pile-up and low-pile-up data and the statistical components are assumed to vanish when including full Run-II data;
- lepton efficiencies : the precision is assumed to be maintained when calculating the efficiencies with same "tag-and-probe" algorithm.
- recoil calibration: the preferred spectrum in mass fit is changed from lepton momentum to W-boson transverse momentum and larger values are estimated from existing ATLAS and CDF results;
- multijet background that dominated the background uncertainty at $\sqrt{s}$ = 7 TeV is reduced in low-pile-up and the methodology is also updated;
- the reduction in the EW correction uncertainties comes from using predictions with NLO EW corrections ;
- using the low-pile-up p_T^W measurement, the corresponding uncertainty decreases from 6 to 3 MeV for the p_{T}^{ℓ} fits, and to below 3 MeV at low pile-up;
- uncertainties in the A_i coefficients are reduced by a factor 2, assuming that the Z polarization measurement will be repeated on the full Run-II dataset;
- a reduction in PDF uncertainty by 30% is assumed, following a study of the impact of precise W and Z cross section measurements on the CT10 NNLO PDF uncertainty.

3 The LHC and ATLAS experiments

The data used in this research is collected by ATLAS (A Toroidal LHC Apparatus), a multipurpose particle detector designed to detect high-energy the proton-proton and heavy ion brunches collisions results, accelerated by LHC (the Large Hadron Collider). The structure, parameters and mechanisms of LHC and ATLAS, besides the complex sub-detecting system introduced in this chapter.

3.1 The LHC

LHC is a circular particle accelerator located at CERN, as the globally largest and strongest one, working to accelerate proton and heavy ion beams' central mass energy (CME) up to 14 TeV. The construction was completed in 2008 and conducing two fruitful periods of running. The main part of LHC lies in a tunnel of 26.7 km in circumference, 50 to 175 meters under the ground of bound of France and Switzerland. The tunnel, with a diameter of 3 meters, was previously used by LEP (Large Electron-Positron Collider) experiment, but originally designed for both by switching the constrained beam to protons for higher energy. Within the tunnel are two adjacent parallel beam pipes, each containing an opposite proton brunch, and surrounded by superconductive magnets. In total there are 1232 dipole magnets and 392 quadrupole magnets, corresponding to the function of circular path constraint and beams focusing. Additional higher-order multipoles, including sextupoles, octupoles and decapoles are equipped closer to collision points to correct the smaller imperfections and improve the possibility of collision.

3.1.1 Acceleration system

Four steps of acceleration are demanded to efficiently injecting protons beams to LHC.

1. Protons derived from the hydrogen gas start the acceleration from LINAC (an 80-meter-long LINear ACcelerator), which accelerates protons to 50 MeV.

2. Protons enter the Proton Synchrotron Booster (PSB), a 157-meters-perimeter circular accelerator and get accelerated up to 1.4 GeV.

3. Protons are injected to the second circular accelerator of 628 m circumference, Proton Synchrotron (PS). The energy is improved to 26 GeV.

4. The last chain is Super Proton Synchrotron (SPS) at 6.9 km long to accelerate protons to 450 GeV before transferring to the LHC main ring.

The beam in one pipe circulates clockwise while the beam in the other pipe circulates anticlockwise, both are accelerated by eight radio frequency (RF) cavities along the beam axis. It takes 4 minutes and 20 seconds to fill each LHC ring, and 20 minutes for the protons to reach their maximum energy. Limited by the operational stability of bending dipole magnets and synchrotron radiation, the maximum achieved beam energy is 6.5 TeV. Then these two 6.5 TeV beams are brought into 13 TeV CME collision, with the help of higher-order multipole magnets, inside four detectors, ATLAS, CMS, LHCb and ALICE. ATLAS and CMS (Compact Muon Solenoid) are two general purpose detectors, studying the high-intensity and high-energy proton and heavy ion collisions for Higgs hunting and new physics signs. The LHCb (Large Hadron Collider beauty) focus on the precise b-physics studies and the ALICE (A Large Ion Collider Experiment) focus on the physics of strongly interacting matter at extreme energy densities and quark-gluon plasma.

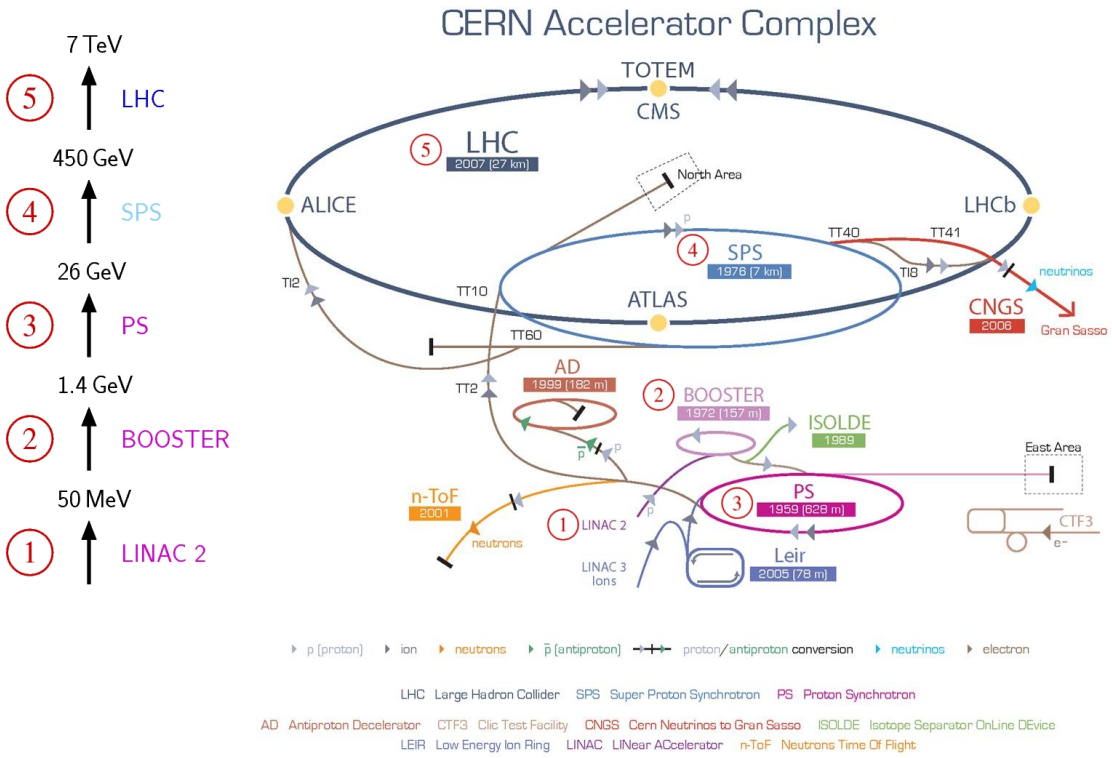

Figure 3.1: LHC accelerator complex.

3.1.2 Luminosity

To describe the number of events or scattering processes (N_{event}) introduced into the experiment, a critical parameter, luminosity L is defined:

$$N_{event} = L\sigma_{event} \tag{3.1}$$

where σ_{event} is the cross section of the inelastic process under study. The luminosity depends only on the beam parameters, considering a gaussian beam distributions, can be written as

$$L = \frac{N_b^2 n_b f_{rev} \gamma_r}{4\pi \varepsilon_n \beta*} \cdot F \tag{3.2}$$

N_b and n_b are corresponding to the number of particles per bunch and number of bunches per beam. f_{rev} represents the revolution frequency, γ_r the relativistic gamma factor E/m_p, ε_n the normalized transverse beam emittance, $\beta*$ the beta function at the collision point, and F the geometric luminosity reduction factor due to the crossing angle at the interaction point (IP), which is sensitive to the full crossing angle, the RMS bunch length and the transverse RMS beam size at the IP.

Maximum luminosity shows the efficiency of statistics acquirement, and its best performance has several limitations: the beam-beam limit that interactions happen between beams within same brunch increase ε_n; the machine design limitation in beam aperture, electromagnetic fields, energy storage and heat load; collective beam instabilities from the vacuum system geometry and its surface properties which limits the beam intensities; lifetime of accelerated particles.

High integrated luminosity means more interaction events and more chance to find rare process, meanwhile precision measurement, especially cross-section related measurement demands good precision of luminosity, which contributes to one of the main uncertainty sources.

3.2 The ATLAS

ATLAS is one of the largest and best designed detector for particle physics frontier general-purpose study, including the validation and development of standard model, searches for the Higgs boson and beyond the standard model. The full luminosity delivered from LHC are taken into this 44-meter long and 25-meter high, forward-backward symmetric cylindrical geometry instrument. As a complex detecting system, ATLAS mainly consists of a coordinate system, the inner detector, the electromagnetic and hadronic calorimeter, the muon spectrometer, trigger system and data acquisition system. Each of these subdetector plays a critical function in the precision and sensitivity to the detecting of objects and energies after collision. From the interaction point, tracks of charged particles are recorded in the inner detector (ID). Then particles enter electromagnetic and hadronic calorimeters, which measure the energy and direction of particles deposited in. Beyond the calorimeters is the muon spectrometer (MS), designed to capture additional muons. The momentum and charge identification of charged particle in ID and MS are based on two magnet systems surrounded.

3.2.1 Magnet systems

The magnet system of ATLAS bends charged particles around the various layers of detector systems, helping to contain the tracks of charged particles and measure their momenta. The main components of the magnet system are: central solenoid magnet, barrel toroid and end-cap toroids.

The superconducting solenoid is of 4.5-cm thick, 5.8-m length and 2.4-m diameter, surrounding the inner detector. It generates 2 T magnetic field aligned with the beam axis.

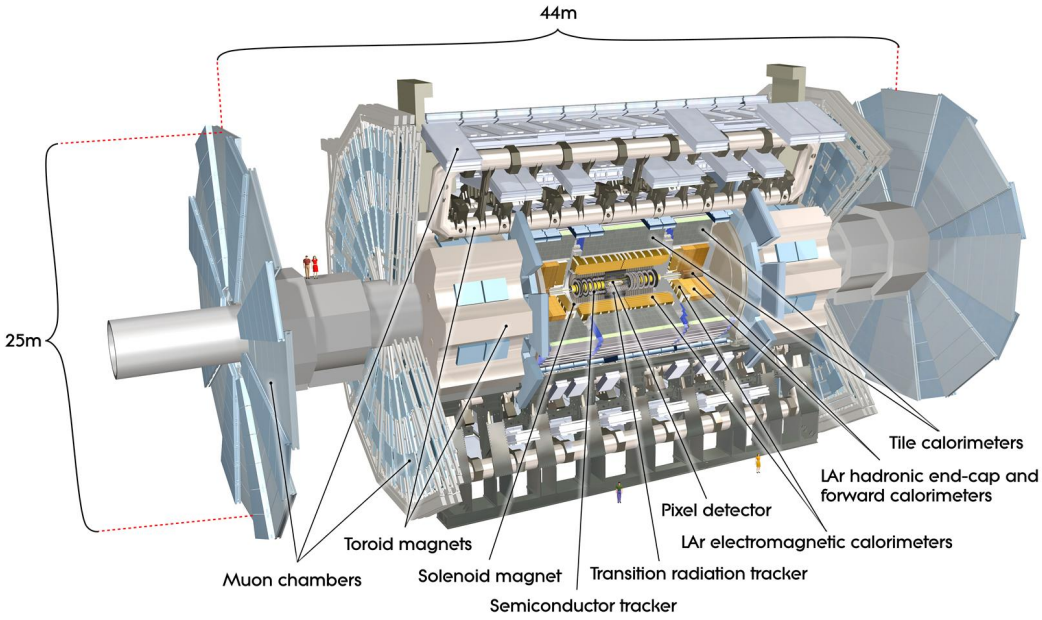

Figure 3.2: Illustration of the ATLAS detector complex

The superconducting toroids, one in the barrel and two in the end-cap, generate a toroidal magnetic field for muon spectrometer. Each toroid is air-core and consists of eight coils. The barrel toriod is 25.3 m long and with 9.4 m and 20.1 m inner and outer diameters, and the end-cap toriods have 5.0 m axial length and 10.7 m outer diameter, so that the muon spectrometer is immersed in generated magnetic field, 0.5 T in barrel and 1 T in end-cap respectively.

3.2.2 Coordinate system

Centered around the interaction point, ATLAS coordinate system is right-handed and forward-backward symmetric, with the z-axis defined as the beam direction and the x-y plane transverse to it. Positive x-axis points to the center of LHC ring, and positive y-axis points upwards. Normally the cylindrical coordinates are used in the x-y plane and some kinematic variables are used to better describe particle state. Let the azimuthal angle be ϕ and polar angle be θ. Then the rapidity is defined as:

$$y = \frac{1}{2}\ln\frac{E + p_z}{E - p_z} \tag{3.3}$$

and the pseudorapidity is defined as:

$$\eta = \ln[\tan(\theta/2)] \tag{3.4}$$

p_x, p_y and p_z represent the component of the momentum vector along each axis, and the transverse momentum pT is defined as that of the transverse component. The three-dimensional angular distance

between two particles (vectors) is defined as

$$\Delta R = \sqrt{\Delta\eta^2 + \Delta\phi^2} \tag{3.5}$$

More related variables will be defined in section that mentioned.

3.2.3 Inner detector

The inner detector (ID), or track detector is the first detector from the interaction point, designed to provide hermetic and robust pattern recognition, excellent momentum resolution and both primary and secondary vertex measurements for charged tracks above 0.5 GeV pT and within $|\eta| < 2.5$. In addition, electron identification over $|\eta| < 2.0$ is also provided. To satisfy the requirements of high granularity and precision performance even at highest luminosity collisions of LHC, it consists of three independent but complementary sub-detectors: Silicon Pixel Detector (PIX), SemiConductor Tracker (SCT) and Transition Radiation Tracker (TRT), within a cylindrical envelope of length ± 3512 mm and of radius 1150 mm, within a solenoidal magnetic field of 2 T. The layout of ID is displayed in Figure 3.3

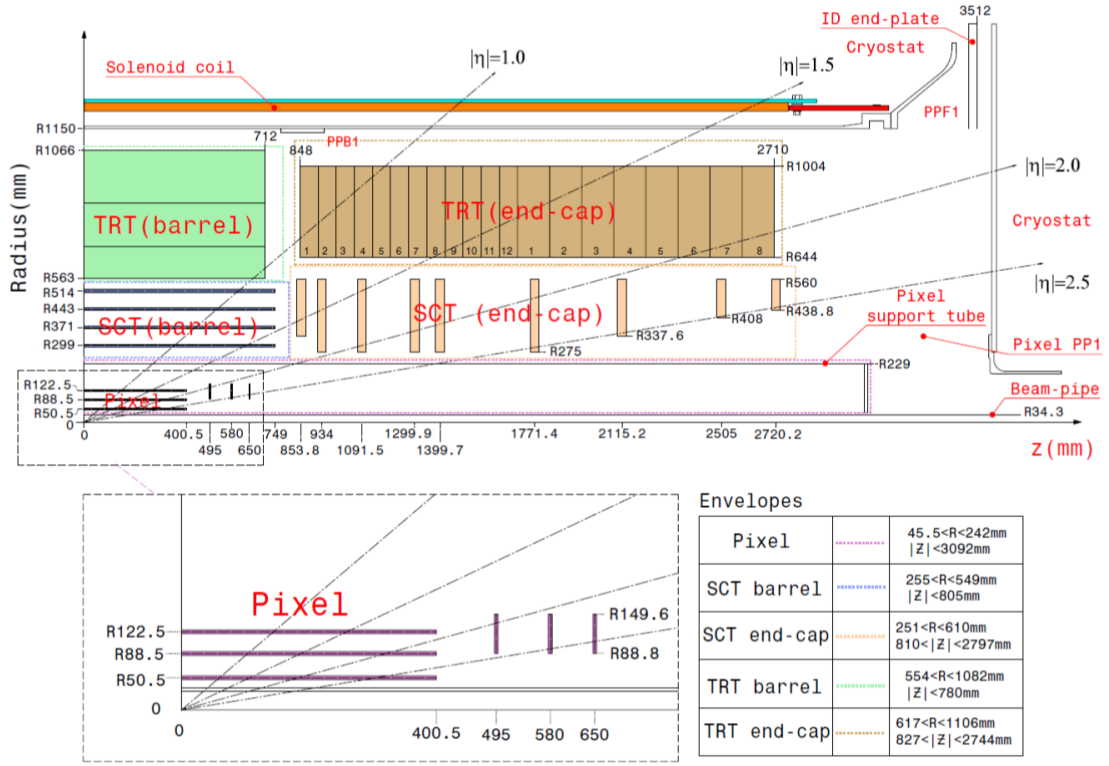

Figure 3.3: View of a quarter-section of the ATLAS inner detector showing each of the major detector elements with its active dimensions and envelopes

As illustrated in Fig. 3.3, the PIX is closest to the beam pipe, composed of silicon pixel sensors arranged in three layers in the barrel, at R = 50.5, 88.5 and 122.5 mm, and three disks in the endcap,

at $|z|$ = 495, 580 and 650 mm in Run-I. Due to the high-radiation environment imposes stringent conditions on the inner-detector sensors, a new layer of PIX, named "Insertable B-Layer" with the highest granularity and of radius 31 mm, is installed between Run-I and Run-II, to further enhance measurement to the tracks and secondary vertex, in compensation of the previously first layer of radius 50.5 mm, so-called "B-Layer". Together PIX provides a intrinsic accuracy at 10 μm in $R-\phi$ and 115 μm in z.

The SCT is a silicone micro-strip detector surrounding the PIX, ranged from R = 275 mm to 560 mm. SCT has four double layers of silicon strip sensors in barrel and nine layers in end-cap, providing four two-dimensional space points thus essential to the momentum and vertex position measurements. The intrinsic accuracy of SCT is 17 μm in $R-\phi$ and 580 μm in z, coarser than PIX due to larger radius.

The TRT is the outmost inner detector working on tracking as well as electron identification, with radius from 563 mm to 1066 mm, based on polyimide drift (straw) tubes of 4 mm diameter and 144 (37 for end-cap) cm length. Each straw tube is filled with $70\%Xe, 27\%CO_2$ and $3\%O_2$. Low energy transition radiation photons from electrons are absorbed in the Xe-based gas mixture, and yield much larger signal amplitudes than minimum-ionising charged particles. Only $R-\phi$ and $z-\phi$ information is measured in TRT, both of an intrinsic accuracy approximating 130 mm.

3.2.4 Calorimetry

Particles enter the calorimeters after passing through the inner detector to measure the energy loss. In most detecting system, calorimeters are designed to absorb all or most of particles, have the energy deposited and measured. The ATLAS calorimetry system contains two sections: the ElectroMagnetic (EM) calorimeter and the hadronic calorimeter. The structure of calorimetry system is displayed in Fig. 3.4. EM calorimeter covers the region of $|\eta| < 3.2$, measures the energy of electrons and photons. The hadronic calorimeter is capable to measure the energy of hadrons within $|\eta| < 4.9$, using different type of calorimeters. In addition, missing energy reconstruction is based on calorimeters and muons have small energy ($\sim$ 3 GeV) deposited.

3.2.5 EM calorimeter

The electromagnetic calorimeter are liquid argon (LAr) detectors with accordion-shape electrodes and lead absorbers, composed of two identical half-barrels ($|\eta| < 1.475$) and two end-caps ($1.375 < |\eta| < 3.2$). The half-barrels are 6.4 m long and with inner and outer radius of 1.4 m and 2 m. Each of the end-caps consists of two co-axial wheels, with inclusive internal and external radius pf 330 mm and 2098 mm. The accordion geometry provides symmetry and full coverage in ϕ and fast readout, while there are cracks along η, at $|\eta| = 0$ (the boundary of two half-barrels), $1.37 < |\eta| < 1.52$ (between barrel and end-cap), and at $|\eta| = 2.5$ (the boundary of inner and outer end-cap wheel).

The total thickness of the EM calorimeter are 22 radiation length (X_0), increasing from 22 X_0 to 33 X_0 in the barrel and varying from 24 X_0 to 38 X_0 in the end-cap. The EM calorimeters has longitudinal samplings, three in the precision-measurement region ($0 < |\eta| < 2.5$) and two in the forward region ($2.5 < |\eta| < 3.2$). In addition there is an individual LAr layer without absorber before EM calorimeter covering $|\eta| < 1.8$ region to recover the energy lost in the upstream material (cryostat, superconducting

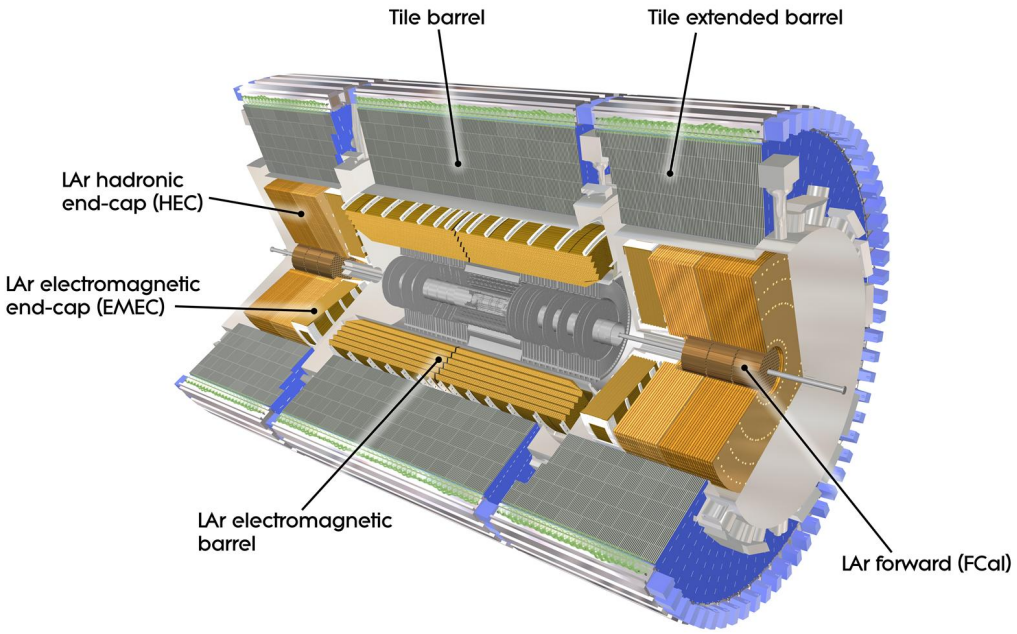

Figure 3.4: Overview of the ATLAS calorimeter

coil, inner detector, etc.). The thickness of 1st, 2nd and 3rd approximates to 4 X_0, 16 X_0 and 2 X_0 respectively, therefore the majority of energy (up to 50 GeV) is deposited in the 2nd sampling. Meanwhile the 2nd sampling has a cell size of $\Delta\eta \times \Delta\phi = 0.025 \times 0.025$, providing significant $\eta - \phi$ coordinates. The 1st sampling, also named "strip" layer, has finest granularity in η but relatively coarse in ϕ. The η granularity of 1st sampling is 8, 6, 4, 2.5 times of 2nd sampling, varying at $|\eta|$ = 1.8, 2.0, 2.2, 2.5, while the ϕ granularity is 1/4. This special "strip" geometry strongly enhances the η resolution thus the identification of photon/π^0, which is not sensitive to ϕ resolution due to the converted photons. The 3rd sampling is arranged with cells of $\Delta\eta \times \Delta\phi = 0.050 \times 0.025$ size. It collects the tail of the electromagnetic shower, therefore less segmented in η.

Particles entering the EM calorimeter interact with the absorbers and generate showers. In each cell, ionization electrons drift to the electrode under high voltage of 2000 V, inducing signal proportional to the deposited energy. Hence energies and positions of showers are recorded by cells of all samplings, accurately locating the interaction point and giving references for electron/photons identification and isolation.

3.2.6 The hadronic calorimeter

The hadronic calorimeter follows behind the EM calorimeter, absorbing and measuring hadronic showers with three types of calorimeters according to the pseudorapidity: the scintillating tile calorimeter in $|\eta| < 1.7$, two LAr calorimeters using different absorbers, named the Hadronic endcap

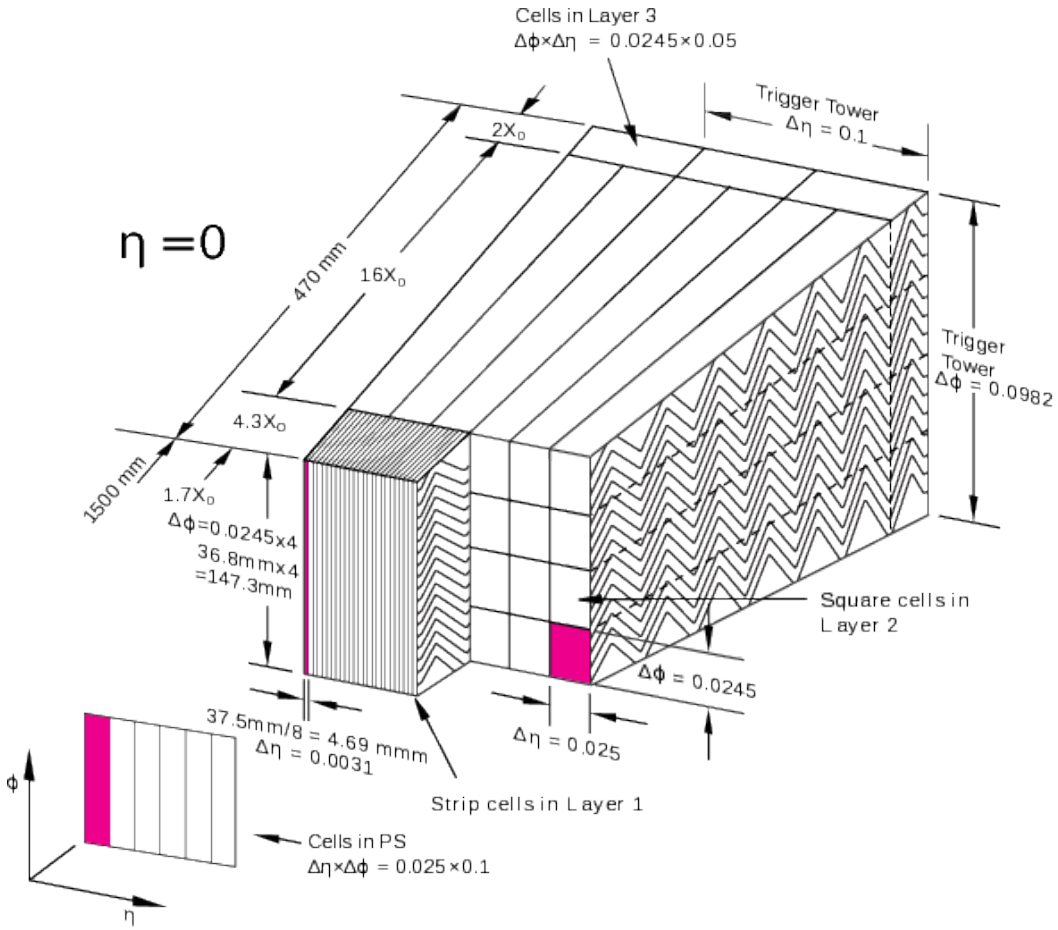

Figure 3.5: Sketch of a barrel module where the different layers are clearly visible with the ganging of electrodes in ϕ. The granularity in h and f of the cells of each of the three layers and of the trigger towers is also shown.

calorimeter (HEC) and forward calorimeter (FCal), covering $1.5 < |\eta| < 3.2$ and $3.1 < |\eta| < 4.9$ regions respectively.

The tile calorimeter surrounds around the EMC, with an inner and outer radius of 2.28 m and 4.25 m, consisting of one 5.8-m-long central barrel and two 2.6-m-long extender barrels. It's a longitudinally sampling calorimeter with polystyrene scintillating tile as the active material and steel as the absorber. There are three samplings with corresponding granularity $\Delta\eta \times \Delta\phi$ equal to 0.1×0.1, 0.1×0.1 and 0.2×0.1. The total thickness is about 7.4 interaction length (λ). Ionising particles crossing the tiles induce the production of ultraviolet scintillation light, which is captured and converted to visible light by the wavelength-shifting fibres placed next to the tile edges. subsequently read out by the photomultiplier tubes (PMT's).

The LAr calorimeters, including HEC and FCal, cover the end-cap and forward regions. In each end-cap the HEC consists of two independent wheels of thickness 0.8 m and 1.0 m with radius 2.09m, the front wheel (HEC1) made of 25-mm-thick copper plates, and the rear wheel (HEC2) made of 50-mm-thick copper plates. Each wheel containing two longitudinal sections. The gap between

plates are constant to be 8.5 mm, divided into four 1.8 mm wide drift spaces by three electrodes. The granularity of the HEC cells is in $\Delta\eta \times \Delta\phi$ = 0.1 x 0.1 when $|\eta|$ < 2.5 and 0.2 x 0.2 for larger value of $|\eta|$. The FCal is a longitudinal sampling calorimeter located at high η, at a distance of approximately 4.7m from the interaction point, with three 45 cm deep modules, one electromagnetic module (FCal1) using copper as the absorber, and two hadronic modules (FCal2 and FCal3) using tungsten as the the absorber. To adjust for the high density detecting requirement, especially large signal frequency from pile-up, the LAr gap width is smaller in FCal comparing to EMC, resulting to 250, 375 and 500 microns. The cell's granularity is $\Delta\eta \times \Delta\phi$ = 0.2 x 0.2.

3.2.7 Muon spectrometer

The muon spectrometer (MS), illustrated in Fig, is a large tracking system surrounding the calorimeter. It's designed to detect charged particles passing through the calorimeter and provide precise muon momenta over the $|\eta|$ < 2.7 region, as well as muon trigger up to $|\eta|$ = 2.4. Muon track is bended in the toroidal magnetic field and captured in tracking chambers.

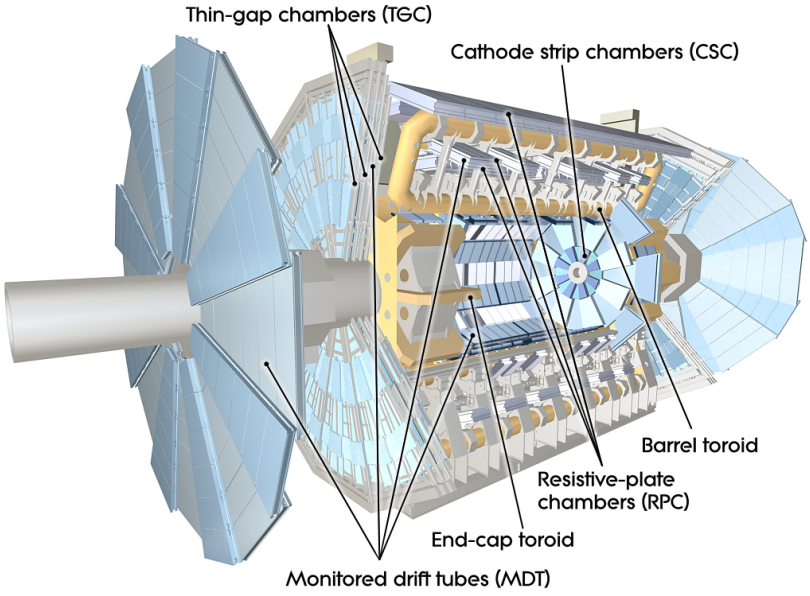

Figure 3.6: Layout of the muon spectrometer [37]

The momenta measurement is performed by the Monitored Drift Tube (MDT) chambers expect for the innermost end-cap layer where the coverage is limited to $|\eta|$ < 2.0. These chambers consist of three to eight layers of pressurised drift tubes, each with a diameter of 29.970 mm, operating with Ar/CO_2 gas (93/7) at 3 bar. In total there are 1,171 chambers with 354,240 tubes and the average resolution is about 80 μm per tube or about 35 μm per chamber in z.

In the innermost end-cap tracking layer of 2.0 < $|\eta|$ < 2.7, the Cathode-Strip Chambers (CSC) are used due to their higher rate capability and time resolution. CSC's are multiwire proportional chambers with cathode planes segmented into strips in orthogonal directions, allowing both coordinates to be

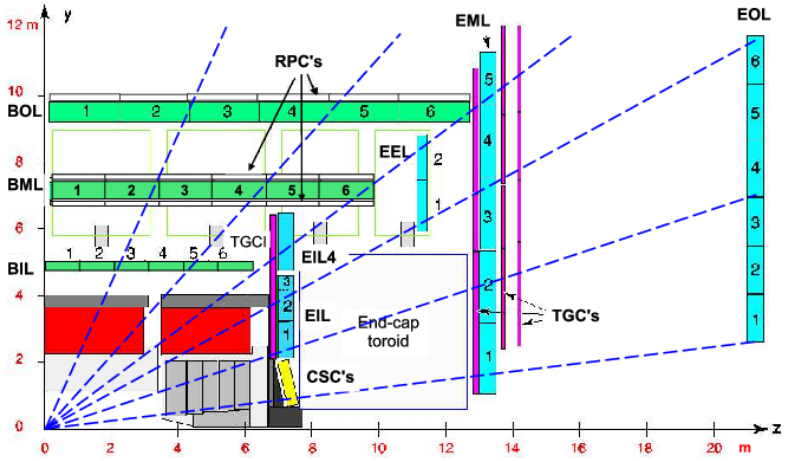

Figure 3.7: Cross-sectional view of the ATLAS muon spectrum from [38].

measured from the induced-charge distribution. Due to the geometry and readout pitch, the resolution is about 5 mm in the transverse plane (ϕ direction), worse than the that in the bending plane which is about 40 μm (R direction).

For trigger function, there are additional two kind of fast trigger chambers in complementation: Resistive Plate Chambers (RPC) covering $|\eta| < 1.05$, and Thin-Gap Chambers (TGC), covering $1.05 < |\eta| < 2.4$. To tag the beam-crossing, the time resolution is 1.5 ns for RPC and 4 ns for TGC, and both chamber types deliver signals with a spread of 15~25 ns. After matching of the MDT and trigger chamber hits in the bending plane, the coordinate of trigger chamber in non-bending plane is adopted as the second coordinate of the MDT measurement to improve the tracking accuracy.

3.2.8 Data taking and trigger system

In ATLAS the proton-proton collision happens every 25 ns, at a frequency of 40 MHz. Moreover, the average number of interactions per bunch crossing is up to 40 in Run-II. This amount of data is impossible to get completely recorded, meanwhile, the interactions are dominated by soft processes and only quite small ratio of events give the physical processes of interest. Therefore a trigger system is implemented to filter the events within the capability of ATLAS' data recording around 200 Hz. ATLAS trigger system consists of three levels of event selection: Level-1 (L1), Level-2 (L2), and event filter.

The L1 trigger, based on the hardware of custom-made electronics, searches for signatures from high-pT muons, electrons/photons, jets, and τ-leptons decaying into hadrons, to decide whether to proceed an event. Reduced-granularity information from calorimeter sub-systems and part of MS (RPC and TGC) are used to give quick response, and the decision is made at most 2.5 μs after the corresponding brunch-crossing. Due to the limit of readout system, the maximum event rate passing L1 is 75 kHz. Besides, the Regions-of-Interest (RoI's), regions with identified L1 trigger objects are also found in L1, and become the seed of L2 trigger.

The L2 trigger uses the RoI's information to suppress the event rate below 3.5 kHz with an average event processing time of around 40 ms. Then the event filter further reduces the rate to approximately 200 Hz, with fully built events and offline analysis procedures. The L2 and event filter together form the High-Level Trigger (HLT). The HLT algorithms use the full granularity and precision data of all sub-detectors, including ID, calorimeter and MS, so that the reconstructed objects is mostly close to offline reconstructions. The average event processing time is of order four seconds.

Besides the L1 and HLT trigger, there is also a data quality monitor to guarantee prompt data for offline analysis. Realtime detecting conditions, such as voltages, temperature, humidity, etc, may shortly go out of control, degrade the data quality but still fire the triggers. These conditions are recorded separately, as Data Quality (DQ) flags, and the data entering experiments are required to pass all DQ flags. DQ flags are stored in Good Run List (GRL), together with the luminosity information of corresponding dataset.

With the complex detecting system, in particular the inner detector, EM calorimeter and MS, ATLAS allows to reconstruct electrons and muons at high efficiency and accuracy. These leptons then enter the selection of W-boson leptonic decay processes. Since kinematics of lepton, especially the rapity and transverse momentum are directly replied on W-bson kinematics, the detector-level energy and momentum calibration of lepton is essential in W-boson measurements.

4 Electron measurements

4.1 Electron reconstruction

The reconstruction of electron and photon relies on the ATLAS electromagnetic calorimeter and inner detector. As described in Chap. 3, energies of electrons are deposited in multi-samplings of calorimeter, which generates electromagnetic showers and induces ionisation in the liquid argon, ultimately converted to signal in electrodes. The shower's energies and positions are then recorded in the cells of each sampling, These cells are grouped into cluster of specific size for reconstruction, named cluster. Meanwhile, the trajectory of charged particle is built in inner detector. If a hard track is matched to the cluster with superior energy, the object is supposed to be an electron candidate, while an unconverted photon candidate is very likely to be reconstructed from a cluster with significant energy but matching to no track.

In each cell of cluster, the energy consists of signal and electronic noise, the later is approximately 10 MeV in first layer and 30 MeV in second and third layer. The noise can be relatively non-negligible regarding additional effect from the pile-up, so a noise threshold is applied when collecting "high-pile-up" data. However this threshold is removed in low-pile-up experiments, thus the difference needs to be studied in this chapter.

Next, there are two algorithms to reconstruct the EM clusters, the sliding-window clustering algorithm and the topological clustering (topocluster) algorithm. The topocluster algorithm builds clusters with 3-dimentional flexible size, has better spatial description to showers, and is more used in hadronic reconstruction. The sliding-window clustering algorithm adopts fixed size clusters and is more efficient for objects with well-defined shower shapes, in particular EM showers of electron and photon objects, hence it's the preferred algorithm.

In the sliding-window algorithm, the cluster in reconstruction is energy tower summing all longitudinal samplings with fixed $\Delta\eta \times \Delta\phi$ size, usually $\Delta\eta \times \Delta\phi = 0.025 \times 0.025$. Cluster of such size contains 3×7 (5×5) cells in second sampling, in barrel (end-cap). The "3×7" or "5×5" also refers to the size of cluster in convention. The procedure proceeds in the following steps:

1. Clusters of 3×5 size with energy above 2.5 GeV initialize the reconstruction, named the "seed clusters".

2. These seed clusters are matched to tracks in ID. Electrons converted from photons are rejected through requesting the tracks are well-recognized, close to the interaction point or hit the PIX.

3. Seed clusters that pass the track-matching are selected. New clusters of 3×7 (5×5) size in the barrel (end-cap) are built around the seed clusters, with possibly extra satellite cluster.

The newly built cluster of the 3×7 (5×5) size plus the satellite cluster within larger size (5×12), are the cluster accounting for EM calorimeter energy deposition. It's originally pure 3×7 (5×5) cluster in order to envelop the electron shower while minimizing the noise, but later developed to the "supercluster" with extra satellite cluster to recover recovering the hard bremsstrahlung effect during Run-II.

Energies and positions of electrons are calculated from these superclusters and information of matched tracks, using a multivariate (MVA) technique. True energies and shower-shapes of electrons, converted photons, unconverted photons in simulation are used in a regression boosted decision tree training to optimized the electron reconstruction. The residual difference of electron energy reconstruction in data and simulation are calibrated offline, in resolution and response.

In addition, there is a likelihood(LH)-based identification for electron candidates to separate electron signal from hadronic jets or converted photon backgrounds, It uses quantities related to the electron cluster and track measurements such as calorimeter shower shapes, information from the transition radiation tracker, track-cluster matching related quantities, track properties, and variables measuring bremsstrahlung effects for distinguishing signal from background. And as multivariate analysis, it simultaneously evaluates several properties of the electron candidates when making a selection decision. Three levels of identification operating points are typically provided for electron identification: LooseLLH, MediumLLH and TightLLH. The MediumLLH is the default option in most analyses.

4.2 Electron energy calibration

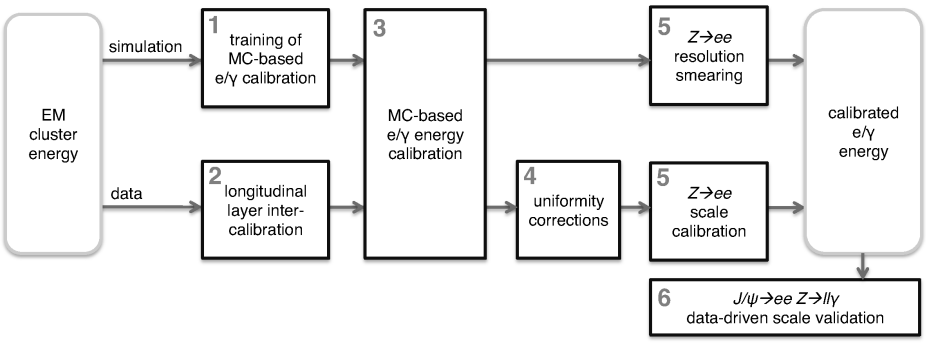

Figure 4.1: Schematic overview of the procedure used to calibrate the energy response of electrons and photons in ATLAS Ref. Aad:2014nim.

The general work-flow of electron energy calibration is illustrated in Fig. 4.1, consisting of three steps [39]:

1. The non-uniformity in detector energy response is mitigated with corrections from the the ratio of the measured calorimeter energy and track momentum from Z boson decays. This is a data-driven correction and only applied to data.

2. The simulation-based calibration in electron reconstruction which is applied to both data and MC to correct the energy and position of EM clusters.

3. A correction to account for the difference in energy resolution between data and simulation is derived, and applied to the simulation. Meanwhile, the data energy scale is adjusted to simulation using a large sample of Z boson.

The first two steps of this procedure are highly dependent on detector capability and expected to be universal for high-plie-up and low-pile-up electrons, but the energy resolution and scales are required to measure in-situ with data and simulations. The energy scale factor α scales the measured energy of data to correct for residual mis-calibration according to the following parametrisation in each phase-space region (typically pseudorapidity of calorimeter cluster) i by

$$E_i^{\text{data}} = E_i^{\text{MC}}(1 + \alpha_i) \tag{4.1}$$

where E_i^{data} and E_i^{MC} are the electron energies in data and simulation and α_i represents the relative deviation of the energy in data from the MC energy. The MC is assumed to be perfectly calibrated. The relative resolution of the calorimeter can be written as:

$$\frac{\sigma(E)}{E} = \frac{a}{\sqrt{E}} \oplus \frac{b}{E} \oplus c \tag{4.2}$$

where a is the stochastic term describing the fluctuations related to the development of the electromagnetic shower, b is the electronic and pile-up noise term, c is the constant term. An additional constant term c_i' is used to enlarge the width of the MC mass distribution up to the data one in a given η_{calo} bin i:

$$\left(\frac{\sigma(E)}{E}\right)_i^{\text{data}} = \left(\frac{\sigma(E)}{E}\right)_i^{\text{MC}} \oplus c_i' \tag{4.3}$$

For low-pile-up run, due to the lack of statistics, it's not quite practical to have the scales measured in-situ. Instead, the electron calibration is developed with the principle to adopt as possibly many high-mu results in the low-pile-up experiments.

To derive the low pileup energy correction scale factors, the dependence of the high pileup data on the pileup is studied Then the high statistics of the high-pile-up data can be directly exploited with an extrapolation approach, which consists of separating the nominal high-pile-up data into different intervals of μ, and using the template method to extract the energy scale factors α separately for each interval of μ. Then a polynomial function fit (order-1 in calibration and order-2 in uncertainty evaluation) is performed to extrapolate the result to μ=0, displayed in Figure 4.2.

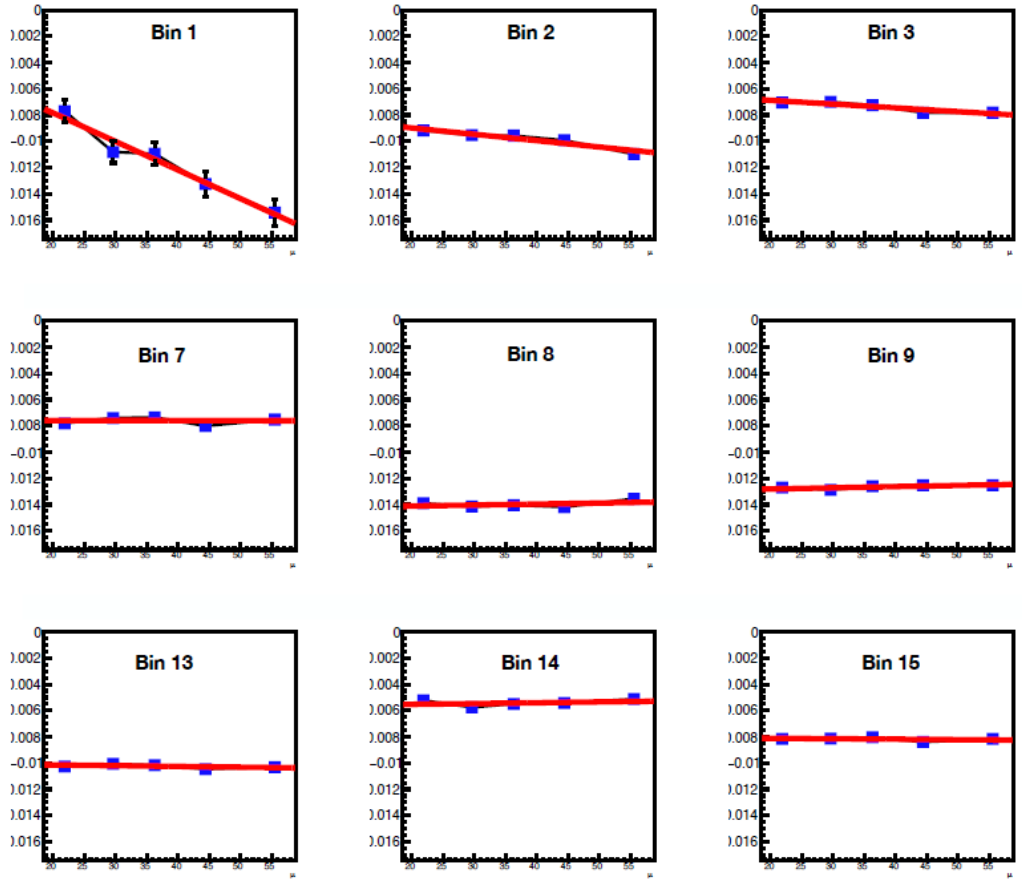

Figure 4.2: Extrapolation results of 2017 for all 24 bins of η calo. the blue points show the energy scale factors for different intervals of μ, the red curve show the extrapolation results to μ=0 using a polynomial function of order 1.

Though this extrapolation works for electron at 0-pile-up, it's still using high-pile-up configure. The discrepancy induced by difference of noise threshold in EM cluster has to be considered. To evaluate it, low-pile-up data and simulations are reprocessed with the low-mu noise threshold. The average difference of $(E^{\text{low-threshold}} - E^{\text{high-threshold}})/E^{\text{low-threshold}}$ between data and simulation is then available with event-by-event calculation and added to the extrapolated energy scales. The result is displayed in Fig. 4.3.

After correcting the pile-up and noise, the extrapolation results in 24 bins of η are closer to the low-pile-up scales extracted directly with the template method, as displayed in figure 4.4. When the crack region is excluded, the difference between the extrapolated and low-pile-up in-situ results is of the order of 0.1% in the barrel region, and increases to 0.5% in the endcap region. The extrapolated energy scales are finally adopted for its significantly better statistical uncertainty.

The data and MC distributions are compared in Figure 4.5 for the low-pile-up data with such calibration. The lower panel shows the data to simulation ratio, together with the systematic uncertainty of high-pile-up runs (described in Ref refAaboud:2018ugz) without including the statistical uncertainty which

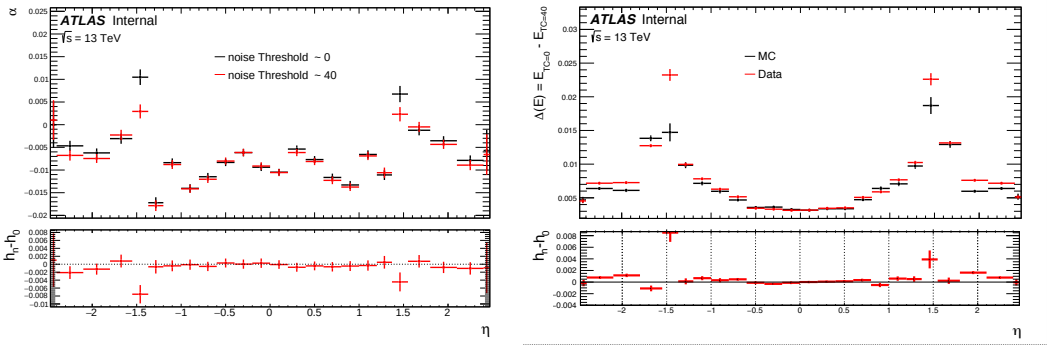

(a) (b)

Figure 4.3: (a) The effect of the difference of the noise threshold between the standard and low pile up runs on the energy scale factors α using the template method; (b) the difference of the energy $E^{high-threshold}$ - $E^{low-threshold}$ between data and simulation.

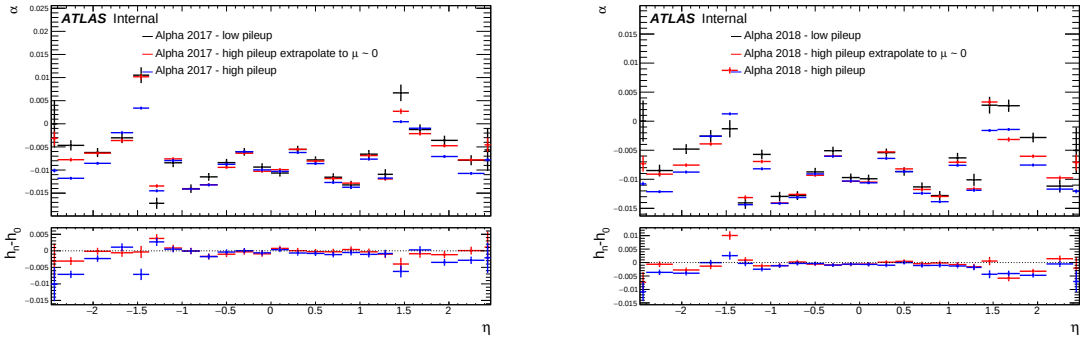

(a) (b)

Figure 4.4: The extrapolation results after correcting the effects of the difference of the noise threshold for 2017 (a) and 2018 (b).

is shown on the data points. The agreement is good in the peak region: the difference remains below 3% and is covered by the quoted uncertainties.

The systematic uncertainties evaluated in Ref. [40] for high-pile-up electrons are valid as well for the low pileup data. In addition, there are other systematic uncertainties related to the extrapolation procedure, denoting the the polynomial functions and the the number of μ intervals in the α extrapolation along $< \mu >$.

Figure 4.6 shows an overview of all systematics of low pile-up runs:

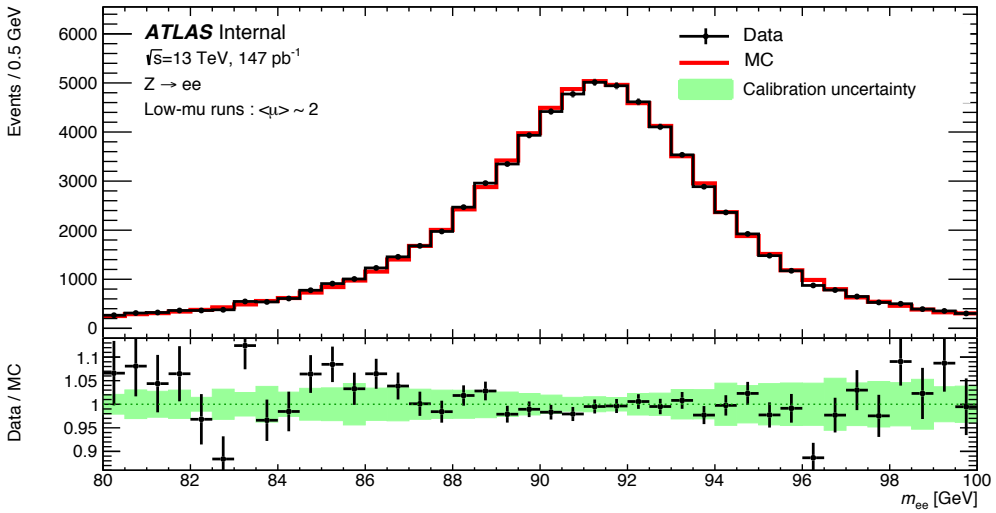

Figure 4.5: The invariant mass distribution around the Z-mass for low pileup Data

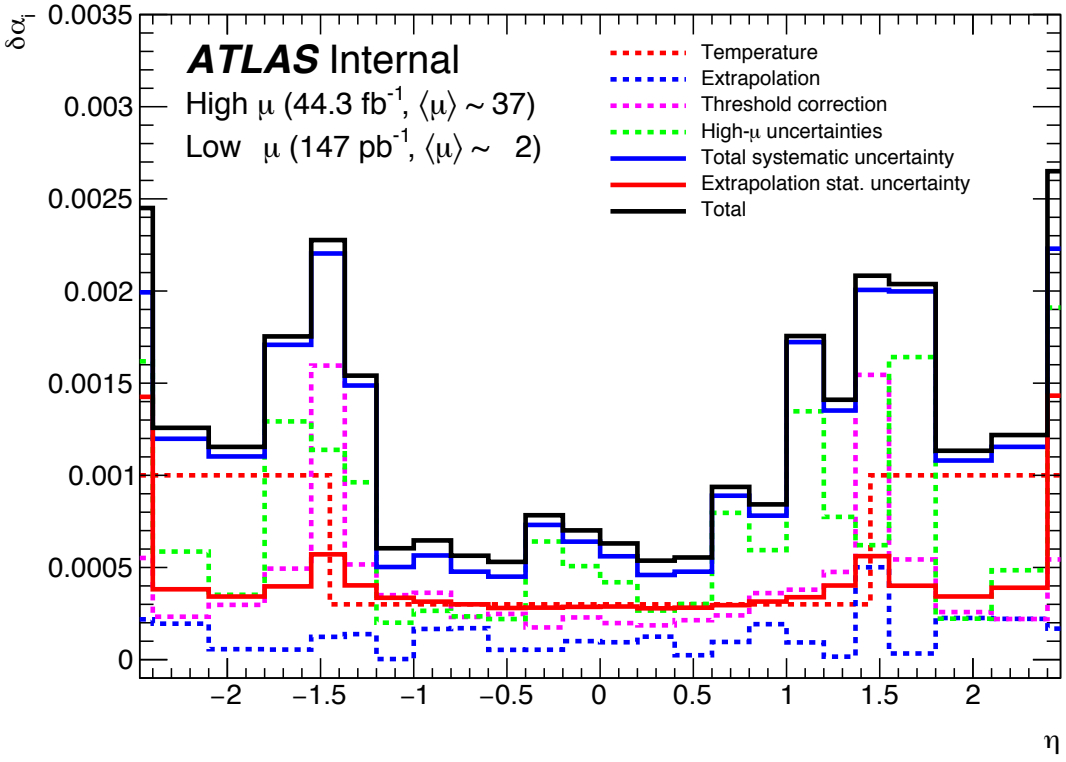

Figure 4.6: Uncertainties on the energy scale corrections as a function of η for the low pile-up data.

4.3 Electron selection efficiency

A set of selections to electrons are used in the W boson analyses. Besides the fundamental cuts on p_T and η due to detecting capability, the successfully reconstructed electrons are also expected to pass the identification, isolation and trigger selections. The reconstruction is about whether an object is well reconstructed as electrons, based on its energy deposits in the electromagnetic calorimeter and a matched track in the inner detector, then identification and isolation criteria rely on the shapes of EM showers in the calorimeter as well as on tracking quantities, to identify electron from other objects, mostly photon and jet. As introduced in Chap. 3, trigger is also considered, which requires the electron candidate to be loose-identified and with energy larger than 15 GeV in low-pile-up samples. The combination of these four selections significantly improves the purity of electron selected in the analysis and rejects most of backgrounds. However, the resulting efficiencies of these selections measured on real data and MC simulation are different, due to complex in-situ detecting environment, imperfect track and cluster simulation, backgrounds and jets activities, etc. In experiments, electron spectra predicted by the simulation must be corrected for instrumentation inefficiencies, such as those related to trigger, reconstruction, and identification, before absolute measurements can be made. To correct this effect, scale factor (SF), are applied to the simulation to account for known discrepancies with the data. This correction factor is defined as the ratio of the efficiency measured in data to that determined from MC samples. The total efficiency correction to a single electron in W events may be factorized as a product of different SFs terms:

$$W_{\text{event}}^{W\to e\nu} = \text{SF}_{\text{reco}} \cdot \text{SF}_{\text{ID}} \cdot \text{SF}_{\text{Isolation}} \cdot \text{SF}_{\text{Trigger}} \tag{4.4}$$

The standard method to measure the electron efficiencies is the "tag-and-probe", which searches for qualified electron-pair candidates in Z-boson-decay events, applies tight selections to one object of each pair to further increase the Z-event purity so that the other object is at high possibility to be an electron, yet blinded to any selection. It can be summarized to several steps:

1. apply $Z \to ee$ selections (Cut1) to get stable and pure source of electron-positron pairs.

2. To one object of each pair (named *tags*) is applied a tight selection (Cut2).

3. In event passing Cut1 and Cut2, the other object is very likely to be a real electron, as *probe*, and the efficiency of given selection can be estimated as the efficiency of the *probe* electron passing it.

4. Uncertainty is evaluated by shifting Cut1 and Cut2 to have different signal purity and backgrounds control.

In the following sections, the SFs for low-pile-up run, measured with 5-TeV and 13-TeV low-pile-up data and MC will be discussed. The order of the requirement: Reco, ID, Isolation, Trigger define also the order of the selection applied on the *probes*.

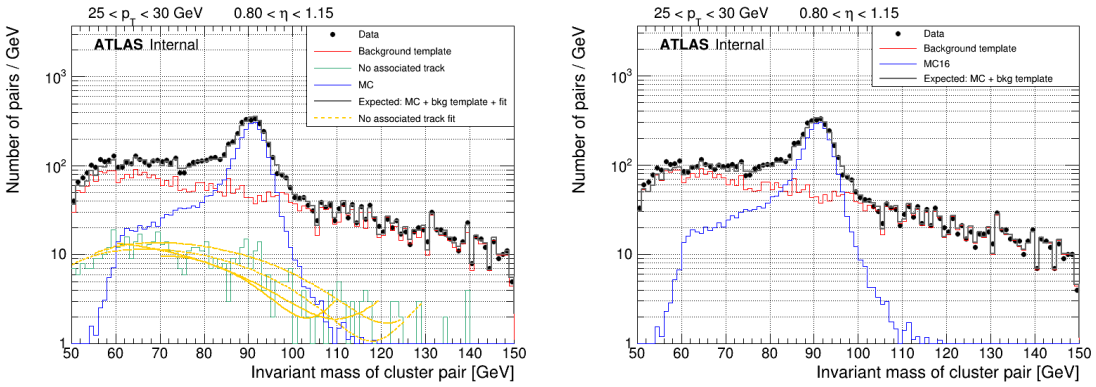

Figure 4.7: Mass distribution of the *tag* and probe pair in Reco efficiency measurement with 13 TeV $339pb^{-1}$ low-pile-up data for the denominator (left) and numerator(right)

4.3.1 Reconstruction efficiency

The reconstruction efficiency is defined as a fraction of all electromagnetic clusters (i.e. all reconstructed electrons and photons) that match an inner detector track. Then an additional requirement of loose track is imposed on numerator electrons: NPix > 1, NSCT > 7 for pixel and SCThits, named "PassTrackQuality".

$$\epsilon^{reco}(p_T, \eta) = \frac{\mathrm{N_{pass}} - \mathrm{N^{bkg}_{pass}}}{\mathrm{N_{pass}} - \mathrm{N^{bkg}_{pass}} + \mathrm{N_{fail}} - \mathrm{N^{bkg}_{fail}} + \mathrm{N_{photon}} - \mathrm{N_{fit}}}, \tag{4.5}$$

where $\mathrm{N_{pass,fail}}$ is the electrons number passing/failing "PassTrackQuality", $\mathrm{N^{bkg}_{pass,fail}}$ is number of electrons in fitted background template passing/failing the track cut, $\mathrm{N_{photon}}$ is the number of photons and $\mathrm{N_{fit}}$ is the number of estimated background photons.

Both *tags* and *probes* electrons are selected in the central precision region of $|\eta| < 2.47$, passing the "isGoodOQ" (is Good Object Quality, a cut-based loose identification requirement for electron and photon objects) quality. Additional cluster quality requirements and a transverse momentum cut of p_T > 20GeV being matched to the trigger element, are applied to the *tags*. *Probes* are required to pass the egamma ambiguity tool (to identify object is an electrons with a track or a photon), p_T > 15GeV and a veto for the probes close by a jet with E_T^{jet} > 20 GeV (ΔR <0.4) is imposed. Converted photons are also excluded from the measurement. The mass distribution of the *tag* and probe candidates is shown in Fig. 4.7 for the denominator (left) and numerator (right).

The results are showed in Fig. 4.8 with reconstruction efficiencies of 13-TeV low-pile-up data and MC, and SFs as their ratio. The 5-TeV results are supposed to be very similar thanks to the clean environment provided by low-pile-up run. So the comparison and availability of combination between 13-TeV and 5-TeV data is are studied in next paragraph.

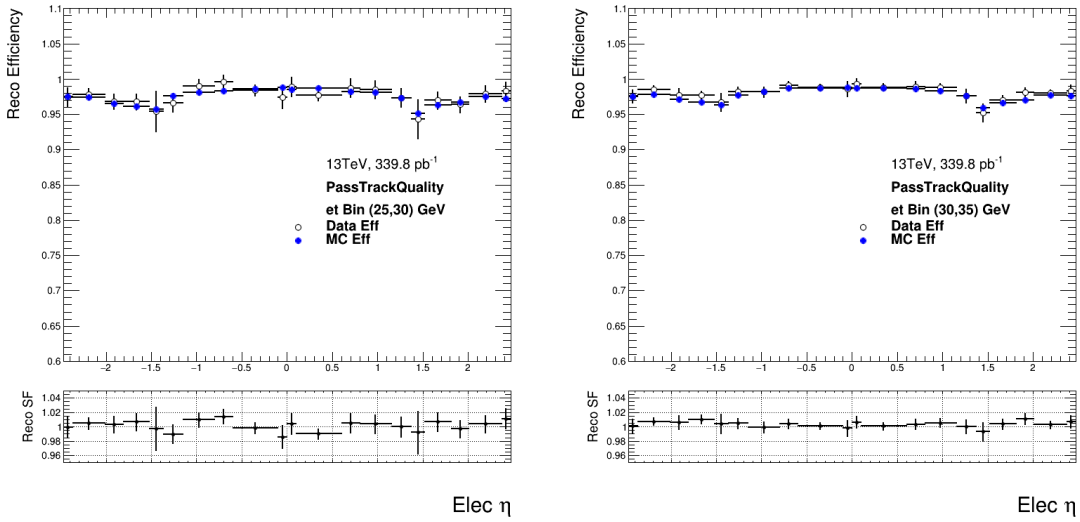

Figure 4.8: Electron reconstruction efficiencies and scale factor using 13 TeV 2017+2018 low-pile-up data. The total uncertainties are included respectively.

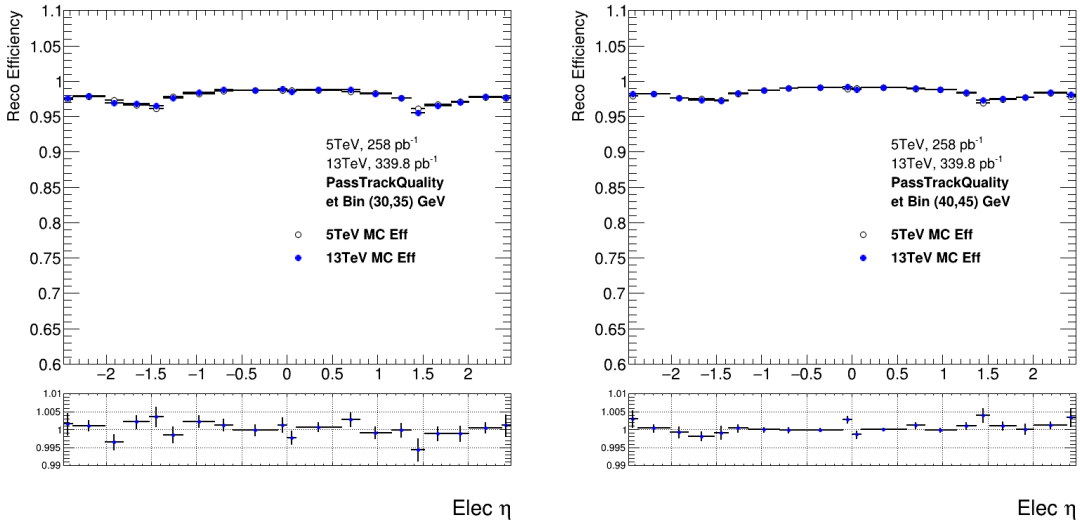

Figure 4.9: Electron reconstruction efficiencies comparisons of 5 TeV and 13 TeV low-pile-up MC in [30,35]GeV (left) and [40,45]GeV (right). The total uncertainties are included respectively.

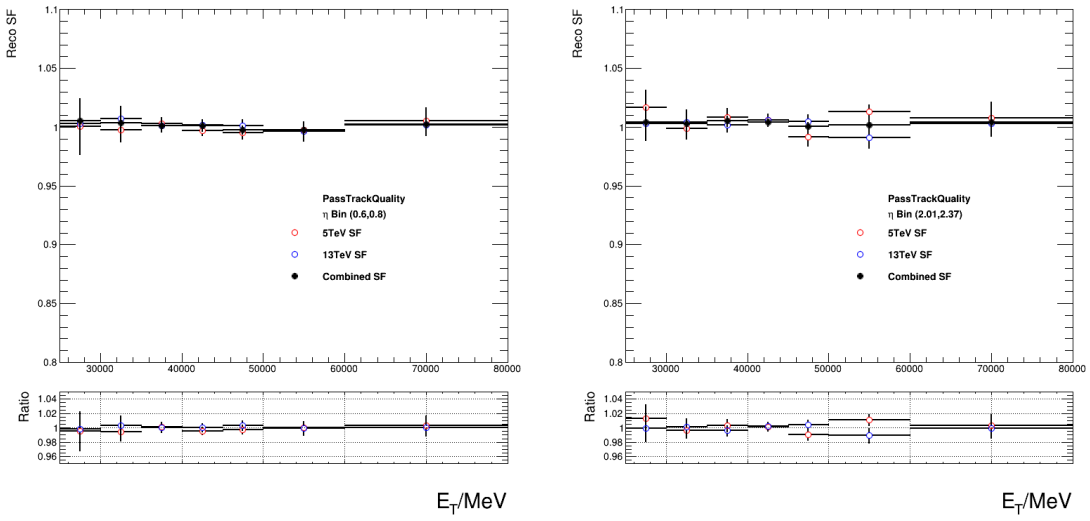

Figure 4.10: Electron Reco SFs comparisons with 5 TeV, 13 TeV and 5+13 combination in η range [0.60-0.80] (left) and [2.01-2.37] (right). The total uncertainties are included respectively.

4.3.2 5 and 13 TeV data combination

Low-pile-up data collected at $\sqrt{s}$ = 5 and 13 TeV suffers from the high statistical uncertainty. *tag* and *probe* candidates which satisfy the reconstruction quality selection are affected by high contamination of fake electron and photon background. The amount of background is evaluated using data-driven template fit in each p_T and η category. The limited data statistics in the low-pile-up run affect the data-driven template fit to evaluate the amount of background. One possible solution to reduce statistical fluctuation will be the combination of 13 TeV and 5 TeV data. To validate the compatibility of the two samples, MC reconstruction efficiency for 5 and 13 TeV samples are compared. Results are shown in Fig. 4.9. It's demonstrated that the difference between 5 TeV and 13 TeV are smaller than 0.2%, covered by statistical uncertainty. Figure 4.10 shows the improvement of the reco SF uncertainty while combining the 5 and 13 TeV data.

4.3.3 Extrapolation method in reconstruction SF

The combination of the 5 and 13 TeV data to improve the precision of reco SF is discussed. To further reduce the statistical uncertainty on the efficiency measurement, in particular for the precision of W-mass measurement, like the strategy in energy calibration, an extrapolation of the reconstruction efficiencies from high-pile-up to low-pile-up data has been explored. To validate this approach the MC reconstruction efficiencies are compared for low-pile-up and high-pile-up dataset as shown in Figure 4.11 and 4.12. Huge difference is observed (~0.2% in barrel and ~0.5% in end-cap, comparable to the total uncertainty), which gets larger along $|\eta|$. But the studies in Ref. [41] and Figure 4.13 illustrate the relation between the reconstruction efficiency/SF and number of primary vertex (Nvtx): although the efficiency varies of about 0.5% from low Nvtx to high Nvtx in data and MC the resulting SF are flat, this means that the number of tracks is well modelled by the MC simulation.

To assure that the extrapolation works correctly it is important as well to check that the different settings on the topo-cluster noise threshold used in the low-pile-up data (set at $\mu = 0$) and in the nominal high pile-up runs (set at $\mu = 40$) is not affecting the reconstruction efficiency and therefore the extrapolation from high Nvtx to low Nvtx. The comparison of low-pile-up MC efficiency with different noise thresholds are displayed in figure 4.14, and a negligible difference (<0.1%) is observed in both barrel and end-cap, thus the effect of the cluster noise threshold difference between high-mu and low-pile-up dataset can be covered with additional 0.1% uncertainty.

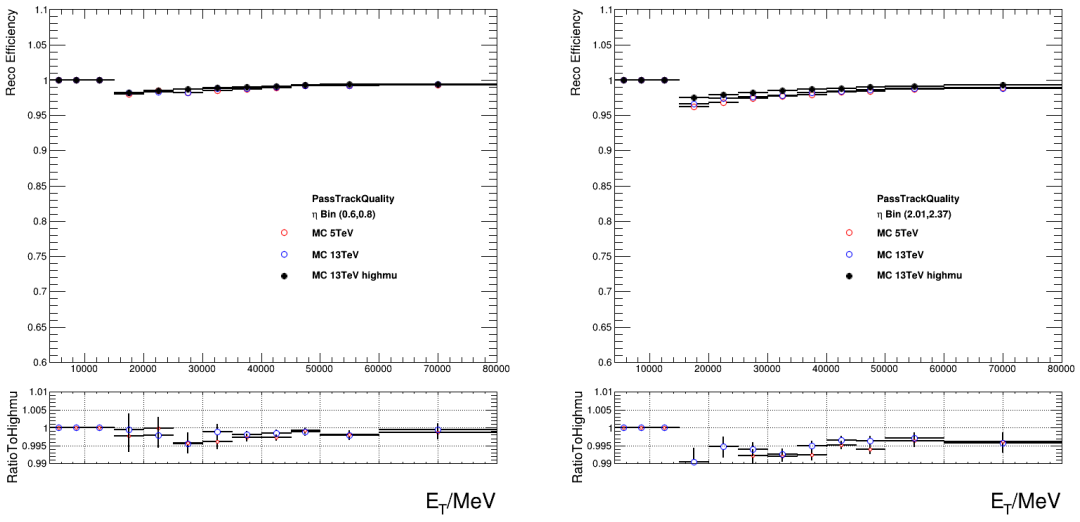

Figure 4.11: Electron reconstruction efficiencies comparisons of low-pile-up MC and high-pile-up MC16d in η range [0.60-0.80] (left) and [2.01-2.37] (right).The total uncertainties are included respectively.

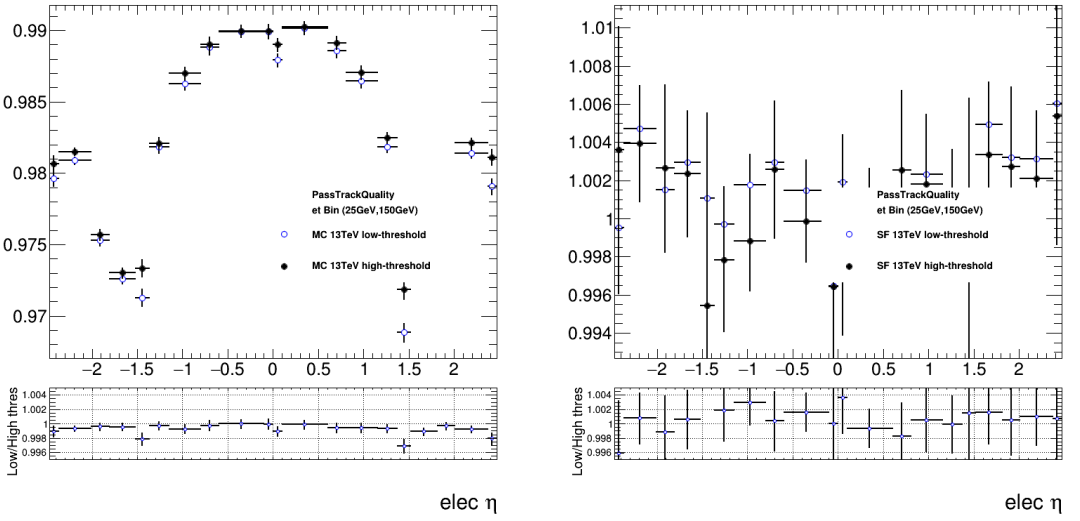

Figure 4.12: Electron reconstruction efficiencies (left) and scale factors (right) comparisons of low-pile-up 2017+2018 data and high-pile-up MC16d and 13-TeV 2017 data. The total uncertainties are included respectively.

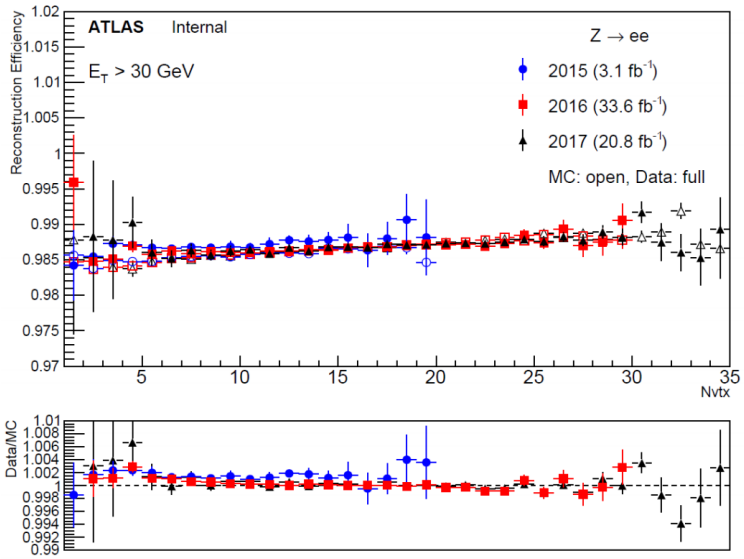

Figure 4.13: Electron reconstruction efficiencies and SFs as a function of the number of reconstructed primary vertices Nvtx using high-pile-up datasets.

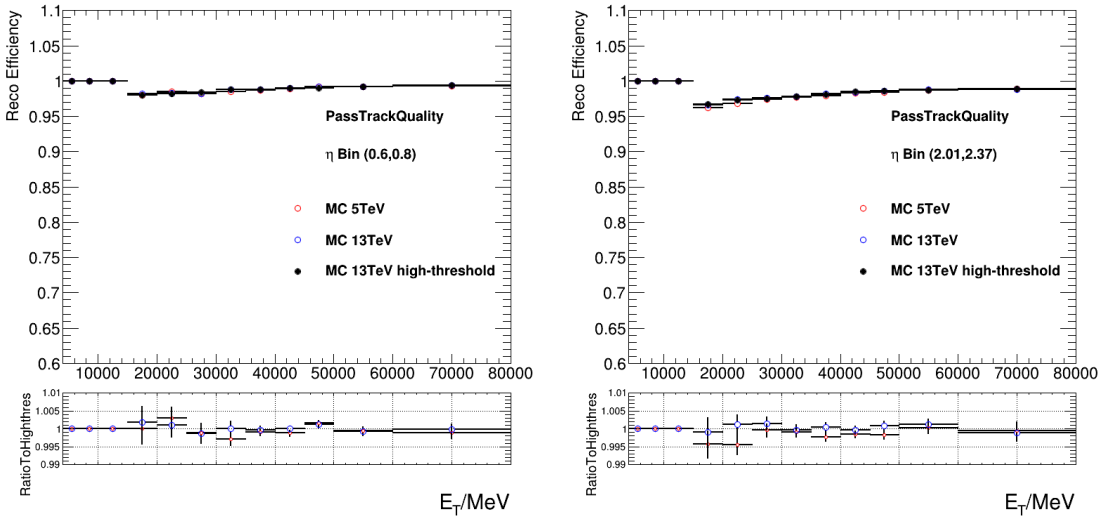

Figure 4.14: Electron reconstruction efficiencies comparisons of low-pile-up MC with low and high noise threshold in η range [0.60-0.80] (left) and [2.01-2.37] (right).The total uncertainties are included respectively.

$\|\eta\|$	$(SF^{highthres} - SF^{lowthres}) + /-(Unc^{SF})$	$(SF^{extrapo}_{Nvtx=20} - SF^{extrapo}_{Nvtx=0}) + /-(Unc^{Fit})$
[0.0, 0.6]	-0.05% +/- 0.11%	+0.11% +/- 0.17 %
[0.6, 1.37]	+0.02% +/- 0.13%	-0.07% +/- 0.24 %
[1.52, 2.47]	+0.03% +/- 0.09%	-0.12% +/- 0.14%

Table 4.1: Extrapolated reconstruction scale factor and uncertainties in η bins.

As it was shown in fig. 4.13 the reco efficiency is increasing with the Nvtx, while the SF are constant. To extrapolate the SF from the high-pile-up (Nvtx=20) to the low-pile-up (Nvtx=0) environment, the reconstruction efficiency and SF are computed as function of Nvtx in different η interval. Electrons with transverse momentum larger than 25 GeV in high-pile-up data collected in 2017 are exploited. Coarse absolute η bins, two bins in barrel and one in end-cap ([0., 0.60], [0.60, 1.37], [1.52, 2.47]) are used. Then the relations of Nvtx and MC efficiencies/SFs are studied with linear fit.

The results are displayed in Figure 4.15. MC-efficiency difference between high-pile-up and low-pile-up dataset, extrapolated from Nvtx = 25 to Nvtx = 0, results into 0.18%, 0.43%, 1.04% in barrel and end-cap. Those differences are compatible on what already shown in Figure 4.11, while for the SF the difference is $-0.13\%, 0.09\%, 0.15\%$, relatively much smaller. An additional $\pm 0.15\%$ uncertainty is sufficient to cover the difference in Nvtx extrapolation.

To summarize the differences and uncertainties on the reconstruction scale factor extrapolation are summarized in table 4.1. The conclusive strategy for the reconstruction SF is therefore to use the 2017 high-pile-up reconstruction SF central value and uncertainty adding a 0.2% global uncertainty to cover the high/low-pile-up differences coming from calorimeter settings and pile-up environments.

Comparison between in-situ measured SF with low-pile-up data and extrapolated SF is displayed in Fig. 4.16. The alternative method, high-pile-up to low-pile-up extrapolation, provides $\sim 0.1\%$ improvements.

4.3.4 Identification efficiency

Electron identification efficiency is defined as the fraction of reconstructed probe electrons passing a given ID working point (WP), which is chosen as MediumLLH in W-boson measurements. Following Reference [42] two methods are used to compute ID SF called *Zmass* and *ZIso*.

Zmass identification efficiency:

Both *tags* and *probes* electrons are reconstructed, within central precision region of $|\eta| < 2.47$, passing the "isGoodOQ" quality. Additional cluster quality requirements and a transverse momentum cut of $p_T > 20$ GeV being matched to the trigger requirement, are applied to *tag*.

Probes are required to pass the egamma ambiguity tool (to identify object is an electrons with a track or a photon), $p_T >$ 15GeV and a veto for the probes being inside of an energetic 0.4 cone jet with E_T^{jet} > 20 GeV is imposed. Converted photons are also excluded from the measurement. Control plots of Zmass method denominator are available in fig. 4.17.

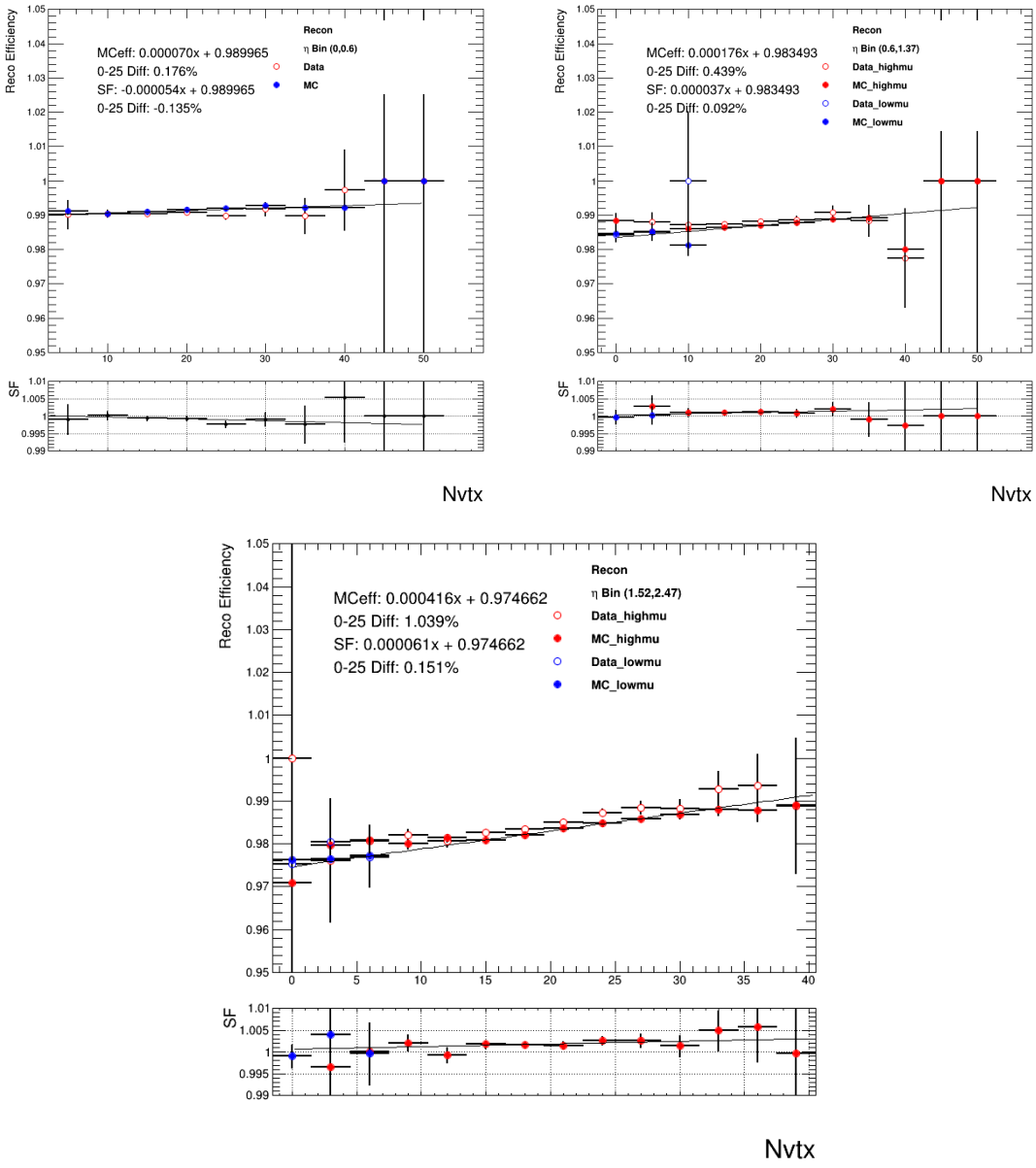

Figure 4.15: Electron reconstruction efficiencies and SFs along Nvtx in different $|\eta|$ bins and linear fit

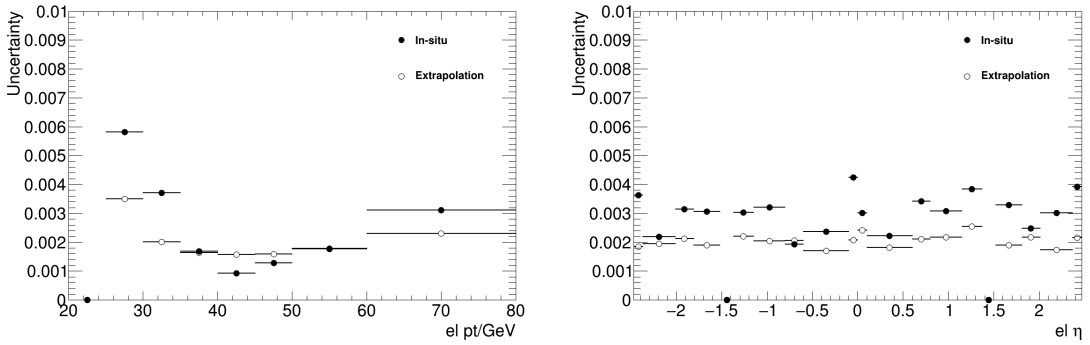

Figure 4.16: uncertainties of extrapolated and in-situ recon SFs in different kinematics with $W^+ \rightarrow e^+\nu$ selection at 13 TeV

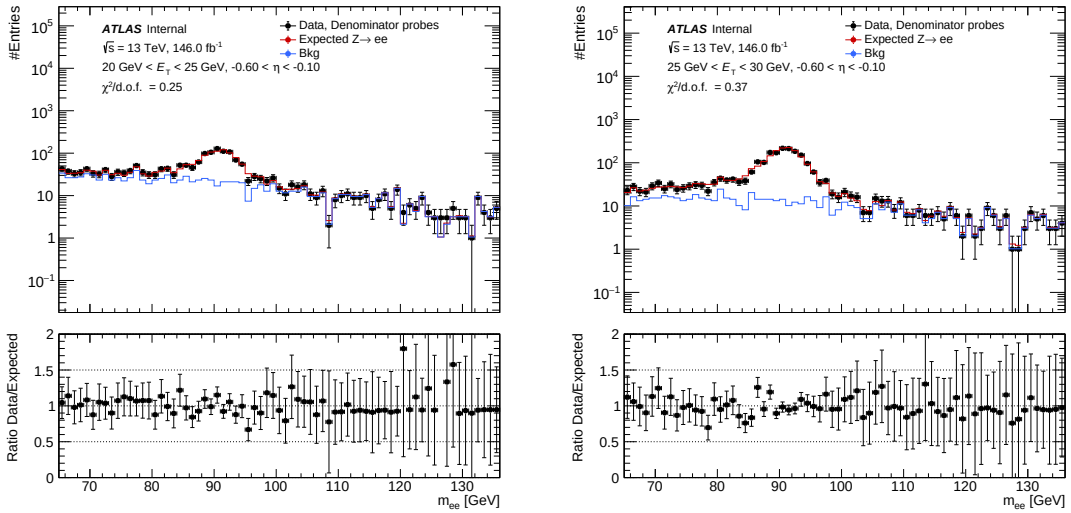

Figure 4.17: ID background template fit in denominator at 13 TeV in transverse momentum (20GeV, 25GeV) (left), and (25GeV, 30GeV) (right)

Fig. 4.18 and 4.19 display some 13 TeV and 5 TeV Medium LLH efficiencies. Complete results will be included in conclusion section of this chapter.

ZIso identification efficiency:

As a discriminating variable between signal and background, the calorimeter energy isolation $E_T^{cone0.3}$ of the probe is used. $E_T^{cone0.3}$ is defined as the calorimeter energy deposit in topological clusters within $|\Delta R|$ around the electron. Therefore, signal electrons should be accumulated around low values of the isolation variable whereas background should be found mainly at high values. And a data-driven method is thus available to evaluate the background contamination (Fig. 4.20).

Ultimate identification SFs and uncertainties are from the combination of *Zmass* and *ZIso* results. Details on how this combination is performed is available in Reference [43]. Results of *ZIso*, *Zmass*

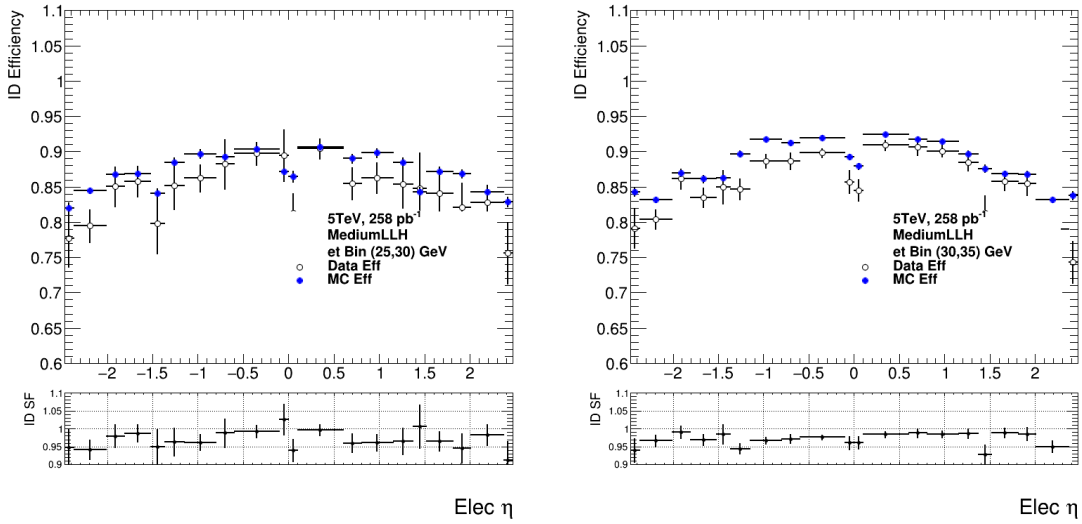

Figure 4.18: Electron identification efficiencies and scale factor in E_T range [25-35] GeV (left) and [30-35] GeV (right) using 13 TeV $339pb^{-1}$ low-pile-up data. Zmass method is exploited and total uncertainties are included respectively.

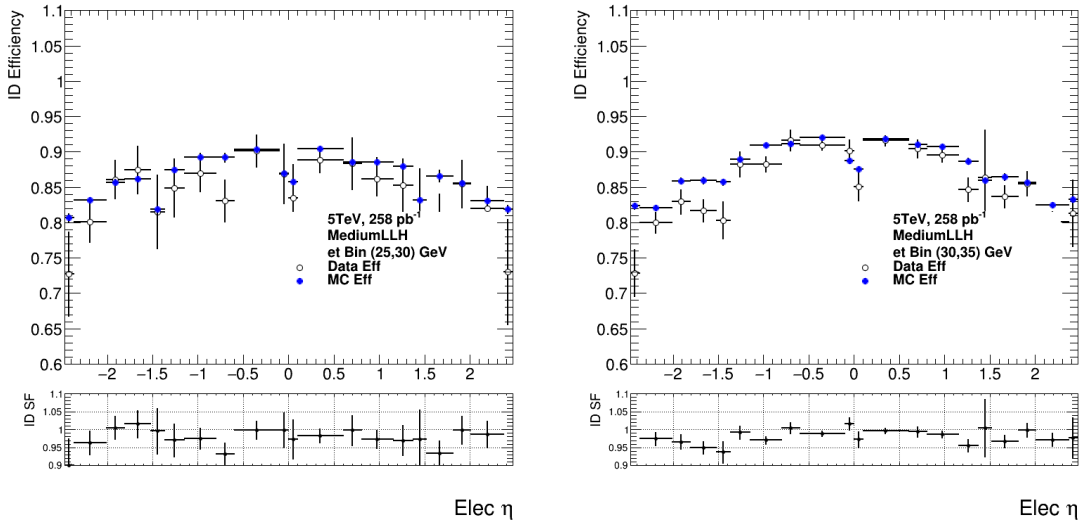

Figure 4.19: Electron identification efficiencies and scale factor in E_T range [25-35] GeV (left) and [30-35] GeV (right) using 5 TeV $258pb^{-1}$ low-pile-up data. Zmass method is exploited and total uncertainties are included respectively.

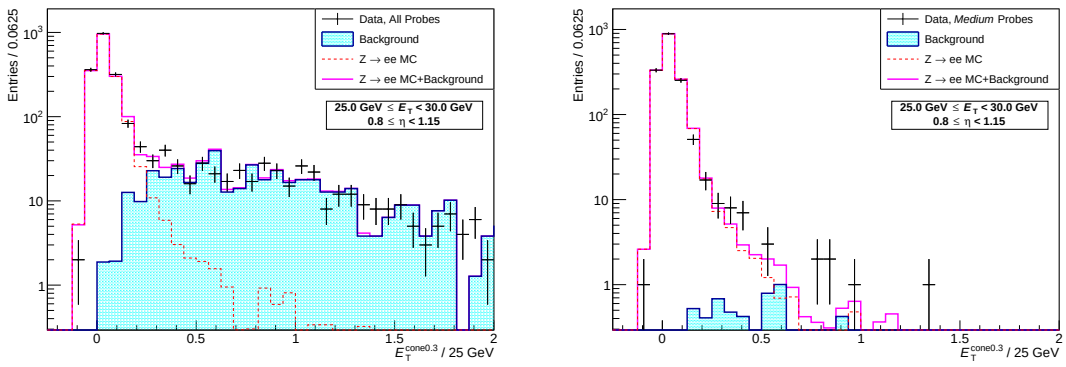

Figure 4.20: Mass distribution of the tag and probe pair in *ZIso* method with 13 TeV 339pb^{-1} low-pile-up data for the denominator (left) and numerator(right)

and combination using 13 TeV data are displayed in Fig. 4.21. Central value of combined ZIso/Zmass SF is between two methods and the Syst is significantly optimized. In the uncertainty map, Fig. 4.22, systematics are obviously reduced.

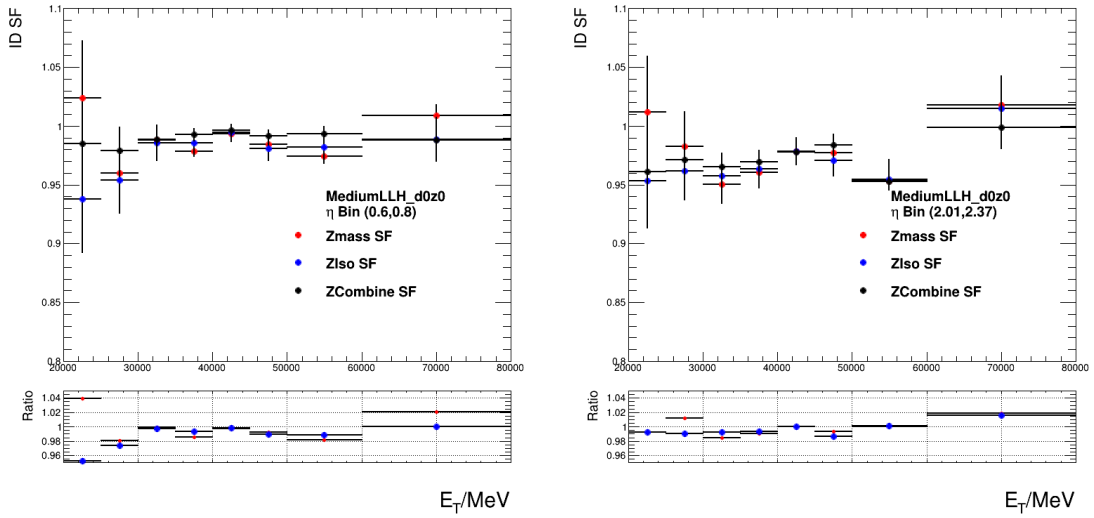

Figure 4.21: Electron ID SFs comparisons with *Zmass* and *ZIso* method in barrel (left) and end-cap(right) using 13 TeV low-pile-up data

As it was discussed in section 4.3.2 for the reconstruction efficiency the same strategy is studied for ID to combine the 5/13 TeV data. Figure 4.23 shows the 5/13 TeV ID MC efficiency comparison. An over 0.5% discrepancy is found in barrel and percent-level discrepancy in end-cap, possibly from the different show shapes. Therefore a direct combination of 5 and 13 TeV data is not possible. In conclusion, ID SF used in low-pile-up analysis will be individual for 5 TeV and 13 TeV, both are merged from *Zmass* and *ZIso* method SFs.

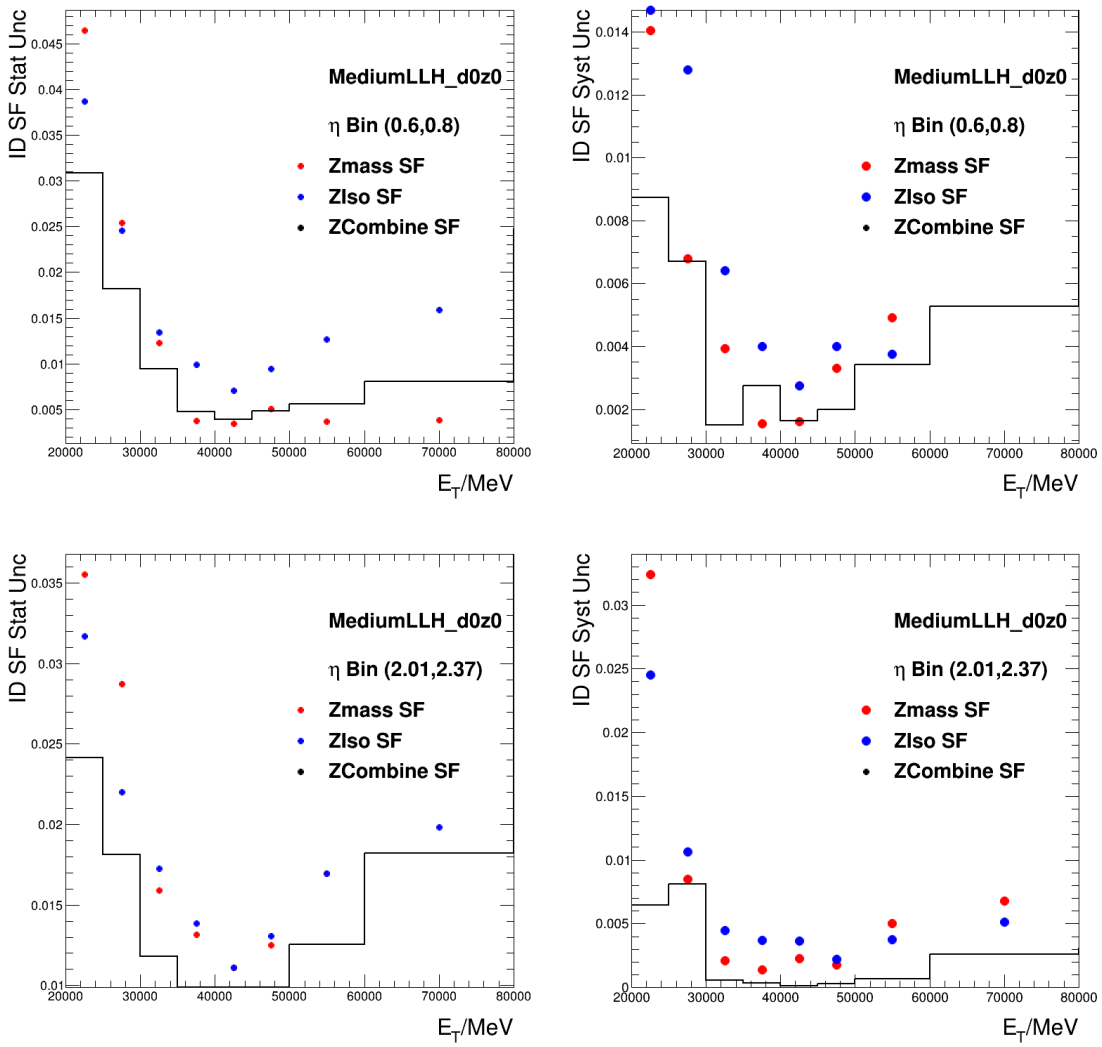

Figure 4.22: Electron ID SF uncertainties comparisons with *Zmass* and *ZIso* method in η range [0.60-0.80] (top) and [2.01-2.37] (bottom) using 13 TeV low-pile-up data. The total uncertainties are included respectively.

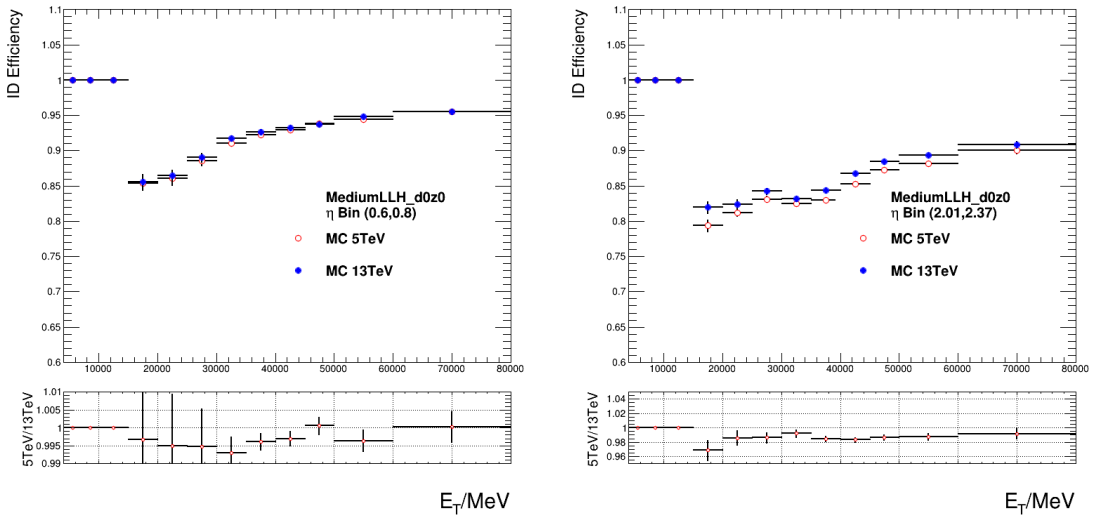

Figure 4.23: Electron ID efficiencies comparisons of 5 TeV and 13 TeV low-pile-up MC in barrel(left) and end-cap(right)

4.3.5 Isolation efficiency

Electron Isolation efficiency is defined as the fraction of reconstructed and MediumLLH-identified electrons passing the given Isolation WP. The isolation WP is defined as "$ptvarcone20/pT^e < 0.1$", where ptvarcone20 is a track isolation variable built by summing the transverse momenta of the tracks in a cone of variable size ΔR around the candidate, excluding the track associated with the candidate itself. It is discussed in Chap. 7.4 how this WP is decided. *Tags* and *probes* electrons are required to pass the same selection as ID efficiency selection, with extra MediumLLH ID applied. The same as reconstruction efficiencies, 5 and 13 TeV MC show compatible isolation efficiencies, so both 5 TeV and 13 TeV experiments will use the same Iso SFs, calculated from combined 5 and 13 TeV data (fig. 4.24).

4.3.6 Trigger efficiency

The Trigger efficiency is defined as the fraction of reconstructed electron passing the MediumLLH identification requirement and isolated also passing the trigger selection. For single lepton trigger, passing the selection means the trigger fires and at least one selected electron is matched to the objects fire the trigger. As the Isolation efficiency, Trigger efficiency is usually rather close to "1", leading to a sub-dominated uncertainty comparing to other efficiencies. *Tags* and *probes* candidates are required to pass the same selection as ID efficiencies, with extra MediumLLH ID and "ptvarcone20/pT < 0.1" Iso applied to both. Trigger efficiencies of 5TeV and 13 TeV MC agree well. For both 5 TeV and 13 TeV dataset the same Trigger SFs are used, calculated from the combination of the two dataset.

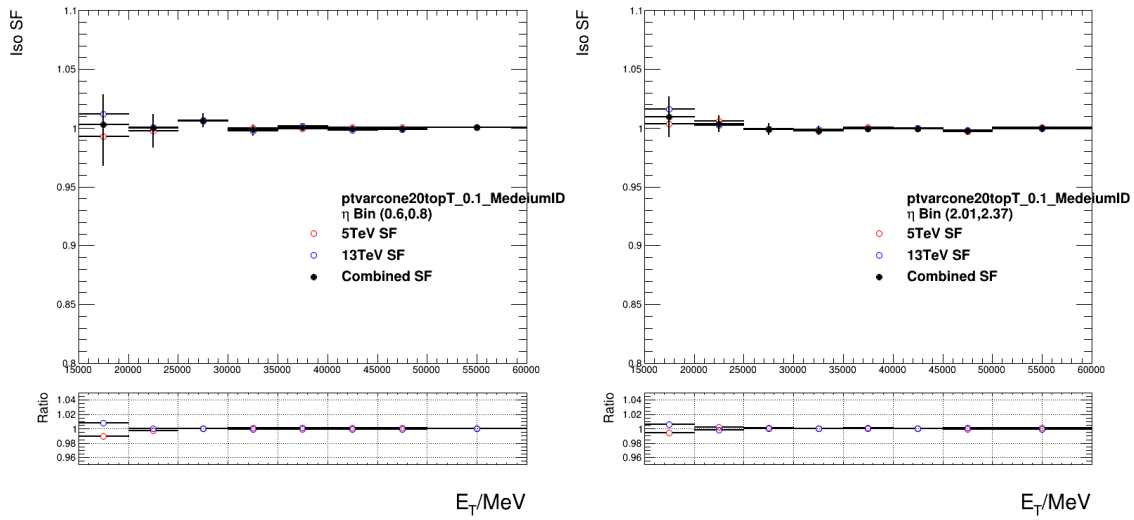

Figure 4.24: Electron Iso efficiencies comparisons of low-pile-up 5 TeV and 13 TeV MC with in η range [0.60-0.80] (left) and [2.01-2.37] (right) using 5-TeV and 13-TeV low-pile-up MC. The total uncertainties are included respectively.

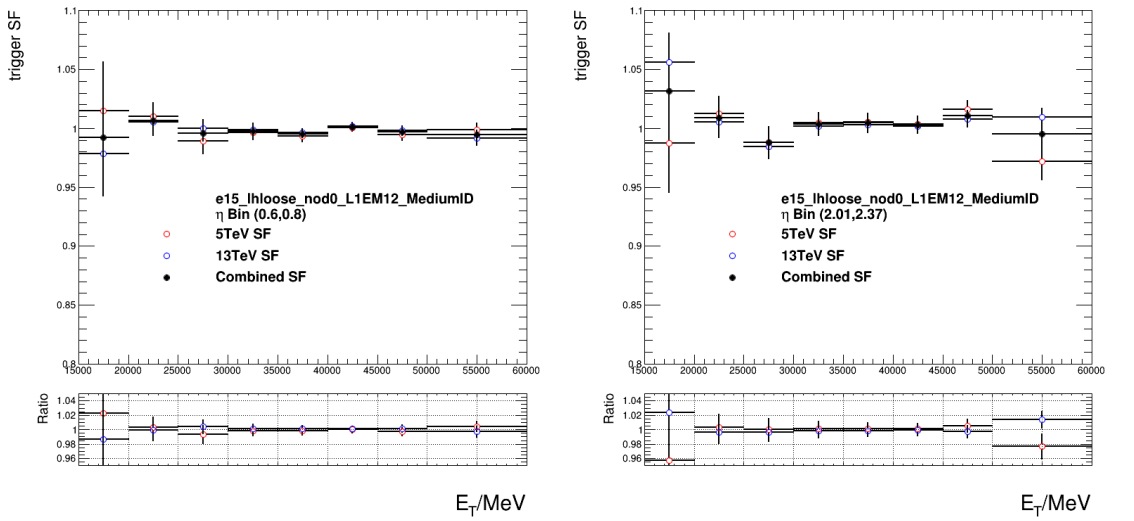

Figure 4.25: Electron trigger efficiencies comparisons of low-pile-up MC with low in η range -[0.60-0.80] (left) and -[2.01-2.37] (right) using 5-TeV and 13-TeV low-pile-up MC. The total uncertainties are included respectively.

4.3.7 Uncertainty evaluation

Efficiency and SF uncertainties come from two sources, statistic uncertainty and systematic uncertainty. In W-boson measurements, electron efficiencies uncertainties are evaluated with "FULL model", a new unfolding strategy provided by egamma group: [43]. The statistical uncertainty for all the electron SFs computed is mainly sensitive to the number of probe-target pairs and it is considered uncorrelated bin by bin. The systematic uncertainties are instead dominated by the photons and backgrounds control performance, and it is considered correlated. Full model evaluate the uncertainty with all ηxpT(~200) uncorrelated uncertainties, plus ~10 correlated across bins uncertainties, providing 100% correct treatment for very precise analysis. Comparing to MCTOY model that uses more than 10k toys, for each electron, around 10 correlated uncertainties that cross all $p_T - -\eta$ bins and 1 uncorrelated uncertainty are considered with full model.

To calculate the Syst uncertainty for each type efficiencies, different strategy are implemented in the tag-and-probe tool namely *ZReco*, *Zmass* and *ZIso*. *ZReco* is only used for Reco efficiency; *Zmass* method is used for ID, Iso and Trig efficiencies; *ZIso* is used as the complement of the *Zmass* method only in ID SF and uncertainty measurement.

Zmass: the M_{ee} region of interest for the determining the numerator and denominator is varied between mass windows of 10, 15, and 20 GeV on either side of the Z mass. The tag identification criterium and background template are also varied.

ZReco: In addition to similar variations as the ones described in *Zmass*, four sideband variations for the fit of the no-Track EM clusters are performed for the estimation of the additional photon background: [70, 80]U[100, 110], [60, 80]U[100, 120], [50, 80]U[100, 130] and [55, 70]U[110, 125] GeV. The MC prediction enters only in the subtraction of the small residual signal in the sidebands used for the fit (Fig. 4.26).

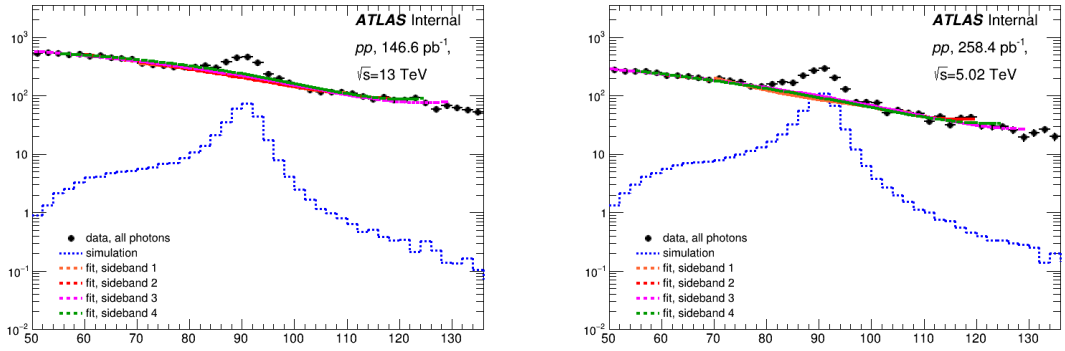

Figure 4.26: Reconstruction photon template fit with different sidebands at $\sqrt{s}$ = 13 TeV (left) and 5 TeV (right)

ZIso: Several variations are considered for this isolation based method, including the invariant mass window, the calorimeter isolation selection, and the data-driven background requirements.

4.3.8 Total uncertainty

The total uncertainties of electron scale factors at $\sqrt{s}$ = 13 TeV measured with Tag-and-probe method are illustrated in fig. 4.27. Globally the reconstruction and the identification uncertainties are dominant.

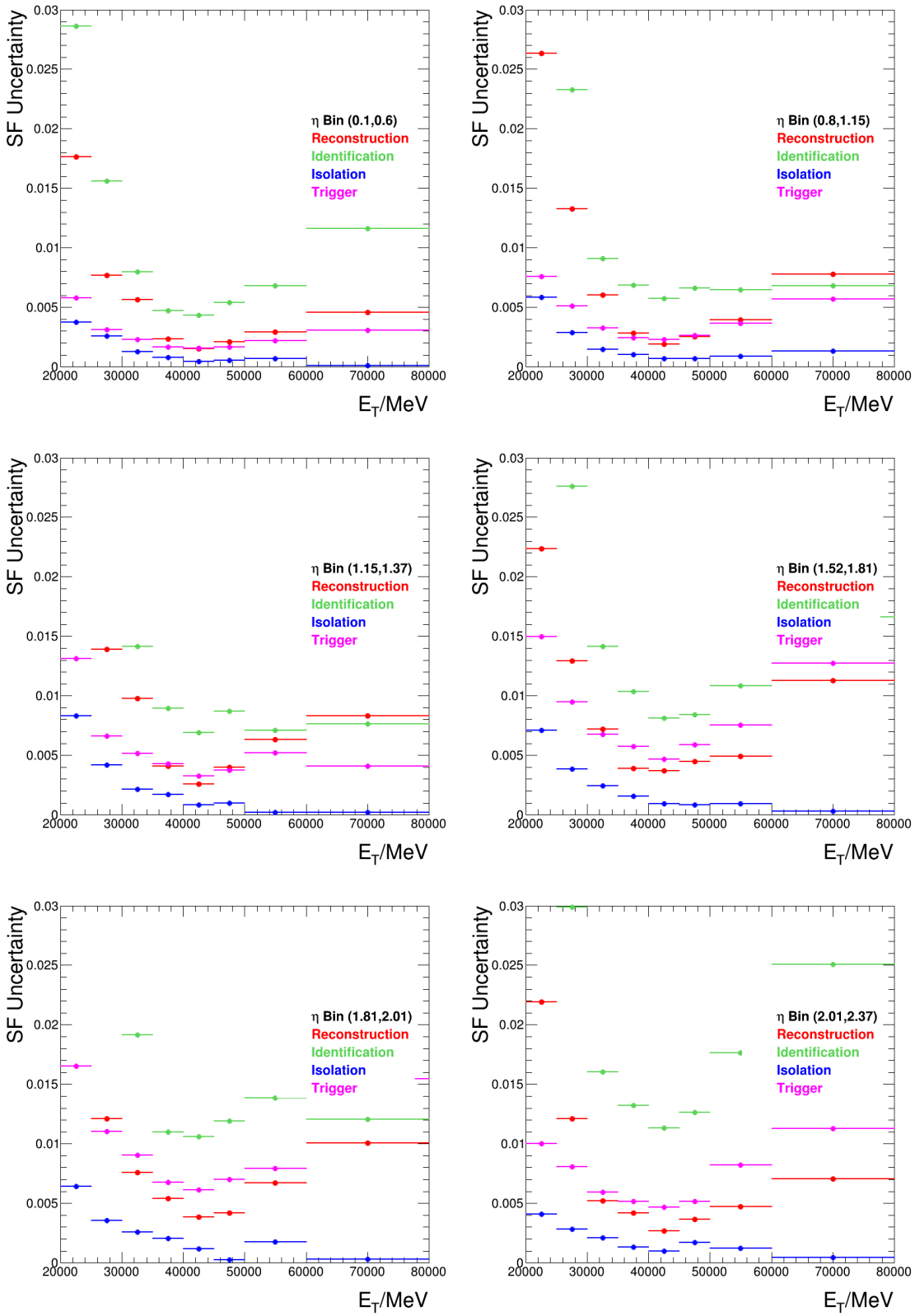

Figure 4.27: Total uncertainties of electron scale factors at $\sqrt{s}$=13 TeV measured with tag-and-probe

4.4 Shower-shape reweighting of electron

Due to that the identification efficiency of electron in MC is significantly smaller than that in data, the identification SF shown in Sec. 4.3, averaging below 95%, is distinct from other SFs, which are generally above 98%. This denotes the imperfect modelling of detector simulation in relevant observables.

The identification of electron is a likelihood-based algorithm, exploiting parameters from hadronic leakage, three samplings of EM calorimeter, TRT, track quality and track-cluster matching. A typical electron object (solid electron from pure process like $Z \rightarrow ee$) usually has negligible energy deposited in the hadronic calorimeter and associated to prompt tracks, so the discrepancy of identification efficiency in data and MC is led by effects in the EM calorimeter. Table 4.2 lists all EM-calorimeter-related parameters used in the electron identification. As the main function of back layer is background rejection, such question comes to how the mis-modelling produced in the 1^{st} and 2^{nd} sampling of the EM calorimeter.

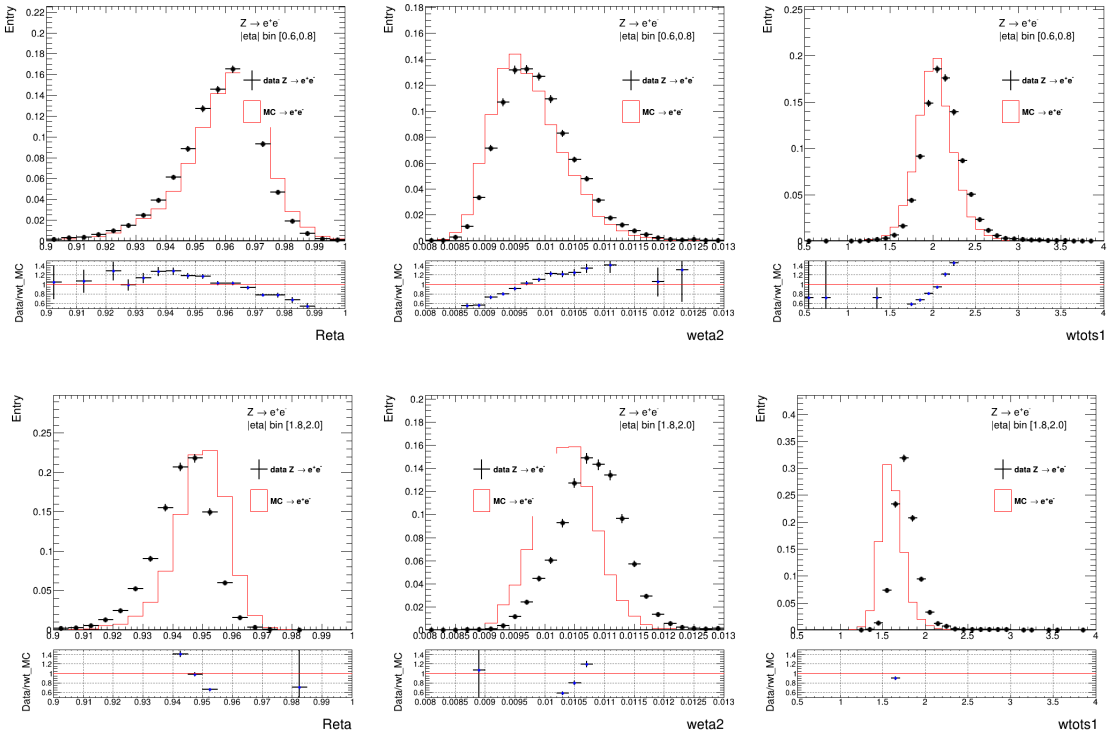

(a) $R\eta$ (b) w_{η^2} (c) w_{tot}

Figure 4.28: The $R\eta$, w_{η^2} and w_{tot} spectra of electrons in data and MC selected with $Z \rightarrow ee$ process in barrel (top) and end-cap (bottom)

Most of the corresponding parameters are illustrated in Fig. 4.28. From the definition, these parameters are based on the shower shape, i.e. the energy shape deposited in EMcluster, thus referred as shower-shape variables in this section. Walking through the spectra of electrons' shower-shape variables in data and MC, the simulation failed to imitate shower shapes of data, mostly due to that the

Type	Description	Name
Strip layer	Shower width, $\sqrt{(\sum E_i(i-i_{max})^2)/((\sum E_i))}$, where i runs over around 20 strips in η and i_{max} is the hotest strip	w_{tot}
	Ratio of the energy difference between the largest and second largest energy Eratio deposits in the cluster over the sum of these energies	E_{ratio}
	Ratio of the energy in the strip layer to the total energy in the EM accordion f1 calorimeter	f_1
Middle layer	Lateral shower width, $\sqrt{(\sum E_i\eta_i^2)/(\sum E_i) - ((\sum E_i\eta_i)/(\sum E_i))^2}$, where E_i and η_i belongs to cell i, summing over a 3×5 cluster	w_{η^2}
	Ratio of the medium layer energy in 3×3 cluster over that in 3×7 cluster	R_{phi}
	Ratio of the medium layer energy in 3×7 cluster over that in 7×7 cluster	R_{phi}
Back layer	Ratio of the energy in the back layer to the total energy in the EM accordion calorimeter	f_3

Table 4.2: Parameters related to EM calorimeter that are used in electron identification.

simulated electron has relatively "narrower" shower width than data. This effect is named as "data energy leakage" in EM calorimeter, an unsolved problem in detector simulation which enlarges the identification uncertainties and potentially introduces bias in the energy calibration.

The source of such leakage is remaining unknown. The material or bremsstrahlung effect may account for the ϕ-direction, but the leading bias in simulation is in η-direction, which more parameters in reconstruction, identification and calibration are associated to as well. The relation between cross-talk in electrodes and leakage was checked [44] yet failed, and no other proposal is sufficient to explain it. Therefore effects of energy leakage is unpractical to be corrected comprehensively from the mysterious source. Instead, it's suggested that to optimize the shower shape itself in simulation is possibly able to absorb all effects from this issue.

4.4.1 Methodology

The general idea of this algorithm is making the deposited energy "wider" in shape in electromagnetic calorimeter, of electrons in MC to reproduce the data energy leakage. Amount of the energy in the center of EM cluster, close to the hottest cell, is redistributed to the tails. It's pretty similar to reweighting method in practice, therefore this algorithm is called "shower-shape reweighting". Showers are reweighted in-situ, with reweighting functions derived from the averaging difference of data and simulation, regarding to the geometry dependence of energy leakage, such that the effects relying on showers are statistically identical in data and MC. Longitudinally, the showers and leakages are relatively independent between samplings, hence the reweighting to first layer (Lr1) and second layer (Lr2) of EM calorimeter are performed separately.

More specifically, the shower-reweighting method is to reweight the energy profile in Lr1 and Lr2 cell-by-cell in η direction of the EM cluster with reference to its real position, because there is only one parameter (R_ϕ) in identification is ϕ-dependent, and the $\eta - \phi$ 2-D reweighting will be practical only after that the 1-D reweighting is proven capable. In addition, Fig. 4.29(a) demonstrates that the leakage in Lr2 is relatively independent of the transverse momentum, while Fig. 4.29(b) illustrates its η-dependence. Besides of the ϕ-symmetry of EM calorimeters, this reweighting is initialized with studying in differential $|\eta|$ bins with inclusive p_T^e selection, $p_T^e > 25$ GeV.

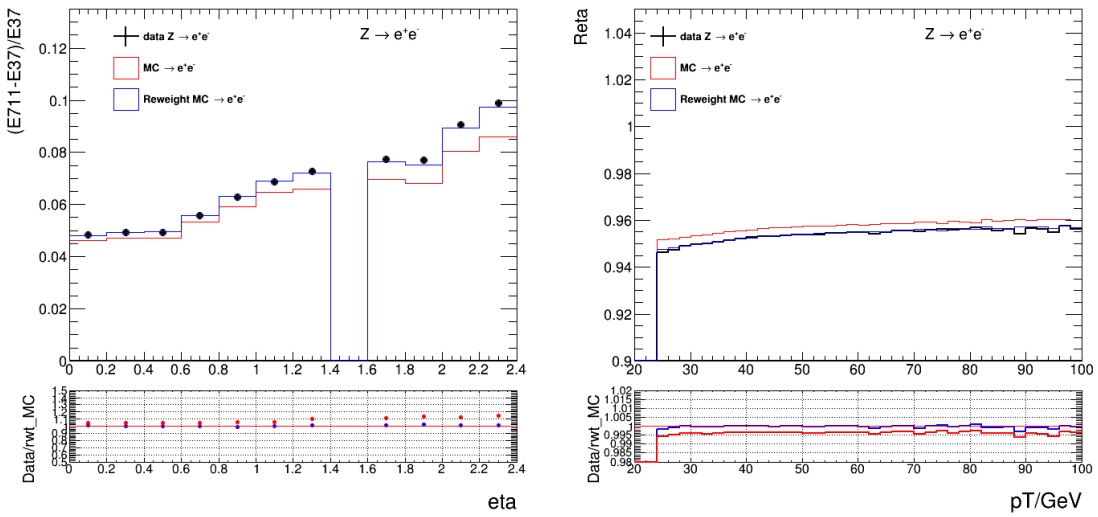

(a) (b)

Figure 4.29: Profile of(E711-E37)/E37 vs. eta (left) and Profile of(E711-E37)/E37 vs. electron P_T (right), where E711 and E37 are sum of Layer2 energy in 7x11 Cluster and 3x7 Cluster. Profile of Data, MC, and MC after cell energy reweighting are provided.

Electrons are divided into different regions with reference to the absolute value of pseudorapidity: [0, 0.2, 0.4, 0.6, 0.8, 1.0, 1.2, 1.3, 1.37] and [1.52, 1.6, 1.8, 2.0, 2.2, 2.4], which also accords to the Lr1 cell cluster topology that in EM cluster element the Lr1 granularity is 8, 6, 4, 2.5 times of Lr2, varying at $|\eta| = 1.8, 2.0, 2.2, 2.5$.

In table 4.2, the identification use up to 20 strips in Lr1. This can be covered by EM cluster of 3x7 (5x5) size in barrel (end-cap). For Lr2, up to 7x7 EM cluster is used (R_η), and account to the bremsstrahlung, the cluster need extension in ϕ-direction. Thus the reweighting element is 3x7 (5x5) cluster for Lr1 and 7x11 cluster for Lr2.

Energies deposited in Lr1, the energy in η-strip n, $E_1(n_\eta)$ are collected by neighboring strips, and n_η is the relative η index of strip, n_η = 1,2,..~ 30, corresponding to all Lr1 strips in cluster. The distribution among strips is like a triangle, centralized to the hottest strip, and with bilateral symmetry. In Lr2, the showers are 2-Dimentiaonal, but after projected to η, i.e. energy in η-column n $E_2(n_\eta) = \sum_{n_\phi} E_2(n_\eta, n_\phi)$, the energy distribution is similar to Lr1, but with much less strips, n_η = 1, 2,...7, correspond to seven η-columns of middle sampling. The energy profile of Lr1 and Lr2 showers are thereby defined as

the average of normalized $E_1(n_\eta)$ and $E_2(n_\eta)$ in each differential $|\eta|$ bins with sufficient number of electrons, written as:

$$P_1^{|\eta_i|}(n_\eta) =< \frac{E_1(n_\eta)}{E_1^{total}} >^{|\eta_i|} \tag{4.6}$$

$$P_2^{|\eta_i|}(n_\eta) =< \frac{E_2(n_\eta)}{E_2^{total}} >^{|\eta_i|} \tag{4.7}$$

where P_N is the energy distribution in layer N, $|\eta_i|$ is the $|\eta|$ region the profile belongs to, n_η denotes the index of cell of cluster in η direction (N = 1,2...7 in P_2 and N = 1~30 in P_1. The η-column of $n_\eta = 4$ is always the hottest one in Lr2.

If correspond each strip of Lr1 or η-column of Lr2 to one bin of histogram, the energy profile and reweighting function also be expressed with histograms. The reweighting functions are defined as:

$$f_1^{|\eta_i|}(n_\eta) = (P_1^{|\eta_i|}(n_\eta))^{data} - (P_1^{|\eta_i|}(n_\eta))^{MC} \tag{4.8}$$

$$f_2^{|\eta_i|}(n_\eta) = (P_2^{|\eta_i|}(n_\eta))^{data} - (P_2^{|\eta_i|}(n_\eta))^{MC} \tag{4.9}$$

f_1 and f_2 represent the difference of data and MC energy profile, integrated to zero.

In summary, the f_2 extraction contains these steps:

1. Electrons and positrons are indistinguishably selected from $Z \rightarrow ee$ process.
2. Rebuild the 7x11 (eta x phi) EM clusters around electrons' seed cluster.
3. Electrons with incomplete 7x11 size Lr2 cells, or cluster across two $|\eta|$ bins or cracks are filtered.
4. The Lr2 cells' energies are normalized with sum of 7x11 cells' energy and filled into the shower energy profile histograms.
5. Calculate the energy profiles and reweighting functions with large samples of data and MC.

It's relatively more complicated in Lr1 case. Reminding that each N_η of cluster consists of 8, 6, 4, 2 Lr1 cell strips, varying at $|\eta|$ = 1.8, 2.0, 2.2, 2.4, and that the EM cluster size is 3x7 in barrel and 5x5 in endcap, the corresponding number of Lr1 strips of interest is 24, 40, 30, 20, varying at $|\eta|$ = 1.52, 1.8, 2.0, 2.2. The procedures are:

1. Electrons and positrons are indistinguishably selected from $Z \rightarrow ee$ process.
2. Rebuild 5x5 (eta x phi) EM clusters around electrons' seed cluster.
3. Select electrons with complete 5x5 size Lr1 cells within the same $|\eta|$ bin. Clusters that cross eta = 0, and crack are rejected.
4. Locate the hottest strip of Lr1, as N_0 and define the Lr1 η index.
5. Find $8/6/4 \times 2$ strips in descending-η and ascending-η side of N_0; Normalize and fill the energy to histograms.
6. Calculate the energy profiles and reweighting functions with large samples of data and MC.

When applying the reweighting function to simulated electrons, all electrons with p_T above 5 GeV regardless of the cluster quality are selected. The Lr2 reweighting workflow is:

1. In 7x11 clusters, calculate the uncorrected η-column energy as E_k^{uncorr} and total Lr2 energy E_{total}. k is from 0 to 7 or smaller, due to dead cells or cracks.
2. Calculate the new η-column energy $E_k^{corr} = E_k^{uncorr} + f_2^{|\eta_i|}(k) \cdot E_{total}$.
3. Multiply the energy of all cells in η-column by t_k: $t_k = E_k^{corr}/E_k^{uncorr}$.

Though the integral of f_2 is 0, the total layer energy may change after reweighting if dead cell included, thus additional energy rescale is applied to guarantee the total energy is constant.

Lr1 reweighting procedures are:

- Rebuild 3x7 for barrel and 5x5 for end-cap cellClusters.
- Calculate the uncorrected Lr1 strip energies E_k^{uncorr} and total Lr1 energy E_{total}.
- Calculate the new strip energies $E_k^{corr} = E_k^{uncorr} + f_1^{|\eta_i|}(k) \cdot E_{total}$ and reset the cell energy.

The total Lr1 energy is also constant with extra scales.

The continuity is necessary in Lr2 when cluster cross two |*eta*| bins, so the reweighting function is always chosen according to the $|\eta|$ of central column, and applied regardless of the real position. For example, for one 7x11 cluster that crosses both bins of [1.8, 2.0] and [2.0, 2.2], if the $|\eta|$ of central cell is within [1.8, 2.0], then all cells in Lr2 of this cluster will be reweighted using function corresponding to bin "[1.8, 2.0]". However, in the same example, the Lr1 cells have to face the boundary issue when picking the reweighting function, because the Lr1 granularity changes at $|\eta|$ 1.8 from 6 to 4. A linear approaching that depends on the distance between the real-position of reweighted strip and the hottest strip is exploited to handle such case.

The "energy shift" is exploited to reweight the energy in stead of scaling the strip energies directly because when reproducing energy leakage, tales of showers will be always enhanced in "scaling" method, so do the fluctuations in tales, if simply multiplied by an factor larger than "1", particularly worse when the energy is recorded in negative value due to the noise. To adopt "shift" method, i.e. increase the energy in tales and subtract the central energy, the shape will be more stable and continuous, and negative noise will also get suppressed. Showers get long tale in strips of Lr1, indicating this effect obviously, shown in the E_{ratio} studies later.

4.4.2 Reweighting performance

Performance of the reweighting algorithm is demonstrated firstly with the energy profiles and then all relevant shower-shape parameters from Tab. 4.2.

Figure 4.30 and 4.31 illustrate the comparisons of electron shower shapes in data, MC and shower-reweighted-MC, for Lr1 and Lr2 respectively. In both layers, the averaging electron energy shape in calorimeter is identical in barrel and end-cap between data and MC after reweighting, marking the successful reproduction of energy leakage.

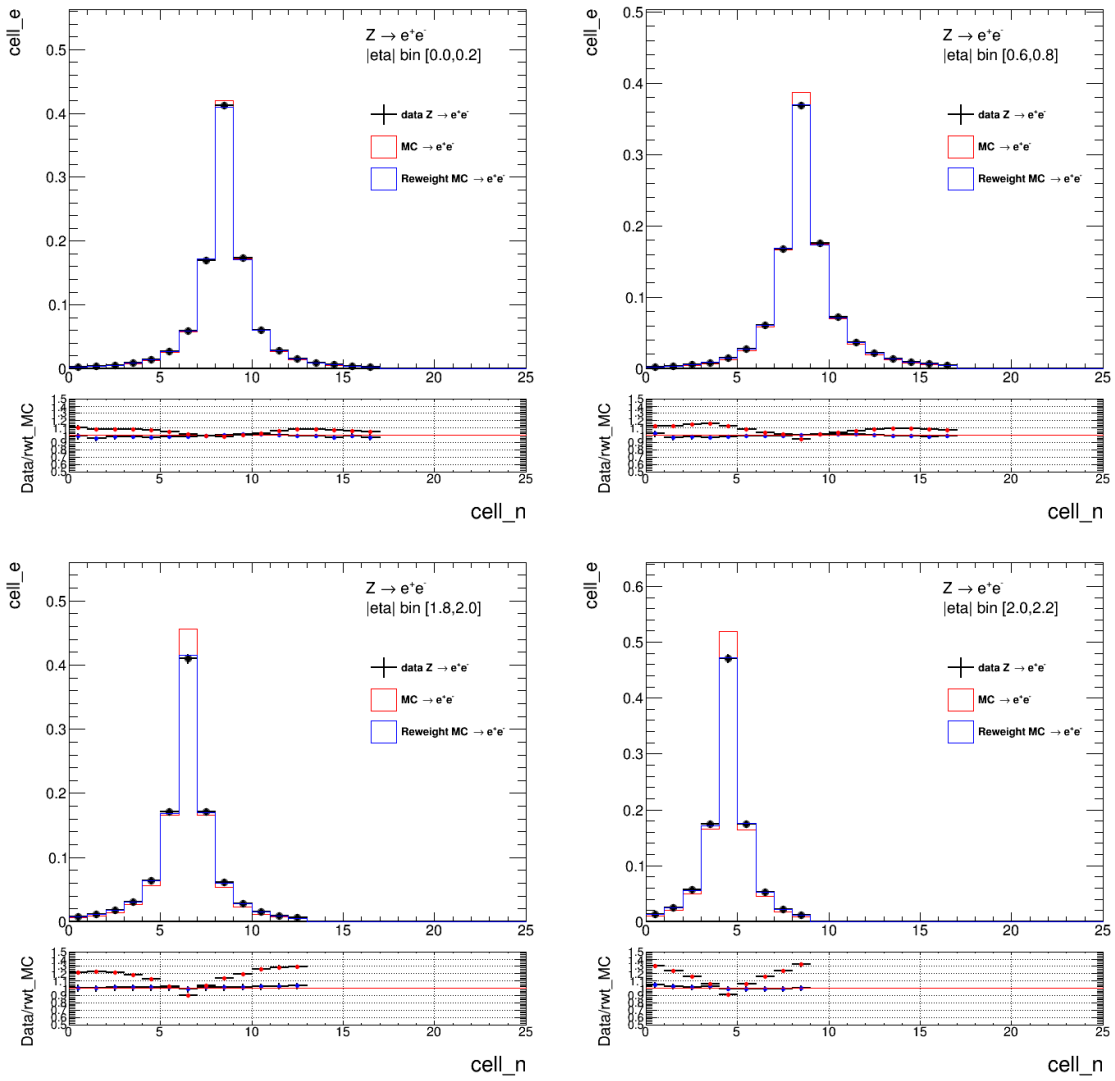

Figure 4.30: EMCluster first layer energy profiles of data, uncorrected and corrected MC samples in different $|\eta|$ bins

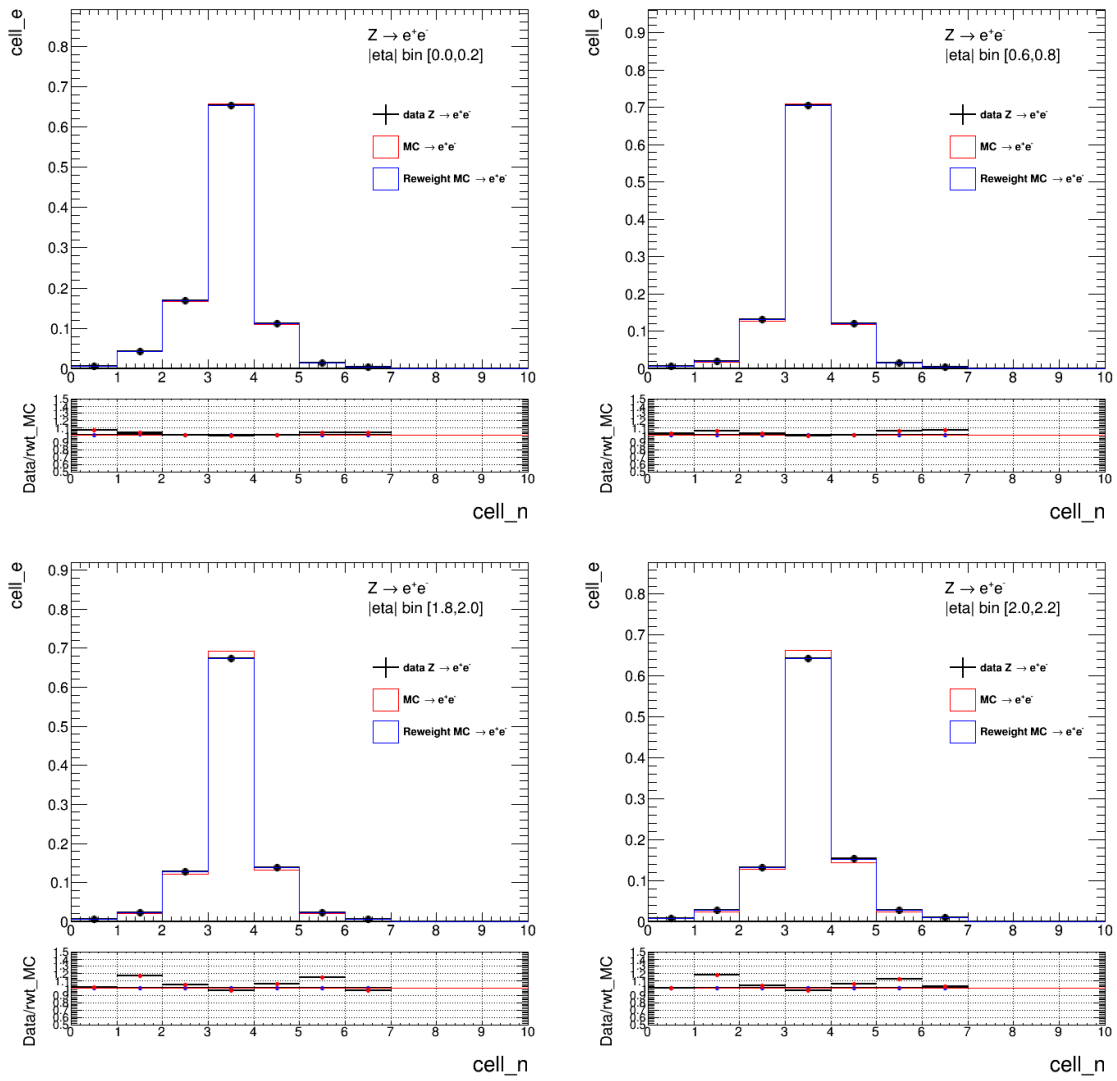

Figure 4.31: EMCluster second layer energy profiles of data, uncorrected and corrected MC samples in different $|\eta|$ bins

The showershape parameters in first and second layer are re-calculated using the same shower-shape rebuilding algorithm (4.4.3), but with EM cluster filled with energy-reweighted cells. The distributions of R_η, w_{η^2}, E_{ratio} and w_{tot} are used to study the performance of new showers. R_η and w_{η^2} are associated to Lr2 showers, both representing the leakage and energy eta shapes, while w_{tot} and E_{ratio} are Lr1 parameters, referring to Lr1 energy width, and the ratio of second and first peak. The comparisons of these parameters before and after correction to data are displayed in Fig. 4.32, 4.33, 4.34 and 4.35. The improvement is adequate to eliminate most of the disagreement, particularly critical in the end-cap region, i due to energy leakage in R_η, w_{η^2} and w_{tot} spectra, The residual difference is likely due to the coarse binning definition of 0.2-$|\eta|$-width and clusters without enough cells to reweight.

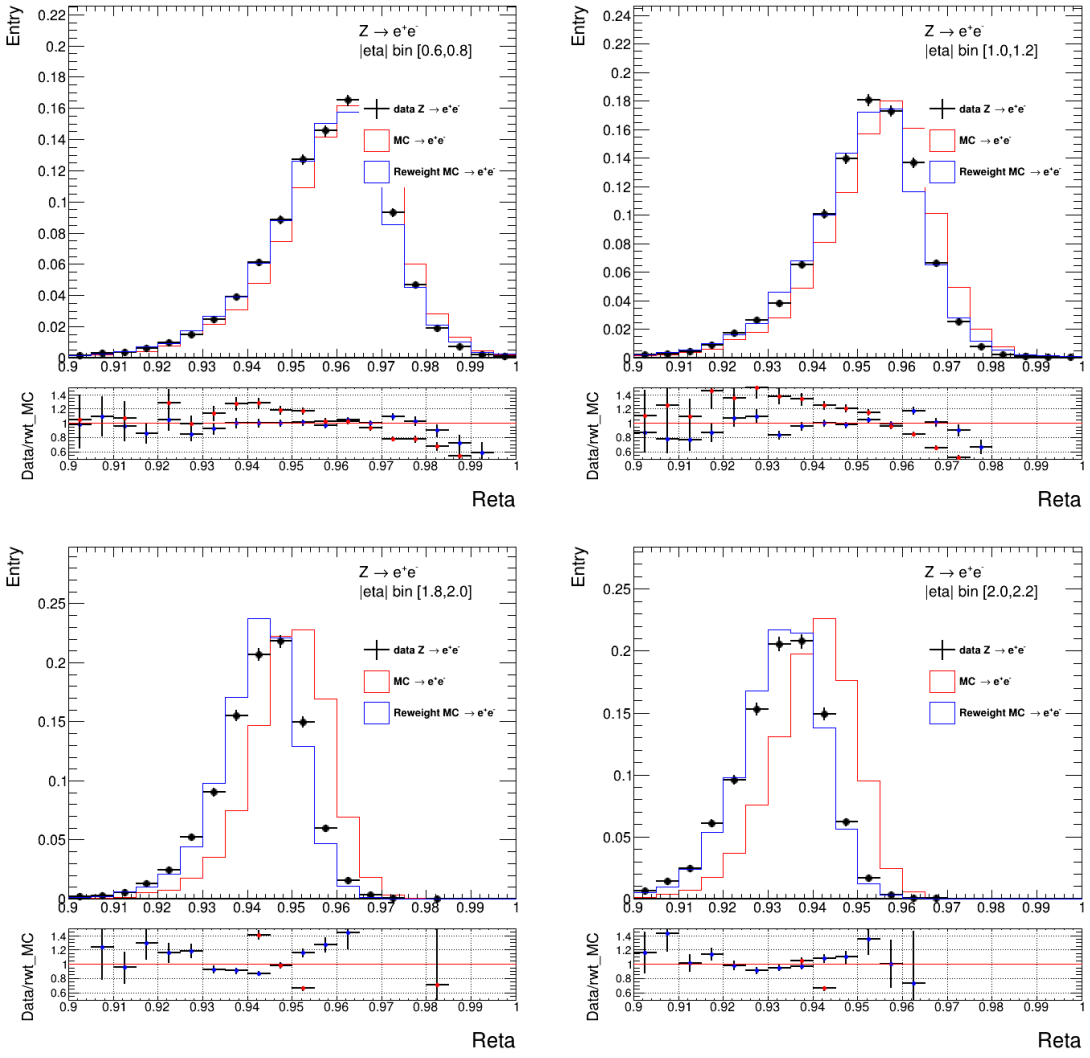

Figure 4.32: Normalized R_η distribution of data, uncorrected and corrected MC samples in different $|\eta|$ bins

However, comparable optimization is not observed in the E_{ratio} distribution in Fig. 4.35. In some $|\eta|$ ranges (like [1.0, 1.2]), the reweighting somehow degrades the E_{ratio} comparing to data. The E_{ratio}

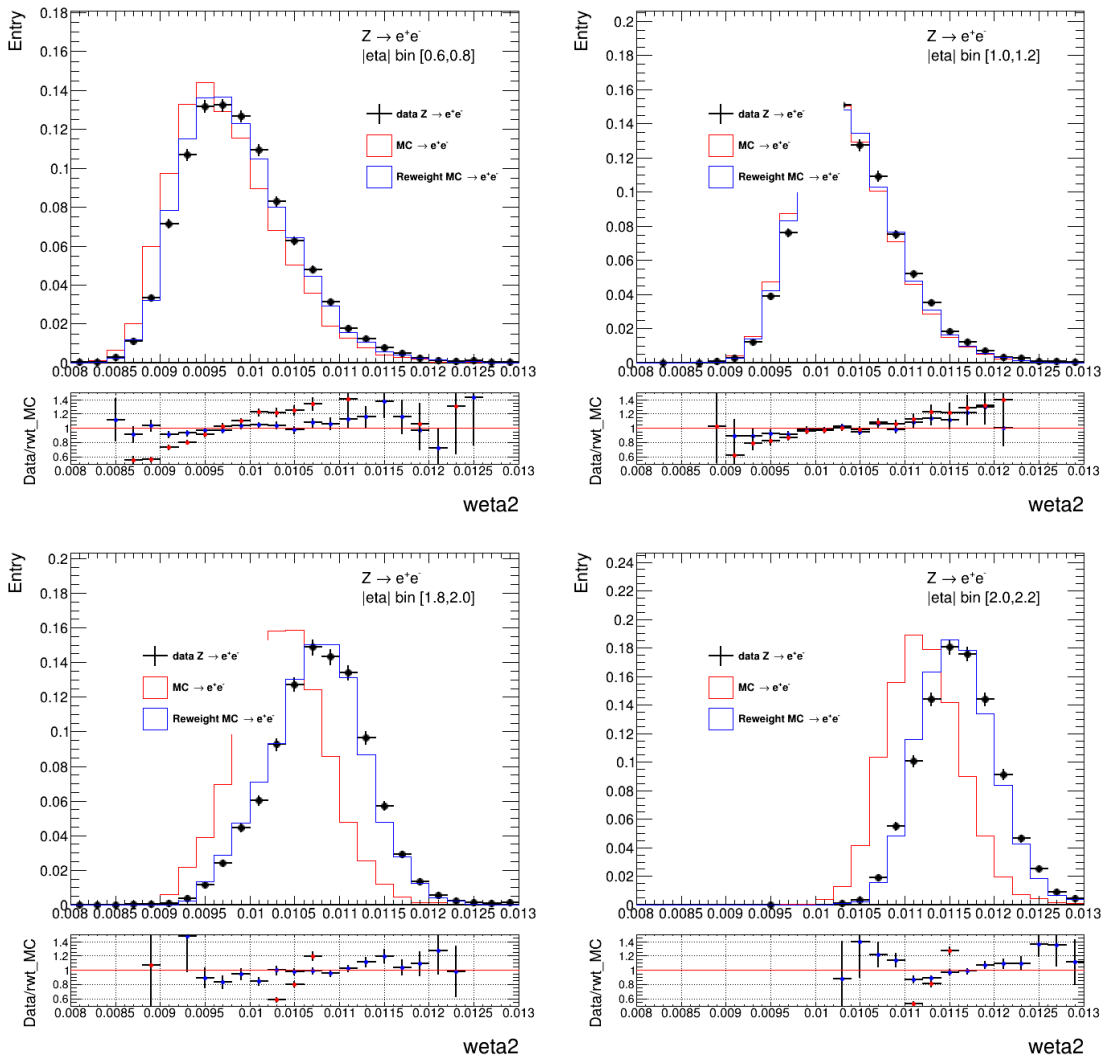

Figure 4.33: Normalized w_{η^2} distribution of data, uncorrected and corrected MC samples in different $|\eta|$ bins

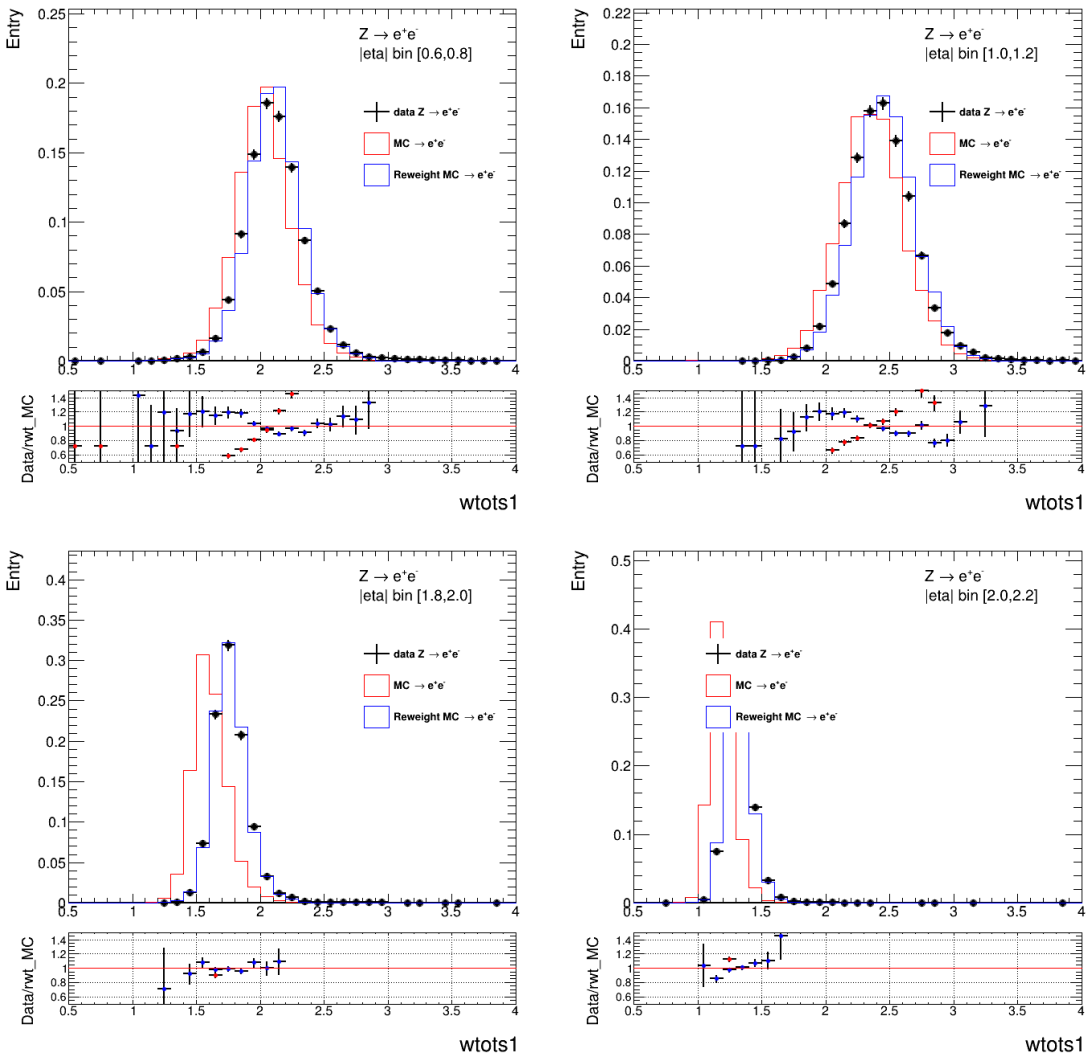

Figure 4.34: Normalized w_{tot} distribution of data, uncorrected and corrected MC samples in different $|\eta|$ bins

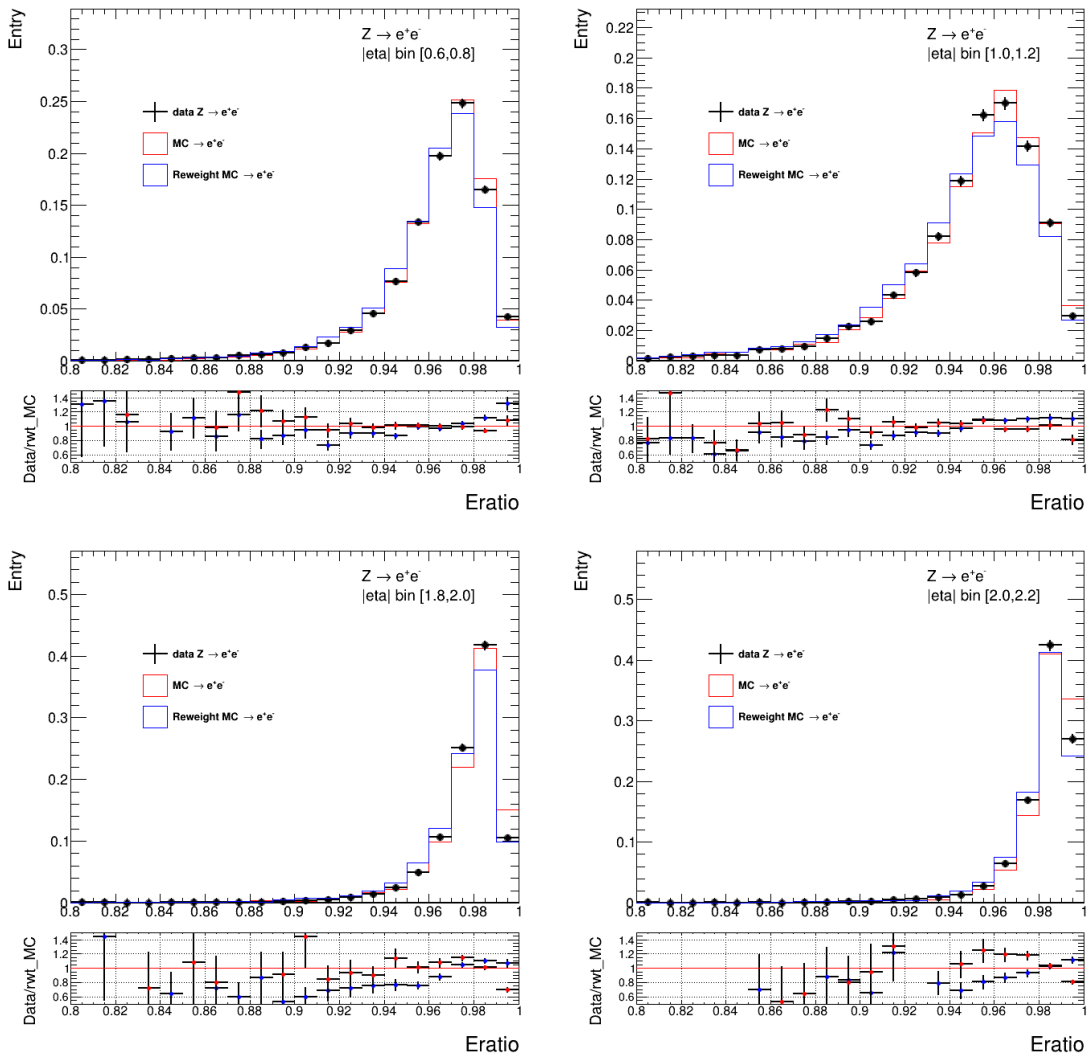

Figure 4.35: Normalized E_{ratio} distribution of data, uncorrected and corrected MC samples in different $|\eta|$ bins

is defined as:

$$E_{ratio} = (E_1 - E_2)/(E_1 + E_2), \tag{4.10}$$

where E_1 and E_2 are the first and second maximum strip energy in Lr1. To figure out the problem in E_{ratio}, E_1 and E_2 are investigated separately. Fig. 4.36 shows the comparison of E_1, E_2 and the distance between the first and second maximum strip in inclusive region, before and after reweighting. The reweighting promotes MC distributions closer to data for all three parameters, conducing a better performance in MC after correction. However the E_1 and E_2 of MC are both relatively higher than data, resulting in a good agreement after calculating ratio, in kind of coincidence.

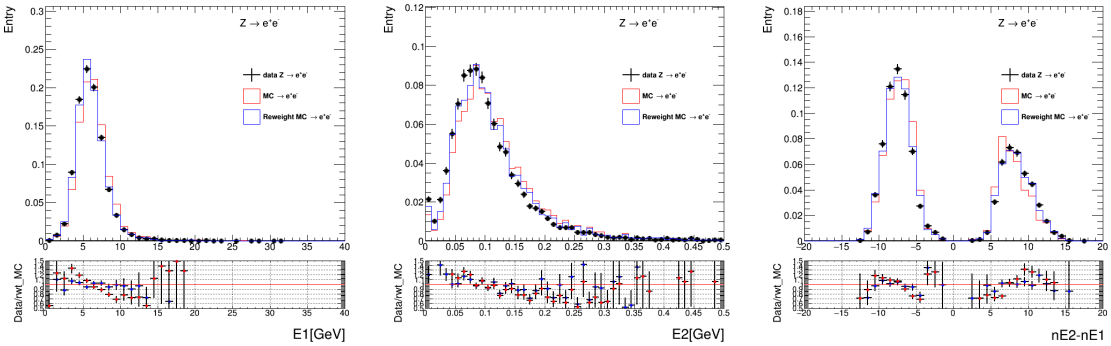

Figure 4.36: Normalized E1 (left), E2 (middle), and "index difference" of E1 and E2 (right) distribution of data, uncorrected and corrected MC samples in $|\eta|$ bin [0.6,0.8]

In conclusion, all shower-shape parameters studied of first and second layer are sufficiently improved after reweighting. The advantage of this study can be taken into different electron studies. Firstly it's manifested in electron identification in this thesis. The MC identification efficiencies are supposed to be optimized and approach to data after reweighting. With tag-and-probe tool, the effect is also viewed, displayed in Fig 4.37.

At all working points, TightLLH, MediumLLH and LooseLLH, the three recommended working points for Run-II study, the SFs are closer "1" during shower-shape reweighting, validating the capability of shower-shape reweighting procedure in optimizing identification efficiencies which can be a candidate in reducing the uncertainty for precision measurement with limited data in future.

4.4.3 ATLAS Modules

The reweighting algorithm behaves excellently in reproducing the data-like shower-shapes in simulation. Photons are identical to electrons in ATLAS object reconstruction (together they're named "e/gamma" in ATLAS analyses), so photons can also benefit from such study. To use the e/gamma objects with new showers in analyses and e/gamma studies, new tools are implemented into the official ATLAS software system:

- CellReweighter: to reweight cells associated to electron and photons, and store cells to a new CellContainer.
- ClusterDecorator: to build new cell cluster and Link new cluster to electrons.

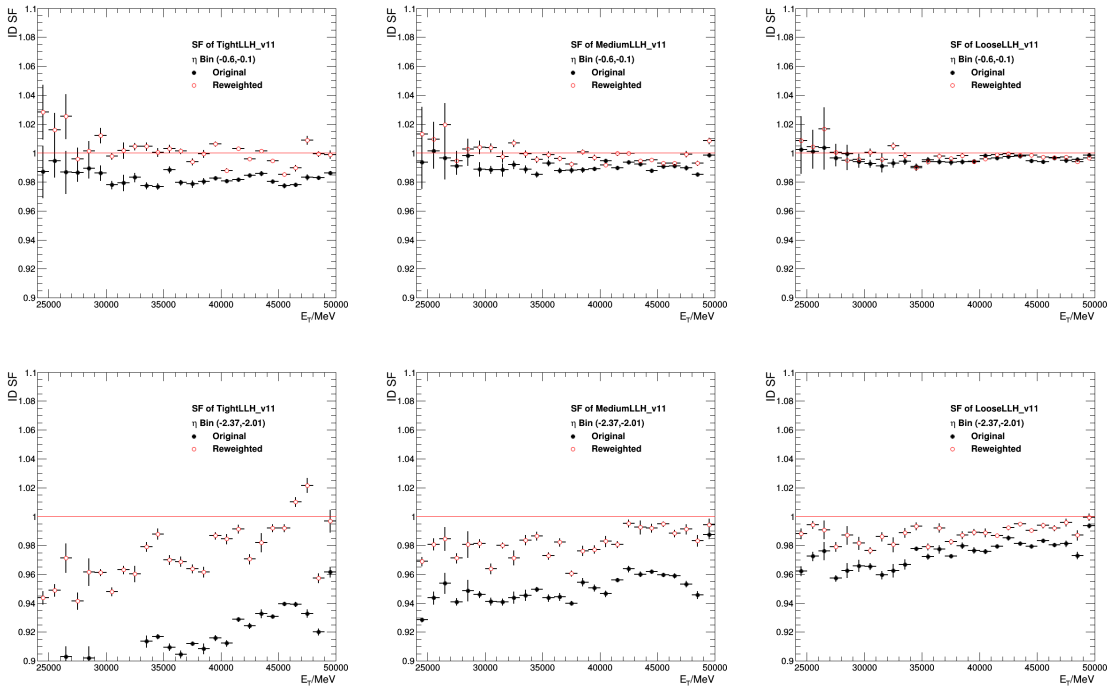

Figure 4.37: TightLLH (Left), MediumLLH (middle), LooseLLH (right) identification scale factors bf/af cell reweighting. Top: barrel; bottom: end-cap.

- EgammaReweighter: to rebuild new shower shape parameters and new associated electrons.

The shower-shape parameters with completed reweighting procedure by the official framework are illustrated in Fig.4.38 in validation. The performance is in line with expectations and the new-shower e/gamma objects are already contained in MC datasets for e/gamma and standard model analyses.

4.4.4 Next Steps

The procedure to have cell-based reweighting for electron shower-shapes in first and second layer of EM calorimeter are developed to reproduce the data-like shapes, in particular the energy leakage, in simulations. This kind of algorithm is already implemented to the ATALS official software system for further study, especially the e/gamma identification and calibration, and standard model precision analyses.

As next step, there are several practical optimizations on the reweighting strategy. First is the dimension-extension, to proceed the method from 1-D to η-ϕ 2-D topology. And since the tools are adapted to photons, the validation and dedicated research to photon shower reweighting would be of interest. In addition, the bremsstrahlung can also be avoided using photons. These two subjects are followed by new qualification tasks in ATLAS egamma performance group. To handle the residual data and MC discrepancy, using the finer binning, or continuous reweighting strategy that depend on the real position may further improve the performance. Like electron with cluster centralized to $\eta = 0.4$ may use

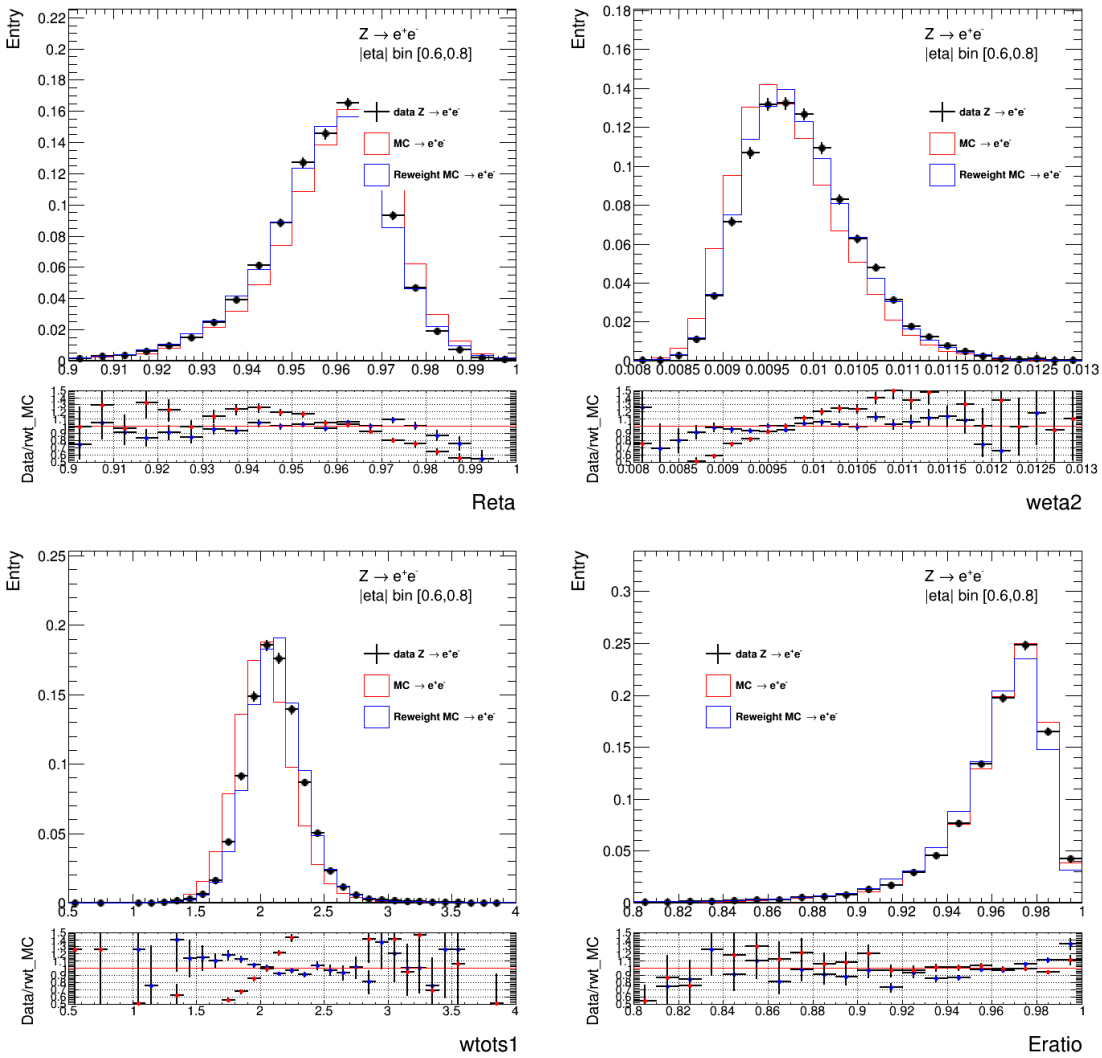

Figure 4.38: Shower shape parameters bf/af reweighting at Rel20.7

the average reweighting function of bin [0.2,0.4] and [0.4, 0.6]. And electron with cluster centralized to $\eta = 0.35$ may use the reweighting function then becomes $0.75 \cdot f(0.2, 0.4) + 0.25 \cdot f(0.4, 0.6)$. Last, introducing the tag-and-probe to the electron selection when extracting reweighting functions will give higher purity and smaller, under-control bias from backgrounds. The uncertainties can be estimated with tag-and-probe as well like the efficiencies.

5 Muon measurements

The relevant calibrations and corrections for muons used in low-pile-up measurements are introduced in this chapter. Most content is based on the study of Ref. [45], in particular the momentum calibration and efficiency calculation, except the mis-alignment correction accounting for charge-dependent bias, derived in-situ from low-pile-up data.

5.1 Muon reconstruction

The momentum reconstruction of muon is performed independently in the inner detector and muon spectrometer side. In the ID, the trajectories are built identically together with all other charged particles, while in the MS, the track candidates are built from fitting the hits in different longitudinal layers, usually initialized from a hit segment "seed" generated in the middle layers of the MS with better trigger sensitivity. The seed is then extended to the inner and outer layers segments according to the hit multiplicity and fit quality of relative positions and angles. In addition, overlap removal and χ^2 fit algorithms are used to handle tracks intersections and improve track quality respectively. Then the individual information of ID and MS tracks are combined to complete muon tracking. Exploiting the tracks and the small amount of energy, typically $\sim$ 3GeV, that muon object would deposit in the calorimeters, four types of muon candidates are defined:

- Combined (CB) muons: prompt muons with tracks reconstructed independently in the ID and MS, and reformed with a global refit.
- Segment-tagged (ST) muons are identified in the ID with a track associated with at least one local track segment in the MDT or CSC chambers.
- Calorimeter-tagged (CT) muons : for candidates in the central gap of MS ($|\eta|$ <0.1), a track in the ID is identified as a muon if it can be matched to an energy deposit in the calorimeter compatible with a minimum-ionizing particle.
- Extrapolated (ME) muons : mostly muons in the ID blinded region of 2.5 < $|\eta|$ < 2.7 whose trajectory is reconstructed based only on the MS track and a loose requirement on compatibility with originating from the IP.

When two muon types share the same ID track, preference is given in the order of CB, ST, and finally CT muons.

To reject the backgrounds dominated by pion and kaon in-flight decays, the muon identification is performed. Several variables have good behavior in discrimination between prompt muons and background muons: $q/psignificance$ defined as the significance of the charge-momentum ratio in ID

and MS; ρ' defined as the absolute value of the difference between the p_T fraction in the ID and MS to the combined track. In addition, specific requirements on the number of hits in the ID and MS are used to ensure a robust muon momentum. By setting different levels of cuts, the muon identification are defined at four working points (WP), Loose, Medium, Tight and High-p_T, specific for different physics analyses.

5.2 Muon momentum calibration

The reconstruction of muons, especially CB muons is led by tracks, and much less sensitive to calorimeter information. The momentum calibration mainly consists of the energy scale and resolution corrections and only works on simulated muons to improve the modelling. The energy scales and resolutions of muons are individual for ID and MS, correcting p_T^{MC} in the form of:

$$p_T^{Cor,Det} = \frac{p_T^{MC,Det} + \sum_{n=0}^{1} s_n^{Det}(\eta,\phi)(p_T^{MC,Det})^n}{1 + \sum_{m=0}^{2} \Delta r_m^{Det}(\eta,\phi)(p_T^{MC,Det})^{m-1} g_m}, \tag{5.1}$$

where "Det" refers to ID or MS, the terms $\Delta r_m^{Det}(\eta,\phi)$ and $s_n^{Det}(\eta,\phi)$ denote the resolution smearing and momentum scale corrections respectively in specific (η,ϕ) region. In particular, s_1^{Det} accounts for inaccuracy in the description of the magnetic field integral and the detector's dimension in the direction perpendicular to it; s_0^{MS} accounts for inaccuracy in the simulation of energy loss between IP and MS; the energy loss is negligible between IP and ID, hence $s_0^{ID} = 0$. Δr_m is drawn from the assuming that the resolution can be parameterized as follows:

$$\frac{\sigma p_T}{p_T} = r_0/p_T \bigoplus r_1 \bigoplus r_2 \cdot p_T \tag{5.2}$$

of which each term represents a effect on resolution: energy loss in the traversed material, multiple scattering, local magnetic field inhomogeneities and local radial displacements of the hits, and intrinsic resolution effects caused by the spatial resolution of the hit measurements and by residual misalignment of the muon spectrometer.

The corrections are applied separately to p_T in ID and MS, and then combined with a weighted average:

$$p_T^{Cor,CB} = f \cdot p_T^{Cor,ID} + (1-f) \cdot p_T^{Cor,MS} \tag{5.3}$$

using the weight derived from simulation.

The parameters in momentum scale and resolution are not significantly dependent on pile-up and center-of-mass energy, therefore the study uses calibrations measured for high-pile-up datasets [45], with validations.

Muons from two resonances are used: $J/\psi \to \mu\mu$ (for muon transverse momenta $5 < p_{\mathrm{T}} < 30$ GeV) and $Z \to \mu\mu$ ($22 < p_{\mathrm{T}} < 300$ GeV). And two parameters are considered for the validation of

corrections: the mean of the mass peak, $m_{\mu\mu}$, which is sensitive to the momentum scale; the width of the mass peak, $\sigma_{\mu\mu}$, which is sensitive to the momentum resolution

Fig. 5.1 give some examples of the validations. In general, the agreement of both the scales and resolutions with data improves after applying the corrections, except for MS tracks of muons from J/ψ decays, which is not within the region of interest in W-boson measurements. Any residual discrepancies are typically covered by systematic uncertainties of the calibration corrections. This confirms that at the current level of the systematic uncertainties, the high-pileup calibration is applicable to the low-pileup data.

5.3 Muon selection efficiencies

Muon candidates used in the W-event reconstruction need to pass several quality requirements. Besides the reconstruction and identification described in 5.1, the isolation and trigger selections are also applied to muons.

- Reconstruction : an true muon is successfully reconstructed in detector with the information of tracks in ID and MS and energy deposition in EMC.
- Identification : an selection to reject backgrounds from in-flight decays of charged hadrons in the ID. The $Medium$ identification criteria provides the default selection for muons in ATLAS, which is adopted as well in low-pile-up analyses. Only CB and ME muons are used, and a loose selection on the compatibility between ID and MS momentum measurement is applied to suppress the fake muons. In addition, the $q/psignificance$ is required to be < 7.
- Isolation : the based track-based isolation variable $p_T^{varcone20}$ is used to define the isolation in W-properties measurements. It's the scalar sum of the transverse momenta of the tracks with p_T > 1 GeV in a cone of size $\Delta R = min(10GeV/p_T^{\mu}, 0.2)$ around the muon of transverse momentum p_T^{μ} excluding the muon track itself. It's the main function is to reject the multi-jet backgrounds. The decision of "$p_T^{varcone20}$ < 0.1" isolation is introduced in Chap.7.4.
- Trigger : a loose trigger fired by at least one muon with transverse momentum larger than 14 GeV, named "HLT_mu14" is used.
- Track-to-vertex-association (TTVA): a new selection of Run-II to improve the ID track resolution, introduced in Chap. 7.2.

Muons that satisfy these five selections are assumed to be pure and of good quality. Since the identification exploits reconstruction information, particularly the CB and ME tracks, the selection of reconstruction and identification is combined to be one, as "Recon/ID". Like electron, the discrepancy of muon selection efficiency between data and MC is corrected by scale factors. The total efficiency correction to a single muon in W events is written as:

$$W_{\text{event}}^{W\to\mu\nu} = \text{SF}_{\text{reco}}^{Medium} \cdot \text{SF}_{\text{TTVA}}\text{SF}_{\text{Isolation}} \cdot \text{SF}_{\text{Trigger}} \tag{5.4}$$

Muon scale factors are calculated with tag-and-probe method, provided by the MCP group, using the same tool and configuration as [46]. In general, muon pairs are selected from $Z \to \mu\mu$ within 10

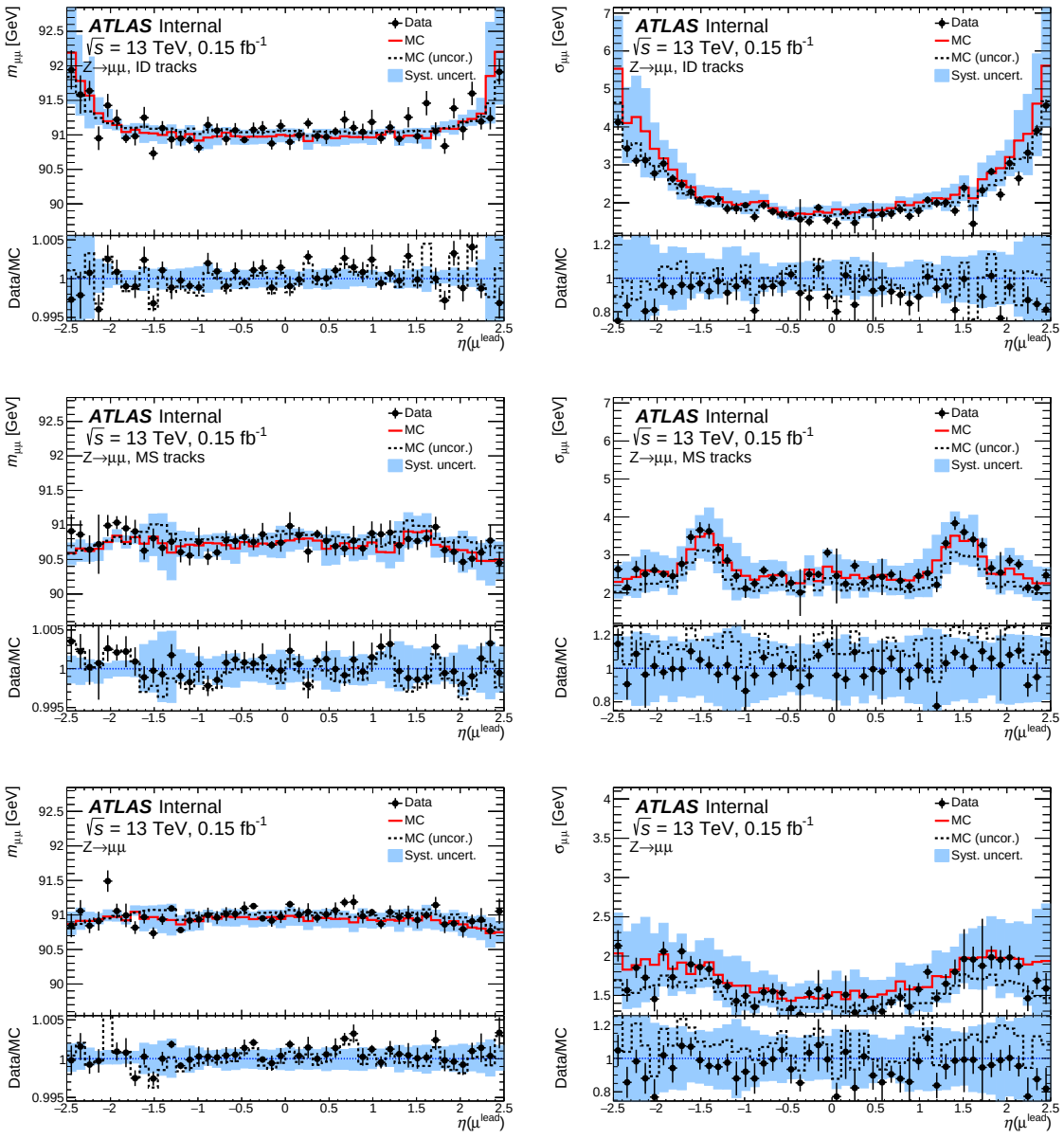

Figure 5.1: Mean (left) and width (right) of the $Z \rightarrow \mu\mu$ mass peak as a function of the leading muon η in 2017 13 TeV data and MC at low pile-up. The mean and width are extracted from Crystal Ball components of the fits. In case of the simulation, both the uncorrected (dashed histogram) and corrected parameters (solid histogram) are shown. The fit results are presented for mass peaks constructed using kinematics of the muon ID tracks (top), ME tracks (middle) or CB tracks (bottom). The bottom panels in each plot show the data/MC ratio for uncorrected (dashed histogram) and corrected simulation (points).

GeV of the Z-mass window. the tag muon needs to pass the Medium identification, *Loose* isolation and TTVA selections, with a p_T^μ of at least 24 GeV, and fire the trigger of event. The probe muon are required to have a p_T^μ larger than 10 GeV, satisfy the *Loose* isolation, with extra cuts applied to ID tracks and calorimeter-tagged (CT) muon probes to increase the purity. Then a probe is considered successfully reconstructed if a reconstructed muon is found within a cone in the $\eta - \phi$ plane of size $\Delta R = 0.05$ around the probe track.

The Recon/ID, TTVA, isolation and trigger efficiencies are measured from these tag-probe pairs. The later three types of efficiencies are calculated with muons already Medium-identified, thus relatively simpler than the Recon/ID calculation, to which the geometry and track quality of muons are critical. The Recon/ID efficiency is measured in two stages: first, the efficiencies related to the inner detector reconstruction are determined, and the second step determines the muon spectrometer reconstruction, extrapolation and the combination, written as [47]:

$$\epsilon\,(\text{Medium}) = \epsilon\,(\text{Medium}|\text{ID}) \cdot \epsilon\,(\text{ID}) = \epsilon\,(\text{Medium}|\text{CT}) \cdot \epsilon\,(\text{ID}|\text{MS})\,. \tag{5.5}$$

This is estimated with approach upon two assumptions:

- the reconstructions of ID track and MS track are independent, so that $\epsilon\,(\text{ID}) = (\text{ID}|\text{MS})$.
- the calo-tagged (CT) muon has the same probability for Medium reconstruction regardless of ID track ($\epsilon\,(\text{Medium}|\text{ID}) = \epsilon\,(\text{Medium}|\text{CT})$).

The residual bias due to such assumptions is taken into account in the systematic uncertainties. Therefore the Recon/ID efficiency is practical with tag-and-probe procedure, so do the scale factors.

All muon efficiencies and scale factors are measured in-situ for full low-pile-up data and MC at 5 and 13 TeV, provided by the Muon Combined Performance (MCP) group. Fig. 5.2 and 5.3 illustrate the measured muon efficiencies and SFs with 2017 13 TeV low-pile-up samples.

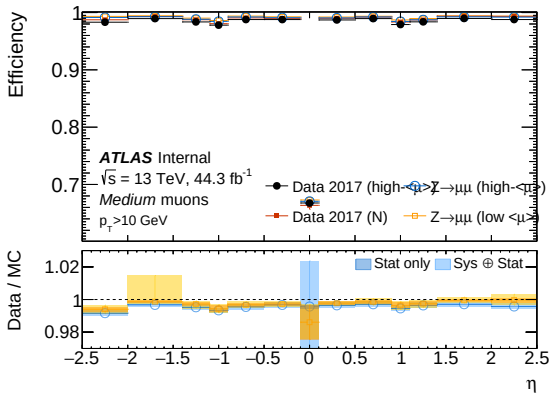

(a) Reconstruction

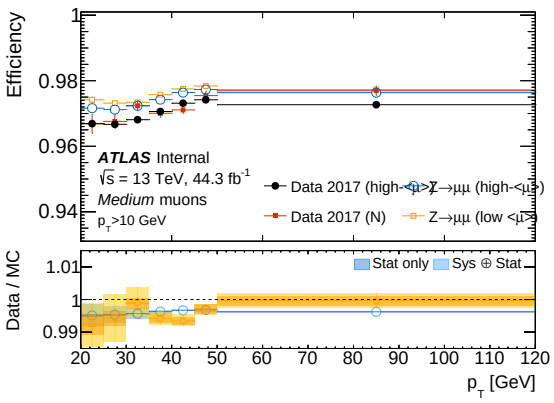

(b) Reconstruction

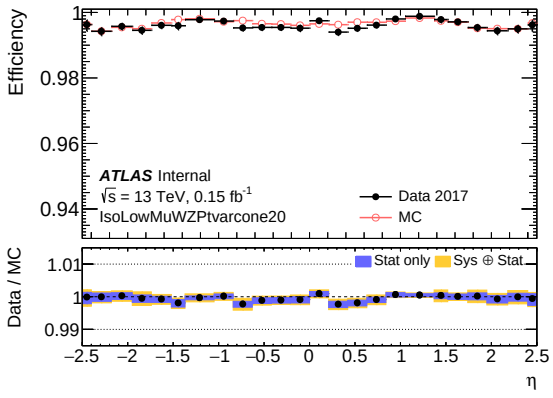

(c) Isolation

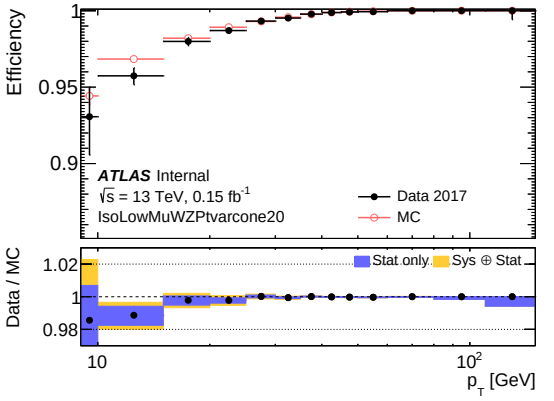

(d) Isolation

Figure 5.2: Reconstruction (with Medium Identification) and Isolation efficiencies and scale factors using low-pile-up datasets in 2017 at $\sqrt{s}$ = 13TeV

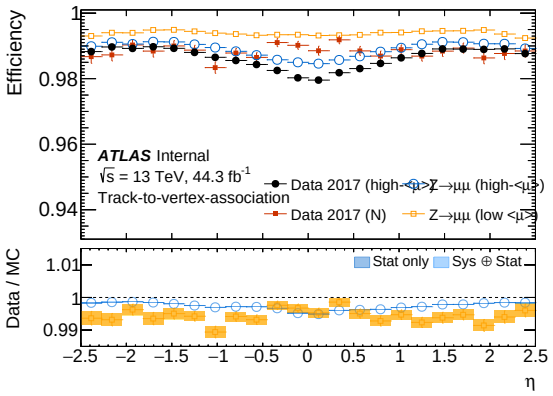

(a) TTVA

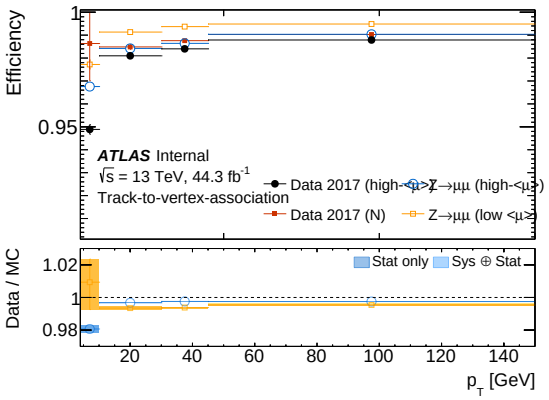

(b) TTVA

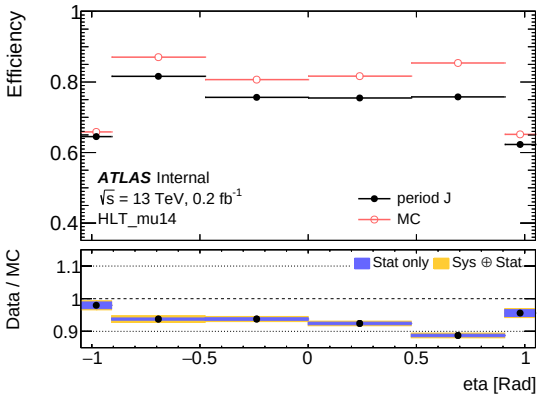

(c) Trigger

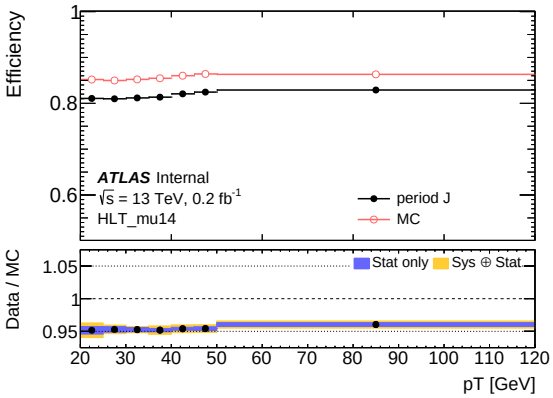

(d) Trigger

Figure 5.3: TTVA and trigger efficiencies and scale factors using low-pile-up datasets in 2017 at $\sqrt{s}$ = 13TeV

5.4 Muon charge dependent correction measurement

5.4.1 Low-pile-up mis-alignment correction

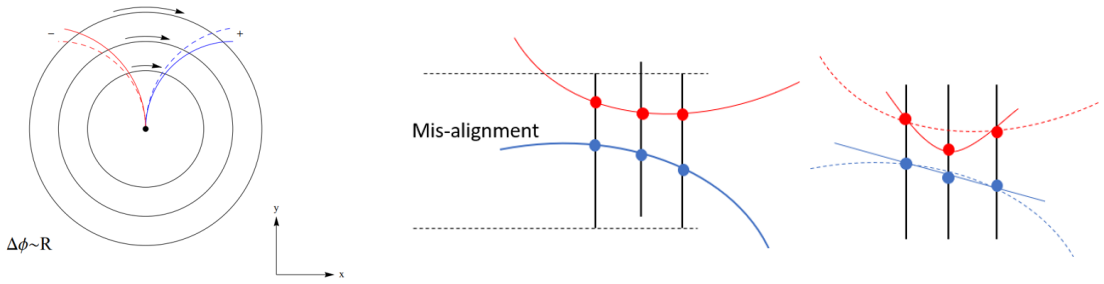

(a) a (b) b

Figure 5.4: Illustration of the sagitta bias in inner detector.

Misalignments within the ID, the MS or in between the ID and MS can introduce a charge dependent bias to the muon momentum reconstruction, which is called sagitta bias, illustrated in Fig. 5.4, mostly happen when one layer of the ID slightly rotates (Fig. 5.4 (a)). The effect on the measured transverse momentum can be parameterised with Eq. 5.6:

$$p_{\mathrm{T}}^{\mathrm{meas}} = \frac{p_{\mathrm{T}}^{\mathrm{reco}}}{1 + q \times \delta_{\mathrm{sagitta}} \times p_{\mathrm{T}}^{\mathrm{reco}}}. \tag{5.6}$$

The task is to determine the "sagitta correction" $\delta_{\mathrm{sagitta}}$, typically as a function of η and potentially ϕ to ensure that momenta of muons and anti-muons from $W \to \mu\nu$ and $Z \to \mu\mu$ processes are correctly measured. Figure 5.5 shows an early version of $Z \to \mu\mu$ data compared to MC simulation, where it is clear from the behavior around the Jacobian peak of $p_{\mathrm{T}} \sim 45$GeV, that the μ^+ and μ^- momenta are oppositely biased. Such effects are critical, for example, in high-precision measurements of W^+/W^- cross-section ratios/asymmetries as well as the W-boson mass-measurement.

The effect is studied in η bins at this stage to reduce statistical fluctuations, as most measurements will to first order not be sensitive to a bias that changes with ϕ. Multiple methods are studied to evaluate the sagitta bias. The results are summarized in figure 5.6.

- The ID momentum measurement can be evaluated using electrons, whose p_{T} is measured using the charge-blind calorimeter measurement and the track direction. Using either $Z \to ee$ and $W \to e\nu$ events, one may determine the charge bias of electron track measurement as:

$$\delta_{\mathrm{sagitta}} = \frac{\langle E/p_{\mathrm{track}} \rangle^{+} - \langle E/p_{\mathrm{track}} \rangle^{-}}{2\langle p_{\mathrm{T}} \rangle}, \tag{5.7}$$

  where p_{track} is the track momentum recorded by the inner detector, E is the calibrated electron energy, mostly from the energy deposition in EMcalorimeter, and p_{T} is the corresponding

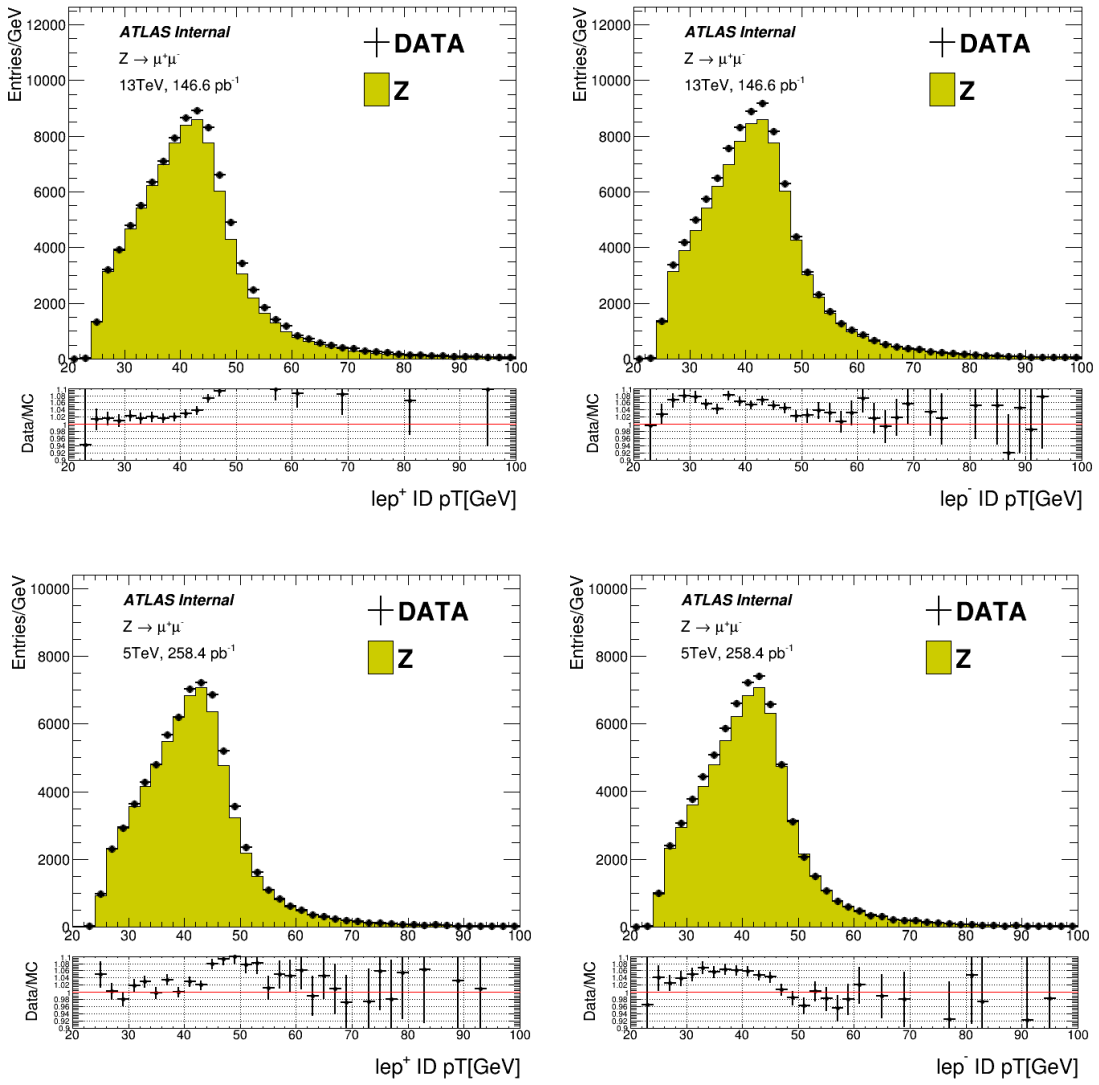

(a) μ^+ (b) μ^-

Figure 5.5: An example of an early data/MC comparison of 2017 data at 13 TeV (top) and 5.02 TeV (bottom). The muon p_{T} is taken from the inner detector (ID) and displays a clear charge-dependent bias compared to the simulation.

calibrated transverse momentum. The symbol $\langle\cdot\rangle$ denotes that the corresponding quantities are averaged in η bins. $Z \to ee$ events have the advantage of less background, while $W \to e\nu$ events have the advantage of about 10 times more reconstructed events for the same data set.

- A method ("$p_{\mathrm{T}}(\mu)$") [48] used by both MCP and alignment groups in high-pileup data determines muon momentum biases by comparing the p_{T} spectra of muons and anti-muons in $Z \to \mu\mu$ events. While these are in theory not exactly identical, it was studied with simulation that the difference due to electroweak effects is very small.

- Another method uses the $Z \rightarrow \mu\mu$ mass peak and is widely used by MCP [48] and and the alignment group, as it typically gives the highest statistical sensitivity. The average relative bias between positive and negative muons can be calculated by determining the bias to the mass-peak position in each event.

The E/p method and $p_{\mathrm{T}}(\mu)$ methods give directly the absolute sagitta bias, while the Z-mass method only provides the differential bias and averages to "0". This feature can be clearly appreciated in Figure 5.6. A good strategy is thus to determine the global offset with a method sensitive to it, while obtaining the η dependence from the Z-mass method.

The sagitta bias in the data sets under consideration was found to be about 5 times larger in data than MC. Ideally corrections should be determined in both data and simulation separately and then be applied to data and MC separately. However, one may also opt to apply the data-MC difference to data to get the same effect in the critical data/MC comparison.

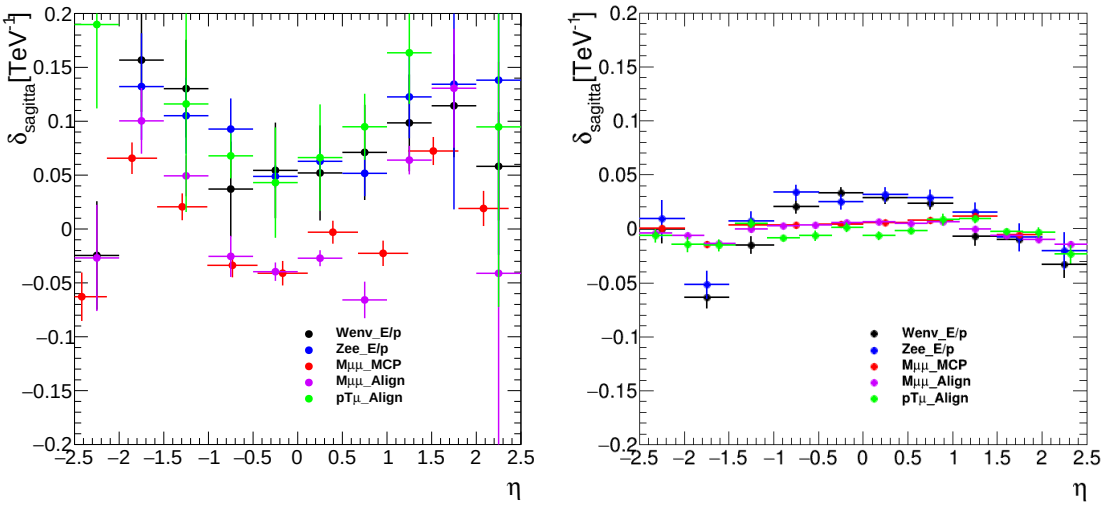

Figure 5.6: Measurement of the sagitta bias in low-pileup data. The corrections were evaluated with two Z-mass methods ("$M\mu\mu$"), the E/p method applied to $W \rightarrow e\nu$ and $Z \rightarrow ee$ events and the $p_{\mathrm{T}}(\mu)$ method. The left plot shows the data results, where with clear η-dependent and overall biases are observed. The right plot shows MC, where a much smaller bias is observed especially for the electron E/p method.

A problem found in the MC sagitta determination is that the bias extracted from muons is much smaller than that of electrons. While muons display a negligible bias in simulation, a rather significant effect is found for electrons. The difference is studied further using the pT(ID)/pT(Truth) distributions in simulation and separated by charge. A sagitta bias is supposed to show an opposite linear bias with p_{T} while a calibration bias is constant. Figure 5.7 illustrates that difference between positive and negative charges in simulation is the same for both electron and muon in barrel and end-cap. This means that the electron sagitta bias cannot be determined at this level using electrons and the observed effect is rather due to other effects. Therefore the final sagitta correction is required to be derived from muons, using results from electrons as cross-check.

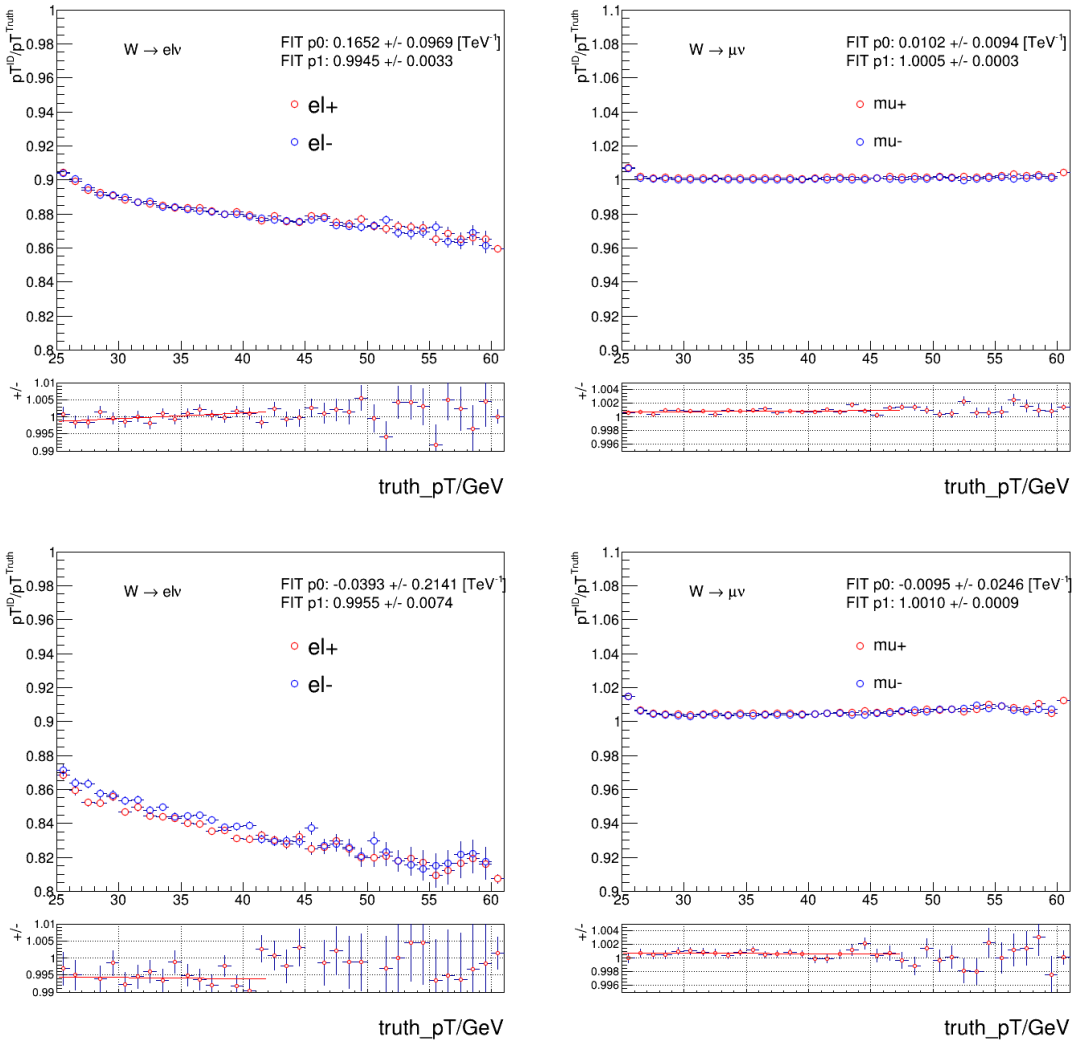

Figure 5.7: The ratio and linear fit of charge-dependent p_T^{ID}/p_T^{Truth} in electron(left) and muon(right) in barrel(top) and end-cap(bottom) from simulated $W \longrightarrow \ell\nu$ events.

As discussed, the general idea is to use a Z-mass differential correction with additional offset. Two methods are developed to evaluate the offset:

1. Calculate the average difference between Z-mass method and $p_{\mathrm{T}}(\mu)$ method and take the result as offset to the Z-mass result.

2. Evaluate the charge asymmetry with a linear fit to the transverse momentum distribution ratio and perform a scan along the offset to find an optimal offset with minimal 0-curve.

Result of method 1. is shown in Figure 5.8. The offsets are found to be:

- E/p $W \rightarrow e\nu$: 0.07 ± 0.04,
- E/p $Z \rightarrow ee$: 0.09 ± 0.05,
- $p_{\mathrm{T}}(\mu)$: 0.11 ± 0.03,

where statistical uncertainties are significant in all cases.

The method 2. fit and scan results are shown in Figure 5.9 and 5.10. $Z \rightarrow \mu\mu$ events are selected from data, with $p_{\mathrm{T}}(\mu) > 25$ GeV, $|\eta_{\mu}| < 2.4$, $Medium$ identification, $FixedCutLoose$ isolation, HLT_mu14 trigger and 66 GeV < $M_{\mu\mu}$ < 116 GeV cuts. Then a list of sagitta bias corrections equal to (Z-mass + offset-x, x = 0.06, 0.07, 0.08...) are applied to positive and negative muons. From Z bosons decay, positive muons and negative muons are expected to have the same transverse momentum distribution. Therefore the ratio of two spectra represents the level of charge-dependent bias. A linear fit is performed along the ratio, and the optimal correction should give this fit "0" slope (right plot of figure 5.9). Figure 5.10 is about the relation between p_{T} spectra ratio linear fit and offset-x, illustrating an optimal offset of 0.11, in good agreement with the $p_{\mathrm{T}}(\mu)$ method. The statistical uncertainty of this fit is ±0.02. In conclusion, the Z-mass sagitta-bias correction is applied with additional offset determined to be 0.11 ± 0.02.

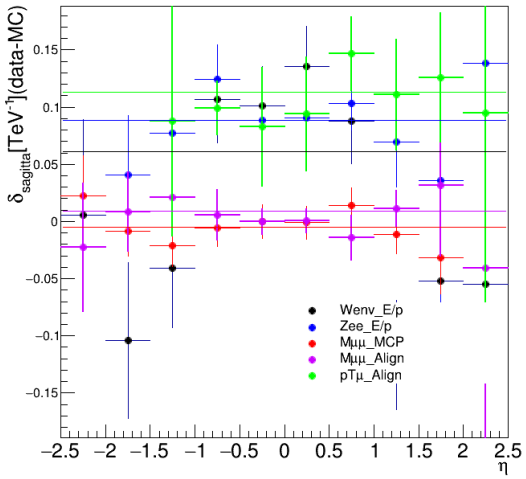

Figure 5.8: Sagitta bias and average value at low-mu run, evaluated with Z mass method, E/p method and $p_{\mathrm{T}}(\mu)$ method. The MC estimates are subtracted from the data measurements.

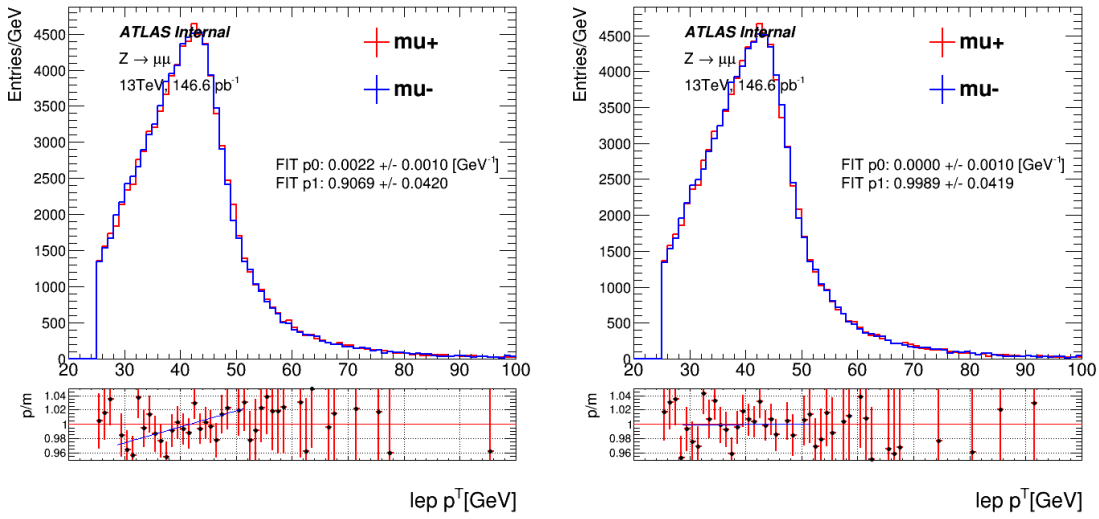

Figure 5.9: Ratio and linear fit of μ^+ and μ^- transverse momentum distribution with 0-offset(left) and 0.11-offset(right) on sagitta bias correction.

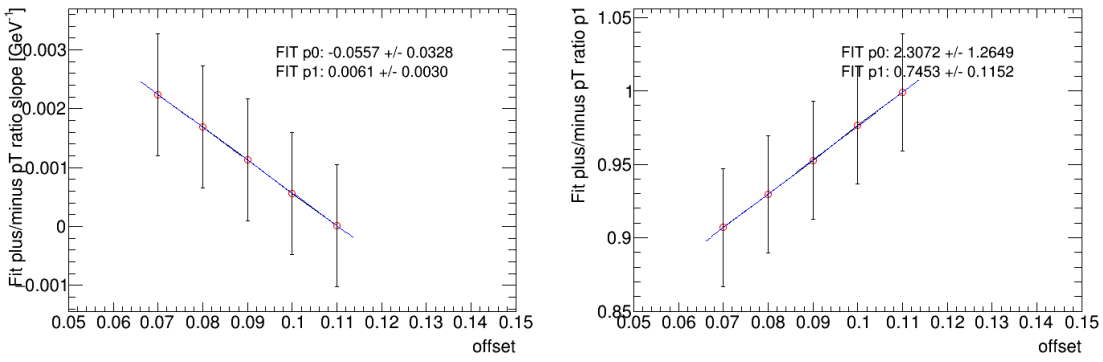

Figure 5.10: Scan of linear fit parameters along offset

5.4.2 Comparison of various sagitta bias corrections

The 2017 low-pile-up datasets at $\sqrt{s}$ = 5.02 TeV and 13 TeV have been reprocessed to account for known misalignments of the ID, which have an impact on the charge-dependent momentum biases. In addition, the MCP group provides sagitta bias corrections derived using the Z-mass method from high-pile-up datasets. These corrections should remove residual biases which could remain after reprocessing.

The effects of the reprocessing and of the sagitta bias corrections provided by MCP as well as those derived for the low-pile-up datasets is studied using several observables in $Z \to \mu\mu$ events:

- residual sagitta bias, δ_{sagitta}, evaluated using the $p_{\text{T}}(\mu)$ method,
- transverse momenta of positive and negative muons,
- forward-backward asymmetry, A_{FB}, calculated in the Collins-Soper frame of reference.

A comparison of δ_{sagitta} determined using either no sagitta bias correction or one of the two corrections under study is shown in Figures 5.11 and 5.12 for the 2017 low-pile-up datasets at 5.02 TeV and 13 TeV, respectively. As discussed in the previous subsection, the non-reprocessed data show a sizeable bias, which is smaller in the barrel region than in the endcap region. The effect of the reprocessing is marginal, with shifts of δ_{sagitta} usually much smaller than its statistical uncertainty. The application of the MCP sagitta bias correction to the reprocessed data has a similarly limited effect in most regions of η. On the other hand, the application of the dedicated low-pile-up correction to both the non-reprocessed and reprocessed data yields significant shifts of δ_{sagitta} towards 0. This indicates a large reduction of the overall bias, even if some dependence of the residual bias on η remains.

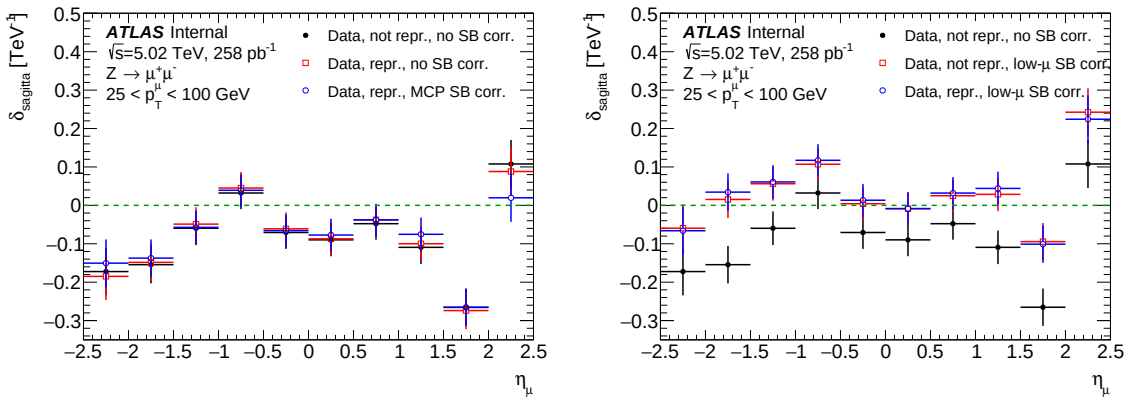

Figure 5.11: Residual sagitta bias determined using the $p_{\text{T}}(\mu)$ method in $Z \to \mu\mu$ events from the 5.02 TeV dataset. The non-reprocessed data are compared to reprocessed data without sagitta bias corrections and with the MCP correction (left). The impact of the dedicated correction for low-pile-up datasets is also shown (right).

Figure 5.13 presents a similar comparison of p_{T}^{μ} distributions for positive and negative muons produced in $Z \to \mu\mu$ decays in the 5.02 TeV dataset. In addition, the data are compared to the $Z \to \mu\mu$ signal MC simulation. The p_{T}^{μ} distributions in the non-reprocessed data are shifted relative to the MC distributions. These shifts are in opposite directions for the two muons charges (towards higher p_{T}^{μ}

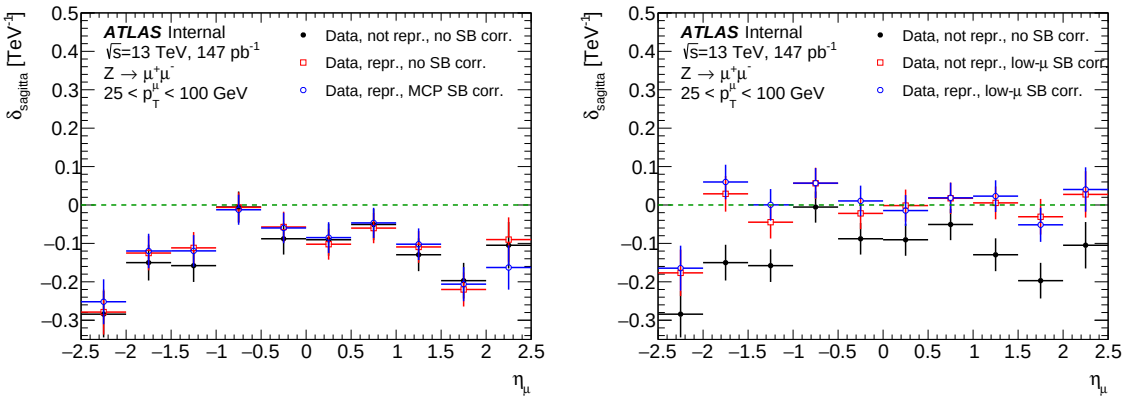

Figure 5.12: Residual sagitta bias determined using the $p_{\mathrm{T}}(\mu)$ method in $Z \rightarrow \mu\mu$ events from the 2017 13 TeV dataset. The non-reprocessed data are compared to reprocessed data without sagitta bias corrections and with the MCP correction (left). The impact of the dedicated correction for low-pile-up datasets is also shown (right).

for positive muons and towards lower p_{T}^{μ} for negative muons), as expected from a charge-dependent momentum bias present in the data. Again, the reprocessing and the MCP sagitta bias correction have only a marginal impact, while the dedicated low-pile-up correction moves the data distributions closer to the simulation.

The impact of the sagitta bias on the p_{T}^{μ} distributions is better visible in the ratios of distributions observed in data and simulation, as shown in Figure 5.14. Here, it is indicated by a sudden increase (decrease) of the ratio around $p_{\mathrm{T}}^{\mu} = 45$ GeV for positive (negative) muons. This feature is present for the non-reprocessed data, as well as for the reprocessed data without correction and with the MCP correction. After applying the dedicated low-pile-up correction, the ratios for both charges become flatter, indicating a vanishing residual bias. Similar observations are made for ratios of p_{T}^{μ} distributions in the 2017 low-pile-up datasets at 13 TeV, which are presented in Figure 5.15.

Although the dedicated low-pile-up sagitta bias correction is based only on the 2017 13 TeV dataset, it is shown to improve distributions of the studied observables in the 5.02 TeV dataset. This is also the case for the 2018 low-pile-up dataset at 13 TeV, as presented in Figures 5.16 and 5.17. Therefore, the current strategy in the analysis is to use the reprocessed 2017 low-pile-up data, and to apply the dedicated low-pile-up sagitta bias correction to all datasets (from 2017 and 2018).

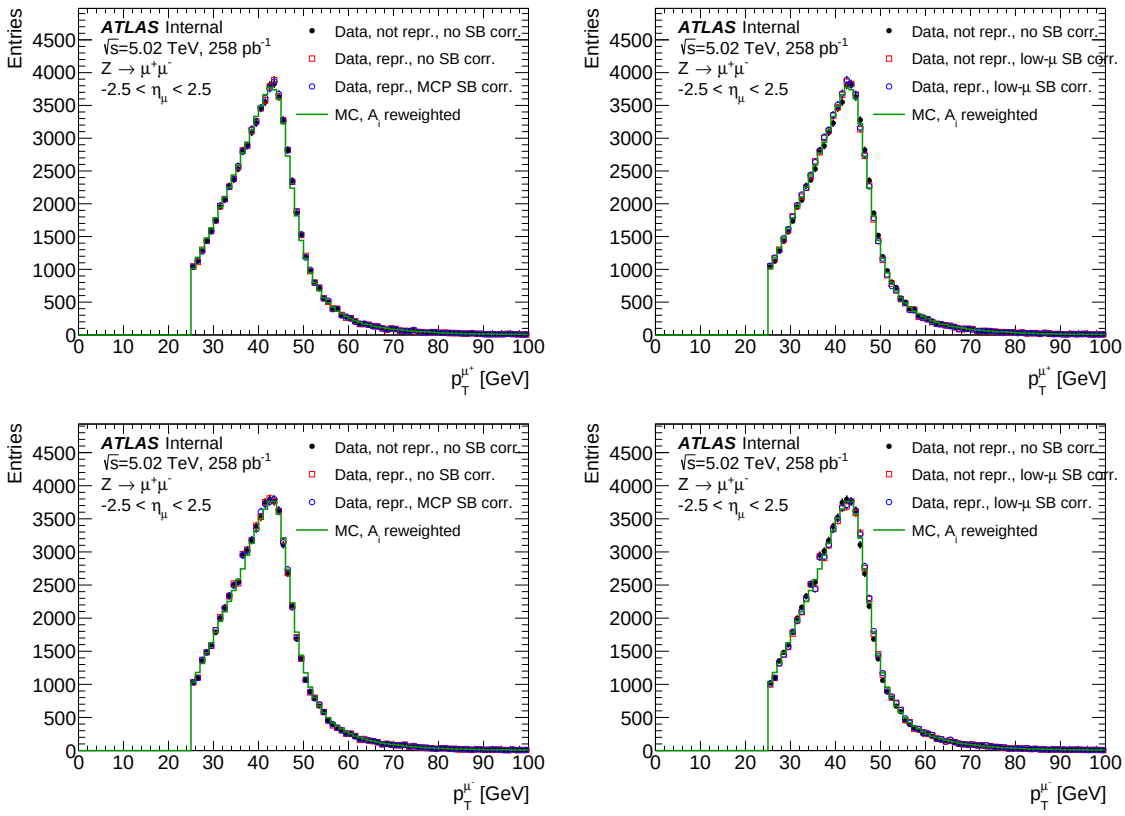

Figure 5.13: Distribution of p_{T}^{μ} for positive (top) and negative muons (bottom) in $Z \rightarrow \mu\mu$ events from the 5.02 TeV data and MC. The non-reprocessed data are compared to reprocessed data without sagitta bias corrections and with the MCP correction (left). The impact of the dedicated correction for low-pile-up datasets is also shown (right).

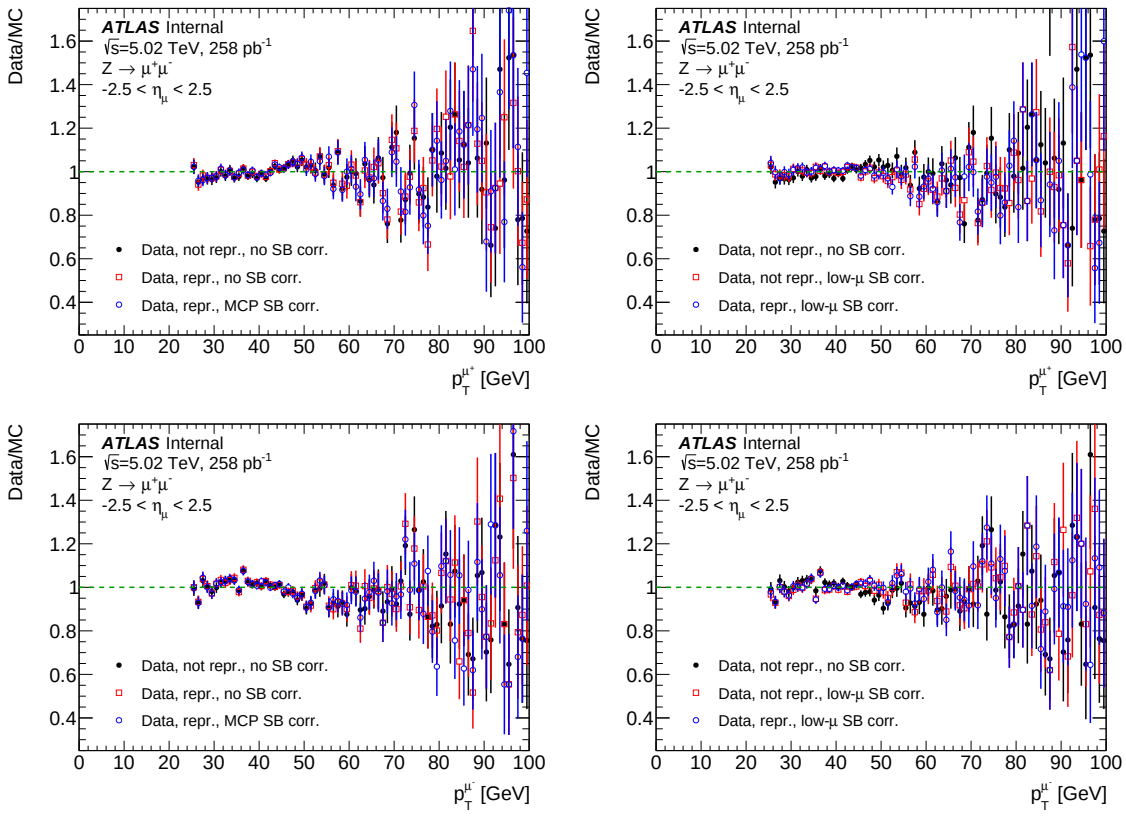

Figure 5.14: Data-to-MC ratio of p_{T}^{μ} distributions for positive (top) and negative muons (bottom) in $Z \to \mu\mu$ events from the 5.02 TeV datasets. The non-reprocessed data are compared to reprocessed data without sagitta bias corrections and with the MCP correction (left). The impact of the dedicated correction for low-pile-up datasets is also shown (right).

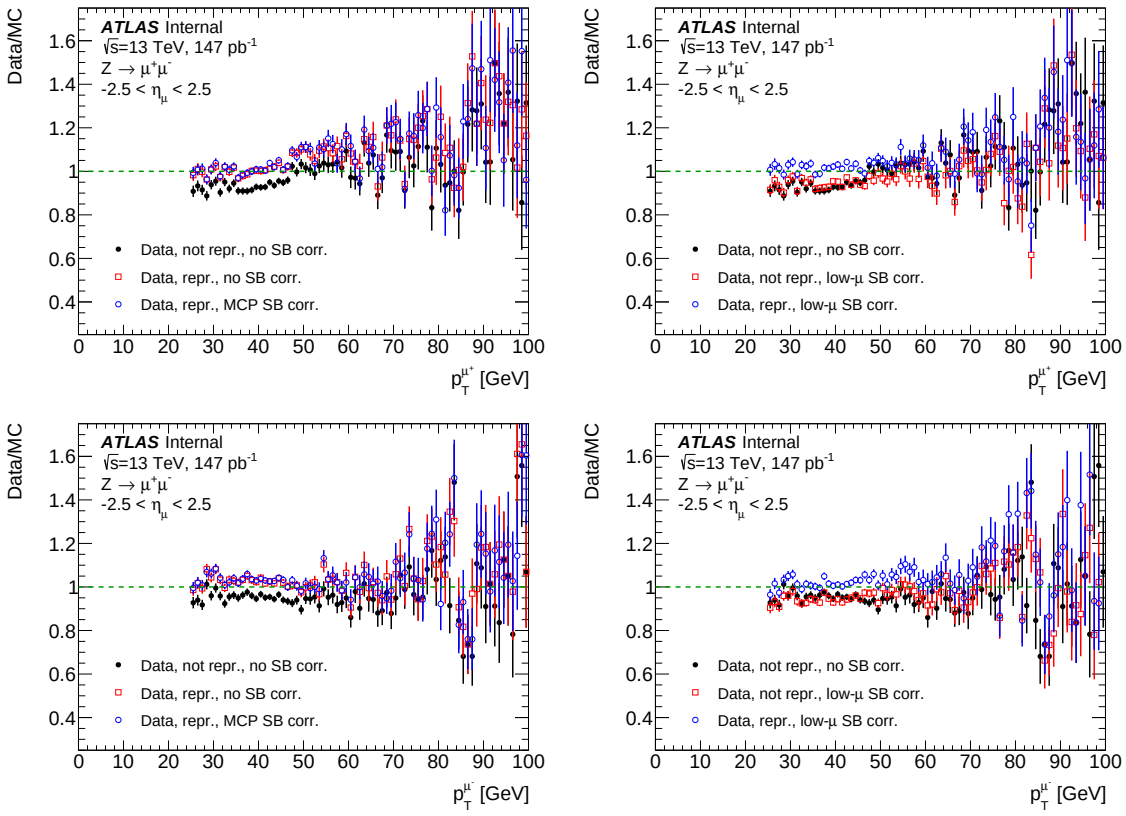

Figure 5.15: Data-to-MC ratio of p_{T}^{μ} distributions for positive (top) and negative muons (bottom) in $Z \to \mu\mu$ events from the 2017 13 TeV datasets. The non-reprocessed data are compared to reprocessed data without sagitta bias corrections and with the MCP correction (left). The impact of the dedicated correction for low-pile-up datasets is also shown (right).

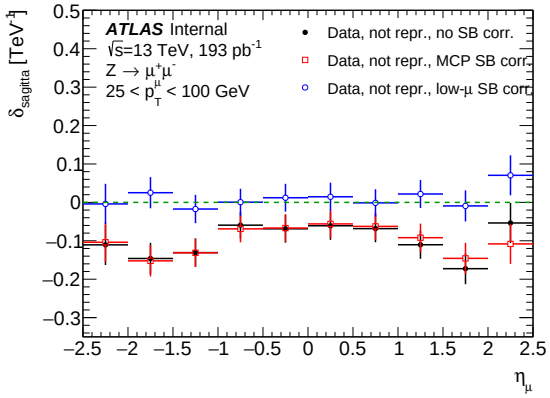

Figure 5.16: Residual sagitta bias determined using the $p_{\mathrm{T}}(\mu)$ method in $Z \to \mu\mu$ events from the 2018 13 TeV dataset. The data without sagitta bias corrections are compared to data with the MCP correction and with the dedicated correction for low-pile-up datasets.

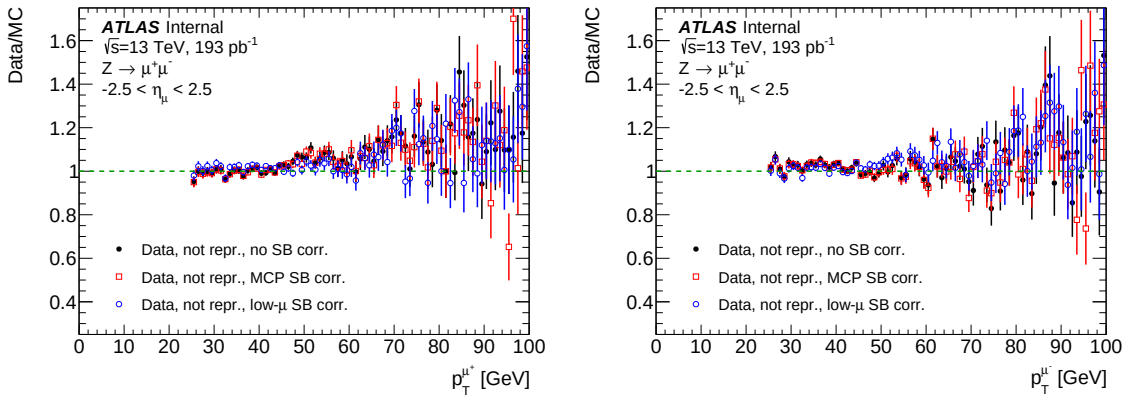

Figure 5.17: Data-to-MC ratio of p_{T}^{μ} distributions for positive (top) and negative muons (bottom) in $Z \to \mu\mu$ events from the 2018 13 TeV datasets. The data without sagitta bias corrections are compared to data with the MCP correction and with the dedicated correction for low-pile-up datasets.

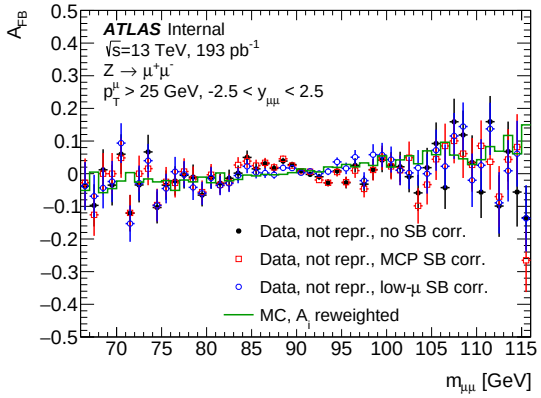

Figure 5.18: Dependence of A_{FB} on $m_{\mu\mu}$ in $Z \to \mu\mu$ events from the 2018 13 TeV dataset. The data without sagitta bias corrections are compared to data with the MCP correction and with the dedicated correction for low-pile-up datasets.

6 Reconstruction and Calibration of the Hadronic Recoil

The determination of the neutrino transverse momentum, which refers to missing transverse energy (E_T^{Miss}) is a big challenge for measurements using the ATLAS detector. The standard strategy for E_T^{Miss} estimation is to use soft terms (deposited energies) and hard terms (hard track jet, lepton, etc), which induces high uncertainties from jet energy calibration, resulting to over 1% in 13 TeV W-boson production measurement [49]; Instead, the hadronic recoil (HR) strategy is used in low-mu analysis to achieve the extreme precision. It's an E_T^{Miss} building strategy that trickily avoids the hard jet calibration, specifically developed for single-vector-boson analyses. And the high resolution of hadronic recoil (HR) in low-mu condition is the substantial motivation to have the low-mu experiments (Chap.2).
The reconstruction and calibration of the HR is introduced in this chapter, based on the study done within the analysis group, documented in Ref. [6].

6.1 Hadronic Recoil Reconstruction

Predicted by pQCD, the transverse momentum of vector boson production is mainly originated by initial (gluon/quark) state radiation (ISR) in the transverse plane, i.e., described by the equation:

$$\vec{p}_T(W/Z) = \vec{p}_T^{\,\text{lepton1}} + \vec{p}_T^{\,\text{lepton2}} = -\sum \vec{p}_T^{\,\text{ISRquark,gluons}} \tag{6.1}$$

$p_T(W/Z)$ and p_T^{lepton} represent the transverse momentum of the W (or Z) boson and its decayed lepton pair. And $\sum \vec{p}_T^{\,\text{ISRquark,gluons}}$, the quantity which accounts for all transverse momenta of the partons from initial state radiation, is the definition of hadronic recoil, denoted as $\vec{u}$.

The transverse momentum of the neutrino, p_T^{ν} from W-boson decay is also available to be determined indirectly with the expression above, written as:

$$\vec{E}_T^{miss} := \vec{p}_T^{\,\nu} = -(\vec{u} + p_T^{l^{\pm}}), \tag{6.2}$$

where $\vec{E}_T^{miss}$ is the missing transverse energy, referring to the p_T^{ν} in W event.

Energies built from topo-cluster and tracks are essential in this estimation. The dedicated energy is calculated using Particle Flow Object (PFO) algorithms, moreover, with the region defined as that the $\Delta R = 0.2$ cone around the lepton direction is excluded from the calculation and replaced with randomly chosen PFO activity far away from the lepton, consequently the choice between muons or electrons does not bias the measurement.

6.1.1 Particle Flow Objects (PFOs)

The "particle flow" is an optimized track-cluster energy separation algorithm with strong suppression on pile-up tracks energies, therefore it suits perfectly in extracting all neutral and charged energies from the interaction, The structure is as follows:

1. Tracks are selected for which the measurement of the particle's momentum by the ID tracker is expected to be superior to that of the calorimeter.
2. Match the tracks with a single calorimeter cluster.
3. A filter is applied by matching the tracks to electrons (with $p_{\mathrm{T}} > 10$ GeV) and muons using medium electron or muon identification criteria.
4. If a match is found, the track is not further considered.

The expected energy in the calorimeter can then be computed based on the cluster position and the track momentum. It is relatively common that a single particle deposits energy in multiple clusters, such that additional clusters have to be added to the system to recover energy deposited in other clusters. At last, the expected energy in the calorimeter is subtracted cell-by-cell. If the remaining energy in the system is consistent with the expected noise of this particle's signal, the remnant cluster is removed.

The PFOs are thereby separated into 2 collections : the neutral PFOs (nPFOs), built from topo-clusters and not associated to charged particles; and the charged PFOs (cPFOs), built from tracks. These collections form 2 separate ensembles. Briefly,

$$PFO = (E_{calo} - E^{all}_{tracks})^{Neutral} + (E^{PV}_{tracks})^{Charged} \tag{6.3}$$

where E^{all}_{tracks} (E^{PV}_{tracks}) denote the energies from all tracks (primary vertex). Pile-up tracks of cPFOs are effectively removed [50].

6.1.2 Lepton energy removal and replacement

To remove any different performances of HR reconstruction between the electron and the muon channels, that could come from the muon energy deposits in the calorimeter, or to out-of-cone effects coming from the development of the electron shower, the PFOs that are located within a cone of radius $R = 0.2$ centered on the lepton axis are removed from the calculation of the recoil. However, the underlying events and un-matched pile-ups are removed meanwhile, leaving the recoil biased. In compensation, the removed cone is replaced by using another same-size cone of activity in the event, which is centered at the same η, but away from any lepton, and also from the hard activity, to avoid any energy bias. The ϕ component of the replacement cone axis is thus a random value which has to be at a minimal distance $\Delta R = 0.4$ of any lepton and of the uncorrected recoil. The replacement cone 2-vector is rotated to the removed lepton direction, and added vectorially to the recoil.

The leptons which are entering this energy veto are defined as follows (they should be within detector acceptance and well measured, that is $|\eta| < 2.4$ for muons, and $|\eta| < 2.47$ for electrons, excluding the crack) : muons have medium identification, $p_{\mathrm{T}} > 10$ GeV. Electrons have $Loose + CutBL$ LH identification, and $p_{\mathrm{T}} > 10$ GeV.

6.1.3 Hadronic recoil and variables

Lepton energy deposits are removed from the PFOs by a technique described in 6.1.2. The hadronic recoil in the transverse plane, $\vec{u_T}$, is then defined as the vector sum of all PFOs transverse momenta (summing both charged and neutral). The module of this 2-vector is simply termed u_T.

$$\vec{u}_T = \sum_i \vec{E}^{cPFO}_{T,i} + \sum_i \vec{E}^{nPFO}_{T,i} \tag{6.4}$$

Relevantly, the scalar sum of all PFOs, termed ΣE_T, is also an important observable which represents the full event activity. To have a better representation of the event activity with no inclusion of any signal jet, one can define the quantity $\Sigma \bar{E_T} = \Sigma E_T - u_T$, which is thus not as dependent on the boson dynamics as ΣE_T. The spectra of $\Sigma \bar{E_T}$ is illustrated in fig. 6.1, which is same for electron and muon channel after lepton cone removal.

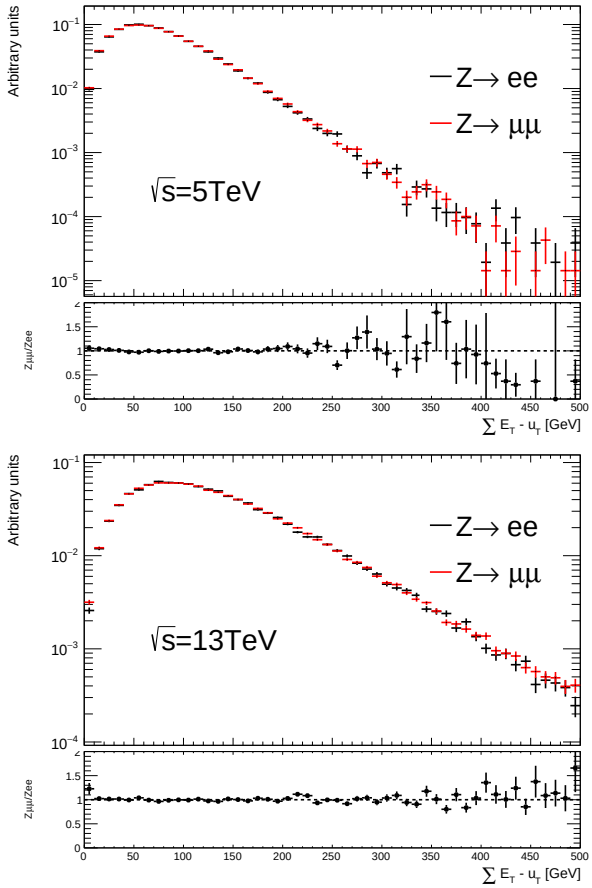

Figure 6.1: Distributions of $\sum \bar{E_T} = \sum E_T - u_T$ for $\sqrt{s}$ = 5 TeV (left) and $\sqrt{s}$ = 13 TeV (right) in $Z \rightarrow \ell\ell$ events. The distributions for the electron and muon channels are compared, showing a good compatibility.

Another two variables are defined in Z-decay channel to better describe the recoil performance, $u^{\ell}_{\perp}$ and $u^{\ell}_{||}$. The component of the recoil perpendicular to this axis, $u_{\perp} \equiv \frac{\vec{u_T} \cdot \vec{p^{\ell}_{\perp}}}{||\vec{p^{\ell}_{\perp}}||}$, gives a distribution

integrated over all events which should be centered at 0, and whose width is the measure of the recoil resolution along this direction. The component parallel to this axis, $u_{\parallel} \equiv \frac{\vec{u_T} \cdot \vec{p_T}}{||\vec{p_T}||}$, should ideally be, on average, the opposite of the boson p_{T}, in the approximation of small intrinsic k_T of the partons. However, due to a non-perfect scale of the recoil in track and cluster energies, the distribution of the bias, $b \equiv u_{\parallel} + p_{\mathrm{T}}$, is centered around a value a bit higher than 0. Fig. 6.3 gives distributions of $u_{\perp}$, $u_{\parallel}$ and the bias in the simulation and in the data after a typical $Z \rightarrow \mu^{+}\mu^{-}$ selection (without any calibration of the hadronic recoil).

A sketch of a boson decaying into leptons and the various projections of the recoil onto the boson axis is given fig. 6.2 for clarity. Fig. 6.3 shows the data and simulated spectra of defined recoil variables in $Z \rightarrow \mu\mu$ channel. The mis-modelling is significant in bias and resolution before calibration.

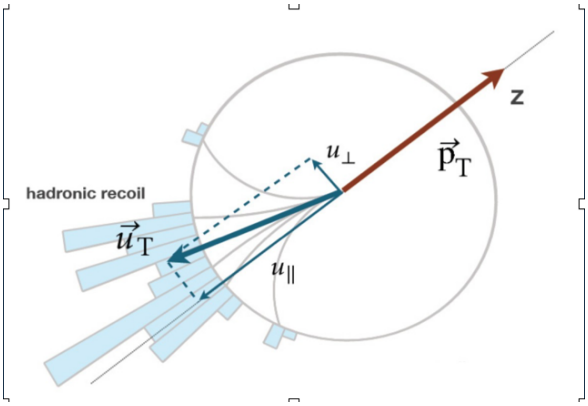

Figure 6.2: Sketch of a Z event and of the projections of the hadronic recoil onto its decay axis.

6.2 Hadronic recoil calibration

To have an accurate and consistent hadronic recoil in data and simulation, the calibration is studied with low-pile-up data in-situ. The calibration uses Z boson events as candidates since the transverse momentum of the Z boson can be determined via the hadronic recoil measurement, but also via the precise measurement of the 4-vectors of its decay leptons, the resolution in the latter case is expected to be one order of magnitude better than in the former case. Benefiting from the experiences of [51], the calibration procedure consists of three steps: the modelling of $\Sigma\bar{E_T}$; the recoil direction correction; the resolution and response correction.

6.2.1 Modeling of $\Sigma\bar{E_T}$

The underlying events activity, $\Sigma\bar{E_T}$, direct affects the recoil resolution, $\sigma(u_{\perp})$. The values of the recoil resolution $\sigma(u_{\perp})$ are obtained from Gaussian fits to the $u_{\perp}$ distributions in each $\sum \bar{E_T}$ bin. The summary figure 6.4 shows the resolution of $u_{\perp}$ as a function of $\sum \bar{E_T}$. $\sigma(u_{\perp})$ get worse at larger $\sum \bar{E_T}$ thus close $\sum \bar{E_T}$ performance is essential for resolution correction.

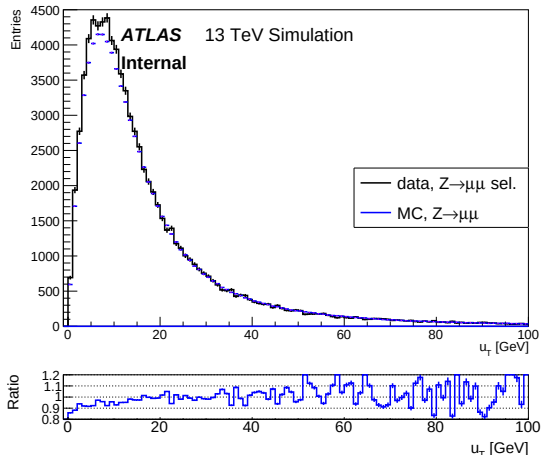

(a) u_T.

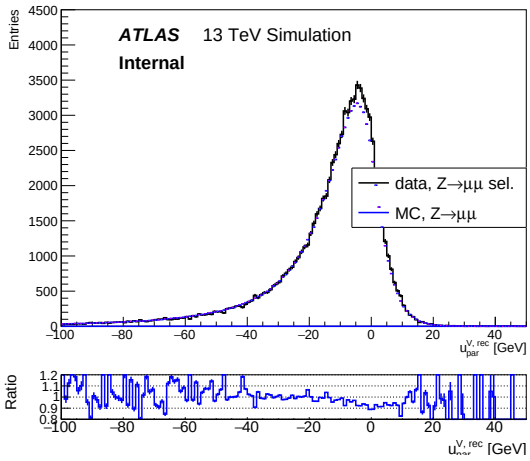

(b) $u_{\parallel}$.

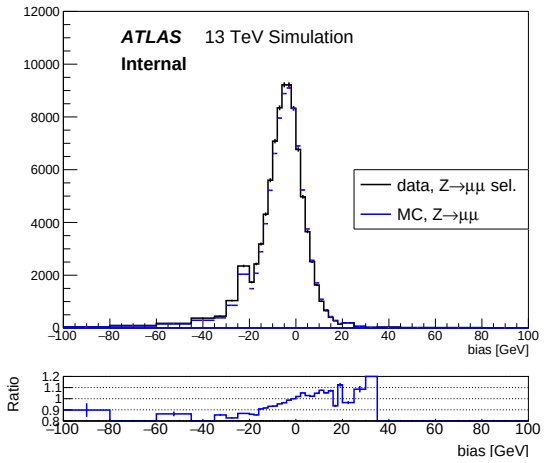

(c) bias.

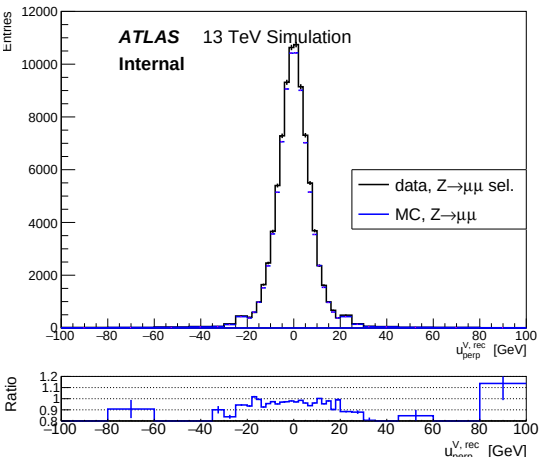

(d) $u_{\perp}$.

Figure 6.3: Recoil distributions in the data and in the simulation, after a $Z \rightarrow \mu\mu$ selection at 13 TeV.

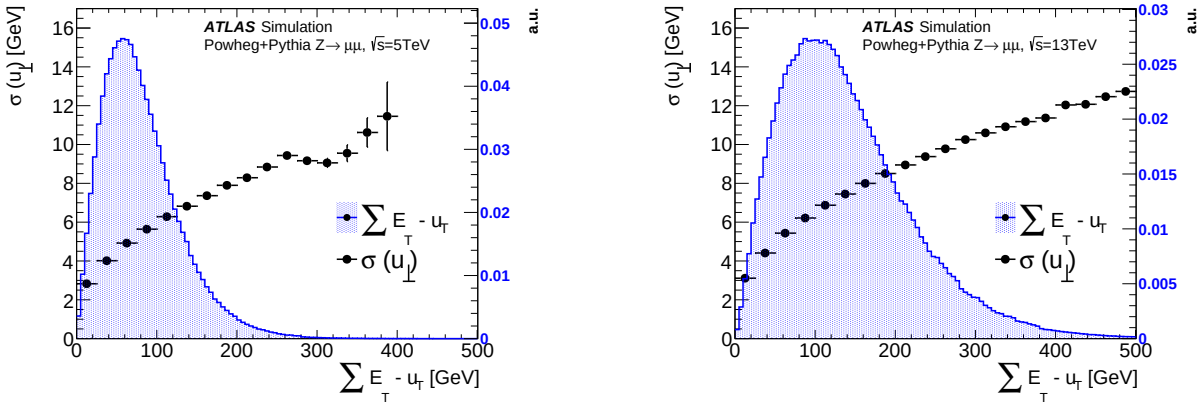

(a) 5 TeV.

(b) 13 TeV.

Figure 6.4: $\sigma(u_\perp)$ as a function of $\Sigma\vec{E}_T$ in $Z \to \mu\mu$ simulated events.

In addition, since Z and W events have different underlying activities and different p_T^V, the transfer of calibration corrections from Z to W requires to obtain the calibration as a function of $\sum \vec{E}_T$ and p_T^V. Therefore a procedure to model the event activity and its correlation with p_T^V is in need. For the Z event, this modeling is proceeded with a 2D reweighting of the ($\Sigma\vec{E}_T$ $p_T^{\ell\ell}$) distribution to the data, defined as :

$$w_{2D}^{Z}(\Sigma\vec{E}_T, p_T^{\ell\ell}) = \frac{h^{data,Z}(\Sigma\vec{E}_T, p_T^{\ell\ell})}{h^{MC,Z}(\Sigma\vec{E}_T, p_T^{\ell\ell})}, \tag{6.5}$$

where h is the normalized 2-dimensional distribution of ($\Sigma\vec{E}_T$, $p_T^{\ell\ell}$). For the W, there is an additional weight to the W signal Monte-Carlo using $p_{\mathrm{T}}^{\mathrm{true}}$ instead of $p_T^{\ell\ell}$, (namely, $w_{2D}^{Z}(\Sigma\vec{E}_T, p_{\mathrm{T}}^{\mathrm{true}})$). This procedure is unfortunately modifying the true p_{T} spectrum of the W boson. For modeling purposes, it is necessary to recover the initial spectrum, by performing a 1D reweighting in $p_{\mathrm{T}}^{\mathrm{true}}$. This additional weight is defined, after the 2D-reweighting from the Z, as :

$$w_{1D}^{W^\pm}(p_{\mathrm{T}}^{\mathrm{true}}) = \frac{h^{MC,W^\pm,mod}(p_{\mathrm{T}}^{\mathrm{true}})}{h^{MC,W^\pm,orig}(p_{\mathrm{T}}^{\mathrm{true}})}, \tag{6.6}$$

h this time being the original (denominator) or modified (numerator) $p_{\mathrm{T}}^{\mathrm{true}}$ distribution in the W simulated events. The total weight to be applied to $W^\pm$ events is then the product:

$$w_{2D}^{Z}(\Sigma\vec{E}_T, p_{\mathrm{T}}^{\mathrm{true}}) \times w_{1D}^{W^\pm}(p_{\mathrm{T}}^{\mathrm{true}}) \tag{6.7}$$

Fig. 6.5 illustrates the good closure in $p_{\mathrm{T}}^{\mathrm{true}}$ after performing this 2D+1D reweighting.

Illustrated in fig. 6.6, the correlation between $\Sigma\vec{E}_T$ and u_T gets closer to the data in MC.

6.2.2 u_X and u_Y correction

Due to the non-perfect detector simulation in beam crossing angle, calorimeter uniformities, etc, the direction of recoil, $\phi(u_T)$ is not well modelled and the bias is proportional to $\Sigma\vec{E}_T$ This can be handled

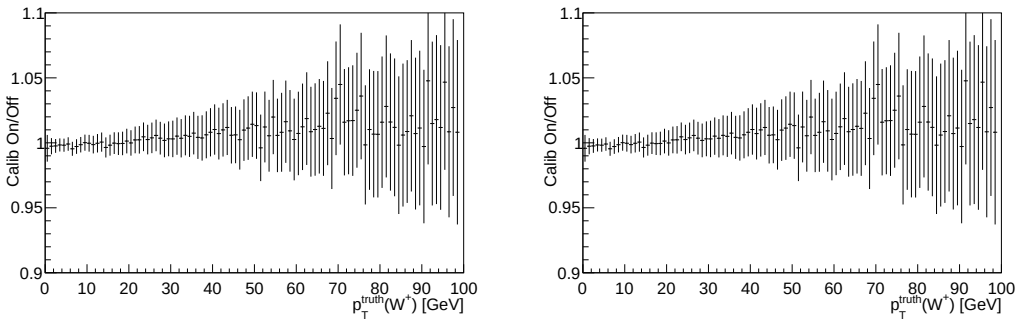

(a) W^+.

(b) W^-.

Figure 6.5: Ratio of $p_{\mathrm{T}}^{\mathrm{true}}$ distributions for the W process at 13 TeV, before over after correction of $\Sigma\bar{E_T}$.

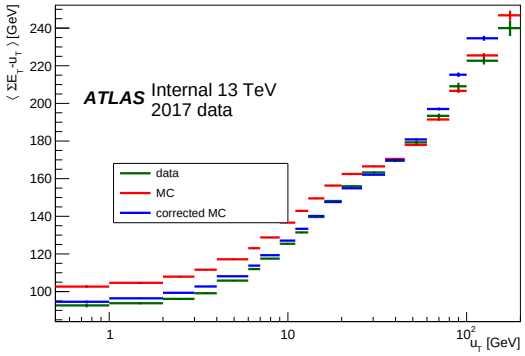

(a) W^+, 13 TeV.

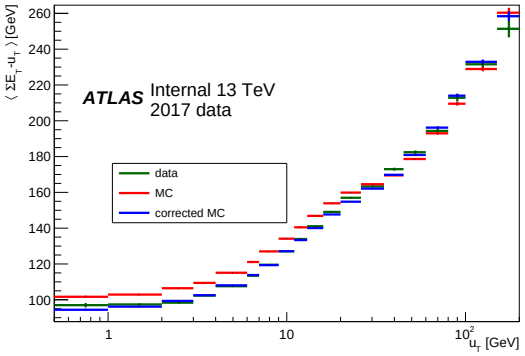

(b) W^-, 13 TeV.

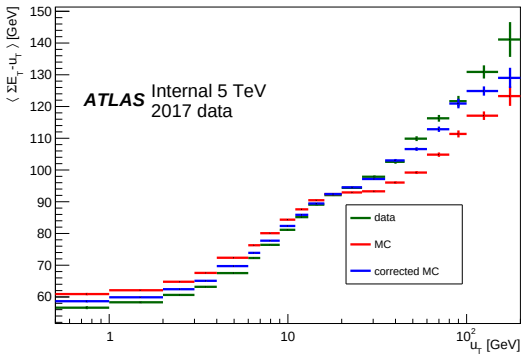

(c) W^+, 5 TeV.

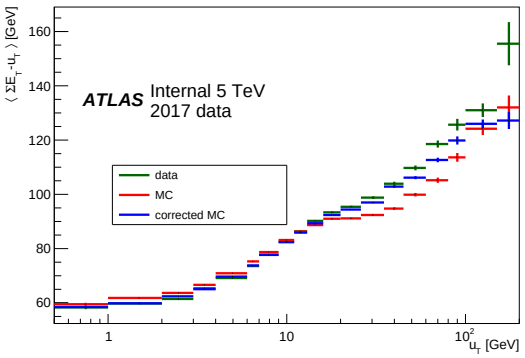

(d) W^-, 5 TeV.

Figure 6.6: Average value of $\Sigma\bar{E_T}$ as a function of u_T in $W \rightarrow \mu\nu$ events. A few backgrounds are missing in the MC curves ($Z \rightarrow \mu\mu$ and multijet).

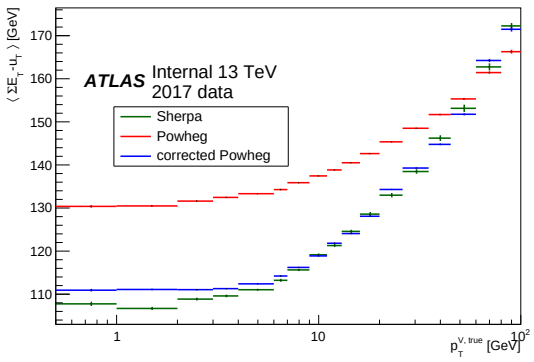

(a) W^+, 13 TeV.

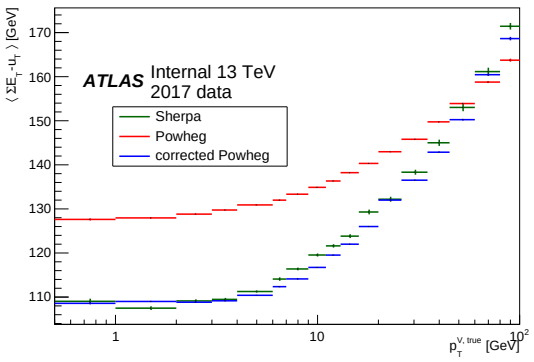

(b) W^-, 13 TeV.

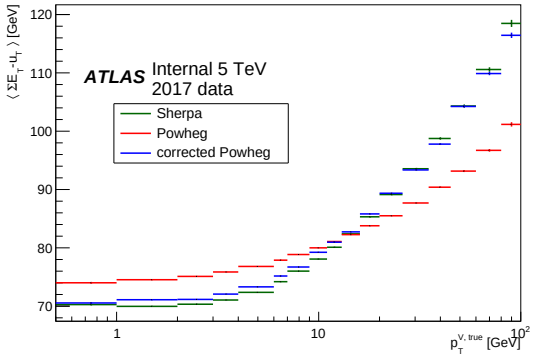

(c) W^+, 5 TeV.

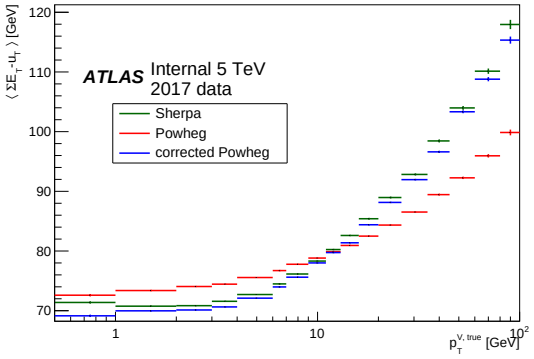

(d) W^-, 5 TeV.

Figure 6.7: Average value of $\Sigma\bar{E_T}$ as a function of $p_{\mathrm{T}}^{\mathrm{true}}$ in simulated $W \to \mu\nu$ events.

with corrections onto X and Y components of the recoil, u_X and u_Y. The differences between the mean values of u_X and u_Y are linearly fitted as a function of $\Sigma\bar{E_T}$ written as:

$$u_X^{MC,corr} = u_X^{MC} + [(\langle u_X^{data}\rangle - \langle u_X^{MC}\rangle)(\Sigma\bar{E_T})] u_Y^{MC,corr} = u_Y^{MC} + [(\langle u_Y^{data}\rangle - \langle u_Y^{MC}\rangle)(\Sigma\bar{E_T})] \quad (6.8)$$

Fig. 6.8 shows how this correction is obtained, and fig. 6.9 shows its impact on $\phi(u_T)$. After correction, data and simulation agrees within statistical uncertainty.

6.2.3 Resolution and response corrections

With significantly improved underlying activity and direction of recoil, the energy resolution and response correction is practical. The $u_\perp$ distribution is, in each bin of (ΣE_T, boson p_{T}), a gaussian distribution centered at 0, gives the resolution of $u_\perp$. The bias ($u_\parallel + p_T^V$) distribution giving the resolution of $u_\parallel$, however, does not center at 0. Therefore they're corrected separately.

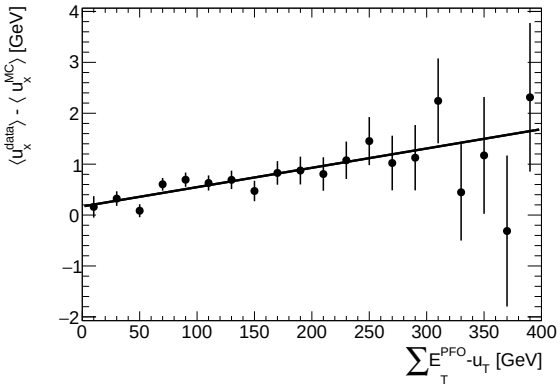

(a) u_X, 13 TeV.

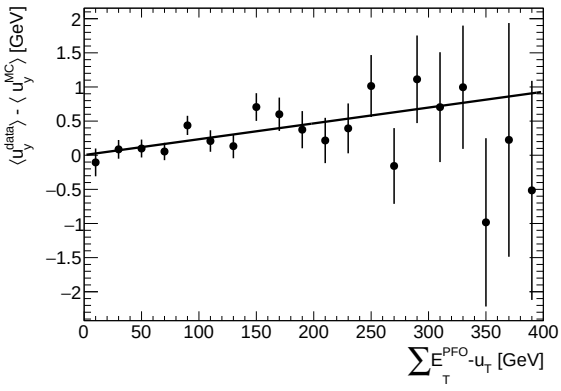

(b) u_Y, 13 TeV.

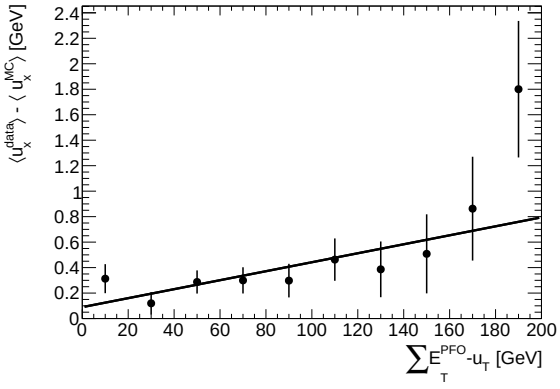

(c) u_X, 5 TeV.

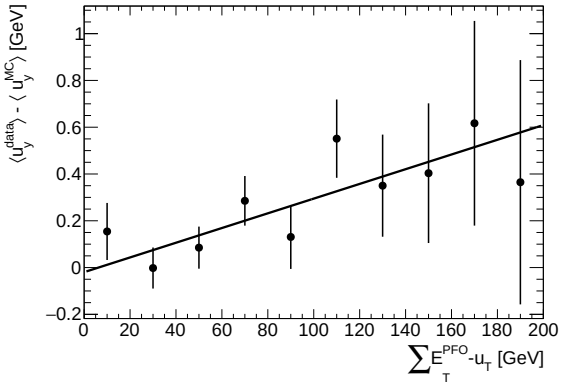

(d) u_Y, 5 TeV.

Figure 6.8: Difference in u_X and u_Y between the data and the simulation as a function of $\Sigma\bar{E_T}$

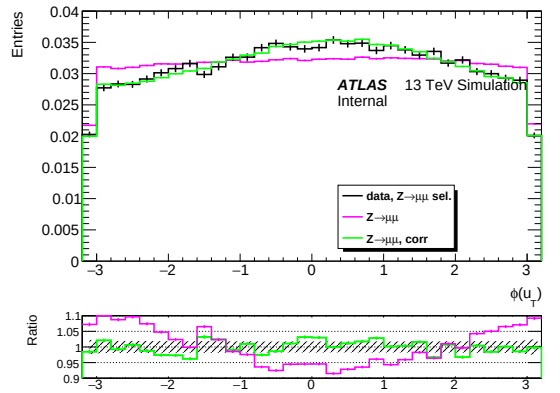

(a) $\phi(u_T)$, 13 TeV.

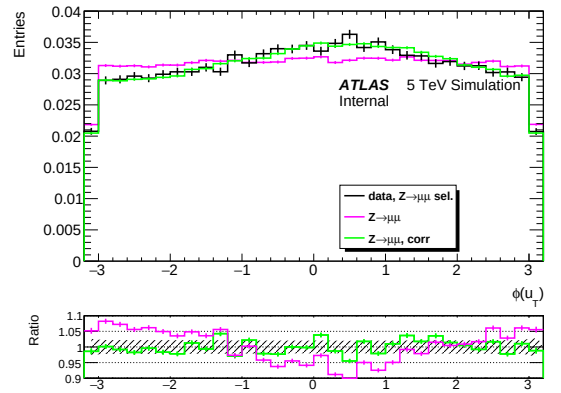

(b) $\phi(u_T)$, 5 TeV.

Figure 6.9: $\phi(u_T)$ at 5 and 13 TeV, for the data and the simulation before and after u_X and u_Y correction.

Regarding the statistical uncertainty and requirement of p_T^V measurement, binning scan is taken to find the optimal bin width for the residual corrections. The correction for $u_\parallel$ is:

$$u_\perp^{corr} = u_\perp \times r,$$

where $r \equiv \frac{\sigma(u_\perp)^{data}}{\sigma(u_\perp)^{MC}}$ is obtained by fits to the resolution in the data and in the simulation as a function of $\Sigma\bar{E_T}$ in bins of p_{T}^Z. The fit function is of the form $f(\Sigma\bar{E_T}) = a + \sqrt{b \times \Sigma\bar{E_T}}$. Similarly for the response correction :

$$b = u_\parallel + p_{\mathrm{T}}^V$$

$$u_\parallel^{corr} = \langle u_\parallel^{data} \rangle + \langle b^{data} - b^{MC} \rangle + (u_\parallel - \langle u_\parallel^{data} \rangle) \times r$$

Here, $\langle u_\parallel^{data} \rangle$ is fitted in bins of $\Sigma\bar{E_T}$ of width 10 GeV, as a function of p_{T}^Z, with a 1-degree polynomial. The quantity $\langle b^{data} - b^{MC} \rangle$ is fitted in the exact same way.

Fig. 6.10 shows the bias and the $u_\perp$ distributions before and after the calibration is applied to the simulated events, together with the distributions obtained in the data. Thanks to the low-pile-up conditions that the resolution is dominated by underlying events rather than pile-up, and that the resolution is excellent and compatible in data and MC after correction, otherwise the dependence of pile-up will degrade it.

6.2.4 Uncertainties of the recoil calibration

The uncertainties related to the calibration mostly come from data statistics in the resolution and response corrections, and from the small non-closure due to the extrapolation from the Z to the W.

For the resolution and response correction, in each of the p_T^V bins, the fit of resolution function gives uncorrelated variations of uncertainties regarding to the parameters. In addition, the Z boson to W boson extrapolation uncertainty needs to be account because he resolution smearing and response correction are both obtained in Z events and subsequently applied to W events. Following the method in [52], the difference of W and Z boson spectra after 2D ($\Sigma\bar{E_T}$, p_T^V) reweighting and FSR photon correction is estimated to be the recoil in-situ difference between W and Z channel, hence given as correlated uncertainty of a function of $p_{\mathrm{T}}^{\mathrm{true}}$.

The non-closure from the extrapolation from the Z to the W is obtained doing a closure test using Sherpa Monte-Carlo events as pseudo-data because Sherpa has relatively closest underlying activities to data. Reweighting 2D-coefficients for Powheg are obtained as in the usual procedure, and applied to the W events. Any remaining deviation from unity in the ratio of Sherpa to Powheg for the W 2D distributions ($\Sigma\bar{E_T}$, $p_{\mathrm{T}}^{\mathrm{true}}$) is indicative of a non-closure that has to be corrected for, applying this ratio of distributions as additional reweighting. Therefore, this additional weight is taken as a correlated systematic variation.

In total, there are 5 correlated uncertainties and 110~130 uncorrelated uncertainties in hadronic recoil calibration to cover the data and simulation discrepancy.

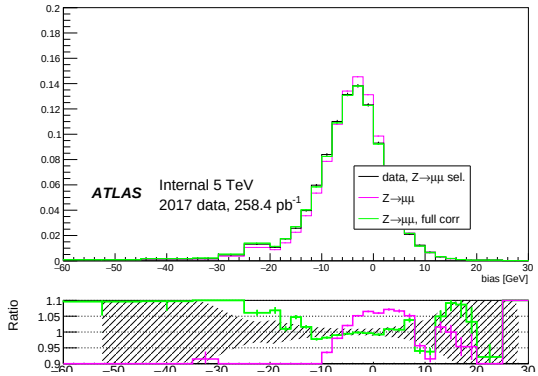

(a) bias, 5 TeV, 2017 data and calibration.

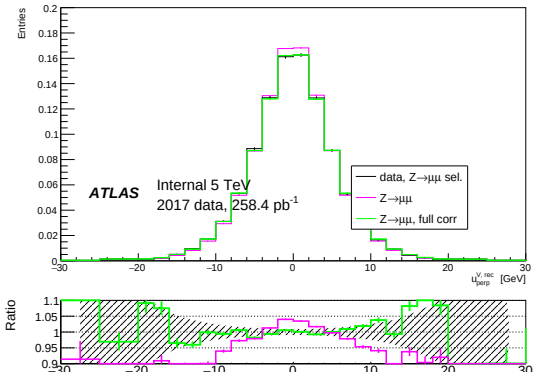

(b) $u_\perp$, 5 TeV, 2017 data and calibration.

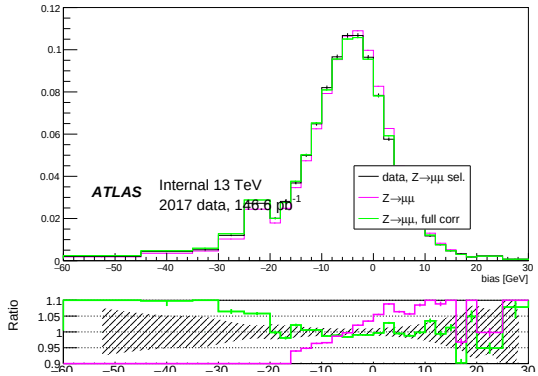

(c) bias, 13 TeV, 2017 data and calibration.

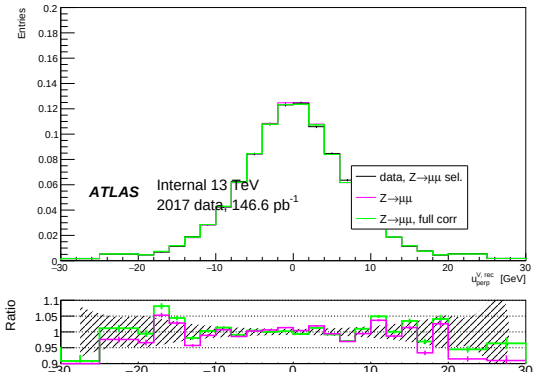

(d) $u_\perp$, 13 TeV, 2017 data and calibration.

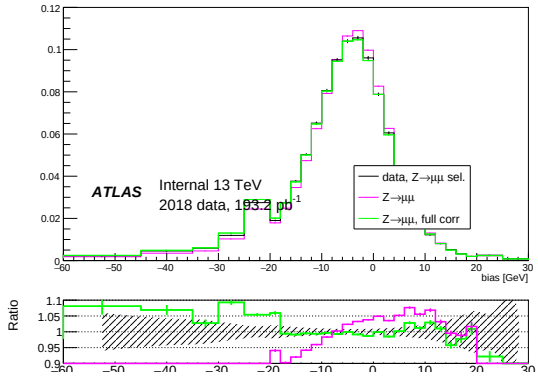

(e) bias, 13 TeV, 2018 data and calibration.

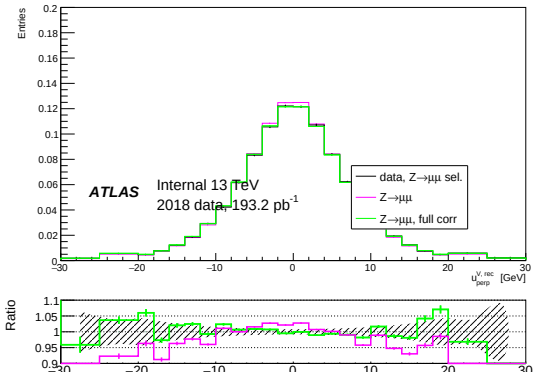

(f) $u_\perp$, 13 TeV, 2018 data and calibration.

Figure 6.10: Data and simulated distribution of $u_\perp$ and of the bias, before and after applying the calibration, in $Z \to \mu\mu$ events.

7 The W signal and background estimation

The W-boson event is reconstructed from one prompt lepton object and one missing transverse energy object. A well-defined selection on objects and events can effectively reject the backgrounds, purify the signal, thus improve the precision of measurements. The definition of this signal phase space is based on the detector capability as well as the performance of Monte Carlo simulation, one of the most essential tools in analyses, providing accurate theoretical prediction to the kinematics and properties of target process.

7.1 Monte Carlo samples in the analyses

Fully simulated and reconstructed Monte Carlo samples are used to model the signal and background processes. The GEANT4 based simulation [53] provides the complete simulation of the ATLAS detector. All MC samples uses settings specific to the special data run conditions, i.e. specifically the pileup overlay. Given that the pileup distribution is already adjusted as to the dataset, no further pile-up-reweighting is performed.

The main signal event samples for W and Z leptonic production are generated using the Powheg event generator [54–57] using the CT10 PDF at NLO, interfaced to Pythia8 [58] using the AZNLO tune [59] for parton showers. Powheg+Pythia8samples are interfaced to Photos++ [60] to simulate the QED effect of final state radiation.

For W and Z processes, the samples are normalized to NNLO calculations performed using the DYTURBO program, an optimised version of DYNNLO [61, 62] using the MMHT2014nnlo PDF set [63]. The numerical values are taken from the corresponding ATLAS publications of the 2015 data at 13 TeV [64] and 5.02 TeV [65]. The uncertainties on those cross-sections arise from the choice of PDF set and PDF set internal uncertainties ($\sim 3-4\%$), from factorization and renormalisation scale dependence ($< 1\%$), and the strong coupling constant α_s ($\sim 1-2\%$). A conservative total uncertainty of 5% is taken as an uncertainty on any event count predictions normalized using these cross-sections, e.g. for use of subtraction of electroweak backgrounds.

Backgrounds from top-quark pair-production $t\bar{t}$ as well as single-top production (Wt, t-channel, s-channel) are generated with Powheg+Pythia8. Various combinations of di-bosons $VV, V = W, Z$ are generated with Sherpa [66] in all decay channels with at least one real lepton in the final state.

7.2 Object definitions and event selection

Candidate events pass the criteria must have at least one primary vertex reconstructed from at least three tracks with p_T larger than 400 MeV and to fire a trigger which requires at least one muon or loose-likelihood identificated electron candidate with transverse momentum above 15 GeV ($HLT_e15_lhloose_nod0_L1EM12$) or 14 GeV ($HLT_mu14$) respectively. Then the good-run-list (GRL) requirement described in Chap. 3 is used to guarantee prompt detecting condition during collisions. After these pre-selections, leptons of candidate events need to satisfy additional selections to get further purified.

Electron candidates, reconstructed from the ID and EM calorimeter, are required to have p_T > 25 GeV and $|\eta|$ < 2.47. Candidates within the barrel-end-cap crack (1.37 < $|\eta|$ < 1.52) are rejected. In addition, medium likelihood identification, "ptvarcone20/pT < 0.1" isolation and match-to-trigger requirements are applied. Muon candidates reconstructed with ID and MS must have p_T > 25 GeV and $|\eta|$ < 2.4, and pass the medium identification, "ptvarcone20/pT < 0.1" isolation and trigger-matching.

Benefiting from the new "insertable B-Layer" (IBL), new track parameters, the transverse impact parameter, d_0, and the longitudinal impact parameter, z_0, are introduced to improve the ID track resolution, and set extra track-to-vertex-association (TTVA) requirements on electron (muon) to qualify the association between the leptonic track and primary vertex [67]: $|d_0|/\sigma_{d_0} < 5(3)$, $|z_0 sin\theta| < 0.5$, θ denoting the track polar angle. The efficiency of such selection is covered by electron identification or muon TTVA efficiency.

Events with W-boson candidate are selected by requiring exactly one electron or muon. The neutrinos are constructed as missing transverse energy objects ($\vec{E}_T^{miss}$). And the transverse mass (m_T) of the W boson candidate is defined as:

$$\vec{E}_T^{miss} = -(\vec{u}_T + \vec{p}_T^{\,l}) \tag{7.1}$$

$$m_T = \sqrt{2p_T^l E_T^{miss}(1 - cos\Delta\phi_{l,E_T^{miss}})} \tag{7.2}$$

The requirement of E_T^{miss} > 25 GeV and E_T^{miss} > 50 GeV is adequate to remove most of the Z-boson and multi-jet backgrounds in signal phase space. Table 7.1 summarizes all selections applied to objects and W-boson event.

7.3 Correction for simulation

The discrepancy between kinematics in prediction and data contributes to the majority of systematical uncertainties in W-boson measurements. This mis-modelling of simulation consists of two aspects of effects, in the detection and the theoretical modellings.

The following types of corrections are included, accounting for detector effect:

- electron energy calibrations, in particular energy scale and resolution corrections;

Preselection		
GRL	Pass Good Run List	
Vertex	Primary Vertex Number > 1	
Object Selection		
	Electron	Muon
p_T	> 25 GeV	> 25 GeV
η	$\|\eta\| < 1.37$ or $1.52 < \|\eta\| < 2.47$	$\|\eta\| < 2.4$
Identification	MediumLH	Medium
Isolation	$ptvarcone^{20}/p_T < 0.1$	$ptvarcone^{20}/p_T < 0.1$
Trigger	$HLT_e15_lhloose_nod0_L1EM12$	HLT_mu14
Event Selection		
N leptons	Exactly 1 lepton	
E_T^{miss}	> 25 GeV, reconstructed from hadronic recoil	
m_T	> 50 GeV	

Table 7.1: Overview of the W-boson event selection at detector level used in low-pile-up measurements.

- electron selection efficiency corrections of reconstruction, identification, isolation, trigger;
- muon momentum scale and resolution corrections;
- muon selection efficiency corrections of reconstruction, TTVA, isolation, trigger;
- underlying activity correction and hadronic recoil calibration.

All of them have been discussed in the corresponding chapters of this thesis.

The physical mis-modellings, denoting the imperfect predictions in the interaction and ISR/FSR, are usually corrected with reweighting procedure at truth level. The Drell-Yan cross-section can be decomposed by factorising the dynamic of the boson production and the kinematic of the boson decay. An approximate decomposition is given by:

$$\frac{d\sigma}{dp_1 dp_2} = [\frac{d\sigma(M)}{dM}][\frac{d\sigma(y)}{dy}][\frac{d\sigma(p_T,y)}{dp_T dy}(\frac{d\sigma(y)}{dy})^{-1}][(1+cos^2\theta)+\sum_{i=0}^{7}A_i(p_T,y)P_i(cos\theta,\phi)] \quad (7.3)$$

Each of the factors in Eq. 7.3 is related to a theoretical correction for cross-section predicted at LO. They're:

- $\frac{d\sigma(M)}{dM}$, according to the Breit-Wigner parameterisation, depends on boson mass M_V and mass width Γ_V:

$$\frac{d\sigma}{dm} \propto \frac{m^2}{(m^2-m_V^2)^2+m^4\Gamma_V^2/m_V^2}, \quad (7.4)$$

  which obeys the SM relation, $\Gamma_W \propto m_W^3$. This equation is the baseline of W boson mass measurement as it describes how the distributions change along the mass, also provides correction to simulations generated at different invariant mass of W boson.

- $\frac{d\sigma(y)}{dy}$, estimated in eq. 2.18, is based on PDFs and fixed order perturbative QCD predictions up to NNLO.

- $\frac{d\sigma(p_T,y)}{dp_T dy}$ denoting the boson momentum at given rapidity, is predicted with parton shower and analytic resummation.
- The angular coefficient A_i which reflects the boson polarization state is predicted from NNLO pQCD [32].

Excluding the Breit-Wigner parameterisation specifically used in W-mass study, the other three physical corrections are introduced to all W-boson measurements. The angular coefficient reweighting is currently calculated with Powheg NLO but will be replaced with NNLO predictions using DYTRUBO. The generation of signal samples used the CT10NLO PDF set, but corrected to CT14NNLO. The W-boson transverse momentum will be measured, result of which as the input of correction to other measurements. In addition, there are QED corrections on final state emissions of photons and fermions. This correction is performed by the Photos [60], interfaced with Powheg+Pythia during generation.

7.3.1 Electroweak and top backgrounds

The sources of backgrounds have been well investigated and understood in previous W-boson experiments and analyses. Two categories of backgrounds are defined that contaminate the W events with leptonic decay: the electroweak (single and di-boson processes) and top-quark backgrounds, obtained from the appropriate MC simulated samples; the multi-jet (MJ) background, estimated with a data-driven method.

The EW backgrounds include single boson productions, $W^{\pm} \rightarrow \tau^{\pm}\nu$, $Z \rightarrow ee, \mu\mu, \tau\tau$, and the di-boson productions, WW, WZ, ZZ. In particular, the Z-boson background from events where one good lepton and one lepton fail the requirement, reconstructed as missing energy can be suppressed by relaxing the lepton selection and exploiting forward muons when reconstructing the hadronic recoil. Events with top quarks has similar signature to W events, especially the $t \rightarrow Wb$ decay, but the contribution to analysis is relatively ignorable due to its low production cross-section.

The fraction of normalized simulated signal and backgrounds to data events are displayed in Tab. 7.2 and 7.3. At both collision energies, the EW backgrounds are led by the Z-boson decay and $W \rightarrow \tau\nu$.

	$W^+ \rightarrow e^+\nu$	$W^- \rightarrow e^-\nu$	$W^+ \rightarrow \mu^+\nu$	$W^- \rightarrow \mu^-\nu$
$W \rightarrow e\nu$	93.48	92.32	–	–
$W \rightarrow \mu\nu$	–	–	93.9	93.1
Z	1.29	1.60	4.09	4.80
top	0.07	0.10	0.07	0.09
Diboson	0.06	0.18	0.06	0.17
$W \rightarrow \tau\nu$	1.67	1.85	1.46	1.51

Table 7.2: Electroweak background contributions estimated from simulation. Expectations are expressed as a percentage of the selected data events coming from the sources listed in the table and passing signal selection in each channel at $\sqrt{s}$ = 13 TeV.

	$W^+ \to e^+\nu$	$W^- \to e^-\nu$	$W^+ \to \mu^+\nu$	$W^- \to \mu^-\nu$
$W \to e\nu$	94.51	92.96	–	–
$W \to \mu\nu$	–	–	95.41	93.07
Z	0.76	1.24	2.98	4.18
top	0.23	0.38	0.23	0.37
Diboson	0.08	0.12	0.08	0.17
$W \to \tau\nu$	1.60	1.79	1.58	2.60

Table 7.3: Electroweak background contributions estimated from simulation. Expectations are expressed as a percentage of the selected data events coming from the sources listed in the table and passing signal selection in each channel at $\sqrt{s}$ = 5 TeV.

7.4 Multi-jets background estimation

The MJ background has major contributions from leptons produced in semi-leptonic decays of heavy quarks, in-flight pion decays, photon conversions, etc. Although this type of background processes is effectively rejected by the isolation selection, E_T^{miss} and m_{T} requirement, due to the large production cross-section, and E_T^{miss} generated through energy mis-measurement in the event, MJ still dominate the backgrounds in high-pile-up W-boson measurements, contributing to over 5% of data events. And because of the difficulties in the precise simulation of these processes, data-driven techniques are used for estimation of MJ background with a method similar to the one described in Ref. [68].

7.4.1 General procedure

The key assumption to this data-driven estimation is that the profiles of MJ kinematics are relatively stable regardless of lepton isolation. By relaxing or inverting the lepton isolation selection, the signal phase space are thus enriched with multi-jet backgrounds, named control region(CR), from which the MJ distribution can be derived. These kinematics spectra are expected to be similar in profile to those in signal region following the assumption,

The event number or fraction of MJ in signal region is evaluated from another template, named fit region (FR), obtained by keeping the signal isolation but relaxing the E_T^{miss} and m_{T} cuts. The FR is therefore dominated by jets at low E_T^{miss}, low m_{T} or low p_T^{lep}, Fitting the MJ profile derived above to data and simulation in there jet-dominant area will provide the event number of MJ background in the fit region, which can be ultimately normalized to signal region when the relaxed cuts are re-applied. The details of the whole procedure are discussed in this section.

First four phase-space regions are defined:

- signal region (SR): isolated leptons, requirements on p_T^{lep}, MET and m_{T};
- fit region (FR): isolated leptons, relaxed kinematic requirements: $E_{\mathrm{T}}^{\mathrm{miss}} > 0$ GeV, $m_{\mathrm{T}} > 0$ GeV;
- control region 1 (CR1): anti-isolated leptons with FR kinematic requirements;
- control region 2 (CR2): anti-isolated leptons with SR kinematic requirements.

Events in these regions are required to pass all non-kinematic selection criteria. The relaxed requirements on E_T^{miss} and m_{T} in FR and CR1 are necessary to have a sufficient number of events for performing the fits to kinematic distributions. The control plots without MJ background in SR and FR are illustrated in Fig. 7.1, where the discrepancy between data and simulation are mostly contributed by MJ. The huge disagreement in FR denotes the creation of jet-enriched area with relaxing the E_T^{miss} and m_{T} selection. Therefore next is to gain the estimated profile of MJ to perform the fit between data, simulation and MJ in this area.

If invert the leptonic isolation, i.e. require each lepton object is accompanied with addition tracks, the MJ in FR and SR are thereby further enhanced, and the new regions are CR1 and CR2 respectively. Fig. 7.2 illustrates the control plot of CR1 and CR2, and both are completely led by the "missing" MJ. The EW fraction is almost negligible, so the MJ distribution is relatively precisely evaluated as the

difference between data and EW simulations. With the assumption in the beginning, the profile of MJ distribution in CR1 is assumed the same to that in FR, and the profile of MJ distribution in CR2 is assumed the same to that in SR. Then the fitting is practiced in FR with MJ profiles derived in CR1.

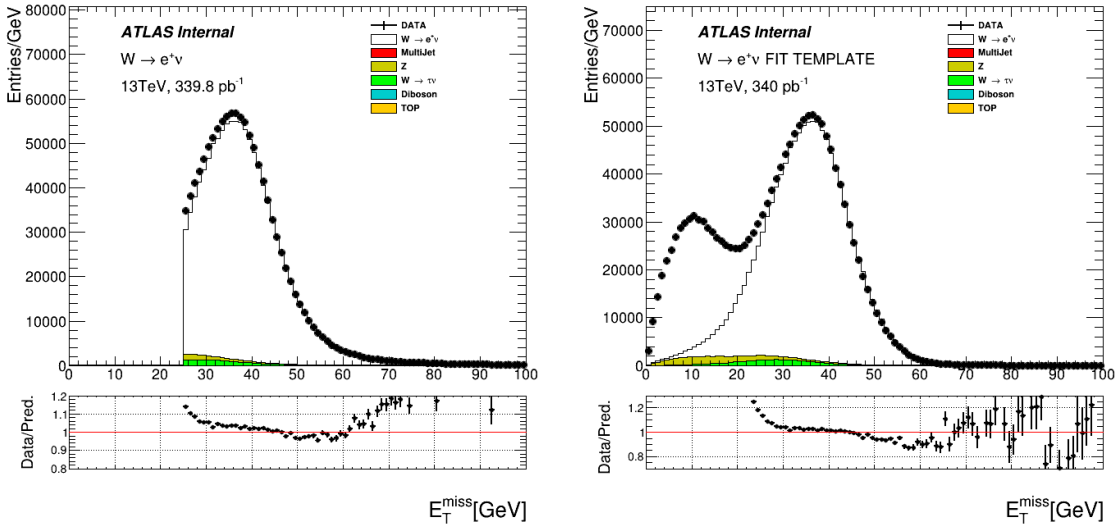

Figure 7.1: Control plot of E_T^{miss} spectrum using low-pile-up datasets at $\sqrt{s}$ = 13 TeV with $W- > e^+\nu$ selection in signal region (left) and fit region (right) without multi-jet background).

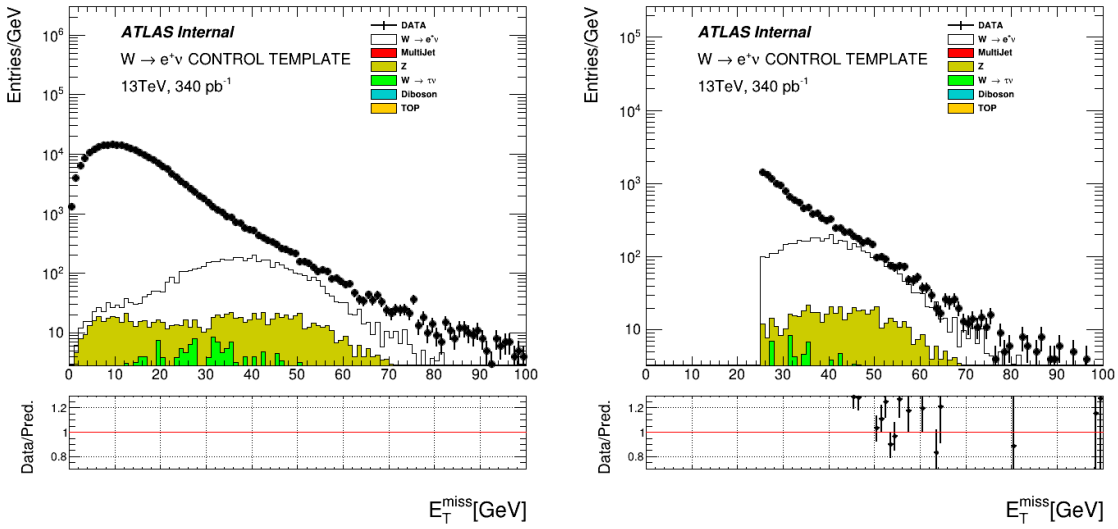

Figure 7.2: Control plot of E_T^{miss} spectrum using low-pile-up datasets at $\sqrt{s}$ = 13 TeV with $W- > e^+\nu$ selection in control region 1 (left) and control region 2 (right) without multi-jet background).

The procedure of evaluating the number of MJ background using a template from inverted-isolation region is as following:

- The number (N_{MJ}^{CR1}) and kinematic distributions (H_{MJ}^{CR1}) of MJ background is derived in jet-dominated invert-isolated region,CR1:

$$N_{\mathrm{MJ}}^{CR1} = N_{\mathrm{data}}^{\mathrm{CR1}} - N_{\mathrm{EW}}^{\mathrm{CR1}} H_{\mathrm{MJ}}^{CR1} = H_{\mathrm{data}}^{\mathrm{CR1}} - H_{\mathrm{EW}}^{\mathrm{CR1}} \tag{7.5}$$

  where H^{CR1} denotes one of the distributions of kinematics used in fitting, usually p_T^{lep}, E_T^{miss} and m_{T}. The difference between data and normalized MC distribution is estimated to account for the multi-jet contribution.

- The fitting is performed in the cut-relaxed yet isolated region, FR. Fig. 7.3 gives an example of the control plot of FR after fitting the MJ profiles derived in CR1 (Fig. 7.3(a)) to the data and EW (Fig. 7.3(b)). The form is:

$$H_{\mathrm{data}}^{\mathrm{FR}} = \alpha \cdot H_{\mathrm{EW}}^{\mathrm{FR}} + T \cdot H_{\mathrm{MJ}}^{\mathrm{CR1}}. \tag{7.6}$$

  The fitting parameter T gives the estimated number of MJ contribution in FR: $N_{MJ}^{FR} \approx T \cdot N_{\mathrm{MJ}}^{CR1}$.

- The N_{MJ}^{FR} are then normalized from fit region to signal region, with the normalization factor ε defined with approaching like:

$$\varepsilon = \frac{N_{\mathrm{MJ}}^{\mathrm{SR}}}{N_{\mathrm{MJ}}^{\mathrm{FR}}} \approx \frac{N_{\mathrm{MJ}}^{\mathrm{CR2}}}{N_{\mathrm{MJ}}^{\mathrm{CR1}}} = \frac{N_{\mathrm{data}}^{\mathrm{CR2}} - N_{\mathrm{EW}}^{\mathrm{CR2}}}{N_{\mathrm{data}}^{\mathrm{CR1}} - N_{\mathrm{EW}}^{\mathrm{CR1}}}, \tag{7.7}$$

  so that one acquire the number of MJ events in signal region:

$$N_{MJ}^{SR} = \varepsilon \cdot N_{MJ}^{FR} \tag{7.8}$$

The isolation-related bias is introduced in the profile-derivation and the normalization factor when the MJ's behavior in isolated regions, SR and FR, are approximated to that in the anti-isolated regions CR2 and CR1 in Eq. 7.6 and 7.7. To recover such bias, a linear extrapolation along isolation is performed by duplicating the estimation in different isolation slices and generally approaching signal isolation. This procedure addresses the following points:

- The MJ template selection is not arbitrary any more, in fact ideally the MJ estimate coming from the extrapolation is the one with the signal region selection.
- The biases in the event kinematics or in the composition of the MJ template become reduced as the MJ selection gets closer to the signal region selection.
- Different variables are used in the MJ extraction fits, and the MJ extrapolation is repeated for each of them.

To perform this linear isolation-extrapolation, control regions, CR1 and CR2 are defined as regions in neighboring isolation slices rather than single region with unique isolation. The signal isolation for W-boson measurement is "ptvarcone20/pT < 0.10" and isolation slices used in MJ estimation are phase spaces with lepton isolation of ptvarcone20/pT in [0.10, 0.15, 0.20, 0.25, 0.30, 0.35, 0.40]. The decision and binning of the lepton isolation is studied dedicatedly for low-pile-up data.

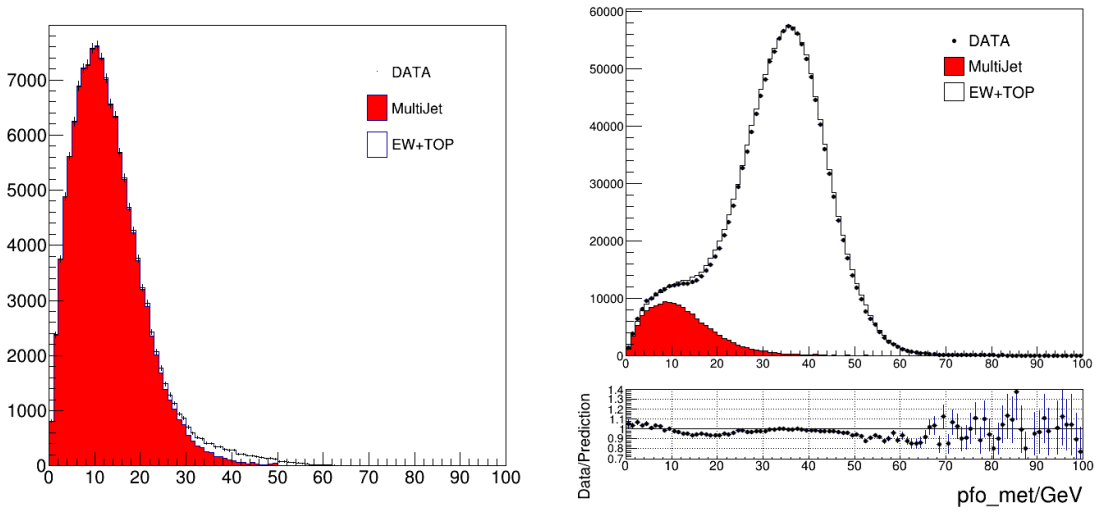

(a) (b)

Figure 7.3: Example of multi-jet profiling and fitting to data and prediction. The MJ profile is derived in MJ-dominated region (CR1, left) and fitted to isolated relaxed region (FR, right)

7.4.2 Decision of Isolation

ATLAS Run-II isolation working points are normally defined by rectangular cuts on two isolation variables:

- $ptvarcone/pT$ – scalar sum of the transverse momenta of tracks with $p_T > 1$ GeV in a cone around the lepton, divided by the lepton p_T;
- $topoetcone/pT$ – sum of the transverse energies of topological clusters in a cone around the lepton, divided by the lepton p_T.

On tracks and clusters separately, $ptvarcone/pT$ and $topoetcone/pT$ cooperate to reject jets in lepton-like object. The optimal isolation is decided from the selection efficiency in data and signal MC samples, such that the one rejects most of the multi-jet background but maintains a high selection efficiency in MC in order to suppress the statistical uncertainty. Moreover, the efficiency is supposed to be linear so that the data-driven multi-jet gets proper modellings.

The data and signal MC efficiencies selected at different up-limit of $ptvarcone/pT$ and $topoetcone/pT$ are illustrated in Fig. 7.4 and 7.6 for electron and muon respectively. Fig. 7.5 and 7.7 display the efficiencies in FR. In fit region, the difference between data and MC is propotional to MJ, providing the tend of how MJ background changes along $ptvarcone/pT$ and $topoetcone/pT$.

For both electron and muon, clear non-linear variation of efficiency to topoetcone/pT selection is observed, expected to bring difficulties in MJ evaluation in signal region definition and control region modelling, so "ptvarcone/pT" is the superior choice in MJ studies, benefiting from its global linear

efficiency and capability in background rejection. The signal isolation working point is defined as "ptvarcone20/pT < 0.1", while the inverted phase space, "ptvarcone20/pT > 0.1" is used to define fit regions. Later of this chapter the relation between lepton $\Delta R < 0.2$ cone and hadronic recoil is studied which demonstrates the ptvarcone20 is relatively optimal isolation definition.

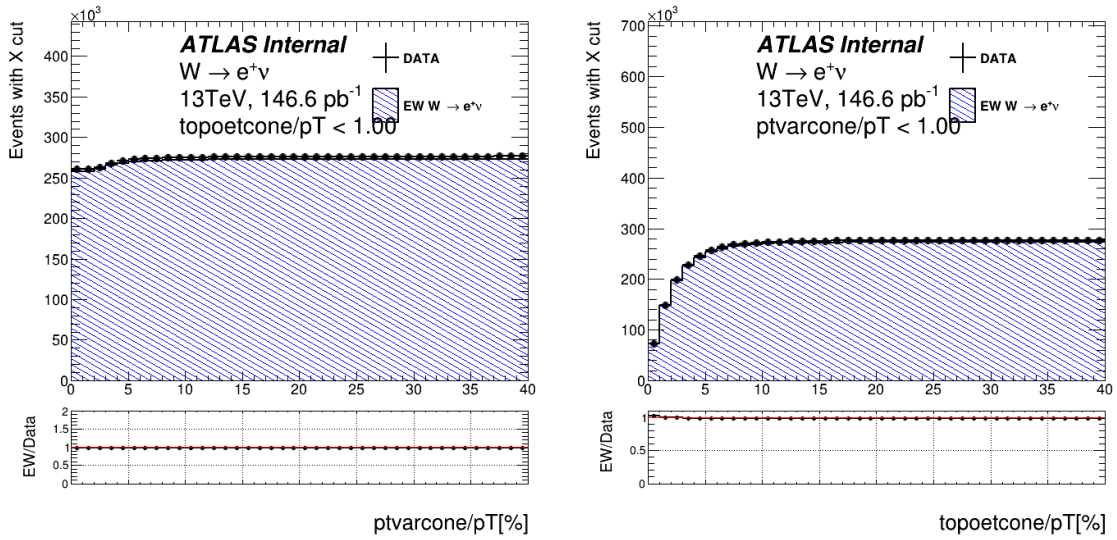

Figure 7.4: Variation of selected data and simulated event number along where the ptvarcone(topoetcone) is cut while topoetcone(ptvarcone) fixed in left(right) for electrons in $W- > e^+\nu$ SR selection

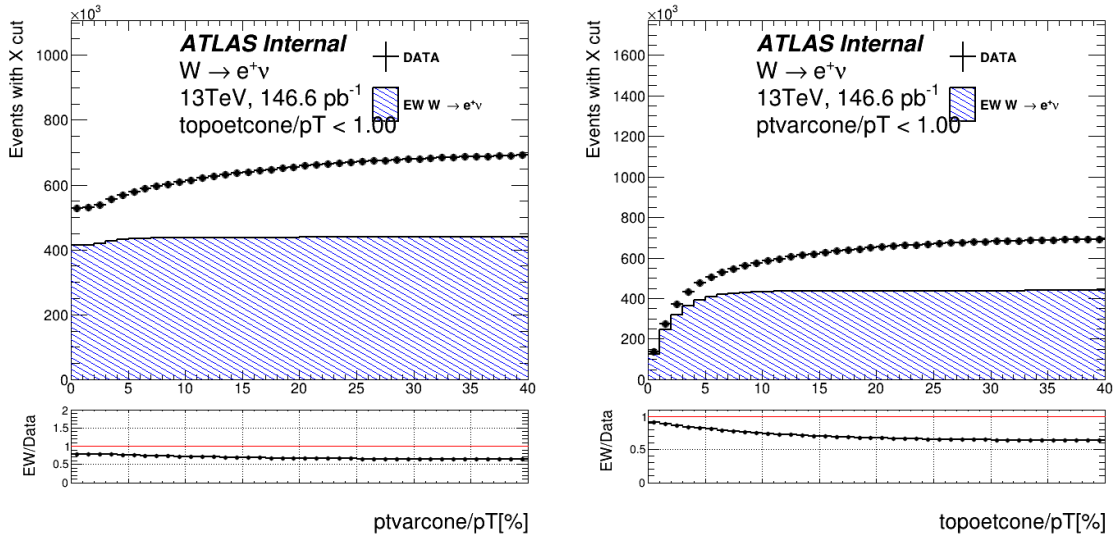

Figure 7.5: Variation of selected data and simulated event number along where the ptvarcone(topoetcone) is cut while topoetcone(ptvarcone) fixed in left(right) for electrons in $W- > e^+\nu$ FR selection

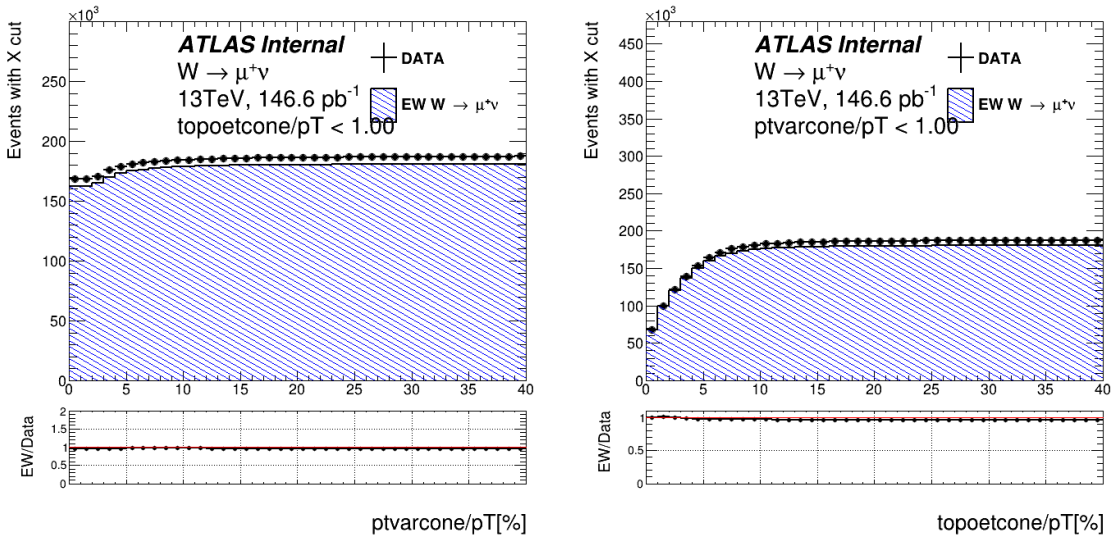

Figure 7.6: Variation of selected data and simulated event number along where the ptvarcone(topoetcone) is cut while topoetcone(ptvarcone) fixed in left(right) for electrons in $W- > \mu^+\nu$ SR selection

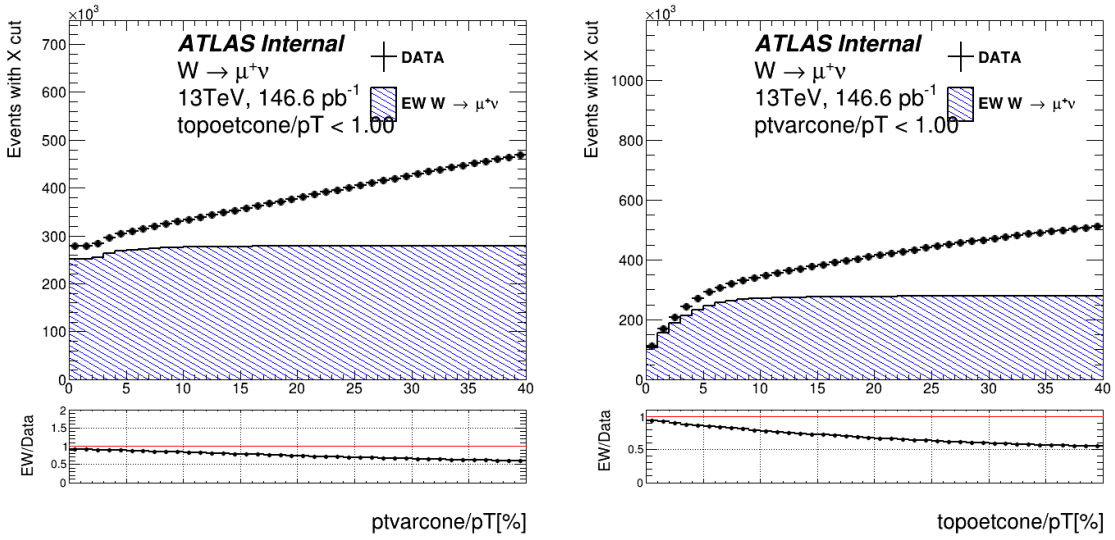

Figure 7.7: Variation of selected data and simulated event number along where the ptvarcone(topoetcone) is cut while topoetcone(ptvarcone) fixed in left(right) for electrons in $W- > \mu^+\nu$ FR selection

7.4.3 Development of the methodology

The data-driven MJ estimation strategy have been exploited in several W-boson measurements and provides acceptable precision. However, there are some residual problems observed. Fig. 7.8 shows some MJ evaluation results in 7 TeV W boson mass measurement [5] and 2015 5.02-TeV W/Z

cross-section measurement [65]. It's illustrated that the template fitting is becoming worse from

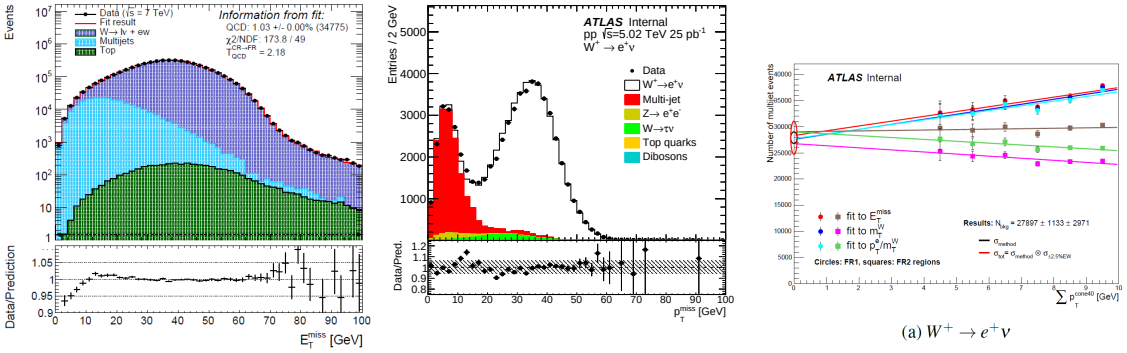

(a) $W^+ \to e^+\nu$

Figure 7.8: Multi-jet background template fit at $\sqrt{s} = 7$ TeV (left) and 5.02 TeV (middle); The linear extrapolations along isolation of estimated MJ events at $\sqrt{s} = 7$ TeV (right)

tight-isolation to loose-isolation slices, and the fitting in first isolation slice next to signal is far from being perfect, which weakens the credibility of data-driven procedure. Moreover, when the isolation get relaxed, the transverse momentum of jets is enhanced, resulting in a larger extrapolation factor ε, thus the estimated number of MJ is expected to increase from tight to loose isolation slices, but it's not observed in (c) of fig. 7.8, results of 7-TeV measurements. These evidences indicate the situation that there is an undiscovered bias in the current procedure.

As this effect grows with the lepton isolation $ptvarcone20/p_T$, and relatively more significant in E_T^{miss} and m_T scans, it is very likely to be a recoil-related bias due to energies around leptons. Therefore the projection of hadronic recoil to lepton momentum direction, is used to study the bias.

The observables are $upar^{lep}$ and $uperp^{lep}$, denoting the component of the recoil parallel and perpendicular to the lepton axis, respectively. Such variables are both supposed to be independent to lepton isolation, thus the mean value of $upar^{lep}$ and $uperp^{lep}$ can reflect the potential bias along isolation variable $ptvarcone20$. The $ptvarcone20$, as the absolute track energy around lepton, instead of the ratio is adopted to maintain linearity. Fig. 7.9 (7.10) displays the relation between $< upar^{lep} >$ ($< uperp^{lep} >$) and $ptvarcone20$ of lepton in MC samples. Different up-limits are set to the "p_T^W", which is equal to the transverse momentum of recoil in absolute value, to study this effect with respect to different levels of underlying events.

As illustrated, the perpendicular component of recoil is much less sensitive to $ptvarcone20$ than the parallel component, and the later behaves kind of proportional correlation to $ptvarcone20$. However, the $< upar^{lep} >$-$ptvarcone20$ correlation in data is opposite (Fig. 7.11). The $< upar^{lep} >$ decreases at larger $ptvarcone20$, to figure out the source of this discrepancy between data and MC is the key to cancel this bias.

A proposal to explain it is that the $ptvarcone20$ in MC is mostly soft tracks from truth radiations and energy leakages, while in data the majority of contribution is by hard tracks of hadrons and jets. The lepton momentum is calibrated to contain these soft tracks, but not for the hard tracks. Then when reconstructing the recoil object, all PFOs excluding cones of $\Delta R = 0.2$ around leptons are collected. In compensation to the underlying events and un-matched pile-ups, the removed cone is replaced by

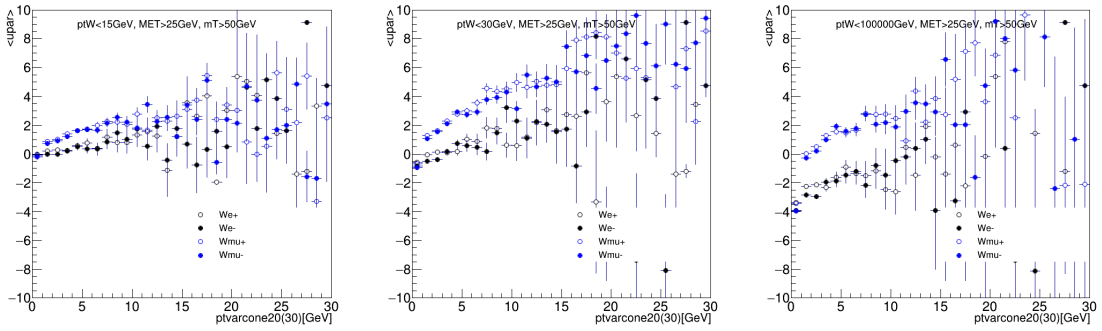

Figure 7.9: Mean value of the parallel component of recoil to the lepton axis along *ptvarcone*20 in all channels using signal MC samples at $\sqrt{s}$ = 13 TeV.

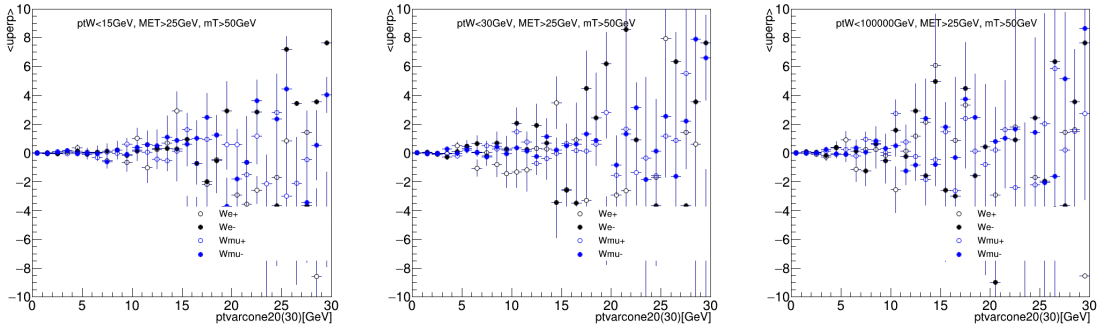

Figure 7.10: Mean value of the perpendicular component of recoil to the lepton axis along *ptvarcone*20 in all channels using signal MC samples at $\sqrt{s}$ = 13 TeV.

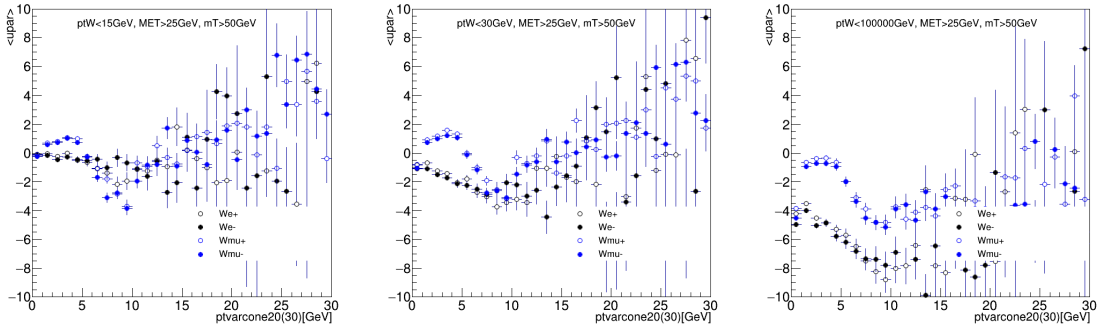

Figure 7.11: Mean value of the parallel component of recoil to the lepton axis along *ptvarcone*20 in all channels using data samples at $\sqrt{s}$ = 13 TeV.

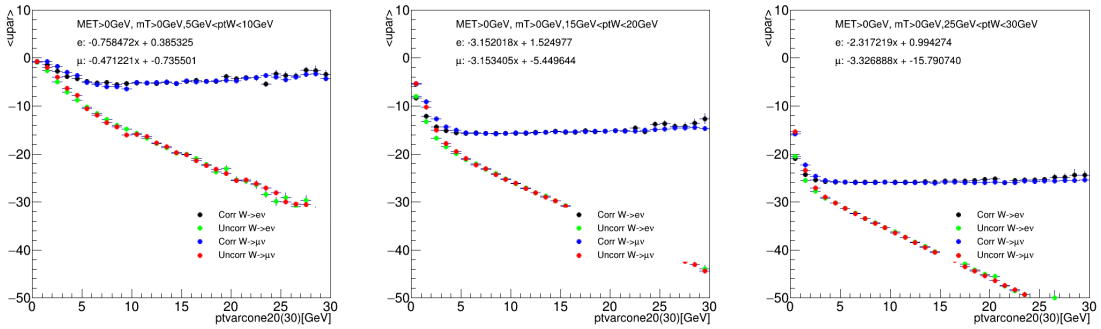

Figure 7.12: $< upar^{lep} >$ before and after correction using data samples at $\sqrt{s}$ = 13 TeV.

using another same-size cone of activity in the event, which is centered at the same η, but away from any lepton, and also from the hard activity, to avoid any energy bias. For MC and data in isolated signal region, it's sufficient and accurate, but in case that hard tracks are neighboring to leptons, the energy of these tracks are not taken into the building of missing energies, thus bias the recoil in lepton axis. In addition, the E_T^{miss} is also underestimated due to this energy loss, dropping the estimated MJ numbers in control regions at higher $ptvarcone20$.

To validate this proposal, a dedicated correction is applied to both data and simulation accounting for the energy loss in control regions, approximately as the sum of tracks' transverse momentum within the $\Delta R = 0.2$ cone around lepton, $ptcone20$, written as:

$$\mathrm{u}^{\mathrm{calib}} = \mathrm{u}^{\mathrm{uncorr}} + \mathrm{MJ}^{\mathrm{recoil}} \tag{7.9}$$

$$\mathrm{MJ}^{\mathrm{recoil}} = \mathrm{LorentzVector}(\mathrm{ptcone20}, \eta^{\mathrm{lepton}}, \phi^{\mathrm{lepton}}, 0) \tag{7.10}$$

Fig. 7.12 shows the correlation between $< upar^{lep} >$ and $ptvarcone20$ in data before and after this correction. Most of the bias are removed with the $ptcone20$ correction. The effect of this ptcone20-based correction will be negligible when approaching signal region from high-$ptvarcone20$, hence the residual bias in this correction is also absorbed by the linear extrapolation.

Displayed in Fig. 7.13, such correction significantly improves both fitting and extrapolation in MJ procedures. The fitting quality is effectively upgraded, and the estimated MJ number get larger in high ptvarcone20/pT regions. Moreover the extrapolated result in signal region (at 0 curve) also increases, from 17k (4k) tp 27k (9k) for electron (muon) after correction. The control plot of transverse mass spectrum after correction is proven to own the better data and prediction agreement in Fig. 7.14.

7.4.4 Multi-jet shape extraction

Due to the residual isolation-dependent effects in MJ extrapolation, the MJ profile in control region is not identical to the profile in the signal region. Therefore the specific extrapolation in "shape" is also required to obtain precise MJ profile in signal region. The isolation slices used in shape estimation are

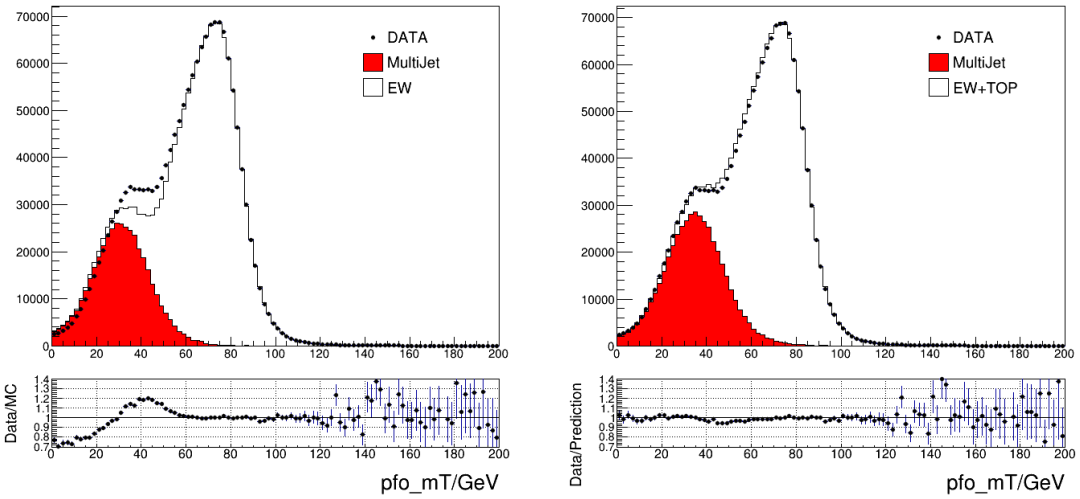

Figure 7.13: Multi-jet background template fits performed in distributions of m_{T} with the MJ template obtained from isolation slice 0.10<ptvarcone20/pt<0.20. The fits are presented in $W^+ \rightarrow e^+\nu$ channel before (left) and after (right) recoil correction.

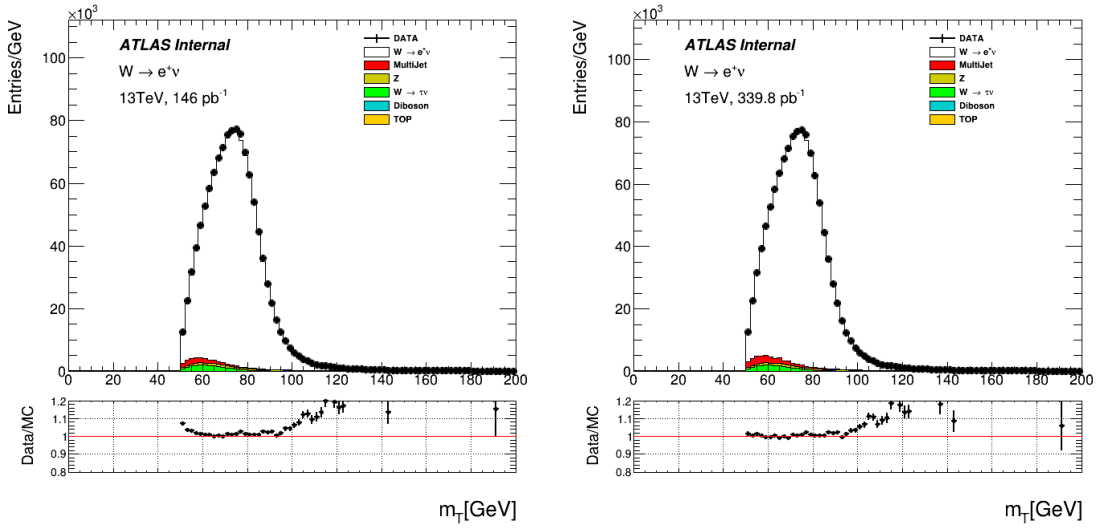

Figure 7.14: $W^+ \rightarrow e^+\nu$ channel signal region transverse mass control plot bf/af (left/right) ptcone20 recoil correction.

three CR2 (anti-isolated signal region) regions with isolation of ptvarcone20/pT in [0.10, 0.20, 0.30 0.40], respectively. For one of the MJ kinematics "X", the averaging difference of profiles between isolation slices, $Detla[X]$, is calculated:

$$hist_{MJ}^{[0.1,0.2]}[X] = hist_{data}^{[0.1,0.2]}[X] - hist_{MC}^{[0.1,0.2]}[X]; \tag{7.11}$$

$$Detla[X] = ((hist_{MJ}^{[0.1,0.2]}[X] - hist_{MJ}^{[0.2,0.3]}[X]) + (hist_{MJ}^{[0.2,0.3]}[X] - hist_{MJ}^{[0.3,0.4]}[X]))/2, \tag{7.12}$$

where $hist_{X}^{[0.1,0.2]}$ is the normalized distribution of "X" in CR2 (anti-isolated signal region) with isolation of "0.1 < ptvarcone20/pT < 0.2". estimated from the MC-subtracted data in CR2. Detla[X] is supposed to be the difference between MJ spectrum in signal region (ptvarcone20/pT < 0.10) and the isolation slice next to it (0.10 < ptvarcone20/pT < 0.20), so the profile in signal region is:

$$hist_{X}^{sig} = hist_{X}^{[0.1,0.2]} - Detla[X] \tag{7.13}$$

associated to large statistical uncertainty, it's not a precise estimation, thereby the shift (Detla[X]) applied is considered as the total shape uncertainty in this evaluation.

$$Detla[X] = Unc[X] \tag{7.14}$$

Fig. 7.15 illustrates the shape extrapolation of lepton and W-boson kinematics. This method is also extended to all other kinematics.

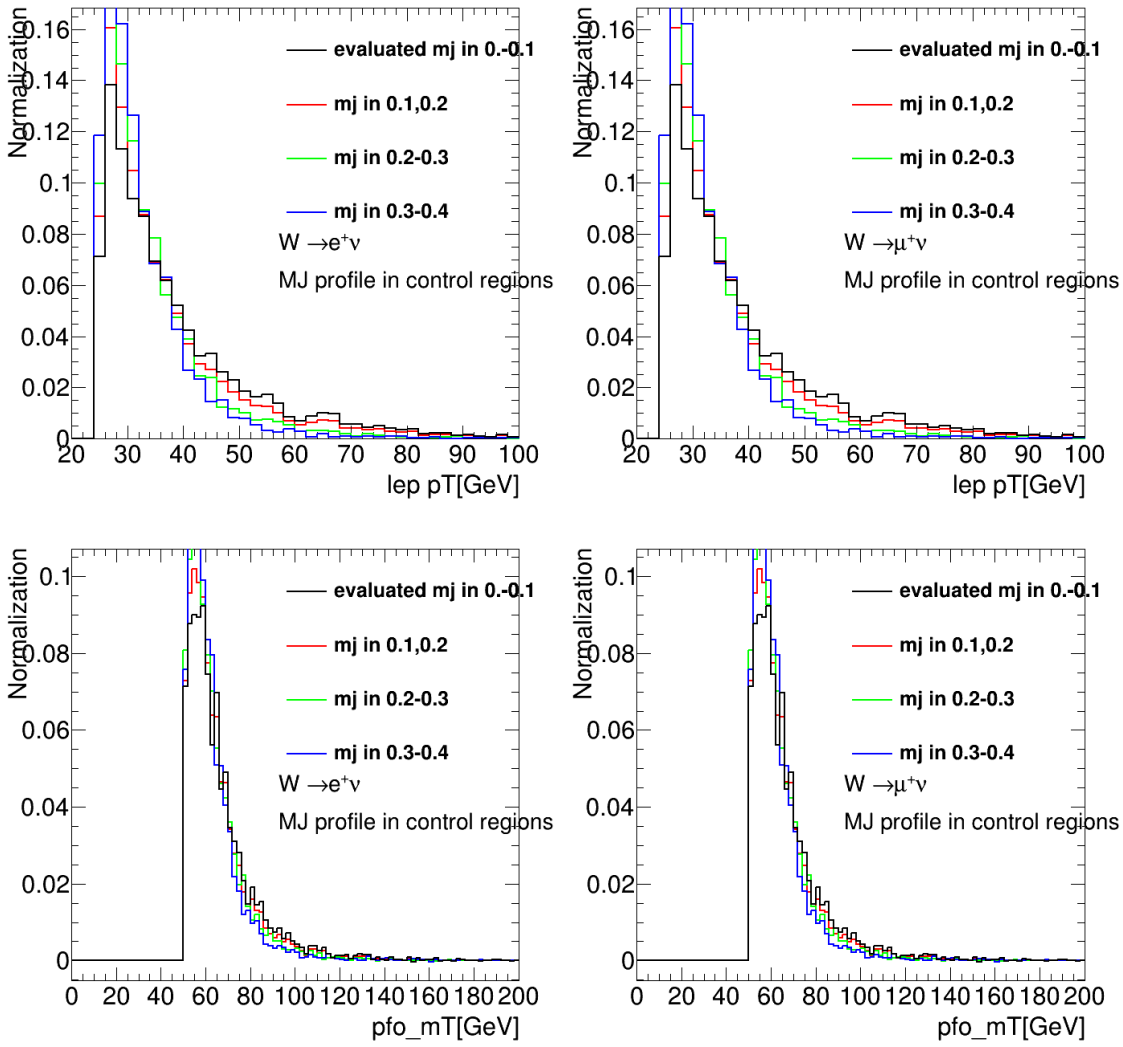

Figure 7.15: Multi-jet profile extrapolation of lepton transverse momentum (top) and trasvers mass (bottom) in $W^+ \rightarrow e^+\nu$ (left) and $W^+ \rightarrow \mu^+\nu$ (right) channel with low-pile-up datasets at $\sqrt{s}$ = 13 TeV

7.4.5 Results of the extrapolation

The isolation binning used for the isolation-extrapolation is defined as ptvarcone20/p_{T} in [0.10, 0.15, 0.20, 0.25, 0.30, 0.35, 0.40], same for electron and muon channels. Control plots of fit region are displayed in fig. 7.16 and 7.17, derived in the first isolation slice [0.10, 0.15]. The quality of fit between data, simulation and data-driven MJ is excellent in all observables and channels.

Fig. 7.18 and 7.19 illustrate the MJ scan results along $ptvarcone20$ for the $W^+ \to e^{\pm}\nu$ channel and the $W^- \to \mu^{\pm}\bar{\nu}$ channel respectively. The errors on each of the scan points are the errors from the template fit, taking into account the discrimination power of the variables, as well as the statistics of the MJ template, multiplied by the $\sqrt{\chi^2/\mathrm{NDoF}}$ of the fit, to account for eventual mismodelling in the considered variables.

The multi-jet backgrounds contributions to data at 13 TeV and 5TeV are:

Channel	13 TeV	5 TeV
$W^+ \to e^+\nu$	27973 ± 1756	3027 ± 554
$W^+ \to e^-\nu$	27388 ± 1962	2401 ± 495
$W^+ \to \mu^+\nu$	9044 ± 796	724 ± 192
$W^+ \to \mu^-\nu$	9053 ± 617	755 ± 160

Table 7.4: Evaluation of multi-jet contributions to 13 TeV and 5 TeV low-pile-up data with W-boson event signal selections

7.4.6 Explanation to the high slope in extrapolation

The linear fit results using different kinematics show excellent agreement when extrapolated to ptvarcone20/pT = 0 at all channels studied. However, in example of Fig. 7.18, one concerning issue illustrated is the over high slope of extrapolating function. The discussion in this paragraph focuses on the investigation to such slope.

Following the procedure, there is one critical assumption that the profile of MJ kinematics is independent to isolation to proceed the estimation. Based on it, two approaches are performed:

- the profile in control region is extracted and taken into the Data-(EW+TOP)-MJ fit in fit region:

$$H_{\mathrm{data}}^{\mathrm{FR}} = \alpha \cdot H_{\mathrm{EW}}^{\mathrm{FR}} + T \cdot H_{\mathrm{MJ}}^{\mathrm{CR1}}; \tag{7.15}$$

- the normalization factor that scale the MJ number from fit region to signal region (re-applying the E_T^{miss} and m_T cuts that removed in FR):

$$\varepsilon = \frac{N_{\mathrm{MJ}}^{\mathrm{SR}}}{N_{\mathrm{MJ}}^{\mathrm{FR}}} \approx \frac{N_{\mathrm{MJ}}^{\mathrm{CR2}}}{N_{\mathrm{MJ}}^{\mathrm{CR1}}} = \frac{N_{\mathrm{data}}^{\mathrm{CR2}} - N_{\mathrm{EW}}^{\mathrm{CR2}}}{N_{\mathrm{data}}^{\mathrm{CR1}} - N_{\mathrm{EW}}^{\mathrm{CR1}}}. \tag{7.16}$$

To separate the effects, the fitted numbers of MJ in fit region before applying the normalization factor are used: $N_{MJ}^{FR} \approx T \cdot N_{\mathrm{MJ}}^{CR1}$. Fig. 7.20 illustrates the comparison of MJ linear extrapolation using the same binning before normalization.

Before normalization, the slopes are found to be significantly smaller, in particular the slope of p_T^{lep} fit goes opposite-sign, proving the high slope in Fig. 7.20 (a) is mostly contributed by the normalization factor ε. Defined in Eq. 7.16, ε is the ratio of estimated MJ number with and without the E_T^{miss} > 25 GeV and m_T > 50 GeV selection in different isolation slices.
ε grows sharply from [0.10, 0.15] to [0.35, 0.4] of $ptvarcone20/p_T^{lep}$. The reason is that p_T^{lep} is relatively independent to isolation, averaging to 35~40 GeV, thus the increasing of $ptvarcone20/p_T^{lep}$ is equal to the increasing of $ptvarcone20$, i.e. the transverse momentum of jets in the cones of fake leptons. The jet p_T spectra of isolation slices are shown in Fig. 7.21, agreeing with this proposal.

As displayed in (Fig. 7.15, the reconstructed E_T^{miss} and m_T are enlarged with higher $ptvarcone20/p_T^{lep}$, i.e. higher jet activity. which consequentially leads to the "high slop" in MJ extrapolation from low $ptvarcone20/p_T^{lep}$ to high.

7.4.7 Extrapolation curve calibration

The number of multi-jet events is evaluated by extrapolating the number from control regions to $ptvarcone20/p_T^{lep} = 0$. However, the averaging value of $ptvarcone20/p_T^{lep}$ in signal region, $< ptvarcone20/p_T^{lep} >^{sig} = X$, is larger than "0", which introduces a bias, approximating to:

$$\Delta\mathrm{MJ}(ptvarcone20/p_T^{lep} = 0 \rightarrow X) \approx \mathrm{k} \cdot X, \tag{7.17}$$

where k is the slope of extrapolation function. Therefore the final central value of the multi-jet-event number need to recover this bias, and the difficulty is how to evaluate X with reasonable uncertainty.

For muon channel, the conclusive solution to this bias is by exploiting the $b\bar{b}$ and $c\bar{c}$ multi-jet simulation, while for electron the simulation is less accurate, and a temporary but practical method is used to handle such bias. Reminding of the four regions defined for estimation: SR, FR, CR1 and CR2, the SR and CR2 use the signal selection except the isolation which are fixed, but the FR and CR1 use relaxed selection, hence flexible. Applying additional selection on FR and CR1 could suppress the jet activity, producing extrapolating function with different slopes. Those functions would intersect at one point within $ptvarcone20/p_T$ < 0.1, referred to X. Moreover, a good compatibility among MJ estimations with various of fit templates is adequate to give strong validation to the estimation procedure.

u_T, transverse momentum of recoil is used to provide suppressions to jet activity. The calibration to central value of MJ-event number is proceeded with following steps:

1. Define a set of FR and CR1 templates with additional u_T up-limits (u_T < 15/30/10000 GeV).
2. The MJ procedure is repeated using different templates.
3. Locate the intersection of the extrapolation using all kinematics, isolation slices and templates with u_T selections.

4. Evaluate the central value and uncertainty of the MJ-event number to the intersection.

An example of 13-TeV electron channel result is illustrated in Fig. 7.22, on which the slopes of linear extrapolation of "u_T < 15 GeV" templates are indeed pretty tiny. Thus the "u_T < 15 GeV" is taken as the baseline, and the intersection curve is set as $ptvarcone20/p_T^{lep} = 0.08 \pm 0.02$, which introduce extra $\sim$ 300 systematic uncertainty to the multi-jet in electron channel, sub-dominant to the major systematic uncertainty from extrapolation.

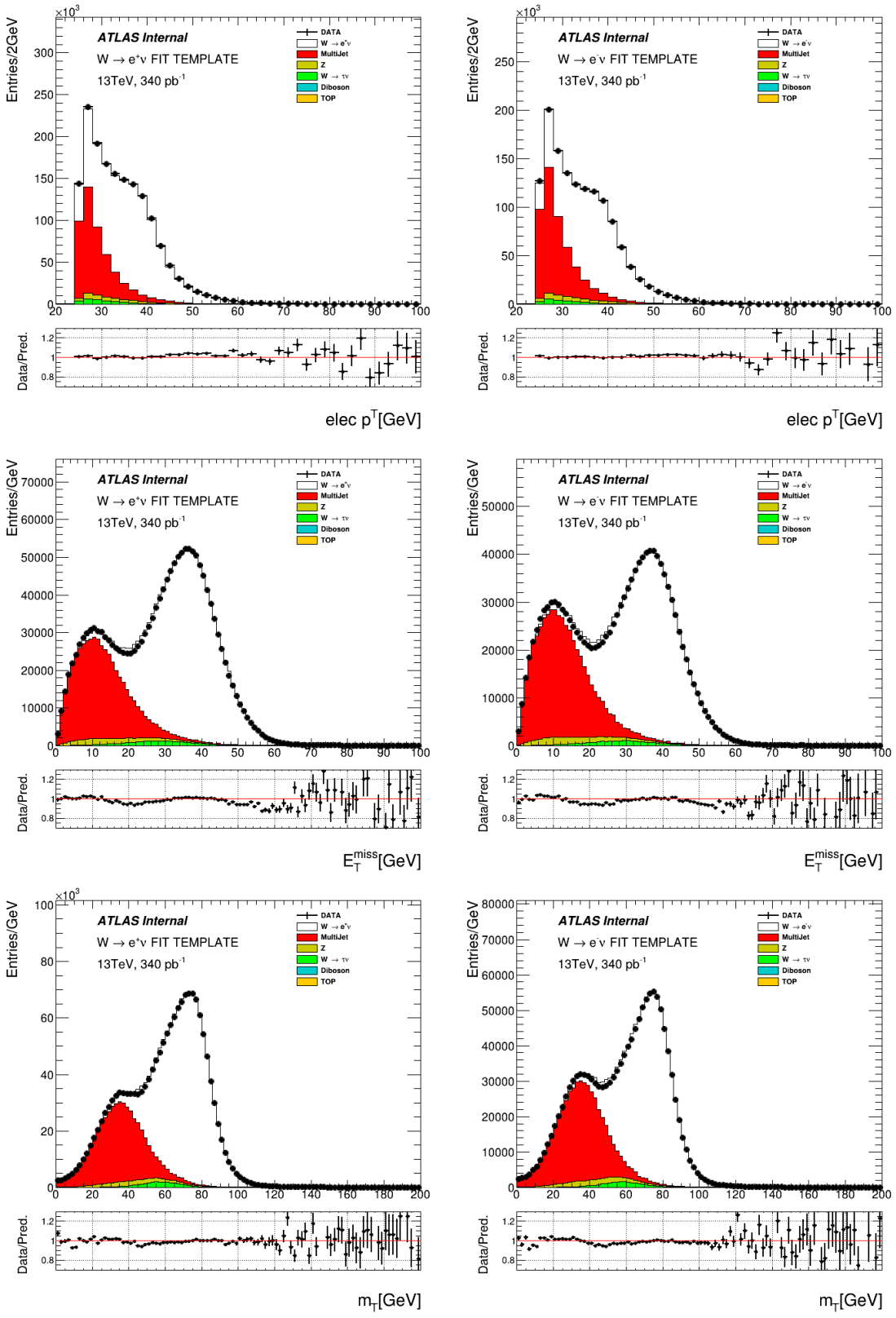

Figure 7.16: Multi-jet background template fits performed in distributions of p_{T}^{e} (top), MET (middle) and m_{T} (bottom) with the MJ template obtained from isolation slice 0.10<ptvarcone20/pt<0.15. The fits are presented for positive (left) and negative (right) electrons.

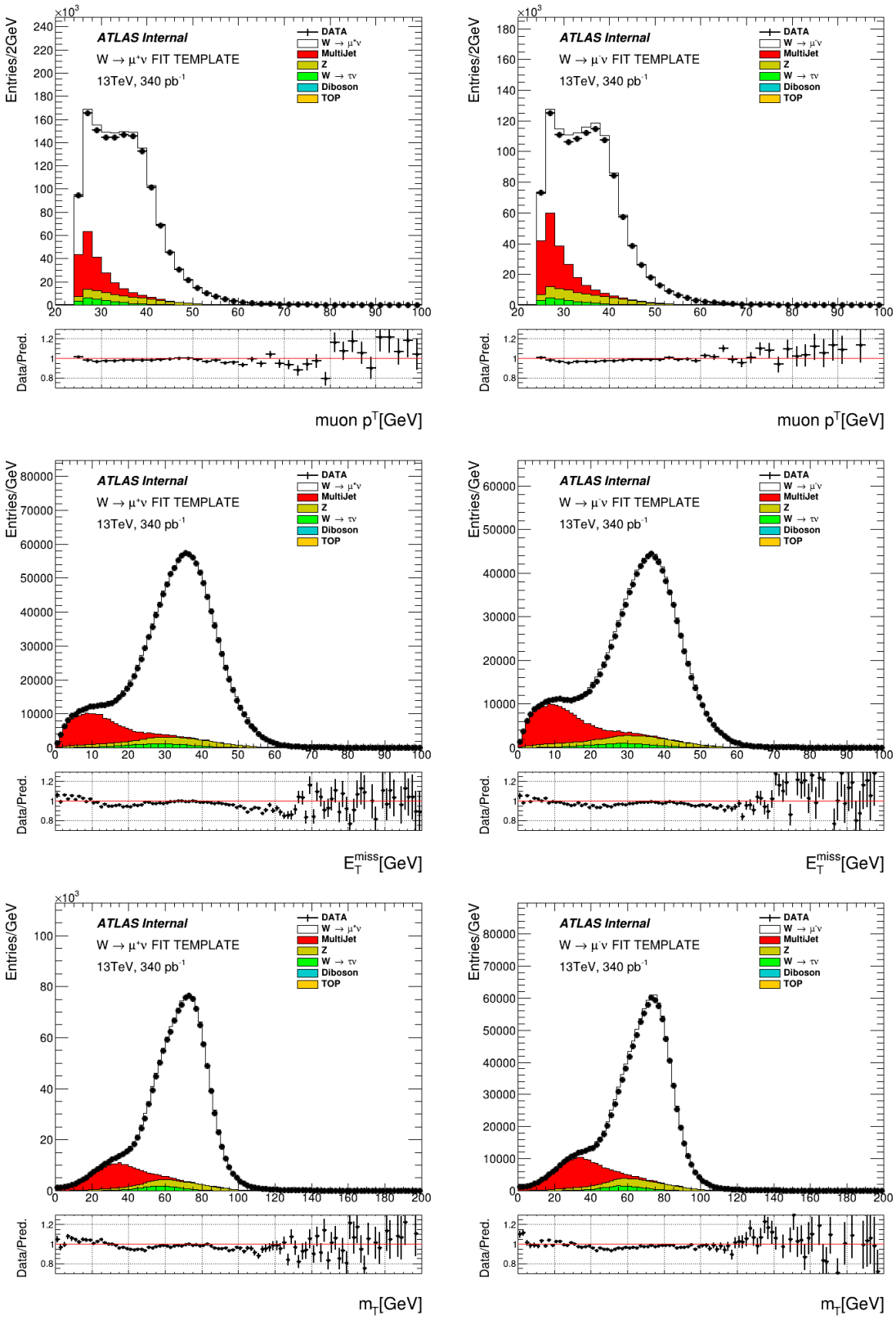

Figure 7.17: Multi-jet background template fits performed in distributions of p_{T}^{e} (top), MET (middle) and m_{T} (bottom) with the MJ template obtained from isolation slice 0.10<ptvarcone20/pt<0.20. The fits are presented for positive (left) and negative (right) muons.

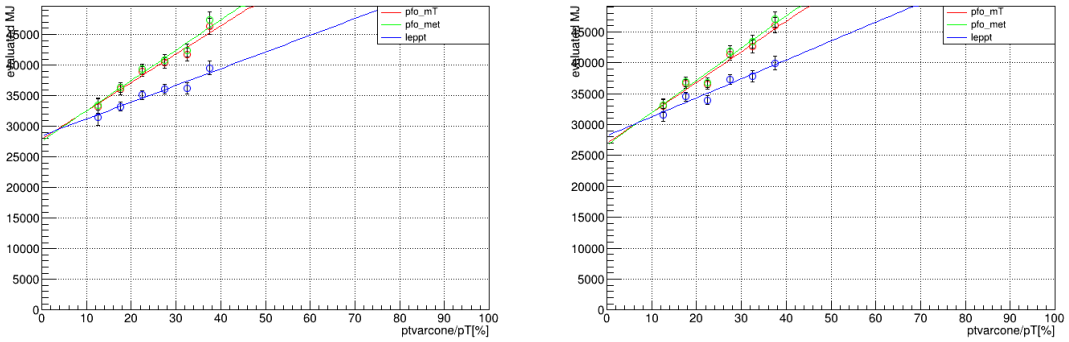

Figure 7.18: Plots of the 0.05-ptvarcone/pT-step scans for ptvarcone20/p_{T} in $W^+ \rightarrow e^+\nu$ channel(left) and $W^- \rightarrow e^-\nu$ channel(right). The errors on each of the scan points are the errors from the template fit multiplied by the fit $\sqrt{(\chi^2/\mathrm{NDoF})}$ and extrapolatory factor uncertainty.

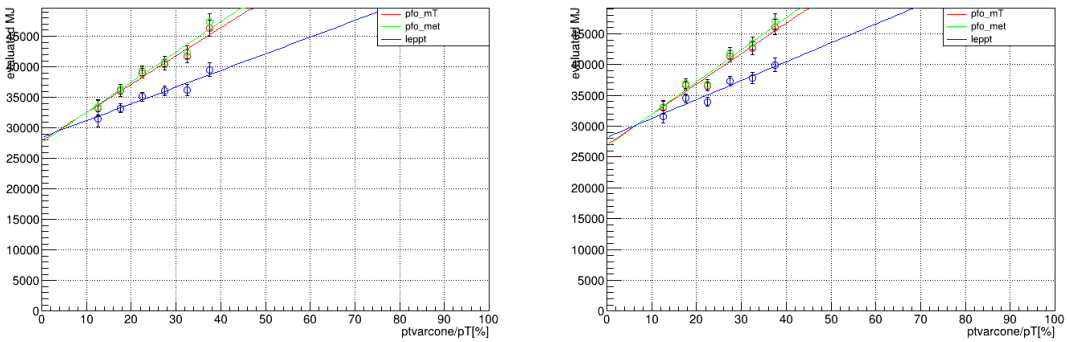

Figure 7.19: Plots of the 0.05-ptvarcone/pT-step scans for ptvarcone20/p_{T} in $W^+ \rightarrow e^+\nu$ channel(left) and $W^- \rightarrow e^-\nu$ channel(right). The errors on each of the scan points are the errors from the template fit multiplied by the fit $\sqrt{(\chi^2/\mathrm{NDoF})}$ and extrapolatory factor uncertainty.

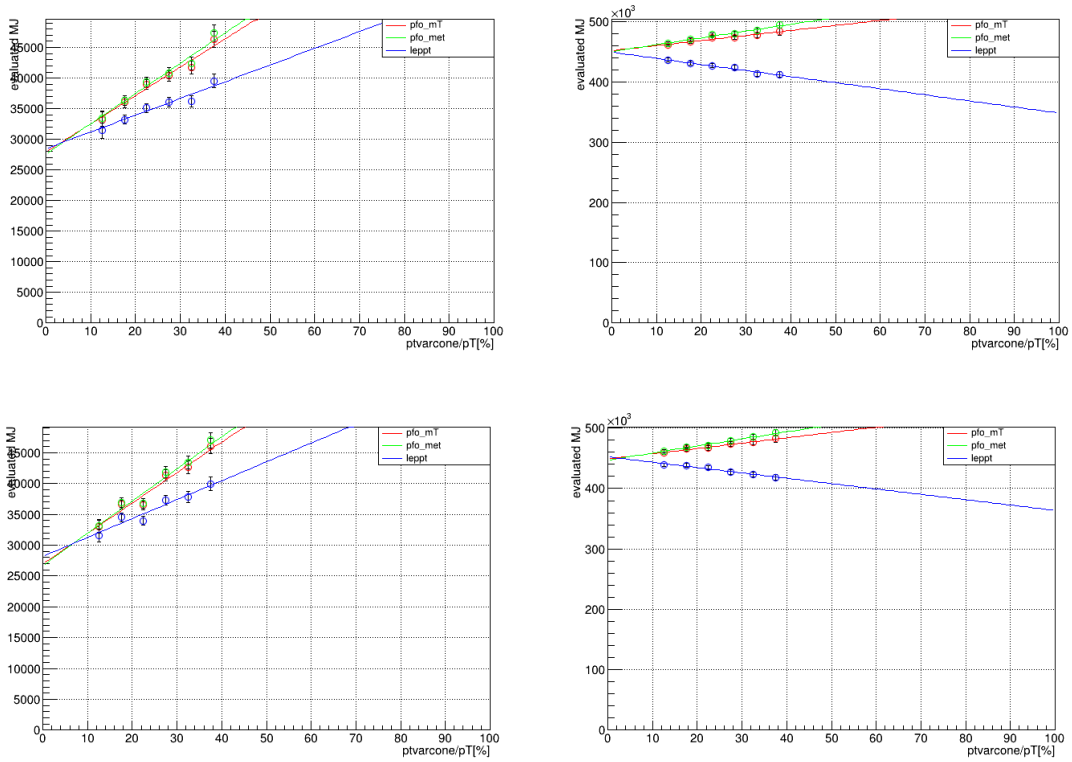

(a) Normalized to signal

(b) Non-normalized

Figure 7.20: The linear extrapolation of multi-jet-event number in signal region (b) and fit region (b) in $W^+ \to e^+\nu$ channel (top) and $W^- \to e^-\nu$ channel (bottom).

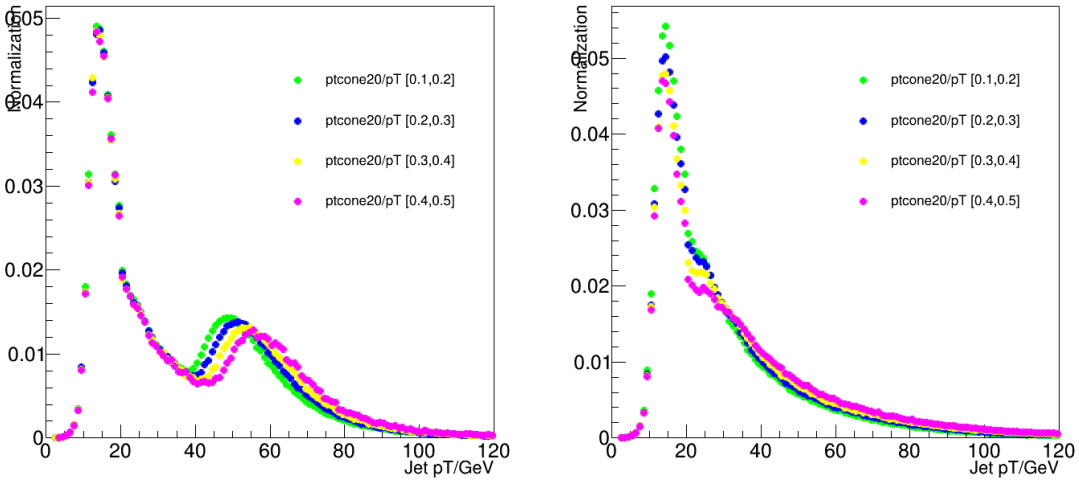

Figure 7.21: Distributions of jet transverse momentum in differential ptvarcone20/pT regions using $W^+ \to e^+\nu$ (left) and $W^+ \to \mu^+\nu$ (right) selection

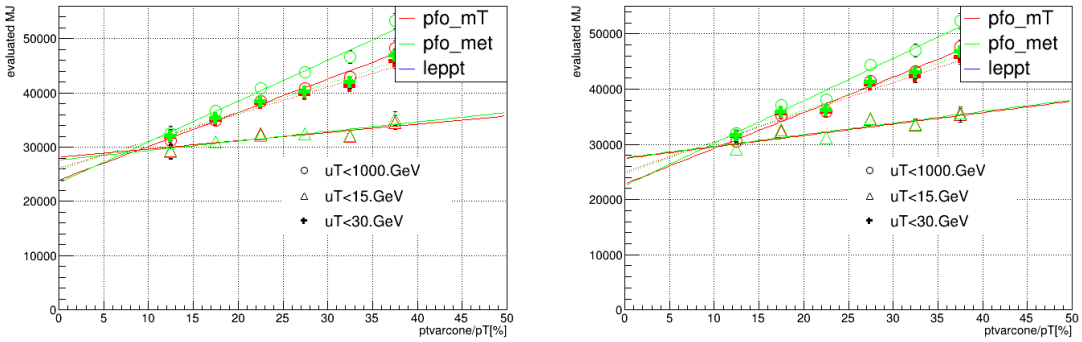

Figure 7.22: Multi-jet isolation extrapolation in $W^+ \rightarrow e^+\nu$ (left) and $W^- \rightarrow e^-\nu$ (right) channel with low-pile-up datasets at $\sqrt{s}$ = 13 TeV

7.5 Results

The distinctive event selection provides a phase space rich of signals for W-boson measurements, with backgrounds controlled under ideal level. The experimental corrections for low-pile-up simulations are calculated and reviewed, including the in-situ measured corrections, electron and muon efficiency scale factors, recoil resolution and response calibration, and extrapolated corrections from high-pile-up samples, consisting of the electron energy and resolution calibration, muon momentum calibration, and part of the electron reconstruction scale factor. Furthermore, the physical corrections from theoretical and optimized multi-jet background estimation algorithm reduce the discrepancy between data and simulations.

Fig. 7.23-7.24 illustrate the comparisons of kinematics spectra in data and simulation in addition to all backgrounds. Uncertainties are not included due to the lack of some corrections, which also slightly degrades the data/prediction agreement in muon channels. In the low-p_T^{lep} region, the agreement between data and prediction is particularly pretty, regardless of the relatively higher MJ contribution and unstable efficiency corrections. The increasing discrepancy at high p_T^{lep} is explained by the mis-modelled W-boson transverse momentum, which will be measured in next chapter. The data/prediction agreement of recoil-leading kinematics E_T^{miss} and m_T is globally superior, besides the multi-jet background enriched regions.

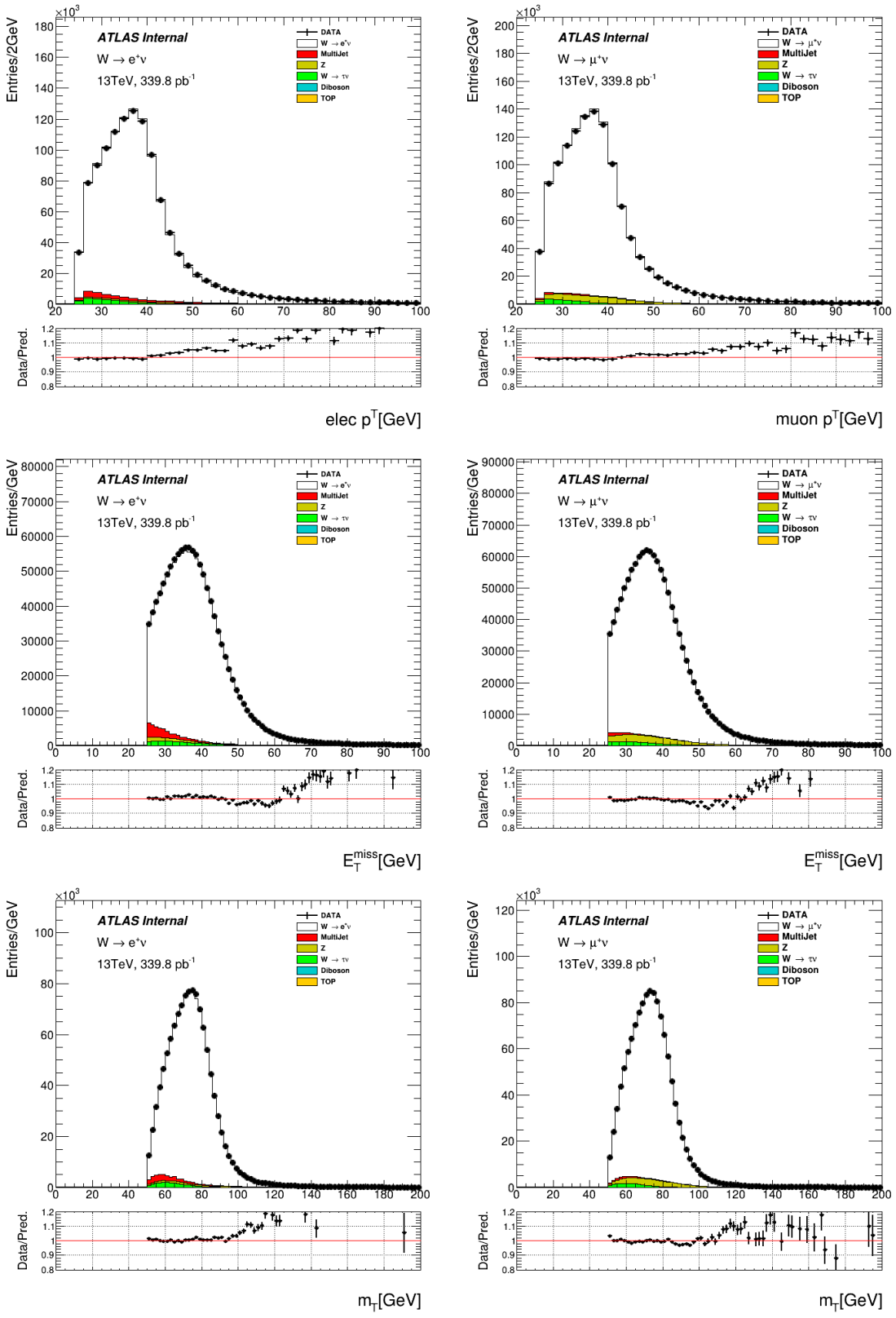

Figure 7.23: Distributions of p_{T}^{e} (top), MET (middle) and m_{T} (bottom) in $W \rightarrow e^{+}\nu$ (left) and $W \rightarrow \mu^{+}\nu$ (right) channel at $\sqrt{s} = 13\ TeV$

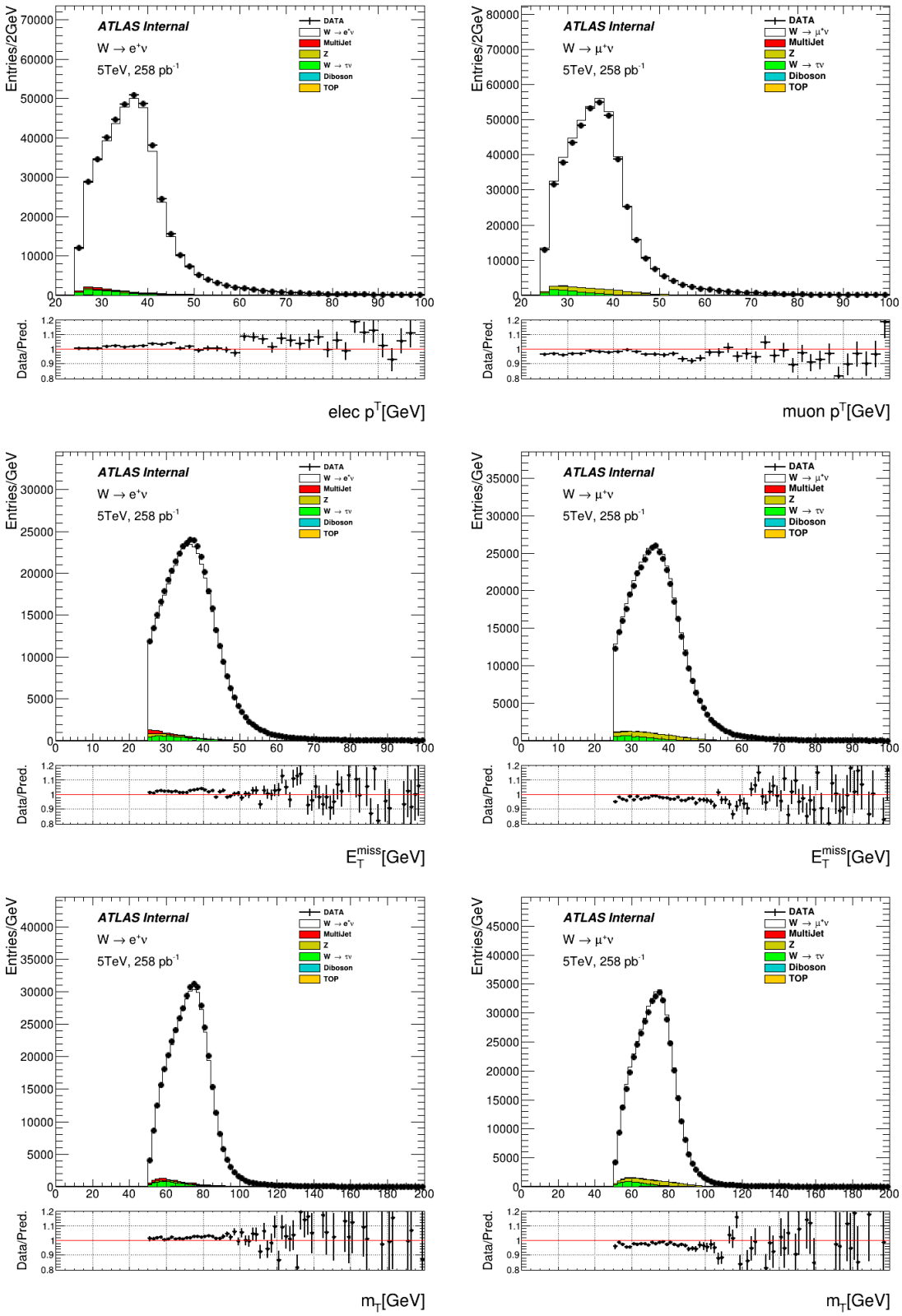

Figure 7.24: Distributions of p_{T}^{e} (top), MET (middle) and m_{T} (bottom) in $W \to e^{+}\nu$ channel(left) and $W \to \mu^{+}\nu$ channel(right) at $\sqrt{s}$ = 5 TeV.

8 Measurement of the W-boson transverse momentum distribution

Measurement to W-boson transverse momentum, p_T^W, is one the essential motivations of low-pile-up run. The target precision of p_T^W spectrum, as discussed in Chap. 2.4, is 1% uncertainty in 5-GeV bins of low-p_T^W region. First results of p_T^W indicate more optimistic accuracy than expectation [69], thanks to the optimized hadronic recoil reconstruction and other corrections. Personal contributions involved in this result include the dedicated event selection, backgrounds estimation and lepton corrections. Therefore more attention are focused on the performance of the background and corrections, while the methodology of p_T^W measurement and corresponding uncertainties are presented briefly in this chapter.

8.1 Methodology

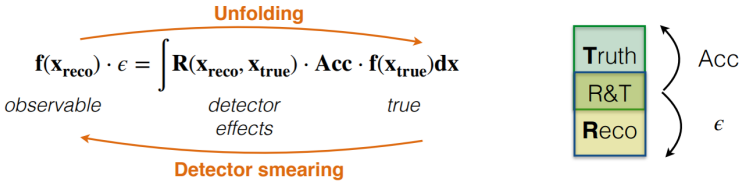

Figure 8.1: Illustration of general unfolding procedure.

In general, the W-boson transverse momentum is measured with the unfolding procedure, containing correcting detector effects like the finite detector acceptance, reconstruction efficiency and energy resolution, from a measured observable in order to determine the true underlying distribution. The conditional probability to observe a reconstructed value in the bin i given a truth value in the bin j is defined by the response matrix R_{ij}. A 2-dimentional histogram with a common matching of truth and reconstructed values ($T\&R$) are filled with events from signal simulation corrected for reconstruction efficiency and truth acceptance, as the response matrix. An example of response matrix is given in Fig. 8.2. The truth acceptance correction A (Fig. 8.3(b)) is the ratio between events passing $T\&R$ criteria and all events passing truth selections T_{fid}. The reconstruction efficiency probability ϵ_j (Fig. 8.3(a)) is the sum of R_{ij} over all possible bins of the observed value, practically the ratio between events passing truth and reconstructed criteria $T\&R$ and all events passing reconstruction selection R_{fid}. The inverse of the acceptance is applied to the unfolded distribution in order to extrapolate to the truth fiducial phase space. The events passing $T\&R$ and R_{fid} selections respectively, receive both

reconstructed and truth weights i.e SF efficiency, hadronic recoil, calibration etc and polarization, generator weights, while the events passing T_{fid} have only truth weights applied.

The expression of this procedure is:

$$D_i = \sum_j R_{ij} T_j + B_i \tag{8.1}$$

where i, j label the bin number of the reconstructed and true distributions respectively; T and D are the underlying true and observed distributions; R_{ij} is the response matrix encoding resolution effects estimated using finite-size Monte Carlo samples and corrected for efficiency and acceptance corrections as explained above. B_i represents the sum of all background contributions in bin i. The unfolding procedure determines the best estimate of the underlying distribution following:

$$U_j = U_{ij} \sum_i (D_i - B_i) \tag{8.2}$$

where U_j is the unfolded spectrum, which estimates the underlying distribution T; and U_{ij} symbolically represents the unfolding transformation, which in the simplest case is just the inverse of the response matrix R_{ij}. The unfolded matrix U_{ij} is determined in this analysis using the iterative bayesian regularized unfolding approach, described in [70]. In addition, a data-driven closure test is performed to estimate bias from unfolding method when applied to data, using simulation of which the truth distribution is known, and the reco-level performance is very similar to data after by reweighting the truth distribution.

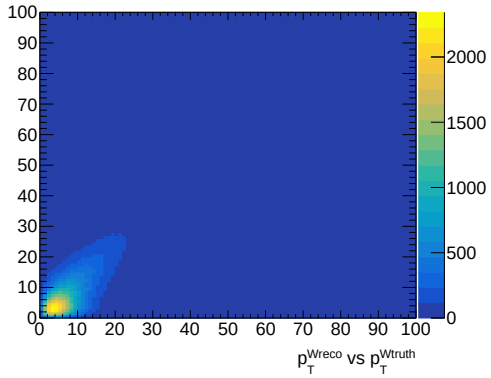

Figure 8.2: Example of migration matrix for $W^- \rightarrow e\nu$ channel at 5 TeV

Statistical uncertainties of p_T^W is estimated with bootstrap method described in Chap. 10.3.4. The systematic uncertainties from background and corrections, following Eq. 8.2, directly reflect the systematic uncertainty of p_T^W.

8.2 Multi-jet background in p_T^W spectrum

The multi-jet background (Chap. 7.4.5) is estimated with an optimized data-driven method based on hadronic recoil and lepton isolation. In particular, Chap. 7.4.4 presents how the distribution of multi-jet

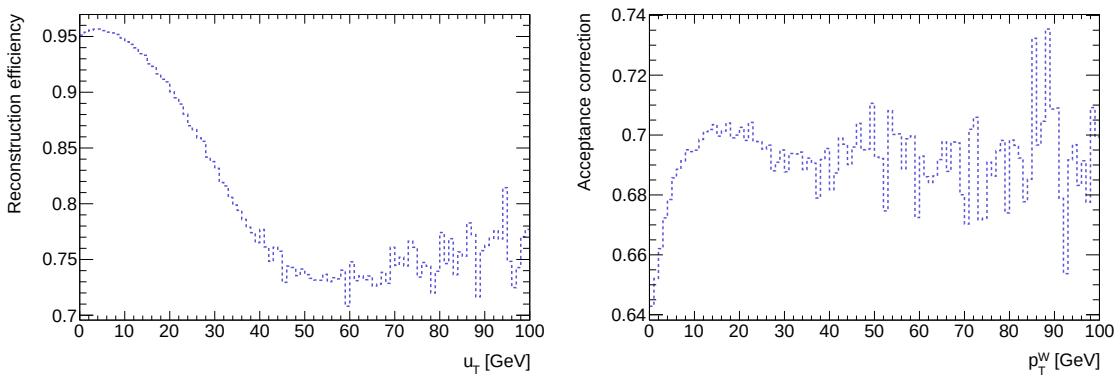

(a) (b)

Figure 8.3: Example of reconstruction efficiency (a) and acceptance corrections (b) for $W^- \rightarrow e\nu$ channel at 5 TeV

background in signal region is estimated from control regions. The background term, subtracted from data in Eq. 8.2, is important to the precision of p_T^W measurement. The ratio between multi-jet and signal is tiny at low p_T^W, but could increase with p_T^W, and in the high-p_T^W regions, the relevant statistical uncertainty is dominant, thus the contribution of multi-jet background to p_T^W spectrum demands more validation.

The uncertainty due to MJ has two components: the systematic one from the isolation extrapolation, influencing the event number of multi-jet, and the statistical one from the finite events in control regions, influencing the shape of estimated spectra. Systematic uncertainty is relatively smaller than statistical uncertainty because of the excellent modelling in isolation extrapolation. Therefore the proposal to cross-check the multi-jet contribution by duplicating the procedure differential p_T^W bins is put forward. Such proposal addresses that the shape uncertainty is replaced with the systematic uncertainty in each bin, and that the shape estimation procedure is verified.

The differential method consists of these steps:

1. Separate the signal region and control regions for MJ estimation into small categories in step of 5-GeV p_T^W.

2. In each category, perform the isolation extrapolation (Chap. 7.4.5) with relaxed isolation binning.

3. Merge the p_T^W using results from all categories and take the uncertainty of each category as the uncertainty in corresponding bin of p_T^W spectrum from multi-jet.

Fig. 8.4 illustrates the comparison of two methods, the "inclusive" method and "differential" method. Results of two methods agree well globally, validating the shape extrapolation in inclusive method is effective. The bin-to-bin uncertainty from inclusive method is obviously smaller than differential method. Moreover the inclusive method is capable in high-p_T^W region while the differential method fails. In conclusion, the inclusive method described in Chap. 7.4.4 is adopted to provide the p_T^W distribution as well as all other distributions for W-boson measurement.

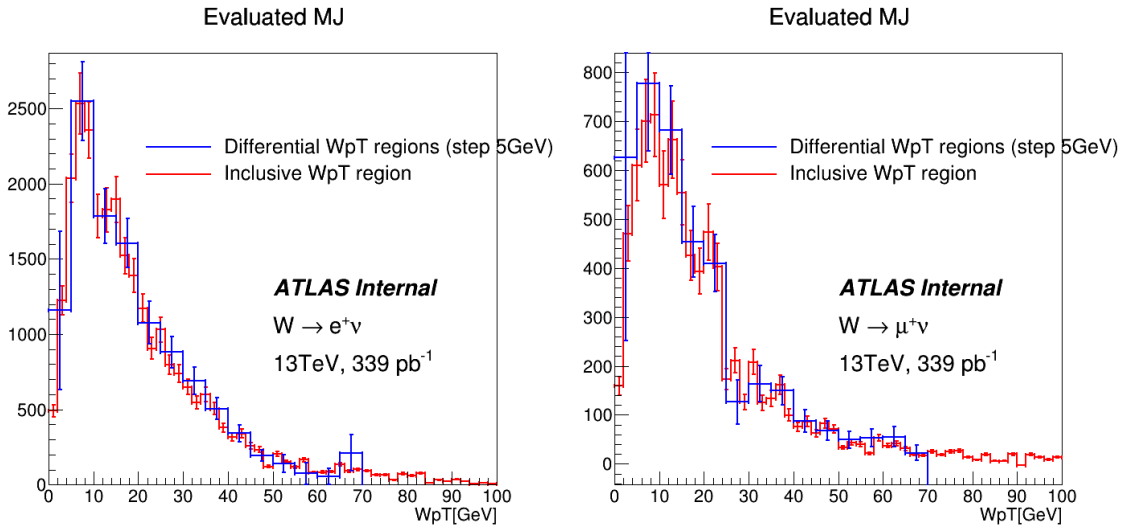

Figure 8.4: Multi-jet WpT distribution evaluation with inclusive and differential regions in $W^+ \to e^+\nu$ (left) and $W^+ \to \mu^+\nu$ (right) channel

8.3 Uncertainty in p_T^W measurement

p_T^W unfolding takes the experimental corrections presented in Chap. 4, 5 and 6. The uncertainty in p_T^W measurement is composed of the systematical uncertainty from background and these corrections, and the statistical uncertainty from data and simulation. Since the performance at high p_T^W is precisely predicted by the pQCD, the low-p_T^W region is of more interest. The estimated uncertainties at unfolded level are displayed in Fig. 8.6 and 8.6 for electron and muon channels respectively.

The hadronic recoil calibration is as expected the leading source of uncertainty, contributing to around 0.5% uncertainty at $\sqrt{s}$ = 5 TeV and 0.5%-1% at $\sqrt{s}$ = 13 TeV. Thanks to the low-pile-up condition, this precision satisfies the requirement at low p_T^W, but the calibration and uncertainty are derived using $Z \to \mu^+\mu^-$ decay thus can't be reduced through channel combination.

The uncertainty due to electron efficiency scale factors are stable, fixed at 0.5% at both $\sqrt{s}$. This result agrees with the total uncertainty of SF illustrated in Chap. 4.3.8. The uncertainty due to muon SFs is around 0.2%, indicating kind of underestimation. A typical muon SF uncertainty is at close level to electron SF, therefore the conclusive SF uncertainty on p_T^W will be approximately 0.5%.

The uncertainties contributed by background estimation, particularly multi-jet, varies most between channels and center-of-mass energies. In muon channel, the uncertainty is below 0.4%, increasing with p_T^W and slightly higher at $\sqrt{s}$ = 13 TeV. In electron channel, the background uncertainty is sub-dominant at $\sqrt{s}$ = 5 TeV, but secondary to recoil at $\sqrt{s}$ = 13 TeV. Generally, the uncertainty from background is sufficient to the requirement of p_T^W in most channels and would gain reduction by channel combination.

In conclusion, the precision of p_T^W well satisfies the expectation in low-pile-up data. In validation of such result, more closure test are on-going and the final results, including the ratio between p_T^W and

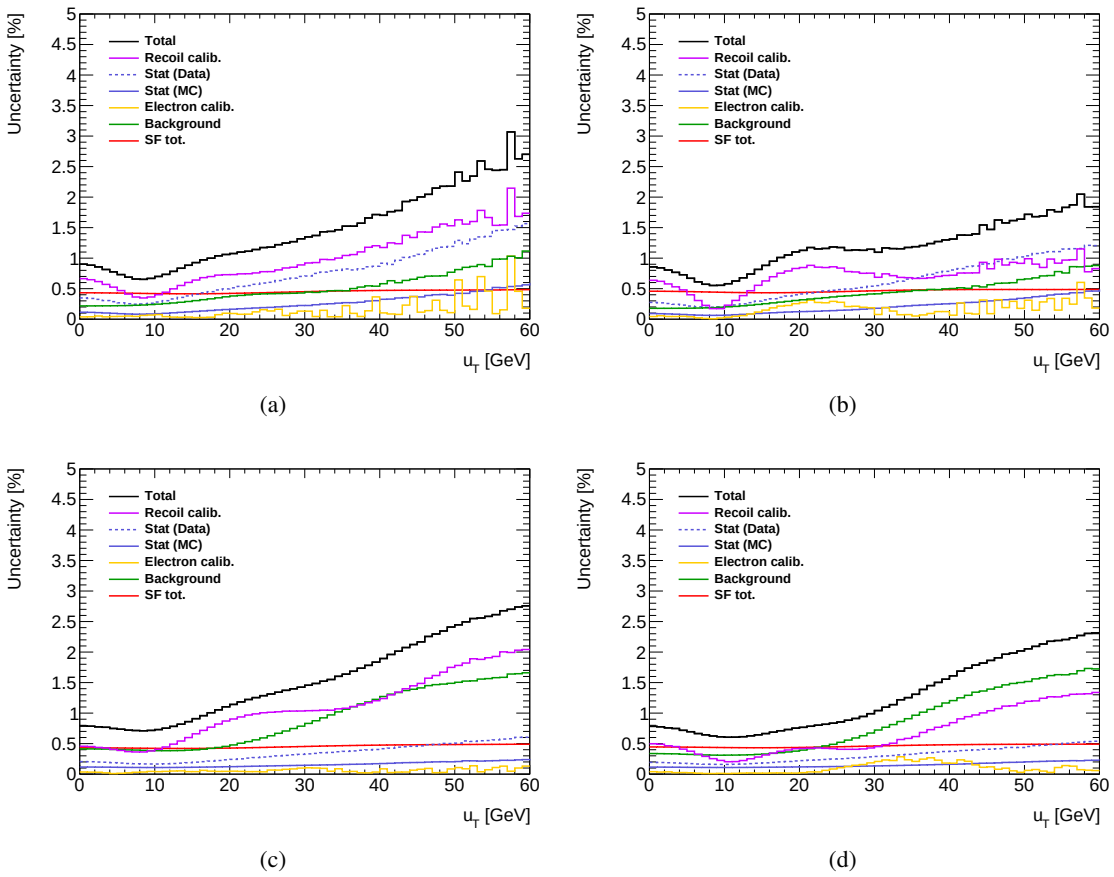

Figure 8.5: Breakdown of systematic uncertainties for 5 (a,b) and 13 TeV (c,d) in the electron channel at the unfolded level

p_T^Z, will be taken into the cross-section and M_W measurement, as well as the tuning of parton shower and resummation calculations.

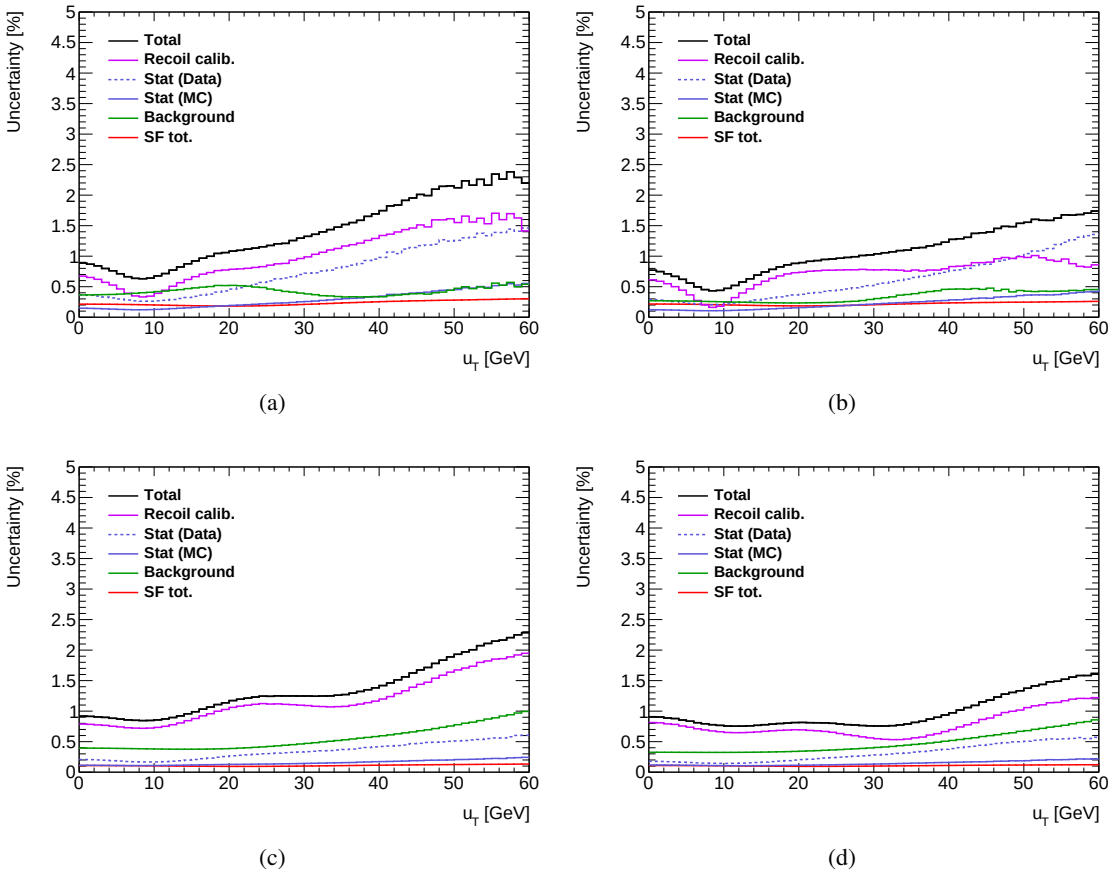

Figure 8.6: Breakdown of systematic uncertainties for 5 (a,b) and 13 TeV (c,d) in the muon channel at the unfolded level

9 W-boson cross section measurements

Measurements of W-boson production at hadron colliders provide a benchmark for the understanding of quantum chromodynamics and electroweak processes. Predictions for the differential and fiducial cross sections are available up to NNLO accuracy in QCD and include EW corrections at next-to-leading-order (NLO) accuracy. The rapidity distribution of Drell-Yan production is sensitive to the underlying QCD dynamics and, in particular, to the parton distribution functions (PDFs) which define the initial kinematics of the hard process. Therefore, measurements of weak-boson production offer an excellent opportunity to test models of parton dynamics.

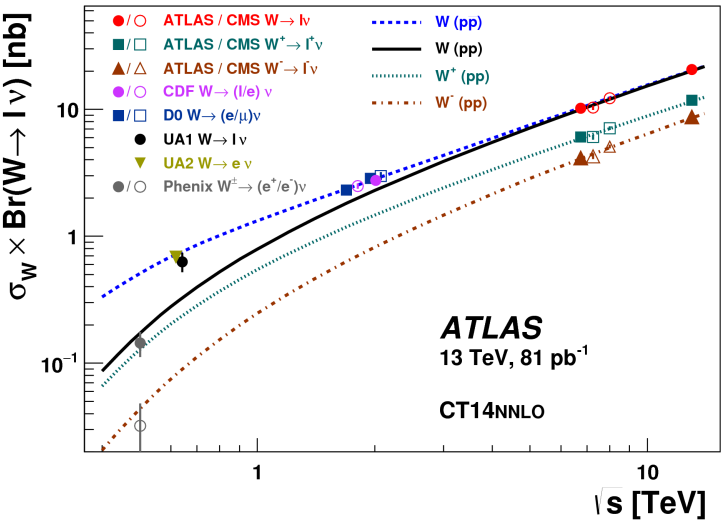

Figure 9.1: The cross-section of W production as a function of $\sqrt{s}$ [49]

The W-boson cross-section has been measured at different center-of-mass energies, with results shown in Fig. 9.1. The latest measurements are performed in pp collisions at $\sqrt{s}$ = 2.76, 7, 8 and 13 TeV, by the collaborations of LHC. Measurements at $\sqrt{s}$ = 7 and 8 TeV have the best precisions, benefiting from the relatively high statistics and medium-level pile-up ($\sim$ 9). The 2.76-TeV measurement is limited by luminosity while 13-TeV measurement suffers high-pile-up effects.

The measurement to W-boson-production cross-section at $\sqrt{s}$ = 13 TeV with high-pile-up data taken in 2015 is described in reference [49]. The systematic uncertainty of cross-section in separate channel is 2%~3%, mostly due to the energy calibration of jet objects that used in E_T^{Miss} building, and the multi-jet background estimation. Thanks to the dedicated low-pile-up procedures, such uncertainties are feasibly suppressed to sufficiently lower level. The hadronic recoil reconstructed from PFO objects rather than hard and soft jets are proven to have much better performance in E_T^{Miss} evaluation, and the

developed multi-jet estimation strategy provides accurate imitation of multi-jet behavior in control regions, effectively improving the precision. Reactivating the measurement with low-pile-up data at $\sqrt{s}$ = 13 TeV will provide a powerful cross check, help to reduce the systematic uncertainty with combination, thus set tighter constraints to PDFs and predictions.

The cross-section measurement at low-pile-up was initialized with data of $< \mu > = 1$, at $\sqrt{s}$ = 5.02 TeV collected from a special LHC run in 2015, using the configuration pretty similar to the low-pile-up data, partly as an early access. It's the first measurements to pp collision production at $\sqrt{s}$ = 5 TeV, energy of LHC proton–lead (p+Pb) and lead–lead (Pb+Pb) collisions. Result from the pp collisions is therefore important reference to the PDFs of both pp and heavy-ion collisions. In addition, new strategies used in the present low-pile-up measurements were initially tested and developed in this measurements, including the NNLO simulation with DYTURBO, multi-jet estimation, reconstruction and calibration of PFO-based hadronic recoil, extrapolated lepton corrections from high-pile-up data and channel combination procedure. All related studies are published in Ref. [65], and as the basis of this chapter.

The main limit of this 5-TeV measurement is the statistics: integrated luminosity is 25 pb^{-1}, one tenth of the 5-TeV data taken in 2017. Therefore the statistical uncertainty is dominant in all corrections, in particular the lepton scale factor and recoil energy calibration. Moreover the data-driven multi-jet evaluation would be biased under this situation, thus a tighter isolation is applied to reject as possibly many MJ background candidates, which potentially degrades the channel agreement due to the mis-modelling in topo-cluster and tracks. Most of these problems are unambiguously solved by exploiting the newly collected data at $\sqrt{s}$ = 5 TeV.

9.1 Methodology

In adapting with the capability of detector, cross sections are measured within a phase space where the detector has high object reconstruction efficiency and accurate energy calibration, named fiducial phase space. The fiducial phase space at $\sqrt{s}$ = 5 and 13 TeV are defined as:

- $\sqrt{s}$ = 5 TeV : $p_T^l > 25$ GeV, $p_T^\nu > 25$ GeV, $|\eta_l| < 2.5$, $m_T > 40$ GeV;
- $\sqrt{s}$ = 13 TeV : $p_T^l > 25$ GeV, $p_T^\nu > 25$ GeV, $|\eta_l| < 2.5$, $m_T > 50$ GeV.

In the fiducial region, the general strategy for cross section measurement is proceeded with this equation:

$$\sigma^{\text{fid}}_{W^\pm \to l^\pm \nu} = \frac{N_W - B_W}{C_W \cdot L_{\text{int}}}, \tag{9.1}$$

In Eq. 9.1, L_{int} is the integrated luminosity of data, i.e. 258.4 pb^{-1} and 339.8 pb^{-1} at $\sqrt{s}$ = 5 TeV and 13 TeV, determined with method introduced in Ref. [71]. N_W and B_W are the number of observed events passing selection in data and estimated backgrounds events with simulation, subtraction is the estimated signal events in data. C_W is the correction for the event detecting efficiency, obtained from the MC samples, written as:

$$C_W = \frac{N_W^{\text{MC,sel}}}{N_W^{\text{MC,fid}}} .$$

where $N_W^{\mathrm{MC,sel}}$ is the number of events passing the selection at the detector level and $N^{\mathrm{MC,fid}}$ is computed applying the fiducial requirements to the generator-level leptons originating from W boson decays, both calculated from the prediction of signal processes. $N_W^{\mathrm{MC,sel}}$ is corrected for the observed differences between data and simulation, while $N^{\mathrm{MC,fid}}$ is selected with the "born" level leptons, i.e. leptons before final-state radiations induced by the QED effect.

The expressions described above is extended to the measurement of differential cross sections as a function of the decay lepton pseudorapidity in W boson production so that the dependence of cross section is comparable to different PDFs. Eq. (9.1) is then adjusted for the measurements in differential bins of absolute pseudorapidity, modified to that the cross sections are divided by the width of the corresponding interval. The boundaries of lepton $|\eta|$ are defined as:

- 0 – 0.21 – 0.42 – 0.63 – 0.84 – 1.05 – 1.37 – 1.52 – 1.74 – 1.95 – 2.18 – 2.50;

which is generic at all center-of-mass energies, following Ref. [72].

9.2 Event selection, corrections and backgrounds estimation

The procedure of cross-section calculation is analogous to the inversion of transverse momentum measurement, so it's natural to study them in same experimental phase space. The selection to signal at detector level is identical to the selection of p_T^W measurement, described in Chap. 7.2. To maintain the independence of the cross-section measurement to p_T^W measurement, there is no selection on p_T^W.

Corrections, same as those in p_T^W analyses, are applied to MC, and cause different effects. The p_T^W measurement is led by the performance of hadronic recoil, while the cross section is more sensitive to lepton corrections, in particular the efficiency scale factors, since the scale factors direct influence the C_W, hence $\sigma^{\mathrm{fid}}_{W^\pm\to l^\pm\nu}$. The recoil calibration varies the events with E_T^{miss} and m_T near the boundary of signal region, and the effect is tiny when E_T^{miss} and m_T cut are remote to the peak.

Physical corrections are sub-dominant here: the QED effects, especially the FSR are absorbed by exploiting "born" level leptons; the QCD effects, including the rapidity correction, and the angular coefficients are negligible when no selection is applied to p_T^W. The PDF mostly contribute to the predicted cross-section of background processes during normalization, thereby estimated in the systematic uncertainty of backgrounds which is dominated by multi-jet.

The sources of uncertainties in cross-section measurements are given by all terms of Eq. 9.1, i.e. N_W, B_W, L_{int} and C_W. N_W is only associated to statistical uncertainty, approximately $\sqrt{N_W}$, subdominant to others.

Luminosity calibration in ATLAS uses the dedicated van der Meer scans [71]. Data analysis yileds a relative systematic uncertainty of 2% (2%) from the scan performed in pp collisions at $\sqrt{s} = 13(5)TeV$, with the LUCID-2 detector for the baseline luminosity measurements [73]. The luminosity uncertainty is led by the systematic effects related to the van der Meer scans and the long-term stability of the luminosity calibration.

The precision of C_W is determined by the corrections applied to simulation, composed of the lepton calibration and efficiency, and hadronic recoil calibration. The dedicated energy scale and resolution are measured for low-pile-up data, and with tag-and-probe framework, the efficiencies are measured at excellent precision. The uncertainty assigned to the hadronic recoil calibration is derived using events with Z boson production to cover the bias in ΣE_T reweighting as well as the residual data-simulation discrepancy in response and resolution.

Uncertainties in the evaluation of EW and top-quark backgrounds are estimated by varying the respective normalisation cross sections. Predictions of the single-vector-boson production are given at NNLO and NNLL, thus have relatively small uncertainty, while for di-boson and top-quark processes the uncertainty in the cross sections is conservatively taken as 10%. Due to different multi-jet production cross sections and kinematics, the fraction of multi-jet events in signal region at $\sqrt{s}$ = 13 TeV is about 3 times of that at $\sqrt{s}$ = 5 TeV. However, thanks to the low-pile-up conditions and optimized estimation procedure, the uncertainty induced by multi-jet is significantly reduced comparing to previous measurements.

9.3 Results using data collected in 2015

9.3.1 Measurement uncertainties

The analysis of data from the scan performed in pp collisions at $\sqrt{s}$ = 5.02 TeVyields a relative systematic uncertainty of 1.9% in the measured luminosity. The efficiency scale factors for 2015-low-pile-up data are calculated in-situ while the energy and resolution calibrations of leptons are based on high-pile-up results with extra uncertainties accounting for the discrepancy. The impact of the recoil calibration on the $u_\perp$ and $u_\parallel + p_{\mathrm{T}}^Z$ distributions varies between a few percent and ~20% in the range $[-15, +15]$ GeV, which dominates the reported cross-section measurements. After applying this correction to events with W^+ and W^- production, the resulting uncertainties on the cross-section measurements are at the level of 0.5% for both the muon and electron channels. A summary of these uncertainties on the inclusive C_W is presented in Table 9.1 and 9.2, with respect to electron channel and muon channel.

In background evaluation, the multi-jet procedure has not been updated then, causing a observable bias in the fit templates, especially in the electron channel, illustrated in Fig. 9.2. To reduce influence from such bias, a rather tight isolation is adopted, named "FixedCutTight", defined as requiring both "ptvarcone20/pT" and "topoetcone20/pT" less than 0.06. And the related uncertainties are consequently evaluated to be 0.7–0.8% in the $W^\pm \to e^\pm \nu$ channels and not more than 0.2% in the $W^\pm \to \mu^\pm \nu$ channels.

Table 9.3 summarises background contributions to the W^+ and W^- boson candidate samples.

9.3.2 Results

Results of cross-section measurements in the electron and muon channels are summarised in Table 9.4 for W^+ boson production and Table 9.5 for W^- boson production. In these tables, the statistical

Process	$W^+ \to e\nu$		$W^- \to e\nu$	
Uncertainties on $\delta C_W/C_W$ (%)	Up	Down	Up	Down
EG_RESOLUTION_ALL	0.07	-0.05	0.05	0.03
EG_SCALE_ALL	0.27	-0.25	0.25	-0.21
EL_EFF_Reco_FULL	0.24	-0.24	0.22	-0.22
EL_EFF_ID_FULL	0.62	-0.62	0.54	-0.54
EL_EFF_Iso_FULL	0.43	-0.43	0.40	-0.40
EL_EFF_Trig_FULL	0.24	-0.24	0.22	-0.22
Recoil_Calibration	0.50	-0.50	0.43	-0.43
Pile-up	-	-	-	-
Charge misidentification	±0.10		±0.10	
Total uncertainty (%)	+0.89	−0.87	+0.78	−0.78

Table 9.1: Summary of the different terms contributing to the uncertainty on C_W for electron final states of 2015-5-TeV data. The decomposition has been made such that correlations between the various contributions are negligible.

Process	$W^+ \to \mu^+\nu$	$W^- \to \mu^-\nu$
Source	**Uncertainty**	
muon reconstruction/identification	0.20%	0.20%
muon isolation	0.37%	0.37%
muon trigger	1.29%	1.29%
muon ID track smearing	0.04%	0.01%
muon MS track smearing	0.08%	0.01%
muon momentum scale	0.14%	0.12%
recoil calibration	0.51%	0.50%
total	1.46%	1.45%

Table 9.2: Systematic uncertainties on the inclusive C_W correction factor in the muon channel.

uncertainty is defined from the variance of background-subtracted number of observed events, and the systematic uncertainty includes all uncertainty components described above, except for the luminosity uncertainty, which is given separately. The systematic uncertainties coming from lepton efficiency corrections are measured as a function of lepton η and p_{T}, and include a significant statistical component due to the number of Z events used to derive the corrections. This statistical component is substantially reduced for the integrated cross sections compared to the differential ones.

9.3.3 Channel combination

To account for the correlations of systematic uncertainties across the channels and bins, the Best Linear Unbiased Estimate (BLUE) method [74] is used to combine measured results from electron and muon channel. The $|\eta_\ell|$ and $|y_{\ell\ell}|$ distributions for the electron channel, muon channel and combined results are shown in Figures 9.3 and the results are listed in Table 9.6 and 9.7. In the interval

Table 9.3: Background contributions as a percentage of the total for the W^+ and W^- candidate samples in the electron (muon) channels.

Background	$W^+ \to e^+\nu$ ($W^+ \to \mu^+\nu$) [%]	$W^- \to e^-\nu$ ($W^- \to \mu^-\nu$) [%]
$Z \to \ell^+\ell^-$, $\ell = e, \mu$	0.1 (2.8)	0.2 (3.8)
$W^\pm \to \tau^\pm\nu$	1.8 (1.8)	1.8 (1.8)
$Z \to \tau^+\tau^-$	0.1 (0.1)	0.1 (0.1)
Multi-jet	0.9 (0.1)	1.4 (0.2)
Top quark	0.1–0.2 (0.1–0.2)	0.1–0.2 (0.1–0.2)
Diboson	0.1 (0.1)	0.1 (0.1)

Table 9.4: Measured fiducial $W^+ \to \ell^+\nu$ differential and integrated cross sections for electron and muon channels.

		$W^+ \to e^+\nu$				$W^+ \to \mu^+\nu$			
$\lvert\eta_\ell\rvert^{\text{min}}$	$\lvert\eta_\ell\rvert^{\text{max}}$	$\mathrm{d}\sigma/\mathrm{d}\lvert\eta_\ell\rvert$ [pb]	$\delta\sigma_{\text{stat}}$ [pb]	$\delta\sigma_{\text{syst}}$ [pb]	$\delta\sigma_{\text{lumi}}$ [pb]	$\mathrm{d}\sigma/\mathrm{d}\lvert\eta_\ell\rvert$ [pb]	$\delta\sigma_{\text{stat}}$ [pb]	$\delta\sigma_{\text{syst}}$ [pb]	$\delta\sigma_{\text{lumi}}$ [pb]
0.00	0.21	448	8	10	8	473	9	15	9
0.21	0.42	463	8	10	9	472	8	11	9
0.42	0.63	453	8	10	9	493	8	11	9
0.63	0.84	460	8	10	9	460	9	12	9
0.84	1.05	466	9	11	9	478	9	13	9
1.05	1.37	469	7	10	9	478	6	10	9
1.37	1.52	–	–	–	–	482	9	12	9
1.52	1.74	460	9	14	9	482	7	10	9
1.74	1.95	454	9	14	8	472	8	10	9
1.95	2.18	453	9	14	8	443	7	10	9
2.18	2.50	370	7	14	7	371	7	9	7
0.00	2.50	2243	13	27	42	2303	12	36	44

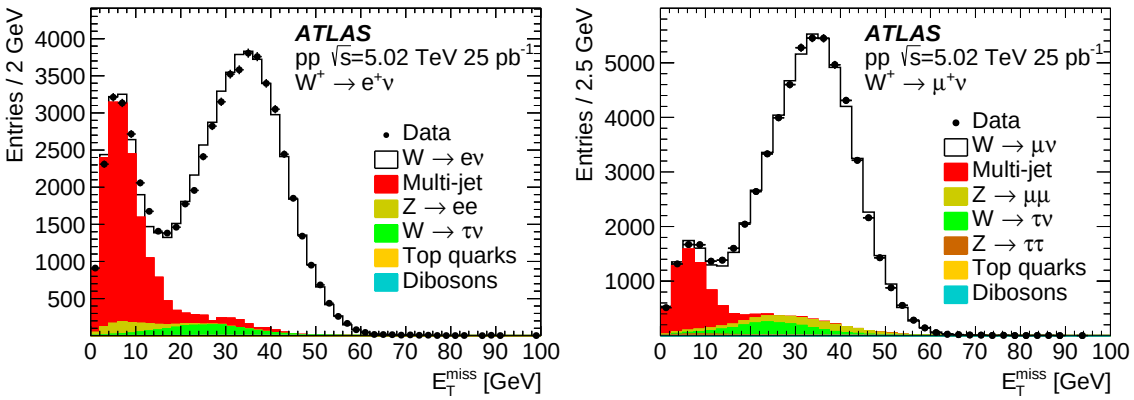

(a) (b)

Figure 9.2: Distributions of $E_{\mathrm{T}}^{\mathrm{miss}}$ used to extract multi-jet yields in the (a) electron and (b) muon channels after performing the template fits. Only the statistical uncertainties of the data are shown.

Table 9.5: Measured fiducial $W^- \to \ell^- \nu$ differential and integrated cross sections for electron and muon channels.

		$W^- \to e^- \nu$				$W^- \to \mu^- \nu$			
$\lvert\eta_\ell\rvert^{\mathrm{min}}$	$\lvert\eta_\ell\rvert^{\mathrm{max}}$	$\mathrm{d}\sigma/\mathrm{d}\lvert\eta_\ell\rvert$ [pb]	$\delta\sigma_{\mathrm{stat}}$ [pb]	$\delta\sigma_{\mathrm{syst}}$ [pb]	$\delta\sigma_{\mathrm{lumi}}$ [pb]	$\mathrm{d}\sigma/\mathrm{d}\lvert\eta_\ell\rvert$ [pb]	$\delta\sigma_{\mathrm{stat}}$ [pb]	$\delta\sigma_{\mathrm{syst}}$ [pb]	$\delta\sigma_{\mathrm{lumi}}$ [pb]
0.00	0.21	322	7	7	6	341	8	10	6
0.21	0.42	316	7	7	6	314	7	6	6
0.42	0.63	303	7	7	6	327	7	6	6
0.63	0.84	294	7	7	6	303	7	7	6
0.84	1.05	300	7	7	6	306	7	8	6
1.05	1.37	280	5	6	5	290	5	5	6
1.37	1.52	–	–	–	–	276	7	6	5
1.52	1.74	270	7	9	5	272	6	5	5
1.74	1.95	260	7	9	5	245	6	5	5
1.95	2.18	255	7	9	5	253	5	5	5
2.18	2.50	220	6	10	4	219	5	5	4
0.00	2.50	1393	10	17	26	1412	9	22	28

$1.37 < |\eta_\ell| < 1.52$, only the muon channel measurements for W boson production are used. The combination yields χ^2/d.o.f= 19.3/10 for the W^+ boson results and χ^2/d.o.f= 15.1/10 for the W^- boson results In view of this remaining discrepancy and of the general trend of the muon channel cross sections to be higher than the electron channel ones, the systematic uncertainties in the efficiency corrections are scaled such that χ^2/d.o.f=1; the correction uncertainties are scaled by a common factor, preserving the uncertainty correlations as a function of lepton p_{T} and η for this source. This scaling is already included in the tables. The measured ratio of fiducial W^+ and W^- production cross sections, as well as ratios of fiducial $W^\pm$ and Z production cross sections, are summarised in Table 9.8.

Table 9.6: Combined fiducial $W^+ \to \ell^+\nu$ differential and integrated cross sections.

		$W^+ \to \ell^+\nu$			
$\lvert\eta_\ell\rvert^{\min}$	$\lvert\eta_\ell\rvert^{\max}$	$\mathrm{d}\sigma/\mathrm{d}\lvert\eta_\ell\rvert$ [pb]	$\delta\sigma_{\mathrm{stat}}$ [pb]	$\delta\sigma_{\mathrm{syst}}$ [pb]	$\delta\sigma_{\mathrm{lumi}}$ [pb]
0.00	0.21	456	6	11	9
0.21	0.42	467	6	9	9
0.42	0.63	471	6	9	9
0.63	0.84	460	6	10	9
0.84	1.05	471	6	11	9
1.05	1.37	474	5	9	9
1.37	1.52	482	9	15	9
1.52	1.74	474	6	11	9
1.74	1.95	465	6	11	9
1.95	2.18	446	6	10	9
2.18	2.50	371	5	10	7
0.00	2.50	2266	9	29	43

Table 9.7: Combined fiducial $W^- \to \ell^-\nu$ differential and integrated cross sections.

		$W^- \to \ell^-\nu$			
$\lvert\eta_\ell\rvert^{\min}$	$\lvert\eta_\ell\rvert^{\max}$	$\mathrm{d}\sigma/\mathrm{d}\lvert\eta_\ell\rvert$ [pb]	$\delta\sigma_{\mathrm{stat}}$ [pb]	$\delta\sigma_{\mathrm{syst}}$ [pb]	$\delta\sigma_{\mathrm{lumi}}$ [pb]
0.00	0.21	329	5	8	6
0.21	0.42	315	5	6	6
0.42	0.63	315	5	6	6
0.63	0.84	298	5	6	6
0.84	1.05	303	5	7	6
1.05	1.37	286	4	5	6
1.37	1.52	276	7	7	5
1.52	1.74	272	4	6	5
1.74	1.95	249	4	5	5
1.95	2.18	253	4	6	5
2.18	2.50	219	4	6	4
0.00	2.50	1401	7	18	27

Table 9.8: Ratios of integrated W and Z production cross sections.

$R^{\mathrm{fid}}_{W^+/W^-}$	1.617 ± 0.012 (stat) ± 0.003 (syst)
$R^{\mathrm{fid}}_{W/Z}$	9.81 ± 0.13 (stat) ± 0.01 (syst)
$R^{\mathrm{fid}}_{W^+/Z}$	6.06 ± 0.08 (stat) ± 0.01 (syst)
$R^{\mathrm{fid}}_{W^-/Z}$	3.75 ± 0.05 (stat) ± 0.01 (syst)

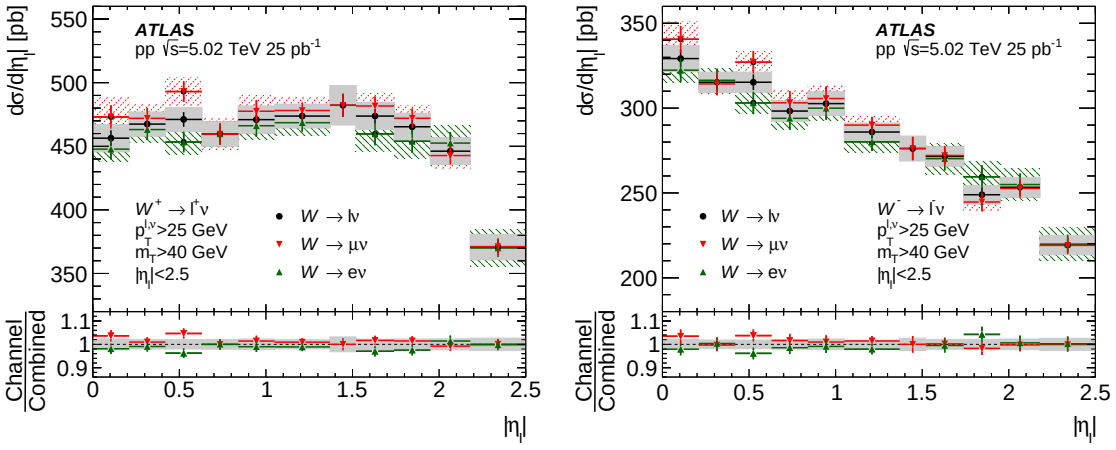

(a) (b)

Figure 9.3: Differential (a) W^+ and (b) W^- boson production cross sections as a function of absolute decay lepton pseudorapidity, for the electron, muon and combined results. Statistical and systematic errors are shown as corresponding bars and shaded bands. The luminosity uncertainty is not included. The lower panel shows the ratio of channels to the combined differential cross section in each bin. In the lower panel, error bars represent statistical uncertainties in the ratio, while the shaded band represents systematic uncertainties in the combined differential cross sections.

This angular difference and the relative yields of W^+ and W^- bosons produced in heavy ion relative to pp collisions manifests itself in a lepton charge asymmetry, defined as a difference in positive and negative lepton yields divided by their sum. A measurement of this asymmetry as a function of pseudorapidity is quite robust, as many systematic effects cancel out in the ratio. Therefore, the W bosons are well suited to probe the characteristics of the initial state of heavy ion collisions at LHC energies. The measurements of differential W^+ and W^- production cross sections allow the extraction of the W boson charge asymmetry, as a function of the absolute pseudorapidity of the decay lepton:

$$A_\ell(|\eta_\ell|) = \frac{\mathrm{d}\sigma_{W^+}/\mathrm{d}|\eta_\ell| - \mathrm{d}\sigma_{W^-}/\mathrm{d}|\eta_\ell|}{\mathrm{d}\sigma_{W^+}/\mathrm{d}|\eta_\ell| + \mathrm{d}\sigma_{W^-}/\mathrm{d}|\eta_\ell|}.$$

Uncertainties in A_ℓ are calculated considering all sources of correlated and uncorrelated systematic uncertainties in the differential cross sections. The resulting dependence of A_ℓ on $|\eta_\ell|$ measured in the electron and muon channels is presented in Figure 9.4 together with the combined values, while the combined results are summarised with the corresponding uncertainties in Table 9.9. The agreement between two channels is found to be quite compatible.

9.3.4 Comparison with theoretical predictions

Theoretical predictions of the fiducial and total cross sections are computed using DYTURBO. DYTURBO is a modified version of DYNNLO 1.5 [61, 62] optimised for speed of computation, providing full NNLO calculations for Drell-Yan processes with parameters set according to the the G_μ scheme [75]. The parameters including the Fermi constant G_F, the masses and widths of

Table 9.9: Charge asymmetry for W bosons as a function of absolute pseudorapidity of the decay lepton.

$\lvert\eta_\ell\rvert^{\text{min}}$	$\lvert\eta_\ell\rvert^{\text{max}}$	A_ℓ	δA_{stat}	δA_{syst}
0.00	0.21	0.163	0.010	0.001
0.21	0.42	0.195	0.009	0.001
0.42	0.63	0.201	0.009	0.001
0.63	0.84	0.213	0.010	0.001
0.84	1.05	0.218	0.010	0.001
1.05	1.37	0.248	0.008	0.001
1.37	1.52	0.272	0.014	0.002
1.52	1.74	0.271	0.009	0.001
1.74	1.95	0.300	0.010	0.001
1.95	2.18	0.276	0.010	0.001
2.18	2.50	0.256	0.010	0.001

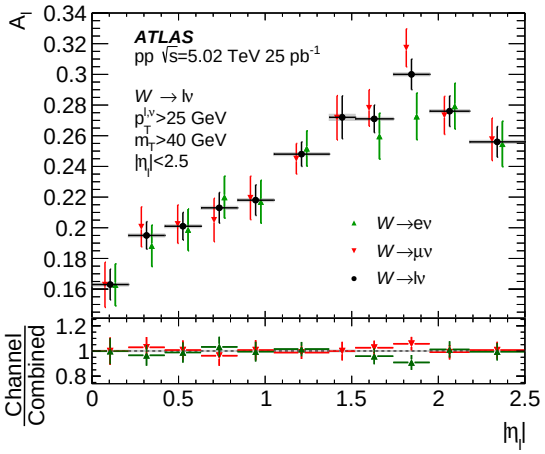

Figure 9.4: Charge asymmetry for W bosons as a function of absolute decay lepton pseudorapidity, for the electron, muon and combined results. Statistical and systematic errors are shown as corresponding bars and shaded bands (not visible for most points). The lower panel shows the ratio of channels to the combined charge asymmetry in each bin. In the lower panel, error bars represent statistical uncertainties in the ratio, while the shaded band represents systematic uncertainties in the combined charge asymmetry.

vector bosons, and the CKM matrix elements) are taken from Ref. [76]. The renormalisation and factorisation scales, respectively denoted as μ_R and μ_F, are also set equal to invariant mass of vector boson. The following PDF sets are used in predictions: CT14NNLO [77], NNPDF3.1 [78], MMHT14NNLO68CL [63], HERAPDF2.0 [79] and ABMP16 [80]. All considered PDF sets except HERAPDF2.0 are evaluated from global fits which include to varying extents the LHC measurements of W/Z boson, Drell-Yan, top-quark and inclusive jet production.

Uncertainties in the prediction and generation are derived from the following sources:

- PDF uncertainties are evaluated from the variations of the NNLO PDFs.
- Scales uncertainties are defined by the envelop of the variations in which the scales are changed

by factors of two subject to the constraint $0.5 \leq \mu_R/\mu_F \leq 2$

- The strong coupling constant α_S is varied by ±0.001 to correspond to 68% CL, following the prescription in Ref. [77].
- Additional systematic uncertainty of 0.7% is given by Ref. [72] due to the intrinsic limitations of the NNLO calculations for fiducial cross-section predictions.
- The uncertainty of the LHC proton beam energy is approximately 0.1%, inducing an uncertainty of 0.1% in the cross-section predictions, but is negligible comparing to other sources.

Differential cross sections are displayed in Fig. 9.5 as a function of $|\eta_\ell|$. The results from the combined measurement are compared to the theoretical predictions calculated with different PDF sets, with uncertainties assigned. In some regions of phase space, a comparison of the differential cross sections shows systematic deviations of the predictions obtained with recent PDF sets from the measured values. These deviations are largest for W^+ boson production and at central rapidity for Z boson production.

The measured lepton charge asymmetry for W bosons shown in Figure 9.6 is compared with predictions calculated with the PDF sets mentioned previously. In most of the $|\eta_\ell|$ range considered, the predictions from all PDF sets tend to underestimate the measured asymmetry by a few percent.

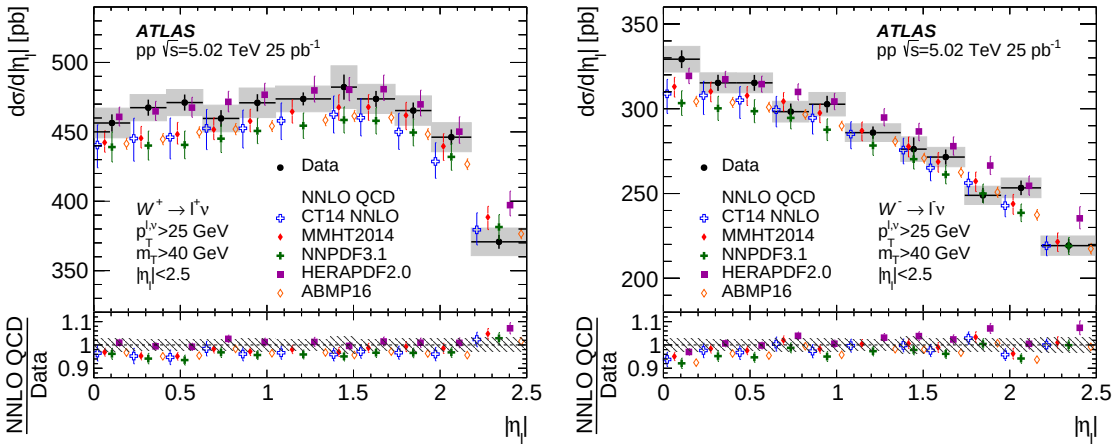

(a) (b)

Figure 9.5: Differential cross sections for (a) W^+ and (b) W^- boson production as a function of absolute decay lepton pseudorapidity compared with theoretical predictions. Statistical and systematic errors are shown as corresponding bars and shaded bands on the data points. The luminosity uncertainty is not included. Only the dominant uncertainty (PDF) is displayed for the theory. The lower panel shows the ratio of predictions to the measured differential cross section in each bin, and the shaded band shows the sum in quadrature of statistical and systematic uncertainties of the data.

As a short summary, the inclusive and differential cross sections are reported in electron and muon decay channels of W-boson production. The lepton charge asymmetry as a function of absolute lepton pseudorapidity is also measured. The agreement between electron and channel results are found to be pretty good regarding the measurement precision. The combined fiducial cross sections are measured

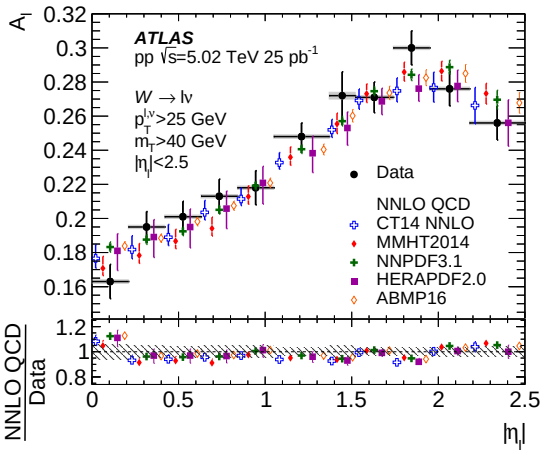

Figure 9.6: Charge asymmetry for W bosons as a function of absolute decay lepton pseudorapidity compared with theoretical predictions. Statistical and systematic errors are shown as corresponding bars and shaded bands on the data points. Only the dominant uncertainty (PDF) is displayed for the theory. The lower panel shows the ratio of predictions to the measured differential cross section in each bin, and the shaded band shows the sum in quadrature of statistical and systematic uncertainties of the data.

with a a precision of 1.2% excluding the luminosity uncertainty. When comparing the differential cross section to predictions obtained with various of recent PDF sets, the deviations show to be globally 1–2σ. These results provide the first measurement of $W^{\pm}$ boson production cross sections at the centre-of-mass energy $\sqrt{s}$ = 5.02 TeV and complement previous measurements at $\sqrt{s}$ = 7, 8 and 13 TeV.

	13 TeV				5 TeV			
Process	$W^+ \to e\nu$		$W^- \to e\nu$		$W^+ \to e\nu$		$W^- \to e\nu$	
Uncertainties on $\delta C_W / C_W$ (%)	Up	Down	Up	Down	Up	Down	Up	Down
EG_RESOLUTION_ALL	0.07	-0.07	0.06	0.06	0.08	-0.08	0.08	-0.08
EG_SCALE_ALL	0.31	-0.29	0.30	-0.27	0.31	-0.29	0.30	-0.27
EL_EFF_Reco_FULL	0.39	-0.39	0.37	-0.37	0.39	-0.39	0.37	-0.37
EL_EFF_ID_FULL	0.41	-0.41	0.38	-0.38	0.40	0.40	0.38	-0.38
EL_EFF_Iso_FULL	0.04	-0.04	0.04	-0.04	0.04	0.04	0.04	-0.04
EL_EFF_Trig_FULL	0.29	-0.29	0.31	-0.31	0.30	0.30	0.31	-0.31
Recoil_Calibration	0.14	-0.14	0.38	-0.38	0.18	0.18	0.12	-0.12
Pile-up	-	-	-	-	-	-	-	-
Charge misidentification	±0.10				±0.10			
Total uncertainty (%)	+0.72	−0.71	+0.80	−0.79	+0.70	-0.71	+0.68	-0.78

Table 9.10: Summary of the different terms contributing to the uncertainty on C_W for electron final states of low-pile-up data.

9.4 Results using low-pile-up data

The measurements with low-pile-up data taken in 2017 and 2018 at $\sqrt{s}$ = 5 and 13 TeV have the same sources of uncertainties.

The luminosity at both center-of-mass energies is uncalibrated yet, thus defined with a uncertainty of 5%. The preliminary estimation provided by the luminosity team is that the uncertainty would be 1.5%–2% after calibration, which is smaller than most of Run-II data benefiting from the special conditions.

The uncertainties assigned to the detection corrections described in Chap. 4, 5 and 6 are displayed in Table 9.10. The hadronic recoil algorithm successfully suppress the missing-energy-related uncertainty under 0.5% and the multi-jet uncertainty is less than 0.2% in all channels.

With these improvements, the systematic uncertainty is reduced to 1% regardless of luminosity calibration, and the channel discrepancy is generally within 1 σ. Moreover, the muon corrections are not finished, thus the ultimate channel agreement is expected to be further enhanced.

Table 9.11–9.14 display the inclusive fiducial cross section calculations in electron channel and muon channel at both center-of-mass energies. All uncertainties are contained, shown in the order of statistical, systematic and luminosity uncertainty. The predicted cross-section in tables are calculated at NNLO with DYTURBO and DYNNLO using CT14NNLO PDF set at NNLO. Critical systematic uncertainty reduction is achieved comparing to the published results at $\sqrt{s}$ = 13 TeV and 5 TeV, in addition to the channel agreement improvement, illustrated in Fig. 9.7 and 9.8.

	$W^+ \to \mu^+\nu$	$W^+ \to e^+\nu$
N_{cand}	1.207e+06 ± 1099	1.165e+06 ± 1079
N_{MJ}	9044 ± 796	27973 ± 1756
N_{bkgsub}	1.132e+06 ± 1132 ± 3099 ± 3689	1.086e+06 ± 1115 ± 7820± 3104
C_W	0.75267 ± 0.00035 ± 0.00753	0.727151 ± 0.0003596 ± 0.00727
σ_{fid} [pb]	4425.1 ± 4.9 ± 45.9 ± 235.7	4393.3 ± 5.0 ± 54.1 ± 232.2
DYNNLO CT14nnlo σ_{fid} [pb]: 4500 ± 130		

Table 9.11: Inclusive fiducial cross-section calculations for $W^+ \to e^+\nu$ and $W^- \to e^-\nu$ production at $sqrts$ = 13 TeV.

	$W^- \to \mu^-\nu$	$W^- \to e^-\nu$
N_{cand}	924395 ± 961.5	915117 ± 956.617
N_{MJ}	9053 ± 617	27388 ± 1962
N_{bkgsub}	855812 ± 996 ± 2749 ± 3307	847610 ± 991± 6597 ± 2353
C_W	0.75688 ± 0.00039 ± 0.007567	0.741686 ± 0.0003993 ± 0.007417
σ_{fid} [pb]	3327.6 ± 4.2 ± 34.9 ± 179.2	3363.2 ± 4.3 ± 42.6 ± 177.5
DYTURBO CT14nnlo σ_{fid} [pb]: 3438 ± 100		

Table 9.12: Inclusive fiducial cross-section calculations for $W^+ \to \mu^+\nu$ and $W^- \to \mu^-\nu$ production at $sqrts$ = 13 TeV.

	$W^+ \to \mu^+\nu$	$W^+ \to e^+\nu$
N_{cand}	457292 ± 676	429574 ± 655
N_{MJ}	724 ± 192	3027 ± 554
N_{bkgsub}	437400 ± 691 ± 1197 ± 1002 ± 3689	415397 ± 666 ± 2296 ± 6012
C_W	0.76608 ± 0.000558 ± 0.00766	0.72700 ± 0.000586 ± 0.00727
σ_{fid} [pb]	2209.6 ± 3.8 ± 22.9 ± 115.5	2211.2 ± 4.0 ± 25.3 ± 113.8
DYTRUBO CT14nnlo σ_{fid} [pb]: 2203 +62/-64(PDF) +18/-11(scale)		

Table 9.13: Inclusive fiducial cross-section calculations for $W^+ \to e^+\nu$ and $W^- \to e^-\nu$ production at $sqrts$ = 5 TeV.

	$W^- \to \mu^- \nu$	$W^- \to e^- \nu$
N_{cand}	285505 ± 534.3	273423 ± 522.9
N_{MJ}	755 ± 160	2401 ± 495
N_{bkgsub}	267603 ± 550.8 ± 970.9 ± 875.9	264316 ± 531.5 ± 1547.8 ± 358.1
C_W	0.765053 ± 0.000707 ± 0.00765	0.740028 ± 0.000732 ± 0.007400
σ_{fid} [pb]	1353.7 ± 3.1 ± 14.4 ± 72.1	1382.2 ± 3.1 ± 16.0 ± 71.0
DYTURBO CT14nnlo σ_{fid} [pb]: 1379 +34/-42(PDF) +11/-8(scale)		

Table 9.14: Inclusive fiducial cross-section calculations for $W^+ \to \mu^+ \nu$ and $W^- \to \mu^- \nu$ production at $sqrts$ = 5 TeV.

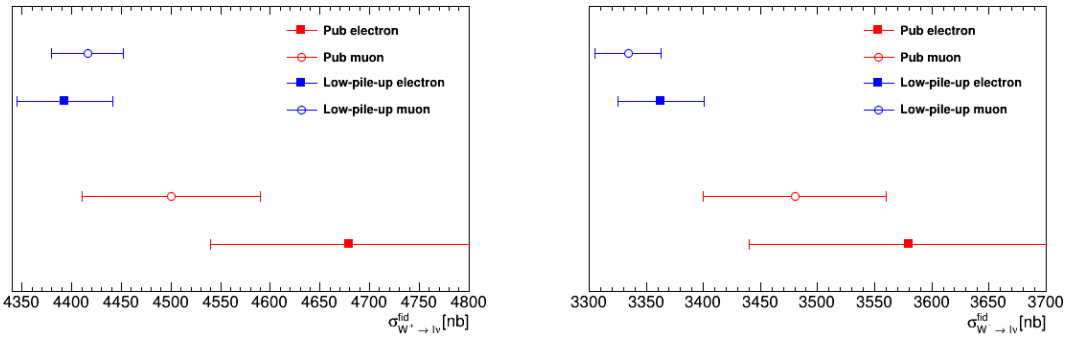

Figure 9.7: Comparison of inclusive W production cross sections and associated total statistical and systematic uncertainty in fiducial region at $\sqrt{s}$ = 13 TeV for W^+(left) and W^-(right) channel between the published results in reference [49] and low-pile-up results.

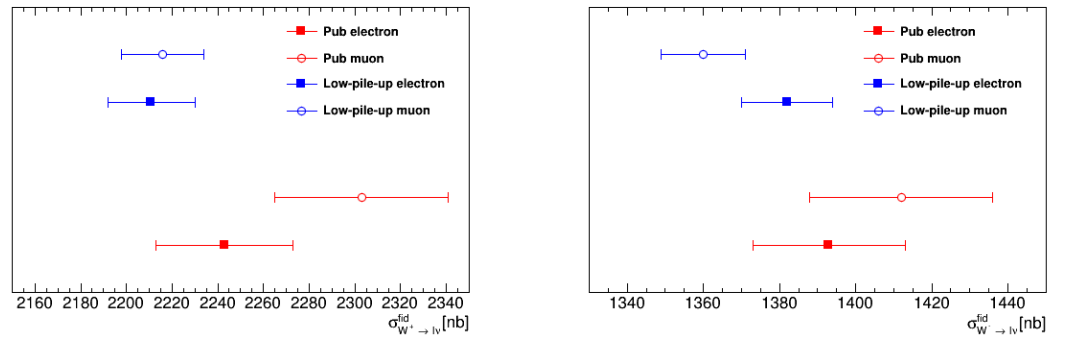

Figure 9.8: Comparison of inclusive W production cross sections and associated total statistical and systematic uncertainty in fiducial region at $\sqrt{s}$ = 5 TeV for W^+(left) and W^-(right) channel between the published results in reference [65] and low-pile-up results.

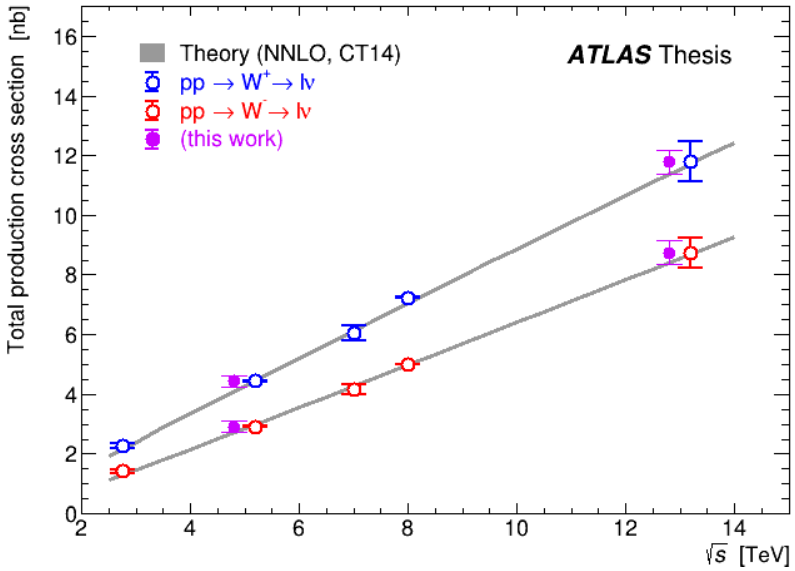

Figure 9.9: All W-boson production cross-sections measured at ATLAS at different $\sqrt{s}$.

10 Measurements of the W-boson mass

The W-mass measurements with low-pile-up data at $\sqrt{s}$ = 5 and 13 TeV are supposed to benefit from the transverse momentum spectrum and cross-section measurements, in the parton shower tune and PDF uncertainty respectively. Proposals to use new fitting algorithm or introduce correlated uncertainties in global W-mass fit are proceeded simultaneously as well. However, the priority is second to finalization of the first two measurements, and no result beyond preliminary uncertainty estimation is available presently. Regardless of the early period, current studies are sufficient for the comparisons of experimental uncertainties between the low-pile-up measurement and the W-mass measurement at 7 TeV, especially the uncertainty in multi-jet background estimation, lepton efficiency and recoil calibration that new strategies. Should the experimental uncertainty comparable to the 7-TeV result, the expected improvements on theoretical uncertainties would be more critical.

10.1 Methodology

The W-mass measurement is performed using fitting procedure with background-subtracted data spectra and set of simulation templates. These templates are originally the MC samples in signal phase space with all corrections applied to preserve the agreement to data. Such simulation are generated with the world-averaged value of W mass as input parameter, but reweighted to various mass windows at truth level exploiting the Breit-Weigner equation:

$$\frac{d\sigma}{dm} \propto \frac{m^2}{(m^2 - m_V^2)^2 + m^4\Gamma_V^2/m_V^2} \tag{10.1}$$

The distribution of observable in data is fit to those templates, and which template provides the optimal agreement is regarded to share the same invariant mass value to data.

More specifically, in this chapter, the standard method in W-mass measurements, χ^2 fit is used for the measurement of central value and uncertainties. The χ^2 is a statistical parameter to describe the difference between the expected frequencies and observed frequencies. To histograms, it's defined as:

$$\chi^2 = \sum_{i=1}^{N_{bin}} \frac{(n_i^{obs} - n_i^{exp})^2}{\sigma_i^2} \tag{10.2}$$

where n_i^{obs} and n_i^{exp} are the number of entries in bin i of the observed (MC templates) and the expected (data) histogram, and σ_i is the statistical uncertainty of $((n_i^{obs} - n_i^{exp})$:

$$\sigma_i = \sigma_i^{obs} \bigoplus \sigma_i^{exp}$$

. The χ^2 equals to zero when the observed and expected histogram is exactly the same.

The χ^2 between data and templates are mapped to different generated masses, thereby the measured W mass is located at the minimum curve of χ^2. In addition, the $\chi^2 - m_W$ map is also used to address the uncertainties of corrections. To minimize the bias in measurements, the target mass of reweighting is shifted by a random value within (-500, 500) MeV, as "blinded mass". This blinding helps to estimate the bias in individual channels as well as the combination to evaluate the level of agreement between electron and muon channel.

All experimental uncertainties in low-pile-up measurement are evaluated with "Full Model" introduced in Chap. 4.3.7, as the correlated uncertainties across all regions, indicating systematic uncertainty and "bin-to-bin" uncorrelated uncertainties, mostly statistical. The variations associated to corrections, modellings and backgrounds are implemented to the blinded signal template to obtain the "pseudo-data" so that the uncertainty of M_W is calculated by duplicating the mass fit with templates and "pseudo-data". The total uncertainty is written as:

$$\Delta_{tot} = \sqrt{\sum_{i=1}^{N}(X_i - X_{base})} \tag{10.3}$$

Ideal observable in M_W fit is required to be sensitive to M_W shifts as well as to have prompt detecting resolution. The transverse momentum of decayed lepton has the best experimental resolution, hence a high sensitivity on M_W. However, the p_T^{lep} distribution also relies on the modelling of PDF and p_T^W, which tend to be the leading uncertainty in p_T^{lep}-fit M_W. In contrast, the W-boson transverse mass, m_T^W, has relatively larger resolution and sensitivity, but it's less dependent on the boson dynamics. At $\sqrt{s}$ = 7 TeV, the m_T^W fit suffers systematic uncertainty from hadronic recoil, and the conclusive M_W adopted the results from single p_T^{lep} fit. But in low-pile-up measurement, the recoil energy is more accurate and since the uncertainty of these two observables are led by different sources, the prospect to have the p_T^{lep}-fit and m_T^W-fit results combined is supposed to reduce the systematic uncertainty and statistical uncertainty. Fig. 10.1 illustrates how the observables' spectra change when reweighted to M_W = 79.3, 80.3, 81.3 GeV.

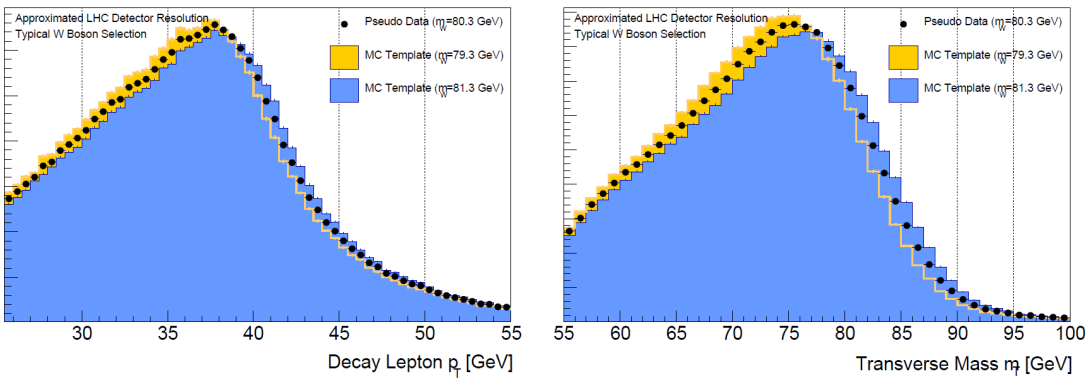

Figure 10.1: p_T^{lep} and m_T distributions of templates reweighted to three W-boson masses [5].

10.2 Event selection and measurement categories

To further upgrade the experimental resolution of observable, there are additional selections to W event applied in W-mass measurement. In addition, categories are defined using the $|\eta|$ of lepton to separate the signal region into regions with relatively better experimental precision (barrel) or better theoretical precision (end-cap). Moreover due the distinct η-geometry of electron and muon detection, the categories are defined independently.

The inclusive signal phase space selection uses all pre-selection and lepton selection of W-event selection in Tab. 7.1 and addition requirement of $p_T^W < 15$ GeV. The performance of this selection is illustrated in Fig. 10.2.

There are three categories exploited in electron channel and four in muon channel:

- Electron channel: $|\eta^{lep}| < 0.6$; $0.6 < |\eta^{lep}| < 1.2$; $1.8 < |\eta^{lep}| < 2.4$.
- Muon channel: $|\eta^{lep}| < 0.8$; $0.8 < |\eta^{lep}| < 1.4$; $1.4 < |\eta^{lep}| < 2.0$; $2.0 < |\eta^{lep}| < 2.4$.

The categorized measurement is essential in M_W. For example, the muon energy scale causes over 100 MeV uncertainty on M_W in the end-cap while less than 10 MeV uncertainty in the barrel region, thus the total momentum uncertainty in category strategy is ~ 5 times smaller than inclusive fit. On the contrary, the PDF uncertainty is smaller in end-cap than barrel.

The $p_T^W < 15$ GeV selection is proved to effectively optimize the resolution in p_T^{lep} and m_T^W, but it would suffer the high uncertainty in p_T^W correction at low p_T^W. New categories using higher p_T^W region, like 15 GeV $< p_T^W <$ 30 GeV, may help to reduce this uncertainty. So the selection and category adopted in this chapter is not yet the consequent decision.

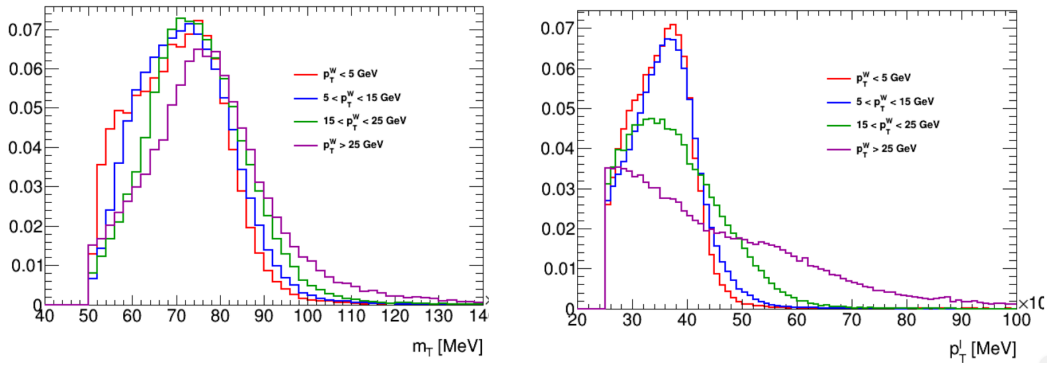

Figure 10.2: p_T^{lep} and m_T distributions with different p_T^W selections at truth level using 13-TeV MC sample.

10.3 Uncertainty evaluation

It's impracticable to have the precise M_W central value measured currently due to the lack of corrections, dedicated selection and category study. The theoretical corrections, including PDF, p_T^W, angular coefficients and QED ISR/FSR haven't been proceeded into the uncertainty calculation step, so only the

impacts on M_W precision of lepton corrections, hadronic recoil calibration and multi-jet background evaluation are reported in this section.

The templates used in W-mass fit are signal MC samples reweighted to $M_W \pm$ [0, 25, 50, 100, 150, 200] MeV which is validated capable in 7-TeV measurement.

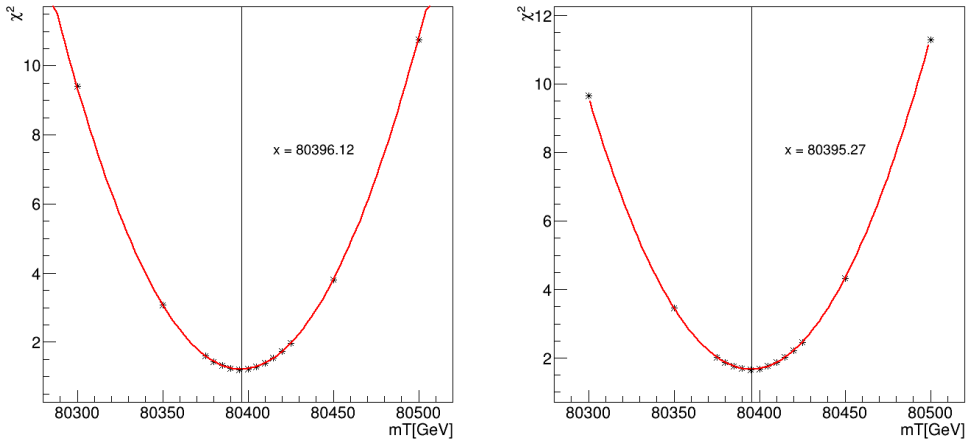

(a) Nominal (b) multijet sys

Figure 10.3: Example of M_W fit using the pseudo-data of nominal and multi-jet-systematic-uncertainty process.

10.3.1 Lepton corrections

The momentum calibration and efficiency correction of leptons are charge-blind. Since the systematic uncertainty is almost identical in W^+ and W^- channel, the results of W^+ are adopted in this section, shown in Tab. 10.1 and 10.2 for electron and muon channel respectively.

Electron

Tab. 10.1 lists the 13-TeV W-mass uncertainties due to energy scale and resolution, the reconstruction, identification, isolation and trigger efficiency scale factors. The energy scale dominates the total uncertainty except the second category in which the identification efficiency overtakes, but the inclusive uncertainty after category combination is completely led by the energy scale. Such uncertainty in p_T^{lep} fit is distinctly at higher level than the uncertainty from 7-TeV energy scale, which is 10/10/16 MeV in the three categories. The major contribution of the calibration uncertainty is the statistical one in extracting energy scales and resolutions from the Z-boson events, hence difficult to lower. The inclusive calibration uncertainty is around 9 MeV.

Uncertainties from efficiency scale factors, as expected, are majorly contributed by the reconstruction and identification. The isolation and trigger uncertainty is negligible to other sources thanks to the pretty loose isolation and trigger criteria, with combined uncertainty around 2-3 MeV, close

$\lvert\eta_\ell\rvert$ range	[0.0, 0.6]		[0.6, 1.2]		[1.82, 2.4]		Combined	
Kinematics	p_{T}^{ℓ}	m_{T}	p_{T}^{ℓ}	m_{T}	p_{T}^{ℓ}	m_{T}	p_{T}^{ℓ}	m_{T}
δm_W [MeV]								
Energy scale	16.7	14.2	19.4	15.8	27.1	23.5	11.6	9.7
Energy resolution	3.3	3.0	2.8	3.5	3.8	3.0	1.5	1.0
Reconstruction efficiency	9.9	8.4	10.9	9.9	8.6	6.6	8.7	7.9
(Reconstruction extrapolation)	3.5	2.1	2.8	2.8	1.6	1.7	2.3	2.3
Identification efficiency	3.8	3.2	13.9	17.6	4.2	2.0	7.9	9.6
(Identification Z-mass)	5.0	3.3	5.9	4.1	5.8	4.1	4.4	3.9
Isolation efficiency	0.3	0.5	0.6	0.7	0.9	0.8	0.7	0.7
Trigger efficiency	1.7	1.2	1.0	1.2	4.1	1.9	1.3	0.7
Total	20.4	17.1	23.2	19.4	29.6	25.0	15.3	13.2

Table 10.1: Systematic uncertainties in the m_W measurement due to electron energy calibration and efficiency corrections for the different kinematic distributions and $|\eta_\ell|$ regions using positive lepton charge.

to the result of 7-TeV, 1-2 MeV. Inclusive uncertainty from reconstruction efficiency is larger than identification when choosing the in-situ measured reconstruction scale factor, calculated from low-pile-up data directly, yet reminded of the alternative method in reconstruction scale factor calculation by extrapolating the high-pile-up reconstruction scale factor to low-pile-up regions with additional uncertainty accounting for the residual discrepancy 4.3, impact of which on M_W is displayed in the row "Reconstruction extrapolation" of Tab. 10.1. This strategy successfully gets rid of over 70% of the reconstruction uncertainty in all categories, halving the total efficiency uncertainty to 5 MeV. Benefiting from the progress of tag-and-probe and the dedicated low-pile-up efficiency studies, the total 13-TeV electron efficiency uncertainty is smaller than ∼10-MeV uncertainty in 7-TeV measurement even with less statistics.

The anomalous identification efficiency number in second category is from the identification scale factor calculated with "Zmass+ZIso" method. The "Zmass" is the default tad-and-probe option for electron SF calculation used in all SFs, while "ZIso" method that exploits the isolation-based data-driven background fit, is only used in electron ID SF. The "ZIso" method is less stable than "Zmass" in background subtraction and left a degraded fit in the second category, thus suffers the high systematic uncertainty. This unusual uncertainty is introduced to final ID SF in the Zmass+Ziso combination, so this issue only happens to 13-TeV "ZIso+Zmass" SF. In the term "Identification Zmass-only", the uncertainty calculated from "Zmass" method is listed, and the second category agrees well with the other two. The solution to background control issue of ZIso method is under investigation and optimization by the tad-and-probe group.

Muon

The M_W uncertainty due to muon corrections are shown in Tab. 10.2. Unlike electron corrections, part of the muon corrections are derived by the MCP group, which are not processed synchronously. The muon momentum calibration is given in the scale, muon spectrometer (MS) correction and

$\lvert\eta_\ell\rvert$ range	[0.0, 0.8]		[0.8, 1.4]		[1.4, 2.0]		[2.0, 2.4]		Combined	
Kinematics	p_{T}^{ℓ}	m_{T}	p_{T}^{ℓ}	m_{T}	p_{T}^{ℓ}	m_{T}	p_{T}^{ℓ}	m_{T}	p_{T}^{ℓ}	m_{T}
δm_W [MeV]										
Muon Scale	27.6	16.8	61.9	32.7	66.1	32.8	92.0	55.5		
Muon ID	4.5	1.8	5.3	12.5	14.4	7.3	44.3	28.6		
Muon MS	3.5	2.1	11.2	6.9	22.9	14.0	29.3	26.9		
Muon Reconstruction & TTVA	0.1	0.1	0.1	0.1	0.1	0.1	0.1	0.1		
Muon Isolation	3.0	1.8	2.4	1.7	5.5	3.4	8.0	5.2		
Muon Trigger	28.2	15.2	26.0	15.3	29.6	20.7	40.7	30.4		
Total										

Table 10.2: Systematic uncertainties in the m_W measurement due to the muon momentum calibration and efficiencies for the different kinematic distributions and $|\eta_\ell|$ regions using $W \to \mu^+\nu$ process.

inner detector (ID) correction, but the "Total" model is applied instead of "Full" model, which means all correlated and uncorrelated uncertainties are added up as one variation, a consequently the related uncertainties are pretty huge to M_W measurement. In addition, the statistical and systematic uncertainties are merged thus unavailable to channel combination. The study to the full model for muon calibration is on-going.

The efficiency uncertainty is dominated by the trigger uncertainty. Ideally the trigger uncertainty is similar to isolation uncertainty and below to reconstruction uncertainty. The statistical uncertainty in trigger efficiency is unusually large, denoting kind of statistics problem. The reconstruction uncertainty is somehow a bit small, which might be from missing uncertainty terms. More efforts have been devoted to muon corrections to handle these problems.

10.3.2 Hadronic recoil calibration

The present hadronic recoil calibration is the binning-based 2-D (ΣE_T-p_T^W) reweighting 6, consisting of three steps: the ΣE_T reweighting between data and simulation, the energy resolution correction and the response correction. Results of 13-TeV positive electron and muon channel are included in Tab. 10.3 and 10.4.

The three components have similar contributions to the uncertainty among categories in same-charge channels, but distinct with respect to channels in Tab. 10.5. Total uncertainty from m_T fit in all channels is 8 MeV, and 4~6 MeV using p_{T}^{ℓ} fit, The combination and optimal-fit-range procedure will have the precision further strengthened.

10.3.3 Multi-jet background

The multi-jet background estimation procedure, as presented in Chap. 7.4.1, though follows the general strategy of 7-TeV MJ estimation, has remarkable optimizations. And thanks to it, as well as the

$\lvert\eta_\ell\rvert$ range	[0.0, 0.6]		[0.6, 1.2]		[1.82, 2.4]		Combined	
Kinematics	p_{T}^{ℓ}	m_{T}	p_{T}^{ℓ}	m_{T}	p_{T}^{ℓ}	m_{T}	p_{T}^{ℓ}	m_{T}
δm_W [MeV]								
ΣE_T reweighting	3.5	7.4	3.6	6.9	4.1	8.2	3.7	6.9
Resolution correction	1.8	3.0	1.8	3.5	2.2	3.3	1.9	3.0
Response correction	2.9	3.5	3.8	3.3	3.4	3.5	3.4	3.2
Total	4.9	8.7	5.5	8.4	5.8	9.4	5.4	8.2

Table 10.3: Systematic uncertainties in the m_W measurement due to the hadronic recoil calibration for the different kinematic distributions and $|\eta_\ell|$ regions using $W^+ \to e^+\nu$ process.

$\lvert\eta_\ell\rvert$ range	[0.0, 0.8]		[0.8, 1.4]		[1.4, 2.0]		[2.0, 2.4]		Combined	
Kinematics	p_{T}^{ℓ}	m_{T}	p_{T}^{ℓ}	m_{T}	p_{T}^{ℓ}	m_{T}	p_{T}^{ℓ}	m_{T}	p_{T}^{ℓ}	m_{T}
δm_W [MeV]										
ΣE_T reweighting	1.0	6.9	0.6	5.7	0.7	5.6	3.0	6.7	1.2	6.2
Resolution correction	2.2	3.7	2.0	3.0	2.3	3.2	2.2	3.0	2.1	3.1
Response correction	3.9	3.4	2.7	3.6	3.8	3.4	3.5	2.0	3.5	3.0
Total	4.6	8.5	3.5	7.4	4.5	7.3	5.1	7.6	4.2	7.6

Table 10.4: Systematic uncertainties in the m_W measurement due to the hadronic recoil calibration for the different kinematic distributions and $|\eta_\ell|$ regions using $W^+ \to \mu^+\nu$ process.

$\lvert\eta_\ell\rvert$ range	[0.0, 0.8]		[0.8, 1.4]		[1.4, 2.0]		[2.0, 2.4]		Combined	
Kinematics	p_{T}^{ℓ}	m_{T}	p_{T}^{ℓ}	m_{T}	p_{T}^{ℓ}	m_{T}	p_{T}^{ℓ}	m_{T}	p_{T}^{ℓ}	m_{T}
δm_W [MeV]										
ΣE_T reweighting	1.4	3.4	1.0	3.0	2.3	2.8	0.9	4.0	1.5	3.2
Resolution correction	2.2	4.6	2.6	3.5	2.1	4.6	2.4	4.6	2.2	4.2
Response correction	6.0	5.6	7.0	5.9	5.6	3.5	6.2	4.5	6.2	4.9
Total	6.5	8.0	7.6	7.5	6.4	6.4	6.7	7.5	6.7	7.2

Table 10.5: Systematic uncertainties in the m_W measurement due to the hadronic recoil calibration for the different kinematic distributions and $|\eta_\ell|$ regions using $W^- \to \mu^-\nu$ process.

low-pile-up condition, multi-jet background should provide the most significant improvement to M_W experimental uncertainty.

The signal phase space is tighter in W-mass measurement, so MJ background demands re-calculation. Categories are not considered in MJ study because as a data-driven method, the estimation is sensitive to the statistics. The extrapolation isolation slices are set the same to Table , i.e. 6 bins from $ptvarcone20/pT$ = 0.10 to 0.40, in step of 0.05. The new multi-jet numbers and systematic uncertainties in all channels are shown in Tab. 10.6. The 85% of 13-TeV multi-jet background and 75% of 5-TeV multi-jet background are rejected by the extra selections for M_W analysis.

Channel	13 TeV	5 TeV
$W^+ \rightarrow e^+\nu$	3202 ± 488	637 ± 255
$W^+ \rightarrow e^-\nu$	3211 ± 451	710 ± 271
$W^+ \rightarrow \mu^+\nu$	1127 ± 261	237 ± 133
$W^+ \rightarrow \mu^-\nu$	1108 ± 250	215 ± 89

Table 10.6: Evaluation of multi-jet contributions to 13 TeV and 5 TeV low-pile-up data with W-mass event signal selections

The uncertainty on MJ event number in Tab. 10.6 is actually the correlated systematic uncertainty. There are also uncorrelated uncertainties in account to the bin-to-bin statistical uncertainty and shape extrapolation uncertainty. Their impacts on M_W are displayed in Tab. 10.7 and 10.8 for data at $\sqrt{s}$ = 13 TeV and 5 TeV respectively. The "Syst" represents the systematic uncertainty in MJ event number extrapolation while the "Stat+shape" denotes the uncorrelated variations. The total uncertainty in all channels is smaller than 4 MeV at $\sqrt{s}$ = 13 TeV and smaller than 3 MeV at $\sqrt{s}$ = 5 TeV. In 7-TeV measurement, the final uncertainty from multi-jet background is 5-10 MeV, over twice the size of low-pile-up results. The channel combination is supposed to improve the uncertainty due to luminosity, MC normalization and statistics.

10.3.4 Statistical uncertainty

The statistical uncertainties in m_W measurement are calculated with simulated samples as well, by scaling the distributions of observables to the event number of data, extracting the statistical error in every bin of rescaled histograms, and performing the fit. Such uncertainty resulted to 6.7 MeV in 7-TeV measurement, as the combination of p_{T}^{ℓ}-fit results of all channels, second to the systematic uncertainty, while for low-pile-up analysis, the limit of luminosity and W-event number is a general issue, which could dominate the conclusive result. Therefore the proposal to combine the results of more than one fits comes up, which is proven practical in the view that the systematic uncertainties associated to two observables, p_T^l and m_T, are comparable.

The "bootstrap" is the strategy to evaluate the correlation between the statistical uncertainties of two observables. 1000 toy are defined, each refers to an additional random event-weight correction following the $\lambda = 1$ poisson function, such that the statistical uncertainty of dataset are propagated as

Process	$W^+ \to e\nu$		$W^- \to e\nu$		$W^+ \to \mu\nu$		$W^- \to \mu\nu$	
Kinematics	p_{T}^{ℓ}	m_{T}	p_{T}^{ℓ}	m_{T}	p_{T}^{ℓ}	m_{T}	p_{T}^{ℓ}	m_{T}
δm_W [MeV]								
Multi-jet Syst	0.8	2.8	0.3	3.1	1.0	1.0	0.7	0.1
Multi-jet Stat+Shape	2.3	2.3	2.9	1.7	1.3	1.3	1.1	1.1
Total	2.4	3.6	2.9	3.5	1.6	1.6	1.3	1.1

Table 10.7: Uncertainties in the m_W measurement due to the multi-jet background estimation for the different kinematic distributions and $|\eta_\ell|$ regions using 13-TeV datasets.

Process	$W^+ \to e\nu$		$W^- \to e\nu$		$W^+ \to \mu\nu$		$W^- \to \mu\nu$	
Kinematics	p_{T}^{ℓ}	m_{T}	p_{T}^{ℓ}	m_{T}	p_{T}^{ℓ}	m_{T}	p_{T}^{ℓ}	m_{T}
δm_W [MeV]								
Multi-jet Syst	1.0	0.3	0.2	2.8	0.2	0.6	0.4	0.1
Multi-jet Stat+Shape	2.2	1.6	2.8	2.4	0.4	0.4	0.9	0.8
Total	2.4	1.6	2.8	2.5	0.5	0.7	0.9	0.8

Table 10.8: Uncertainties in the m_W measurement due to the multi-jet background estimation for the different kinematic distributions and $|\eta_\ell|$ regions using 5-TeV datasets.

the uncertainties of all toys, i.e.:

$$\delta_{stat}(X) = \sqrt{\sum_{i=1}^{N=1000} (X_i - \bar{X})^2} \tag{10.4}$$

$$r = \frac{\sum_{i=1}^{N=1000}(X_i - \bar{X})(Y_i - \bar{Y})}{\delta_{stat}(X) \cdot \delta_{stat}(Y)} \tag{10.5}$$

where $\delta_{stat}(X)$ is the statistical uncertainty of observable "X" and r is the correlation between "X" and "Y". The bootstrap statistical uncertainty and covariance evaluated with MC sample are different to data uncertainty, but the correlation between p_{T}^{ℓ} and m_{T} is identical when MC modelling is perfect. Fig. 10.4 displays the m_W obtained from two observables of all toys in categories. RMS of x-axis or y-axis is M_W statistical uncertainty of corresponding observable, and the covariance divided by the product of $\delta_{stat}(X)$ and $\delta_{stat}(Y)$ is estimated correlation. In all categories the correlation is around 0.55, indicating a less effective observable combination.

The numbers of data event number, M_W statistical uncertainties with two observables in addition to the correlation and combination are recorded in Tab. 10.9 and 10.10, respective to electron channel and muon channel. The statistical uncertainties measured with m_{T} fit and p_{T}^{ℓ} fit are at the same level, comparing to that $\delta_{stat}(m_{\mathrm{T}})$ is approximately two times of $\delta_{stat}(p_{\mathrm{T}}^{\ell})$ at $\sqrt{s} = 7$ TeV, due to the improved recoil resolution. The m_{T}-p_{T}^{ℓ} combined statistical uncertainty is about 16 (23) MeV and 17 (26) MeV for positive and negative channel at $\sqrt{s} = 13$ (5) TeV, marking the M_W result in individual channel is completely led by the statistical uncertainty. If have all channels combined, this uncertainty is roughly halved, to 8 MeV(12 MeV) at $\sqrt{s} = 13(5)$ TeV, comparable to 6.7 MeVof 7-TeV result.

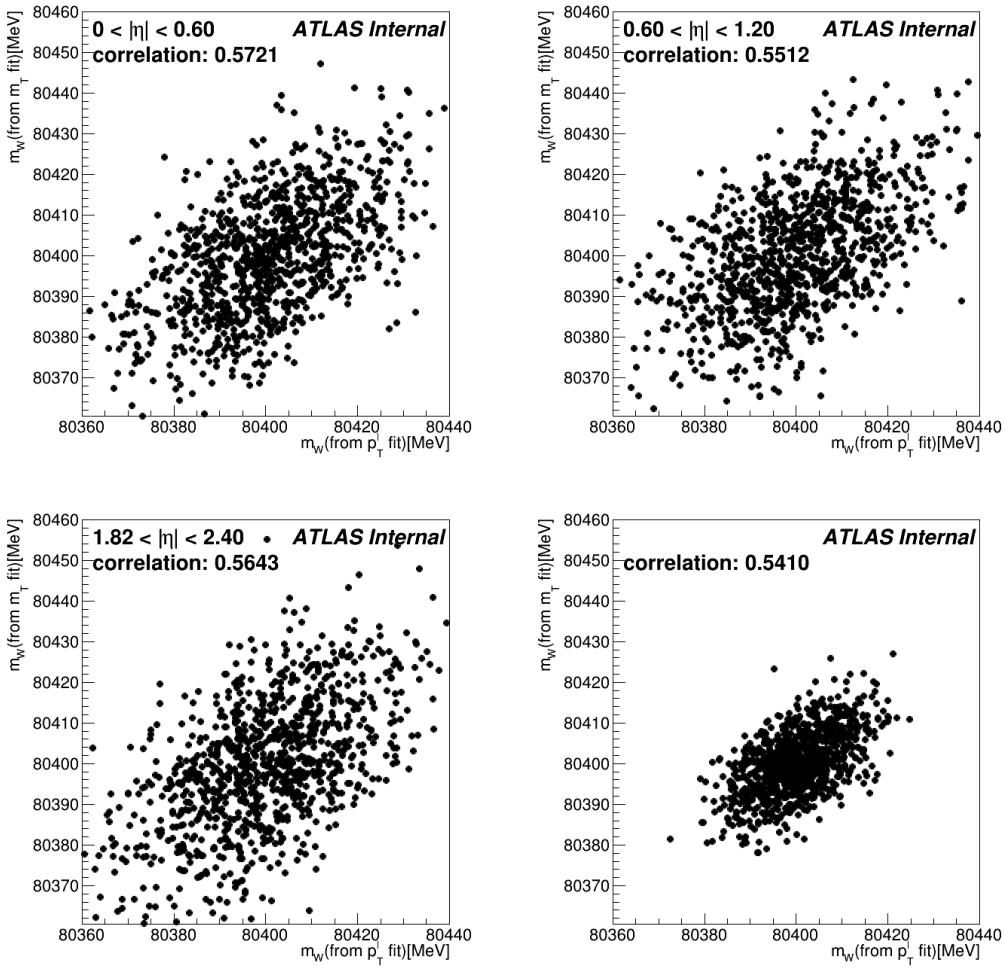

Figure 10.4: M_W obtained from p_{T}^{ℓ} and m_{T} of all toys in bootstrap methods and the p_{T}^{ℓ}-m_{T} correlation in $|\eta|$ categories using $W^+ \to e\nu$ channel at $\sqrt{s}$ = 13 TeV.

10.4 Summary

Preliminary uncertainties of M_W measurement are evaluated with χ^2-fit. The systematic uncertainties due to lepton corrections are no worse than 7-TeV results. In addition, the electron efficiency study, especially the reconstruction and isolation, achieve to decrease the uncertainty using less Z events. The low-pile-up condition significantly upgrades the hadronic recoil performance, as well as the multi-jet background estimation. The later, also with respect to the development of methodology, contributes the prime improvement to experimental systematic uncertainty. Final experimental uncertainties from mT fit and p_{T}^{ℓ} fit are comparable, indicating the 2-dimentional fit a practical prospect.

The statistical uncertainty, suffering the finite integrated luminosity, is always the leading uncertainty in individual and combined results. Considering an ideal statistical uncertainty is supposed to be at most half of the systematic uncertainty, and that the systematic uncertainties from lepton and recoil

$\|\eta_\ell\|$ range	[0.0, 0.6]		[0.6, 1.2]		[1.82, 2.4]		Combined	
Kinematics	p_{T}^{ℓ}	m_{T}	p_{T}^{ℓ}	m_{T}	p_{T}^{ℓ}	m_{T}	p_{T}^{ℓ}	m_{T}
$13\ TeV\ W^+ \to e\nu, N_{data}$				1177k				
Stat[MeV]	32.9	33.8	34.5	34.7	35.4	36.7	17.8	18.2
correlation	0.5721		0.5512		0.5643		0.5410	
$p_{\mathrm{T}}^{\ell} + m_{\mathrm{T}}$[MeV]	29.6		30.5		31.9		15.8	
$13\ TeV\ W^- \to e\nu, N_{data}$				926k				
Stat[MeV]	33.6	34.2	35.4	35.9	40.4	41.2	18.8	19.1
correlation	0.5301		0.5791		0.5173		0.5522	
$p_{\mathrm{T}}^{\ell} + m_{\mathrm{T}}$[MeV]	29.6		31.7		35.5		16.7	
$5\ TeV\ W^+ \to e\nu, N_{data}$				433k				
Stat[MeV]	51.5	46.2	52.8	47.5	52.8	49.1	26.9	24.6
correlation	0.5746		0.6012		0.5957		0.5962	
$p_{\mathrm{T}}^{\ell} + m_{\mathrm{T}}$[MeV]	43.4		44.9		45.5		23.0	
$5\ TeV\ W^- \to e\nu, N_{data}$				276k				
Stat[MeV]	54.2	48.9	56.8	51.6	70.0	66.2	30.8	28.2
correlation	0.5632		0.5992		0.5945		0.5392	
$p_{\mathrm{T}}^{\ell} + m_{\mathrm{T}}$[MeV]	45.6		48.5		60.8		25.9	

Table 10.9: Statistical uncertainties in the m_W measurement for the different kinematic distributions and their combination in $|\eta_\ell|$ regions using the electron channels of 13-TeV and 5-TeV datasets.

correction are as well affected by the number of Z-boson events, 2~3 times more data collected at low-pile-up condition should have this problem solved essentially. The prospect to have weaks- to month-long low-pile-up data taking during Run-III or high-lumi LHC is under inverstigation, which, should be approved, will completely change the game in electroweak precision measurements.

Finally, the top priority is yet to accomplish the low-pile-up measurements to optimize p_T^W and PDF accuracy. Meanwhile the test of various new fitting procedures, for instance, profile-likelihood method, and checking of new correlations between statistical uncertianties will be of values. In addition, the theoretical and experimental improvements is equally applicable to 7-TeV measurement, thus by estimation, to reactivate 7-TeV mass measurement could reduce the conclusive 7-TeV uncertainty from 19 MeV to 13 MeV. And a ultimate ATLAS W-mass combination using 5-TeV, 7-TeV and 13-TeV data is likely to reach the edge of SM prediction, which is foreseen in the coming years.

$\|\eta_\ell\|$ range	[0.0, 0.8]		[0.8, 1.4]		[1.4, 2.0]		[2.0, 2.4]		Combined	
Kinematics	p_{T}^{ℓ}	m_{T}	p_{T}^{ℓ}	m_{T}	p_{T}^{ℓ}	m_{T}	p_{T}^{ℓ}	m_{T}	p_{T}^{ℓ}	m_{T}
13 TeV $W^+ \to \mu\nu, N_{data}$					1251k					
Stat[MeV]	31.9	31.7	34.8	34.9	33.1	34.6	40.9	42.3	17.3	17.6
correlation	0.5761		0.5356		0.5451		0.5290		0.5608	
$p_{\mathrm{T}}^{\ell} + m_{\mathrm{T}}$[MeV]	28.2		30.6		29.7		36.4		15.4	
13 TeV $W^- \to \mu\nu, N_{data}$					970k					
Stat[MeV]	31.7	31.7	36.3	37.0	35.5	36.7	46.2	48.7	18.1	18.5
correlation	0.5068		0.5486		0.5589		0.5907		0.5646	
$p_{\mathrm{T}}^{\ell} + m_{\mathrm{T}}$[MeV]	27.5		32.2		31.9		42.3		16.2	
5 TeV $W^+ \to \mu\nu, N_{data}$					458k					
Stat[MeV]	49.2	44.8	54.3	49.9	50.2	47.0	60.1	57.4	26.4	24.5
correlation	0.5665		0.6087		0.6054		0.6069		0.5665	
$p_{\mathrm{T}}^{\ell} + m_{\mathrm{T}}$[MeV]	41.6		46.7		43.5		52.7		22.5	
5 TeV $W^- \to \mu\nu, N_{data}$					289k					
Stat[MeV]	51.7	47.4	59.4	53.5	60.0	54.5	82.2	79.1	30.2	27.7
correlation	0.5647		0.5926		0.6185		0.5688		0.5647	
$p_{\mathrm{T}}^{\ell} + m_{\mathrm{T}}$[MeV]	43.8		50.4		51.5		71.4		25.6	

Table 10.10: Statistical uncertainties in the m_W measurement for the different kinematic distributions and their combination in $|\eta_\ell|$ regions using the muon channels of 13-TeV and 5-TeV datasets.

11 Conclusion

Standard model is one of the most successful theories in particle physics, perfectly describing three types of interactions. In the validation of standard model and searching for new physics beyond the standard model the precise measurements of electroweak processes play an important role, in particular the Drell-Yan process, defined as that "one vector boson generated from two quarks decays into two leptons", which is well predicted by theory and practicable to be measured at extreme precision experimentally.

A valuable opportunity of Drell-Yan process is provided by the mass of W boson (M_W). In the electroweak sector of standard model, the W-boson mass is strongly dependent on the mass of top quark (M_t) and Higgs boson (M_H). Given the known values of M_t and M_H, standard model predicts M_W to be 80360 ± 8 MeV. However, effects from various BSM theories, like supersymmetry and effective field theory, could shift the central value of M_W by 10-100 MeV. Therefore a direct measurement to M_W with uncertainty less than 10 MeV will provide a stringent probe to BSM physics. The latest experiment was performed using data collected by the ATLAS detector during the Run-I of LHC, with uncertainty of 19 MeV, including 14-MeV theoretical uncertainty, composed of uncertainties due to electroweak effects, strong interaction effects and particle distribution function (PDF) effects, and led by the PDF uncertainty and W-boson-transverse-momentum (p_T^W) uncertainty from the mis-modelling of strong effects.

To gain the target precision, accuracy of p_T^W and PDF demands upgrades. PDF can't be directly predicted from theory, and the experimental inputs are essential to the calculation of PDF. At vector boson mass scale, PDFs are proportional to the generated cross section of Drell-Yan process along rapidity, thus a measurement to W and Z boson cross-section along rapidity is capable to constrain the PDFs and minimize the discrepancy between prediction and reality, hence the uncertainty. The transverse momentum of W boson is endued by higher-order strong effects. It used to be predicted from simulation or calculation, but both failed to simulate the behavior of p_T^W above second order. A measurement to p_T^W under extreme low underlying activity (interactions other than signal) is supposed to half the related uncertainties and resolve the mis-modelling.

The data of collisions under extreme underlying activity is taken in a special low-pile-up run of LHC Run-II by the ATLAS detector, structures and mechanisms of both are introduced in this thesis. Components of ATLAS detector, inner detector, calorimeters and muon spectrometer co-work to record the leptons and hadrons used in the reconstruction of W-boson events. For the special data taking, dedicated detector calibration corrections are introduced first in this document, including the reconstruction and calibration of the hadronic recoil as the neutrino, the momentum calibration and selection efficiency of leptons. The availability of exploiting the high-pile-up data in the calculation of electron corrections to avoid high statistical uncertainty is also tested and validated. Besides, a shower-shape reweighting algorithm is introduced to optimize the identification of electrons from

the electromagnetic calorimeter, and provide a new tool to understand and suppress the residual discrepancy between the energy shapes of electrons in data and simulation. For muon, a customized correction to restore the bias induced by the mis-alignment problem in tracking system acts superior performance than the official version.

The selection of W-boson signal and rejection of backgrounds, particularly the multi-jet background that can't be evaluated through simulation are specifically discussed as well. This document describes an enhanced data-driven method for the multi-jet background evaluation. By switching the "isolation" selection of lepton, inclusive phase space is separated to sets of jets-enriched regions, where the profile and amount of multi-jet background is derived and extrapolated to signal region. A novel correction to hadronic recoil helps to solve the long-term-remained issue in the degraded background modelling and improves the accuracy. Together this method sets an advanced standard to multi-jet background estimation in single W-boson study.

The measurement to W-boson transverse momentum distribution and production cross-sections are performed based on these corrections and modellings with traditional distribution and cross-section measurement methodology. The results of p_T^W measurement sufficiently satisfy the experimental expectation, with less than 1% uncertainty in individual channels. The cross-section measurements achieve the best precision ever obtained at two collision energies and the results will be important inputs in upcoming PDFs calibration. The preliminary result of M_W measurement using low-pile-up data is also presented. Comparing to the previous M_W measurement of LHC Run-I, the uncertainty due to lepton correction is at the same level, while the recoil and multi-jet-estimation related uncertainties obviously decrease, all of which are remarkable regarding the much less W events in low-pile-up data. The ultimate combination of ATLAS results between Run-I and Run-II, with corrected p_T^W, PDFs and other updates are expected to significantly reduce the total uncertainty, providing the most accurate M_W globally.

Bibliography

[1] C. F. von Weizsacker, *The History of Nature*, () 71 (cit. on p. 13).

[2] G. Arnison et al., *Experimental Observation of Isolated Large Transverse Energy Electrons with Associated Missing Energy at s**(1/2) = 540-GeV*, Phys. Lett. **122B** (1983) 103, [,611(1983)] (cit. on pp. 14, 23).

[3] P. Bagnaia et al., *Evidence for Z0 —> e+ e- at the CERN anti-p p Collider*, Phys. Lett. **129B** (1983) 130, [,7.69(1983)] (cit. on p. 14).

[4] M. Baak et al., *The global electroweak fit at NNLO and prospects for the LHC and ILC*, Eur. Phys. J. C **74** (2014) 3046, arXiv: 1407.3792 [hep-ph] (cit. on pp. 14, 24, 25).

[5] ATLAS Collaboration, *Measurement of the W-boson mass in pp collisions at $\sqrt{s} = 7$ TeV with the ATLAS detector*, Eur. Phys. J. C **78** (2018) 110, arXiv: 1701.07240 [hep-ex] (cit. on pp. 14, 24–26, 123, 164).

[6] M. Li et al., *Hadronic recoil reconstruction and calibration for low pile-up runs taken in 2017 and 2018*, tech. rep. ATL-COM-PHYS-2019-078, CERN, 2019, URL: https://cds.cern.ch/record/2657182 (cit. on pp. 16, 101).

[7] C.-N. Yang and R. L. Mills, *Conservation of Isotopic Spin and Isotopic Gauge Invariance*, Phys. Rev. **96** (1954) 191, [,150(1954)] (cit. on p. 17).

[8] S. L. Glashow, *Partial Symmetries of Weak Interactions*, Nucl. Phys. **22** (1961) 579 (cit. on p. 17).

[9] S. Weinberg, *A Model of Leptons*, Phys. Rev. Lett. **19** (1967) 1264 (cit. on p. 17).

[10] A. Salam, *Weak and Electromagnetic Interactions*, Conf. Proc. **C680519** (1968) 367 (cit. on p. 17).

[11] D. J. Gross and F. Wilczek, *Asymptotically Free Gauge Theories - I*, Phys. Rev. **D8** (1973) 3633 (cit. on p. 19).

[12] D. J. Gross and F. Wilczek, *ASYMPTOTICALLY FREE GAUGE THEORIES. 2.*, Phys. Rev. **D9** (1974) 980 (cit. on p. 19).

[13] P. W. Higgs, *Broken Symmetries and the Masses of Gauge Bosons*, Phys. Rev. Lett. **13** (1964) 508, [,160(1964)] (cit. on p. 19).

[14] P. W. Higgs, *Broken symmetries, massless particles and gauge fields*, Phys. Lett. **12** (1964) 132 (cit. on p. 19).

[15] G. S. Guralnik, C. R. Hagen and T. W. B. Kibble, *Global Conservation Laws and Massless Particles*, Phys. Rev. Lett. **13** (1964) 585, [,162(1964)] (cit. on p. 19).

[16] F. Englert and R. Brout, *Broken Symmetry and the Mass of Gauge Vector Mesons*, Phys. Rev. Lett. **13** (1964) 321, [,157(1964)] (cit. on p. 19).

[17] S. D. Drell and T.-M. Yan, *Massive Lepton Pair Production in Hadron-Hadron Collisions at High-Energies*, Phys. Rev. Lett. **25** (1970) 316, [Erratum: Phys. Rev. Lett.25,902(1970)] (cit. on p. 20).

[18] ATLAS and CMS Collaborations, *Combined Measurement of the Higgs Boson Mass in pp Collisions at $\sqrt{s} = 7$ and 8 TeV with the ATLAS and CMS Experiments*, Phys. Rev. Lett. **114** (2015) 191803, arXiv: 1503.07589 [hep-ex] (cit. on pp. 24, 25).

[19] B. Abbott et al., *A measurement of the W boson mass*, Phys. Rev. **D58** (1998) 092003, arXiv: hep-ex/9712029 [hep-ex] (cit. on p. 23).

[20] T. Affolder et al., *Measurement of the W boson mass with the Collider Detector at Fermilab*, Phys. Rev. **D64** (2001) 052001, arXiv: hep-ex/0007044 [hep-ex] (cit. on p. 23).

[21] V. M. Abazov et al., *Improved W boson mass measurement with the DØ detector*, Phys. Rev. **D66** (2002) 012001, arXiv: hep-ex/0204014 [hep-ex] (cit. on p. 23).

[22] V. M. Abazov et al., *Combination of CDF and D0 Results on W Boson Mass and Width*, Phys. Rev. **D70** (2004) 092008, arXiv: hep-ex/0311039 [hep-ex] (cit. on p. 23).

[23] ALEPH Collaboration, S. Schael et al., *Measurement of the W boson mass and width in e^+e^- collisions at LEP*, Eur. Phys. J. C **47** (2006) 309, arXiv: hep-ex/0605011 (cit. on pp. 23, 25).

[24] DELPHI Collaboration, J. Abdallah et al., *Measurement of the Mass and Width of the W Boson in e^+e^- Collisions at $\sqrt{s} = 161 - 209$ GeV*, Eur. Phys. J. C **55** (2008) 1, arXiv: 0803.2534 [hep-ex] (cit. on pp. 23, 25).

[25] L3 Collaboration, P. Achard et al., *Measurement of the mass and the width of the W boson at LEP*, Eur. Phys. J. C **45** (2006) 569, arXiv: hep-ex/0511049 (cit. on pp. 23, 25).

[26] OPAL Collaboration, G. Abbiendi et al., *Measurement of the mass and width of the W boson*, Eur. Phys. J. C **45** (2006) 307, arXiv: hep-ex/0508060 (cit. on pp. 23, 25).

[27] CDF Collaboration, T. Aaltonen et al., *Precise measurement of the W-boson mass with the CDF II detector*, Phys. Rev. Lett. **108** (2012) 151803, arXiv: 1203.0275 [hep-ex] (cit. on p. 25).

[28] D0 Collaboration, V. M. Abazov et al., *Measurement of the W Boson Mass with the D0 Detector*, Phys. Rev. Lett. **108** (2012) 151804, arXiv: 1203.0293 [hep-ex] (cit. on p. 25).

[29] ATLAS Collaboration, *Measurement of the top quark mass in the $t\bar{t} \to$ dilepton channel from $\sqrt{s} = 8$ TeV ATLAS data*, Phys. Lett. B **761** (2016) 350, arXiv: 1606.02179 [hep-ex] (cit. on p. 25).

[30] ALEPH, DELPHI, L3, OPAL Collaborations, LEP Electroweak Working Group, S. Schael et al., *Electroweak Measurements in Electron-Positron Collisions at W-Boson-Pair Energies at LEP*, Phys. Rept. **532** (2013) 119, arXiv: 1302.3415 [hep-ex] (cit. on p. 25).

[31] CDF and D0 Collaborations, T. Aaltonen et al., *Combination of CDF and D0 W-Boson Mass Measurements*, Phys. Rev. D **88** (2013) 052018, arXiv: 1307.7627 [hep-ex] (cit. on p. 25).

[32] G. Aad et al., *Measurement of the angular coefficients in Z-boson events using electron and muon pairs from data taken at $\sqrt{s} = 8$ TeV with the ATLAS detector*, JHEP **08** (2016) 159, arXiv: 1606.00689 [hep-ex] (cit. on pp. 25, 116).

[33] N. Davidson, T. Przedzinski and Z. Was, *PHOTOS interface in C++: Technical and physics documentation*, Comput. Phys. Commun. **199** (2016) 86, arXiv: 1011.0937 [hep-ph] (cit. on p. 25).

[34] *Example ATLAS tunes of Pythia8, Pythia6 and Powheg to an observable sensitive to Z boson transverse momentum*, tech. rep. ATL-PHYS-PUB-2013-017, CERN, 2013, URL: https://cds.cern.ch/record/1629317 (cit. on p. 25).

[35] *Prospects for the measurement of the W-boson transverse momentum with a low pileup data sample at* $\sqrt{s}$ = 13 *TeV with the ATLAS detector*, tech. rep. ATL-PHYS-PUB-2017-021, CERN, 2017, URL: https://cds.cern.ch/record/2298152 (cit. on pp. 27, 28).

[36] *Luminosity determination in pp collisions at* $\sqrt{s}$ = 13 *TeV using the ATLAS detector at the LHC*, tech. rep. ATLAS-CONF-2019-021, CERN, 2019, URL: http://cds.cern.ch/record/2677054 (cit. on pp. 27, 29).

[37] E. Diehl, 'Calibration and Performance of the ATLAS Muon Spectrometer', *Particles and fields. Proceedings, Meeting of the Division of the American Physical Society, DPF 2011, Providence, USA, August 9-13, 2011*, 2011, arXiv: 1109.6933 [physics.ins-det] (cit. on p. 39).

[38] G. Aad et al., *The ATLAS Experiment at the CERN Large Hadron Collider*, JINST **3** (2008) S08003 (cit. on p. 40).

[39] ATLAS Collaboration, *Electron and photon energy calibration with the ATLAS detector using data collected in 2015 at* $\sqrt{s}$ = 13 *TeV*, ATL-PHYS-PUB-2016-015, 2016, URL: https://cds.cern.ch/record/2203514 (cit. on p. 44).

[40] C. Bittrich et al., *In-situ scale factors from Zee events*, tech. rep. ATL-COM-PHYS-2017-757, CERN, 2017, URL: https://cds.cern.ch/record/2268800 (cit. on p. 47).

[41] o. b. o. t. T. g. Podberezko Pavel, *Multi-jet background in low-pile-up runs taken in 2017 and 2018*, tech. rep., CERN, 2017, URL: https://indico.cern.ch/event/649891/contributions/2746585/attachments/1554454/2443938/Reco_And_ID_Effs_in_2017.pdf (cit. on p. 52).

[42] M. Aaboud et al., *Electron reconstruction and identification in the ATLAS experiment using the 2015 and 2016 LHC proton-proton collision data at* $\sqrt{s}$ = *13 TeV*, Submitted to: Eur. Phys. J. (2019), arXiv: 1902.04655 [physics.ins-det] (cit. on p. 55).

[43] N. Andari, J. Mitrevski, K. Brendlinger, P. Sommer and O. A. Ducu, *Electron and photon performance measurements with the ATLAS detector using the 2015-2017 LHC proton-proton collision data*, tech. rep. ATL-COM-PHYS-2019-043, CERN, 2019, URL: https://cds.cern.ch/record/2655306 (cit. on pp. 57, 63).

[44] A. A. Abdelalim, 'Study on the Impact of Cross-Talk in the ATLAS Electromagnetic Calorimeter on the Signal Prediction in the Strip Layer', MA thesis: Geneva U., 2008 (cit. on p. 67).

[45] G. Aad et al., *Muon reconstruction performance of the ATLAS detector in proton–proton collision data at* $\sqrt{s}$ =*13 TeV*, Eur. Phys. J. **C76** (2016) 292, arXiv: 1603.05598 [hep-ex] (cit. on pp. 81, 82).

[46] N. M. Koehler et al., *Muon Efficiency Measurements on the Full Run 2 dataset*, tech. rep. ATL-COM-PHYS-2019-176, CERN, 2019, URL: https://cds.cern.ch/record/2665704 (cit. on p. 83).

[47] N. Koehler et al., *Muon Efficiency Measurements on the Full Run 2 dataset*, ATL-COM-PHYS-2019-176, ANA-MUON-2018-03-INT1, 2019, URL: https://cds.cern.ch/record/2665704 (cit. on p. 85).

[48] ATLAS Collaboration, *Study of alignment-related systematic effects on the ATLAS Inner Detector track reconstruction*, ATLAS-CONF-2012-141, 2012, URL: https://cds.cern.ch/record/1483518 (cit. on pp. 89, 90).

[49] ATLAS Collaboration, *Measurement of W and Z production cross sections in pp collisions at 13 TeV with the ATLAS detector. Auxiliary material*, 2013, URL: https://atlas.web.cern.ch/Atlas/GROUPS/PHYSICS/PAPERS/STDM-2015-03/ (cit. on pp. 101, 147, 161).

[50] M. Aaboud et al., *Jet reconstruction and performance using particle flow with the ATLAS Detector*, Eur. Phys. J. **C77** (2017) 466, arXiv: 1703.10485 [hep-ex] (cit. on p. 102).

[51] A. Dimitrievska, N. Vranjes, M. Schott and M. Boonekamp, *Measurement of m_W at 7 TeV: Hadronic recoil corrections*, (2015), URL: https://cds.cern.ch/record/2013274 (cit. on p. 104).

[52] M. Aaboud et al., *Measurement of the W-boson mass in pp collisions at $\sqrt{s}$ = 7 TeV with the ATLAS detector*, Eur. Phys. J. **C78** (2018) 110, [Erratum: Eur. Phys. J.C78,no.11,898(2018)], arXiv: 1701.07240 [hep-ex] (cit. on p. 110).

[53] S. Agostinelli et al., *GEANT4: A Simulation toolkit*, Nucl. Instrum. Meth. **A506** (2003) 250 (cit. on p. 113).

[54] P. Nason, *A New method for combining NLO QCD with shower Monte Carlo algorithms*, JHEP **11** (2004) 040, arXiv: hep-ph/0409146 (cit. on p. 113).

[55] S. Frixione, P. Nason and C. Oleari, *Matching NLO QCD computations with Parton Shower simulations: the POWHEG method*, JHEP **11** (2007) 070, arXiv: 0709.2092 [hep-ph] (cit. on p. 113).

[56] S. Alioli, P. Nason, C. Oleari and E. Re, *NLO vector-boson production matched with shower in POWHEG*, JHEP **0807** (2008) 060, arXiv: 0805.4802 [hep-ph] (cit. on p. 113).

[57] S. Alioli, P. Nason, C. Oleari and E. Re, *A general framework for implementing NLO calculations in shower Monte Carlo programs: the POWHEG BOX*, JHEP **06** (2010) 043, arXiv: 1002.2581 [hep-ph] (cit. on p. 113).

[58] S. M. T. Sjöstrand and P. Skands, *Brief Introduction to PYTHIA 8.1*, Comput. Phys. Comm. **178** (2008) 85, arXiv: 0710.3820v1 [hep-ph] (cit. on p. 113).

[59] ATLAS Collaboration, *Measurement of the Z/γ^* boson transverse momentum distribution in pp collisions at $\sqrt{s}$ = 7 TeV with the ATLAS detector*, JHEP **09** (2014) 145, arXiv: 1406.3660 [hep-ex] (cit. on p. 113).

[60] P. Golonka and Z. Was, *PHOTOS Monte Carlo: A Precision tool for QED corrections in Z and W decays*, Eur. Phys. J. **C45** (2006) 97, arXiv: hep-ph/0506026 (cit. on pp. 113, 116).

[61] S. Catani and M. Grazzini, *An NNLO subtraction formalism in hadron collisions and its application to Higgs boson production at the LHC*, Phys. Rev. Lett. **98** (2007) 222002, arXiv: hep-ph/0703012 [hep-ph] (cit. on pp. 113, 155).

[62] S. Catani, L. Cieri, G. Ferrera, D. de Florian and M. Grazzini, *Vector boson production at hadron colliders: A Fully exclusive QCD calculation at NNLO*, Phys. Rev. Lett. **103** (2009) 082001, arXiv: 0903.2120 [hep-ph] (cit. on pp. 113, 155).

[63] L.A. Harland-Lang, A. D. Martin, P. Motylinski, R. S. Thorne, *Parton distributions in the LHC era: MMHT 2014 PDFs*, Eur. Phys. J. C **75** (2015) 204, arXiv: 1412.3989 [hep-ph] (cit. on pp. 113, 156).

[64] ATLAS Collaboration, *Measurement of $W^{\pm}$ and Z-boson production cross sections in pp collisions at $\sqrt{s}$ = 13 TeV with the ATLAS detector*, Phys. Lett. B **759** (2016) 601, arXiv: 1603.09222 [hep-ex] (cit. on p. 113).

[65] ATLAS Collaboration, *Measurements of W and Z boson production in pp collisions at $\sqrt{s}$ = 5.02 TeV with the ATLAS detector*, Eur. Phys. J. C **79** (2019) 128, arXiv: 1810.08424 [hep-ex] (cit. on pp. 113, 124, 148, 161).

[66] S. Hoche, F. Krauss, M. Schonherr and F. Siegert, *NLO matrix elements and truncated showers*, JHEP **1108** (2011) 123, arXiv: 1009.1127 [hep-ph] (cit. on p. 113).

[67] A. Wharton, W. Yao and R. Jansky, *ATLAS Inner Detector Track Quality Cuts for Run 2*, tech. rep. ATL-COM-PHYS-2014-1084, CERN, 2014, URL: https://cds.cern.ch/record/1752536 (cit. on p. 114).

[68] ATLAS Collaboration, *Measurement of $W^{\pm}$ and Z-boson production cross sections in pp collisions at $\sqrt{s}$ = 13 TeV with the ATLAS detector*, Phys. Lett. B **759** (2016) 601, arXiv: 1603.09222 [hep-ex] (cit. on p. 118).

[69] H. Atmani et al., *Measurement of the p_{T} spectrum of W- and Z-bosons produced in pp collisions at $\sqrt{s}$ = 5 TeV and 13 TeV in low-pileup runs*, tech. rep. ATL-COM-PHYS-2018-1084, CERN, 2018, URL: https://cds.cern.ch/record/2632159 (cit. on p. 141).

[70] G. D'Agostini, *A Multidimensional unfolding method based on Bayes' theorem*, Nucl. Instrum. Meth. **A362** (1995) 487 (cit. on p. 142).

[71] ATLAS Collaboration, *Luminosity determination in pp collisions at $\sqrt{s}$ = 8 TeV using the ATLAS detector at the LHC*, Eur. Phys. J. C **76** (2016) 653, arXiv: 1608.03953 [hep-ex] (cit. on pp. 148, 149).

[72] ATLAS Collaboration, *Precision measurement and interpretation of inclusive W^+ , W^- and Z/γ^* production cross sections with the ATLAS detector*, Eur. Phys. J. C **77** (2017) 367, arXiv: 1612.03016 [hep-ex] (cit. on pp. 149, 157).

[73] G. Avoni et al., *The new LUCID-2 detector for luminosity measurement and monitoring in ATLAS*, JINST **13** (2018) P07017 (cit. on p. 149).

[74] A. Valassi, *Combining correlated measurements of several different physical quantities*, Nucl. Instrum. Meth. A **500** (2003) 391 (cit. on p. 151).

[75] W. F. L. Hollik, *Radiative Corrections in the Standard Model and Their Rôle for Precision Tests of the Electroweak Theory*, Fortsch. Phys. **38** (1990) 165 (cit. on p. 155).

[76] Particle Data Group, K. A. Olive et al., *Review of Particle Physics*, Chin. Phys. C **38** (2014) 090001 (cit. on p. 156).

[77] S. Dulat et al., *New parton distribution functions from a global analysis of quantum chromodynamics*, Phys. Rev. D **93** (2016) 033006, arXiv: 1506.07443 [hep-ph] (cit. on pp. 156, 157).

[78] R. D. Ball et al., *Parton distributions from high-precision collider data*, Eur. Phys. J. C **77** (2017) 663, arXiv: 1706.00428 [hep-ph] (cit. on p. 156).

[79] H1 and ZEUS Collaborations, *Combination of measurements of inclusive deep inelastic $e^{\pm}p$ scattering cross sections and QCD analysis of HERA data*, Eur. Phys. J. C **75** (2015) 580, arXiv: 1506.06042 [hep-ex] (cit. on p. 156).

[80] S. Alekhin, J. Blümlein, S. Moch and R. Plačakytė, *Parton distribution functions, α_s, and heavy-quark masses for LHC Run II*, Phys. Rev. D **96** (2017) 014011, arXiv: 1701.05838 [hep-ph] (cit. on p. 156).

Acknowledgements

The finalization of this section is postponed due to a serious historical event, the corna-19 pandemic. No one could escape from its influence and I can't express more gratitude to those devoting to fight against it. My mind is also deeply changed (of course with no acknowledgment). This disaster sets us in the world described by "The Plague" of Albert Camus, confronting with the inherent and constant absurdity of universe.

In physics, we're trying to figure out everything the nature wants to show, to untangle every myth the nature wants to tell, like loyal servants. And the CERN was once the Great Potala in my imagination. However it's not correct. The nature has no mercy or crudity. Nowadays one's survival relies on the whole industry, and the communication is between cultures via internet. Billions and the history make my body and thought. I'm not defined by myself or the nature but we're defined by ourselves, and the essence of man is ultimately closer to the sum of all social relations. The supports from others form the will of moving forward which preserves the civilization in time and selection. I'd like to believe it's this will, written in the gene, that lets the human climb the Mount Everest or ship to the moon, not because the mountain or the moon is there. And to the people supported me to find some values in the particle physics and finish this thesis, I must present my thanks.

All others are my saviors. It's a pity I can't thank one-by-one, hereby these acknowledgements are for people around me. I'm deeply indebted to my two supervisors, Mr. Maarten Boonekamp and Prof. Zhengguo Zhao, who not only teach me the knowledges and methodologies of particle physics and support my healthy living, but also uncloud my outlooks. Everything I learnt and cognized during the first 20 years was discrete and partial. It's under their supervisions that I integrated these parts and built a system of understanding and cogitation to have my own way to think, talk and live. I'm extremely grateful to Prof. Yanwen Liu, Prof. Matthias SCHOTT , Prof. Yusheng Wu and Mr. Aram Apyan. Thanks for their attendance of my defense, their inspiring questions and valuable suggestions to my work. And Prof. Jianbei Liu, despite I'm not his student officially, he lends me all his instructions generously and guides me entering the hall of experimental particle physics. I would also like to extend my deepest gratitude to all my colleagues in the two ATLAS groups I attend, particularly Fabrice, Oleh, Nansi, Ludovica, Mykola, Jan, Jakub, Mirta, Yufeng, Changqiao, Hanlin and Yicheng, who offer me their priceless cares, kindness and help. Without them I can't make it to the end.

The CERN is no doubt the frontline of human exploration. Its instruments and itself are the fruit of human

civilization. It's an organization of people with real belief and culture. I hold great thankfulness to the experiments, the data, the software, the computing, the hostage, and everything it selflessly provides. USTC changed my fate at the age of 15. It illustrates me how a world of world looks like, gives me the chance to choose and equips me with the will of truth. It definitely holds the spirit of science and investigation, and passes it to all her student. CEA/Irfu offers me the chance to leave my motherland and embrace the world for the first time. It provides superior supports in both experiments and life. Many thanks to USTC and CEA/Irfu for mostly making me who I am and lifting me to the position where I'm standing. And special thanks to the Chinese Scholarship Council for the supports to my living and research in France.

université PARIS-SACLAY | ÉCOLE DOCTORALE PHENIICS

Titre : Mesures des propriétés du boson W à partir de données à bas taux d'empilement enregistrées par le détecteur ATLAS, auprès du LHC, à des énergies de $\sqrt{s}$ = 5 et 13 TeV

Mots clés : Boson W, ATLAS, Physique des particules, Electron

Résumé : Cette thèse présente des mesures des propriétés du boson W à partir de données a bas taux d'empilement enregistrées par le détecteur ATLAS, auprès du LHC, a des énergies de $\sqrt{s} = 5$ et 13 TeV. Ces données permettent une reconstruction optimale de l'énergie transverse manquante et ont un intérêt particulier pour la mesure précise de la production du W. Des calibrations dédiées ont été développées spécifiquement pour ces échantillons, comme la reconstruction et la calibration du recul hadronique, la calibration de la mesure de l'impulsion des leptons, et la modélisation de leur efficacité de sélection. De plus, un nouvel algorithme est présente qui permet de corriger la modélisation du développement des gerbes électromagnétiques dans le calorimètre d'ATLAS, résultant en un meilleur accord entre données et simulation pour les variables d'identification associées. La sélection d'évènements W et l'estimation des bruits de fond sont ensuite discutées en détail, avec une attention particulière portée sur le bruit de fond venant de la production de jets, dont une nouvelle méthode permet une évaluation améliorée. Ces résultats sont utilisés pour les mesures des spectres en impulsion transverse des W, et de leur section efficace de production. Des études préliminaires concernant l'application de ces données pour la mesure de la masse du W sont enfin présentées.

Title : Measurements of W boson properties at $\sqrt{s} = 5$ and 13 TeV with the ATLAS detector at the LHC

Keywords : W boson, ATLAS, particle physics, Electron

Abstract : This thesis presents measurements of W boson properties at center-of-mass energies of $\sqrt{s} = 5$ and 13 TeV with special low-pile-up data-set recorded by the ATLAS detector at the LHC. Thanks to an optimal reconstruction of missing transverse momentum, such data have particular importance for precision measurements of W-boson production. Dedicated detector calibration corrections are introduced first in this document, including the reconstruction and energy calibration of the hadronic recoil, the momentum calibration and selection efficiency of leptons. Besides, a new shower-shape reweighting algorithm optimizes the identification electrons with the electromagnetic calorimeter. The thesis describes the selection the W boson signal and devotes specific attention to the evaluation of backgrounds, presenting in particular a new method for the data-driven estimation of backgrounds from multi-jet production. Based on these studies and theoretical predictions, the W-boson transverse momentum distribution and production cross-sections are measured with high precision at two center-of-mass energies. Preliminary studies of the application of these data to the measurement of the W-boson mass are also presented.

Université Paris-Saclay
Espace Technologique / Immeuble Discovery
Route de l'Orme aux Merisiers RD 128 / 91190 Saint-Aubin, France